Effect of residual impurities in the ITS-90 freezing point of aluminium: a systematic evaluation of contemporary correction methodologies

by

Rodrigo Da Silva

Department of Physics

Royal Holloway, University of London

This thesis is submitted for the degree of

Doctor of Philosophy

February 2017

Declaration of Authorship

I, Rodrigo Da Silva, hereby declare that this thesis and the work presented in it is entirely my own. Where information has been derived from other sources, I confirm that this has been clearly stated in the thesis.

Signature: _____

Date: _____

Abstract

The International Temperature Scale of 1990 (ITS-90) defines that the calibration of standard platinum resistance thermometers (SPRTs) is based upon the use of temperature fixed points. Since residual impurities (even below parts-per-million levels) present in the fixed point cells influence their realisation temperature (in the order of a few millikelvins), the fixed point material employed in the cell must be ≥ 99.9999 % pure. Impurities usually constitute the most substantial contribution to the uncertainty of primary SPRT calibrations. With a view to tackle this matter, the Consultative Committee for Thermometry (CCT) of the Bureau International of Weights and Measures (BIPM) has recommended the use of a specific correction methodology (the sum of individual estimates, SIE) but other methods have also emerged, each being advocated by a particular National Metrology Institute.

The study reported in this thesis aims at investigating the application of seven available correction methodologies to the freezing point of aluminium (660.323 °C) to identify the most consistent methods together with any difficulties related to their implementation. In order to achieve this, a suite of five aluminium fixed point cells have been constructed according to a rigorous protocol, each cell using metal samples sourced from a different supplier. Glow discharge mass spectrometry (GDMS) assays have been obtained from three independent laboratories. Besides, for each cell constructed, a set of long duration freezing curves have been measured under nominally identical conditions. They provided the basis for the calculations of the correction methodologies investigated. The most consistent corrections were achieved with a hybrid method that combines the SIE and the overall maximum estimate (OME): the hybrid SIE/modified OME method. Furthermore, the correction methodology based on the fitting of a Scheil solidification model to the measured freezing curves was found to be highly consistent, provided certain constraints are applied.

Acknowledgements

First and foremost, I shall thank and praise the Lord God Almighty for his wondrous love and mercy, for his salvation, his blessings, for choosing me and always carrying me all the way to victory – all of which I do not deserve but which are proof of His love for me. I also thank Him for the project He has for me, which has been unveiling every day in my life, leading me through ways that are beyond my comprehension (a major part being the family I started thanks to the PhD, during which I met the love of my life Paula).

I dedicate this work to my beloved wife Paula and newly born son Isaac, who are the reason why I breathe. I could only accomplish this remarkable achievement because of their constant support and encouragement. I also have to thank all my family back in Brazil, especially the ones who raised me and kept me motivated: my grandmother Alice (*in memoriam*), my mother Terezinha and my aunt Cida. I am also grateful for the help and support from my friends and family in Christ who kept me in their prayers.

I would like to thank Dr. Andrew Casey for being my advisor, for all his help and guidance. I also have to thank Dr. Graham Machin and Dr. Jonathan Pearce for seeing in me the potential to pursue this degree, for the unique opportunity to be part of the thermometry group at the National Physical Laboratory and do this research in their facilities, and for all their efforts to help and encourage me until the end. I also want to thank the colleagues at NPL that somehow contributed to my research, especially Dr. Radka Veltcheva, who helped me considerably.

This research was carried out with the support of CNPq (National Council for Scientific and Technological Development – Brazil) and was also funded by the EURAMET European Metrology Research Programme (EMRP) project 'Novel Techniques for Traceable Temperature Dissemination (NOTED)'.

O the depth of the riches both of the wisdom and knowledge of God! How unsearchable are his judgments, and his ways past finding out!

For who hath known the mind of the Lord? or who hath been His counsellor?

Or who hath first given to Him, and it shall be recompensed unto him again?

For of Him, and through Him, and to Him, are all things: to whom be glory for ever. Amen.

Romans 11:33-36

Table of Contents

1. **Introduction** 21

1.1. The need for an international scale 21

1.2. An overview of the ITS-90 22

1.3. Motivation and objective of the research presented in this thesis 24

2. **The state of the art of realising the defining fixed points of the International Temperature Scale of 1990 (ITS-90)** 27

2.1. Platinum Resistance Thermometry and the ITS-90 27

2.2. Fixed point cells 32

2.2.1. Definition and related terminology 32

2.2.2. Working principle of the aluminium freezing point 34

2.2.3. Essential technical requirements to establish reproducible experimental conditions for fixed point cells 36

2.3. Addressing the impurity-related aspects and effects 40

2.3.1. Fundamentals of the behaviour of impurities in phase transitions 41

2.3.2. Current methodologies for estimating the effect of impurities in fixed point cells 44

2.3.2.1. Sum of Individual Estimates (SIE) 44

2.3.2.2. Overall Maximum Estimate (OME) 47

2.3.2.3. Hybrid SIE/Modified OME 48

2.3.2.4. Scheil model 49

2.3.2.5. Gradient method 51

2.3.2.6. Thermal analysis 52

2.3.2.7. Direct cell comparison 54

2.3.2.8. Difficulties in applying the methodologies 56

2.3.2.9. Controversy around the topic 57

2.3.3. Previous investigations at the freezing point of aluminium 58

2.3.4. Delimitation of the study 64

3. Construction of the aluminium cells 66
3.1. Selection of materials 66
3.1.1. Description of the aluminium samples 67
3.1.2. Description of the graphite components 68
3.1.3. Description of the quartz tubes 70
3.1.4. Details of the argon gas 70
3.1.5. Other materials 71
3.2. Preparation of materials 72
3.2.1. Handling and inspection of parts 72
3.2.2. Auxiliary equipment 72
3.2.3. Further cleaning of quartz parts 73
3.2.4. Furnace tests 73
3.2.5. Manufacture of gaskets 73
3.2.6. Baking of graphite pieces 75
3.3. Construction of cells 79
3.3.1. Design of the fixed point crucibles 79
3.3.2. Procedure for casting the aluminium ingots 83
3.3.3. Final assembly of the cells 88
3.3.4. Basic characteristics of each cell after the construction 90

4. Evaluation of aluminium cells 92
4.1. Equipment 92
4.1.1. Furnace 93
4.1.2. Standard platinum resistance thermometers 98
4.1.3. Thermometry bridge 100
4.1.4. Standard resistor 100
4.1.5. Pre-heat furnace 101
4.1.6. Triple point of water reference cells 101
4.1.7. Reference aluminium cell 102
4.1.8. Auxiliary equipment 103
4.1.9. Data acquisition 103

4.2. Measurement of phase transition curves 104
4.2.1. Melting curves 104
4.2.2. Freezing curves 107
4.2.2.1. Cell comparisons 109
4.2.2.1.1. Determination of the self-heating effect 110
4.2.2.1.2. Hydrostatic head correction 112
4.3. Chemical analyses 113
4.3.1. Sample preparation 114
4.4. Numerical conversions and calculations 117
4.4.1. Converting elapsed time into solid fraction 117
4.4.2. Converting resistance ratio into temperature 118

5. Results of chemical assays and measurements of freezing curves 121
5.1. Chemical assays provided by the metal suppliers 121
5.2. GDMS analyses provided by third party laboratories 124
5.3. Freezing curve measurements 138

6. Results for the calculations of the various impurity correction methodologies investigated 144
6.1. Sum of individual estimates correction and uncertainty calculation 144
6.2. Overall maximum estimate uncertainty calculation 156
6.3. Hybrid SIE / modified OME correction and uncertainty calculation . . . 168
6.4. Scheil model correction and uncertainty calculation 186
6.4.1. Scheil model – free k 186
6.4.2. Scheil model ($k = 0$) 205
6.5. Gradient method correction and uncertainty calculation 224
6.6. Thermal analysis correction and uncertainty calculation 233

6.7. Direct cell comparison 243

6.8. Summary of results 252

7. Conclusions and suggestions for further research 260

7.1. Suggestions for further research 265

References 267

Appendix A 271

List of figures

Figure 1: Detail of the ITS-90, showing the range which has the SPRT as the interpolation instrument 27

Figure 2: Structure of a typical aluminium freezing curve 35

Figure 3: Discontinuity in measurements due to the withdrawal of the thermometer 36

Figure 4: Position of an aluminium fixed point cell in the three-zone furnace 39

Figure 5: Fit of the Scheil expression to a measured freezing curve 50

Figure 6: The same freezing curve now analysed by the gradient method 51

Figure 7: Example of thermal analysis of a freeze plateau 53

Figure 8: Metal samples supplied to this study 68

Figure 9: A set of specialty graphite components selected to be baked 69

Figure 10: Graphite felt discs cut to fit inside the quartz envelope 69

Figure 11: Highlights of the manufacture of the silicone gasket 74

Figure 12: Set-up for the bake of the graphite pieces and casting of the ingots .. 76

Figure 13: Testing the seals in the metal cap with the leak detector 77

Figure 14: Graphite crucible assembly during bake at 1100 °C 78

Figure 15: Schematic diagram of the aluminium fixed point open cell design ... 80

Figure 16: Dimensions of the crucible and re-entrant well 81

Figure 17: Full-scale crucible assembly 82

Figure 18: Block of aluminium supplied by Sumitomo ready to be cut 83

Figure 19: Weighing the portions of aluminium to transfer to the crucible 84

Figure 20: Crucible containing 200 g of aluminium shot, ready to be melted 84

Figure 21: Inspection of the ingot formed from the first load of metal 86

Figure 22: Measurement of the height of the re-entrant well to be pushed through the metal once it becomes liquid 87

Figure 23: Inspection of the ingot after insertion of the re-entrant well 88

Figure 24: An assembled aluminium cell ready for testing 89

Figure 25: All five cells stored after the construction stage 90

Figure 26: Apparatus for inducing and maintain the freezing curves 93

Figure 27: Set-point stability of furnace Fluke 9114 A63118 after freezing of cell Al-E (ESPI) 95

Figure 28: Results of the thermal profile measurements performed with various zone controller settings 97

Figure 29: Details of the sensing element of the SPRT Chino RS-129-03 98

Figure 30: Melting of cell Al-E in 14 August 2014 105

Figure 31: Detailed melting of cell Al-E (ESPI) with SPRT Chino RS129-03 in 14 August 2014 106

Figure 32: Typical raw data of the freezing of cell Al-H (Honeywell) 108

Figure 33: A sequence of automatic measurements to calculate the self-heating effect of the SPRT Chino RS129-03 in the cell Al-E 112

Figure 34: Preparation of the samples for GDMS analysis 115

Figure 35: SEM results of aluminium samples 116

Figure 36: Identification of the end of the freezing curve in cell Al-H (Honeywell) in 28 July 2014 118

Figure 37: Freezing of cell Al-H (28 July 2014) after data conversions 119

Figure 38: Detail of the graph of the freezing of cell Al-H (28 July 2014) after the required data conversions 120

Figure 39: Elements commonly found in trace amounts in high purity Al 123

Figure 40: Uncertainties declared by AQura for the 70 elements scanned 136

Figure 41: The four freezing curves measured in cell Al-A (alfa Aesar) 138

Figure 42: The four freezing curves measured in cell Al-E (ESPI) 139

Figure 43: The four freezing curves measured in cell Al-H (Honeywell) 139

Figure 44: The four freezing curves measured in cell Al-N (New Metals) 140

Figure 45: The four freezing curves measured in cell Al-S (Sumitomo) 140

Figure 46: Detail of representative freezing curves for each of the five cells 144

Figure 47: Modified OME component for cell Al-S, curve 1 177

Figure 48: Modified OME component for cell Al-S, curve 2 177

Figure 49: Modified OME component for cell Al-S, curve 3 178

Figure 50: Modified OME component for cell Al-S, curve 4 178

Figure 51: Modified OME fittings of four freezing curves with cell Al-A 180

Figure 52: Modified OME fittings of four freezing curves with cell Al-E 181

Figure 53: Modified OME fittings of four freezing curves with cell Al-H 182

Figure 54: Modified OME fittings of four freezing curves with cell Al-N 183

Figure 55: Scheil model applied to cell Al-S, curve 1 (lower limit) 187

Figure 56: Scheil model applied to cell Al-S, curve 2 (lower limit) 188

Figure 57: Scheil model applied to cell Al-S, curve 3 (lower limit)..... 188

Figure 58: Scheil model applied to cell Al-S, curve 4 (lower limit) 189

Figure 59: Scheil model applied to cell Al-S, curve 1 (upper limit) 189

Figure 60: Scheil model applied to cell Al-S, curve 2 (upper limit) 190

Figure 61: Scheil model applied to cell Al-S, curve 3 (upper limit) 190

Figure 62: Scheil model applied to cell Al-S, curve 4 (upper limit) 191

Figure 63: Scheil model applied to cell Al-A (Alfa Aesar), curve 1 192

Figure 64: Curves for cell Al-A fitted with high *k* values, lower range 193

Figure 65: Curves for cell Al-A fitted with high *k* values, upper range 194

Figure 66: Scheil model applied to cell Al-E (ESPI); *free k*; lower limit 196

Figure 67: Scheil model applied to cell Al-E (ESPI); *free k*; upper limit 197

Figure 68: Scheil model applied to cell Al-H (Honeywell); *free k*; lower limit 199

Figure 69: Scheil model applied to cell Al-H (Honeywell); *free k*; upper limit 200

Figure 70: Scheil model applied to cell Al-N (New Metals); *free k*; lower limit ... 202

Figure 71: Scheil model applied to cell Al-N (New Metals); *free k*; upper limit ... 203

Figure 72: Scheil model applied to curve 1 of cell Al-S; $k = 0$; lower limit 205

Figure 73: Scheil model applied to curve 2 of cell Al-S; $k = 0$; lower limit 206

Figure 74: Scheil model applied to curve 3 of cell Al-S; $k = 0$; lower limit 206

Figure 75: Scheil model applied to curve 4 of cell Al-S; $k = 0$; lower limit 207

Figure 76: Scheil model applied to curve 1 of cell Al-S; $k = 0$; upper limit 207

Figure 77: Scheil model applied to curve 2 of cell Al-S; $k = 0$; upper limit 208

Figure 78: Scheil model applied to curve 3 of cell Al-S; $k = 0$; upper limit 208

Figure 79: Scheil model applied to curve 4 of cell Al-S; $k = 0$; upper limit 209

Figure 80: Scheil model applied to curve 1 of cell Al-A (Alfa Aesar); $k = 0$ 211

Figure 81: Curves (cell Al-A) fitted with Scheil equation after the range adjustments; lower limit, $k = 0$ 212

Figure 82: Curves (cell Al-A) fitted with Scheil equation after the range adjustments; upper limit, $k = 0$ 213

Figure 83: Scheil model applied to cell Al-E (ESPI); $k = 0$; lower limit 215

Figure 84: Scheil model applied to cell Al-E (ESPI); $k = 0$; upper limit 216

Figure 85: Scheil model applied to cell Al-H (Honeywell); $k = 0$; lower limit ... 218

Figure 86: Scheil model applied to cell Al-H (Honeywell); $k = 0$; upper limit ... 219

Figure 87: Scheil model applied to cell Al-N (New Metals); $k = 0$; lower limit 221

Figure 88: Scheil model applied to cell Al-N (New Metals); $k = 0$; upper limit 222

Figure 89: Gradient method applied to curve 1 of cell Al-S (Sumitomo) 224

Figure 90: Gradient method applied to curve 2 of cell Al-S (Sumitomo) 225

Figure 91: Gradient method applied to curve 3 of cell Al-S (Sumitomo) 225

Figure 92: Gradient method applied to curve 4 of cell Al-S (Sumitomo) 226

Figure 93: Gradient method applied to cell Al-A (Alfa Aesar) 228

Figure 94: Gradient method applied to cell Al-E (ESPI) 229

Figure 95: Gradient method applied to cell Al-H (Honeywell) 230

Figure 96: Gradient method applied to cell Al-N (New Metals) 231

Figure 97: Thermal analysis method applied to curve 1 of cell Al-S 234

Figure 98: Thermal analysis method applied to curve 2 of cell Al-S 234

Figure 99: Thermal analysis method applied to curve 3 of cell Al-S 235

Figure 100: Thermal analysis method applied to curve 4 of cell Al-S 235

Figure 101: Thermal analysis method applied to curve 1 of cell Al-A 237

Figure 102: Thermal analysis method applied to cell Al-A (Alfa-Aesar) 238

Figure 103: Thermal analysis method applied to cell Al-E (ESPI) 239

Figure 104: Thermal analysis method applied to cell Al-H (Honeywell) 240

Figure 105: Thermal analysis method applied to cell Al-N (New Metals) 241

Figure 106: SPRT measurements to determine the self-heating effect of the sensor inside the aluminium cell Al-S (Sumitomo) 244

Figure 107: SPRT measurements to determine the self-heating effect of the sensor inside cell 768 (triple point of water) 244

Figure 108: Results of the comparison traced to the national standard, cell ‘Al sealed’ 250

Figure 109: Comparison of the corrections yielded by the different methods investigated, for the five cells 256

List of tables

Table 1: Defining fixed points of the ITS-90 23

Table 2: Constants of the ITS-90 reference functions (range below TPW) 31

Table 3: Constants of the ITS-90 reference functions (range above TPW) 32

Table 4: Values of the liquidus slopes of impurities in aluminium in the low concentration limit 45

Table 5: Uncertainty budget for the direct comparison of cells 55

Table 6: Basic characteristics concerning the mass of metal and immersion depth of each assembled aluminium crucible 91

Table 7: Thermal profile tests of furnace Fluke 9114 A63118 done with cell Al-H (Honeywell) and SPRT Chino RS129-03 97

Table 8: Thermal profile tests of furnace Carbolite CTF 12/100/700 102

Table 9: Properties of materials used as ITS-90 fixed points in the range above 0 °C 113

Table 10: Summary of the chemical assays provided by the metal suppliers 122

Table 11: Results of the GDMS analyses for batch of metal from Alfa Aesar 125

Table 12: Results of the GDMS analyses for batch of metal from ESPI Metals 127

Table 13: Results of the chemical analyses for batch of metal from Honeywell 129

Table 14: Results of the GDMS analyses for batch of metal from New Metals 131

Table 15: Results of the GDMS analyses for batch of metal from Sumitomo 133

Table 16: Uncertainties declared by AQura for the 70 elements scanned 137

Table 17: Calculation of SIE correction and uncertainty for Al metal sample from Sumitomo based on the assay provided by the metal supplier ... 146

Table 18: Calculation of SIE correction and uncertainty for Al metal sample from Sumitomo based on the chemical analysis supplied by AQura 148

Table 19: Calculation of SIE correction and uncertainty for Al metal sample from Sumitomo based on the chemical analysis supplied by NRC 150

Table 20: Calculation of SIE correction and uncertainty for Al metal sample from Sumitomo based on the chemical analysis supplied by NIM 152

Table 21: Summary of SIE results 154

Table 22: Calculation of OME estimate and uncertainty for Al metal sample from Sumitomo based on the assay provided by the metal supplier ... 158

Table 23: Calculation of OME estimate and uncertainty for Al metal sample from Sumitomo based on the assay provided by AQura 160

Table 24: Calculation of OME estimate and uncertainty for Al metal sample from Sumitomo based on the assay provided by NRC 162

Table 25: Calculation of OME estimate and uncertainty for Al metal sample from Sumitomo based on the assay provided by NIM 164

Table 26: Summary of OME results 166

Table 27: Calculation of the hybrid SIE correction and uncertainty for sample from Sumitomo based on the assay from the metal supplier 169

Table 28: Calculation of the hybrid SIE correction and uncertainty for Al metal sample from Sumitomo based on the assay by Aqura 171

Table 29: Calculation of the hybrid SIE correction and uncertainty for Al metal sample from Sumitomo based on the assay by NRC 173

Table 30: Calculation of the hybrid SIE correction and uncertainty for Al metal sample from Sumitomo based on the assay by NIM 175

Table 31: Results of Hybrid SIE/Modified OME methodology for cell Al-S 179

Table 32: Results of the hybrid SIE/modified OME methodology for cell Al-A 180

Table 33: Results of Hybrid SIE/Modified OME methodology for cell Al-E 181

Table 34: Results of Hybrid SIE/Modified OME methodology for cell Al-H 182

Table 35: Results of Hybrid SIE/Modified OME methodology for cell Al-N 183

Table 36: Summary of hybrid SIE/modified OME results 185

Table 37: Estimates based on least square fitting of Scheil equation to the freezing curves measured with cell Al-S (Sumitomo) 191

Table 38: Results based on least square fitting of Scheil equation to the freezing curves measured with cell Al-S (Sumitomo) 191

Table 39: Estimates based on least square fitting of Scheil equation to the freezing curves measured with cell Al-A (Alfa Aesar) 194

Table 40: Results based on least square fitting of Scheil equation to the freezing curves measured with cell Al-A (Alfa Aesar) 195

Table 41: Estimates based on least square fitting of Scheil equation to the freezing curves measured with cell Al-E (ESPI) 197

Table 42: Results based on least square fitting of Scheil equation to the freezing curves measured with cell Al-E (ESPI) 198

Table 43: Estimates based on least square fitting of Scheil equation to the freezing curves measured with cell Al-H (Honeywell) 200

Table 44: Results based on least square fitting of Scheil equation to the freezing curves measured with cell Al-H (Honeywell) 201

Table 45: Estimates based on least square fitting of Scheil equation to the freezing curves measured with cell Al-N (New Metals) 203

Table 46: Results based on least square fitting of Scheil equation to the freezing curves measured with cell Al-N (New Metals) 204

Table 47: Estimates based on least square fitting of Scheil equation to the freezing curves measured with cell Al-S (Sumitomo) 209

Table 48: Results based on least square fitting of Scheil equation to the freezing curves measured with cell Al-S (Sumitomo) 209

Table 49: Estimates based on least square fitting of Scheil equation (with $k = 0$) to the freezing curves measured with cell Al-A (Alfa Aesar) ... 214

Table 50: Results based on least square fitting of Scheil equation (with $k = 0$) to the freezing curves measured with cell Al-A (Alfa Aesar) 214

Table 51: Estimates based on least square fitting of Scheil equation to the freezing curves measured with cell Al-E (ESPI) 216

Table 52: Results based on least square fitting of Scheil equation to the freezing curves measured with cell Al-E (ESPI) 217

Table 53: Estimates based on least square fitting of Scheil equation to the freezing curves measured with cell Al-H (Honeywell) 219

Table 54: Results based on least square fitting of Scheil equation to the freezing curves measured with cell Al-H (Honeywell) 220

Table 55: Estimates based on least square fitting of Scheil equation to the freezing curves measured with cell Al-N (New Metals) 222

Table 56: Results based on least square fitting of Scheil equation to the freezing curves measured with cell Al-N (New Metals) 223

Table 57: Results of the gradient method for cell Al-S 226

Table 58: Results of the gradient method for cell Al-A 228

Table 59: Results of the gradient method for cell Al-E 229

Table 60: Results of the gradient method for cell Al-H 230

Table 61: Results of the gradient method for cell Al-N 231

Table 62: Results of the thermal analysis method for cell Al-S 236

Table 63: Results of the thermal analysis method for cell Al-A 238

Table 64: Results of the thermal analysis method for cell Al-E 239

Table 65: Results of the thermal analysis method for cell Al-H 240

Table 66: Results of the thermal analysis method for cell Al-N 241

Table 67: Uncertainty budget for the direct comparison of cells 245

Table 68: Detailed description of the standard uncertainties involved in the direct comparison of cells 246

Table 69: Results of the SPRT resistance measurements and the extrapolation of the means to 0 mA 248

Table 70: Calculation of *W* values for the cells used in the comparison 249

Table 71: Results of the corrections assigned to the five aluminium cells tested ... 250

Table 72: Corrections obtained with the various methods tested for cell Al-A 252

Table 73: Corrections obtained with the various methods tested for cell Al-E 253

Table 74: Corrections obtained with the various methods tested for cell Al-H 253

Table 75: Corrections obtained with the various methods tested for cell Al-N 254

Table 76: Corrections obtained with the various methods tested for cell Al-S 254

Table 77: Summary of the results according to the various methodologies investigated for the five aluminium cells constructed 255

Chapter 1

Introduction

Temperature is a property of matter that is very familiar to almost everyone, even though its presence may usually be unnoticed. Most people intuitively have a qualitative idea of temperature; for example, how hot or cold something is (or in other words, the ‘degree’ of hotness/coldness of an object) [1]. There are claims that temperature is the most measured quantity in industry as practically every process is temperature dependent. Temperature measurement evolved with and was demanded by the development of science (a more detailed historical perspective can be found in [2, 3, 4]). Taking into consideration the important role that temperature plays, its accurate measurement is pivotal in a broad variety of industrial applications, namely: aerospace, environmental, biomedical, pharmaceutical, petrochemical, superconductivity, energy, cryogenic engineering, liquid natural gas, electrical, food engineering and processing, plastics, polymers, glass, ceramics, refractories, steel and semiconductors, among others. Accuracy in thermometry is necessary to ensure the maximum efficiency in processes and quality of products [5, 6].

1.1. The need for an international scale

At the time the first temperature scales were devised, artisans would construct their thermometers according to their own arbitrary parameters and later standards. Lack of precision was a limitation for the construction of thermometers. The need for a uniform temperature scale emerged as the first prototypes for the metre were about to be constructed, in 1878, since variations in temperature (due to thermal expansion of the

platinum-iridium metre bars) had to be monitored in order to maintain the stability and agreement of the value of the metre artefact standard. Two mercury-in-glass thermometers, of very good quality, were to be supplied with each metre prototype [3].

The first International Temperature Scale was devised in 1927 (the ITS-27) with the objective of providing a practical scale, based on easily reproducible measurement methods. At its heart were fixed points of defined temperature and stable interpolating instruments. After the adoption of this scale, it has undergone periodical revisions, which in turn, originated several successor scales in 1948, 1960, 1968 and 1990 [7].

1.2. An overview of the ITS-90

In 1989 the International Committee of Weights and Measures, CIPM, adopted the International Temperature Scale of 1990, the ITS-90, as the successor of both the International Practical Temperature Scale of 1968 (amended in 1975) and the Provisional Temperature Scale of 1976 (0.5 K to 30 K) [8, 9]. It occurred after the request contained in Resolution 7 of the 18th General Conference of Weights and Measures (CGPM) of 1987. According to that document, the unit of the physical quantity thermodynamic temperature, *T*, was defined as being the kelvin, symbol K, which is the fraction 1/273.16 of the thermodynamic temperature of the triple point of water. However, due to historical reasons, it is still regular practice to express temperatures in relation to its difference from the ice point (273.15 K), the so-called Celsius temperature, *t* (whose unit is the degree Celsius, °C). Following this perspective, the equivalence between these is given by (equation 1):

$$\boldsymbol{t/°C = T/K - 273.15} \tag{1}$$

The ITS-90 covers the range from 0.65 K up to the highest temperature measurable, by means of the Planck radiation law using monochromatic radiation. According to ITS-90, T_{90} is defined through a set of interpolating instruments that cover each part of the scale. In the range between 0.65 K and 5.0 K T_{90} is defined by vapour-pressure temperature relations of ^{3}He and ^{4}He and the range from 3.0 K and the triple point of neon (24.5561 K) is defined by a helium gas thermometer. Between the triple point of

equilibrium hydrogen (13.8033 K) and the freezing point of silver (961.78 °C) it is interpolated by standard platinum resistance thermometers (SPRTs). Above this temperature, the combination of one defining fixed point and the Planck radiation law in ratio form is used to define T_{90}. The ITS-90 defining fixed points are listed in table 1.

Substance	**Definition**	**Temperature**		W_r (T_{90})
		T_{90} /K	t_{90} /°C	
He	Vapour	3 to 5	–270.15 a –268.15	
e-H_2	Triple point	13.8033	–259.3467	0.001 190 07
e-H_2 (or He)	Vapour pressure *	≈ 17	≈ –256.15	0.002 296 46
e-H_2 (or He)	Vapour pressure *	≈ 20.3	≈ –252.85	0.004 235 36
Ne	Triple point	24.5561	–248.5939	0.008 449 74
O_2	Triple point	54.3584	–218.7916	0.091 718 04
Ar	Triple point	83.8058	–189.3442	0.215 859 75
Hg	Triple point	234.3156	–38.8344	0.844 142 11
H_2O	Triple point	273.16	0.01	1.000 000 00
Ga	Melting	302.9146	29.7646	1.118 138 89
In	Freezing	429.7485	156.5985	1.609 801 85
Sn	Freezing	505.078	231.928	1.892 797 68
Zn	Freezing	692.677	419.527	2.568 917 30
Al	Freezing	933.473	660.323	3.376 008 60
Ag	Freezing	1234.93	961.78	4.286 420 53
Au	Freezing	1337.33	1064.18	
Cu	Freezing	1357.77	1084.62	

* Vapour pressure point or gas thermometer point

Table 1: Defining fixed points of the ITS-90 as contained in [8].

It is important to stress that the scale has been conceived in a manner that, throughout its entire extension, any T_{90} numerical value is the best approximation to the value of T, following the best estimates available at the time the scale was

developed and adopted. When compared to direct measurements of thermodynamic temperatures, measurements of T_{90} are much more easily carried out and more precise, and are highly reproducible.

1.3. Motivation and Objective of the research presented in this thesis

In recent years, with the new technological advances and achievements, National Metrology Institutes (NMIs) around the world have been developing new methods aimed at more practicability and greater measurement accuracy, improving their calibration and measurement capabilities. In parallel with this comes the concern with the reduction of uncertainties associated with such measurements, providing more reliability to their services and research.

In Thermometry, the leading NMIs are investigating new metals to use as reference materials for new fixed points, a possible redefinition of the current International Temperature Scale and better understanding of phenomena which interferes with measurements. The work in this thesis contributes to the latter activity.

The main uncertainty in primary contact thermometry is the uncertainty due to the unknown impurity concentration in the fixed point materials (mostly metals). Even though only metals of the highest purity available are used and in most cases the impurities are only present at the parts per million (ppm) level, they still cause the freezing temperature of the material to depart in a significant way from the values defined on the ITS-90 [10]. This fact limits the ability, for example, of reliably comparing fixed points. This is because even if one finds very small temperature differences when comparing two fixed point standards, the uncertainty for this difference will be 10-100 times larger due to the uncertain impurity concentration in the metal. Because of this a better understanding of the effect of these impurities will facilitate significant reduction of measurement uncertainties.

In 2005, the CCT recommended two methods to approach correcting for impurities in thermometric fixed points. These were based on a chemical assay of the metal to quantify the residual impurities in the sample. The two methods were the Sum of

Individual Estimates (SIE) and Overall Maximum Estimate (OME) methods [10, 11]. The SIE method is the preferred option as it relies on estimates of each individual impurity, yielding results that are more reliable than the OME. The SIE requires a knowledge of the liquidus slope (rate of change of freezing temperature with impurity concentration) or distribution coefficient (molar ratio of solid solubility to liquid solubility of the impurity) in the low concentration limit. Reliable values of these quantities are hard to obtain, though substantial progress has been made in populating the record in the last few years [12, 13]. However, a number of drawbacks of the SIE method have been pointed out [14, 15, 16, 17], in particular the high demand placed on the accuracy and sensitivity of chemical assays, and the unknown relationship between the sample analysed and the condition of the same sample after being used to construct a fixed point cell. In addition, the large uncertainties of assays provided even by leading practitioners in the field often render determining corrections by the SIE method of little value. In view of this a number of complementary methods have been proposed, which make use of the shape of the freezing curve itself [17, 18, 19, 20, 21, 22, 23, 24]. The principal advantage of these methods is the lack of dependence on chemical assays; however, the disadvantage is that they rely heavily on various assumptions about the relationship between the shape of the freezing curve and the impurities. Ideally, an assessment of the effect of the impurities on fixed point behaviour would draw on a variety of different complementary techniques.

Among the ITS-90 metal fixed points, aluminium was chosen for this investigation because of its importance in SPRT calibrations: it is the highest temperature fixed point accessible to SPRTs, and a key fixed point for the calibration of high temperature SPRTs (HT-SPRTs). It presents high affinity for oxygen and is also the most difficult to obtain in high purity so that characterisation and quantification of impurity effects is crucial for this fixed point. It has also exhibited peculiar impurity effects [25, 26, 27, 28, 29, 30, 31]. Recently, after the publication of a comprehensive survey of distribution coefficients and liquidus slopes [12, 13] it has become possible to fully implement the SIE for the aluminium point.

The objective in this thesis was to construct a suite of five aluminium fixed point cells, each using metal from a different source, so as to have five cells exhibiting a wide range of impurity effects. The available range of impurity correction techniques

were then systematically applied to all cells in order to identify which techniques were most consistent across the five cells, and to examine any difficulties associated with the implementation of each method.

The rest of the thesis is structured as follows: Chapter 2 describes important definitions and technical requirements related to the state of the art of realising the defining fixed points of the International Temperature Scale of 1990 (ITS-90); Chapter 3 describes the construction of the cells, Chapter 4 defines the measurements performed with the cells in order to allow the application of the methodologies employed in the study; Chapter 5 presents the results of the measurements and calculations; Chapter 6 addresses the discussions on the results presented and Chapter 7 presents the conclusion of the thesis.

Chapter 2

The State of the Art of realising the defining fixed points of the International Temperature scale of 1990 (ITS-90)

2.1. Platinum Resistance Thermometry and the ITS-90

The standard platinum resistance thermometer is defined as the interpolation sensor for the ITS-90 in the temperature range from the triple point of equilibrium hydrogen (13.8033 K) to the freezing point of silver (961.78 °C) (figure 1).

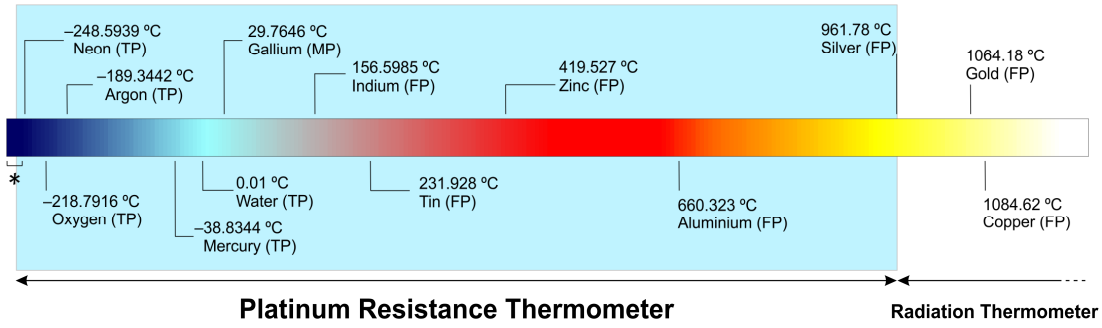

Figure 1: Detail of the ITS-90, showing the range which has the SPRT as the interpolation instrument.

Platinum resistance thermometers have different constructions, according to the conditions of use imposed by the temperature range they are intended to cover. Generally, these are capsule type (c-SPRT) for cryogenic use, standard platinum resistance thermometers (SPRT) with a nominal room temperature resistance of 25 ohms for use up to the aluminium point and high temperature standard platinum resistance thermometers (HT-SPRT) with a nominal room temperature resistance of

2.5 ohm (or even 0.25 ohm) for use up to the silver point. To obtain the best performance they usually require some specific heat treatment if exposed to certain temperatures (cryogenic temperatures and above 420 °C).

For the whole range the PRT is used to interpolate the ITS-90, temperatures are determined essentially from the ratio $W(T_{90})$, which represents the ratio of the resistance $R(T_{90})$ measured at a given temperature T_{90} to the resistance measured at the triple point of water, R(TPW) (equation **Erro! Fonte de referência não encontrada.**):

$$W(T_{90}) = \frac{R(T_{90})}{R(TPW)} \tag{2}$$

The PRT is calibrated against defined fixed points of the ITS-90. But in order to be calibrated, the platinum wire from which the thermometer is made has to fulfil certain conditions, i.e. pure and strain free. Practically, this is expressed by W being greater or lesser than certain values at the Ga melting point (equation 3) and Hg triple point respectively (equation 4):

$$W(29.7646\ °C) \geq 1.118\ 07 \tag{3}$$

$$W(-38.8344\ °C) \leq 0.844\ 235 \tag{4}$$

For the range that the SPRT is defined as the interpolation instrument, the ITS-90 is broken into sub-ranges to minimise the uncertainty of the calibration (details of these can be found in [8]). In those subranges T_{90} is ultimately obtained from the deviation function $W(T_{90}) - W_r(T_{90})$ where the latter term is the W of a group of PRTs that were used to establish the reference function of the ITS-90 and the former term is the W for the thermometer being calibrated. So, the fixed points that make up a particular sub-range, the deviation is obtained directly from the calibration of the thermometer (equations 5 and 6 for the range below the triple point of water and equations 7 and 8 for the range above the triple point of water). At intermediate temperatures, it is calculated using the appropriate deviation functions (equations 9 – 12), according to the calibration range.

$$\ln[W_{\mathrm{r}}(T_{90})] = A_0 + \sum_{\mathrm{i}=1}^{12} A_{\mathrm{i}} \left[\frac{\ln(T_{90}/273.16\ \mathrm{K}) + 1.5}{1.5}\right]^{\mathrm{i}} \tag{5}$$

The inverse function is:

$$T_{90}/273.16\ \mathrm{K} = B_0 + \sum_{\mathrm{i}=1}^{15} B_{\mathrm{i}} \left[\frac{W_{\mathrm{r}}(T_{90})^{1/6} - 0.65}{0.35}\right]^{\mathrm{i}} \tag{6}$$

For the positive range, the equation is:

$$W_{\mathrm{r}}(T_{90}) = C_0 + \sum_{\mathrm{i}=1}^{9} C_{\mathrm{i}} \left[\frac{T_{90}/\mathrm{K} - 754.15}{481}\right]^{\mathrm{i}} \tag{7}$$

Whose inverse function is:

$$T_{90}/\mathrm{K} - 273.15 = D_0 + \sum_{\mathrm{i}=1}^{9} D_{\mathrm{i}} \left[\frac{W_{\mathrm{r}}(T_{90}) - 2.64}{1.64}\right]^{\mathrm{i}} \tag{8}$$

The deviation function for the range from the triple point of equilibrium hydrogen (13.8033 K) to the triple point of water (273.16 K) is given by:

$$\begin{aligned} W(T_{90}) - W_{\mathrm{r}}(T_{90}) = a[W(T_{90}) - 1] + b[W(T_{90}) - 1]^2 \\ + \sum_{i=1}^{5} c_i\, [\ln W(T_{90})]^{i+n} \end{aligned} \tag{9}$$

From the triple point of argon (83.8058 K) to the triple point of water, the function is:

$$W(T_{90}) - W_{\mathrm{r}}(T_{90}) = a[W(T_{90}) - 1] + b[W(T_{90}) - 1] \ln W(T_{90}) \tag{10}$$

From the triple point of water to the freezing point of aluminium, the deviation function is:

$$W(T_{90}) - W_{\mathrm{r}}(T_{90}) = a[W(T_{90}) - 1] + b[W(T_{90}) - 1]^2 + c[W(T_{90}) - 1]^3 \quad (11)$$

From the triple point of water to the freezing point of silver, the function is:

$$W(T_{90}) - W_{\mathrm{r}}(T_{90}) = a[W(T_{90}) - 1] + b[W(T_{90}) - 1]^2 + c[W(T_{90}) - 1]^3 + d[W(T_{90}) - W(660.323\ ^{\circ}\mathrm{C})]^2 \quad (12)$$

Concerning the freezing point of aluminium, it is one of the mandatory fixed points in the following sub-ranges:

- From 0 °C to the freezing point of silver (961.78 °C) ⇨ the thermometer has to be calibrated at the triple point of water (0.01 °C) and at the freezing points of tin (231.928 °C), zinc (419.527 °C), aluminium (660.323 °C) and silver (961.78 °C).

- From 0 °C to the freezing point of aluminium (660.323 °C) ⇨ the thermometer has to be calibrated at the triple point of water (0.01 °C) and at the freezing points of tin (231.928 °C), zinc (419.527 °C) and aluminium (660.323 °C).

It is also possible to have a same thermometer calibrated from 0 °C to 660.323 °C and in the negative range down to the argon triple point (–189.3442 °C), but no more than these limits.

The constants in the reference functions (equations 5 – 8) are given in tables 2 and 3.

A_0	– 2.135 347 29	B_0	0.183 324 722
A_1	3.183 247 20	B_1	0.240 975 303
A_2	– 1.801 435 97	B_2	0.209 108 771
A_3	0.717 272 04	B_3	0.190 439 972
A_4	0.503 440 27	B_4	0.142 648 498
A_5	– 0.618 993 95	B_5	0.077 993 465
A_6	– 0.053 323 22	B_6	0.012 475 611
A_7	0.280 213 62	B_7	– 0.032 267 127
A_8	0.107 152 24	B_8	– 0.075 291 522
A_9	– 0.293 028 65	B_9	– 0.056 470 670
A_{10}	0.044 598 72	B_{10}	0.076 201 285
A_{11}	0.118 686 32	B_{11}	0.123 893 204
A_{12}	– 0.052 481 34	B_{12}	– 0.029 201 193
		B_{13}	– 0.091 173 542
		B_{14}	0.001 317 696
		B_{15}	0.026 025 526

Table 2: Constants of the ITS-90 reference functions
(range below the triple point of water).

C_0	2.781 572 54	D_0	439.932 854
C_1	1.646 509 16	D_1	472.418 020
C_2	– 0.137 143 90	D_2	37.684 494
C_3	– 0.006 497 67	D_3	7.472 018
C_4	– 0.002 344 44	D_4	2.920 828
C_5	0.005 118 68	D_5	0.005 184
C_6	0.001 879 82	D_6	– 0.963 864
C_7	– 0.002 044 72	D_7	– 0.188 732
C_8	– 0.000 461 22	D_8	0.191 203
C_9	0.000 457 24	D_9	0.049 025

Table 3: Constants of the ITS-90 reference functions
(range above the triple point of water).

It is not possible to give all details concerning the ITS-90 in this thesis. The interested reader is referred to [8, 32, 33, 34] where much more information is to be found.

2.2. Fixed point cells

2.2.1. Definition and related terminology

In regard to thermometry, a fixed point cell is a general term used to describe a device that contains and protects a sample of pure reference material so that the melting/freezing/triple point of the material can provide a reference temperature. In use, the cell realises a phase transition corresponding to, for e.g. a triple point (water, mercury, argon, etc.), a melting point (gallium) or a freezing point (indium, tin, zinc, etc.). The fixed point cells, whose temperatures are defined with zero uncertainty on

the ITS-90, are used for the calibration of thermometers, the designated phase transition being established by various means. As this thesis focuses on the Al freezing point, I define here the terminology related only to aspects of freezing [35].

Reference temperature – a temperature which is fixed and well reproducible, to which a value is assigned. It is used for the calibration of temperature sensors.

First cryoscopic constant, A – a constant of proportionality which correlates the depression in the freezing point temperature to the concentration of impurities in the material. This is achieved through the knowledge of the properties L (molar heat of fusion of the pure material), R (molar gas constant) and T (thermodynamic temperature of fusion) of the reference material, given by (equation 13):

$$A = \frac{L}{R[T_{pure}]^2} \tag{13}$$

Freeze – an experiment done with the use of a fixed point cell in which the reference material is forced to solidify.

Freezing curve – the complete time-temperature relation of the fixed point material during its freeze comprising all stages: from totally molten to entirely frozen.

Freezing plateau – the region of the freezing curve in which the temperature does not change substantially over the time, presenting a steady behaviour.

Freezing range – the range over which almost all the metal solidifies. This is related to the presence of impurities that causes the slopes observed in real curves, as opposed to flat plateaus of ideal 100 % pure materials.

Nucleation – the formation of crystals in the liquid (when in a super-cooled state).

Recalescence – the abrupt increase in the temperature of the reference material (occurring right after nucleation takes place), followed by crystal growth, due to the fact that latent heat of fusion of the reference material is released.

Reference material – the material inside a cell that is forced to melt and freeze during its use.

Supercooled state – the meta-stable state in which the reference material presents a temperature lower than the freezing point but the material is still in the liquid phase.

Undercool – the temperature depression (with the material in the supercooled state) that occurs right before nucleation takes place. For aluminium, the typical undercool is 0.4 K to 1.5 K [35]. For the cells studied in this thesis, the undercool was around 1.6 K for all five cells.

2.2.2. Working principle of the aluminium freezing point

A pure substance exhibits uniform behaviour during its freeze. It is this fundamental characteristic that makes a freezing point a convenient reproducible reference point for the calibration of temperature sensors. This is because an ideally pure material, at a fixed pressure, freezes (and melts) at a unique temperature when its solid and liquid phases are in thermal equilibrium. However, in real measurements the phase transition from liquid to solid exhibits a complex time versus temperature relation. This is due to a number of confounding factors, the main ones being a) because there is heat flux during the freeze and in reality quasi thermal equilibrium is only ever established and b) the presence of impurities in the material. The effect of the latter forms the main research discussed in this thesis.

The freezing point, its repeatability as well as the duration of the freezing plateau (for a given freezing rate) will all depend on the purity of the reference material. The purity must be suitable to its use. In very general terms a reference material with 10 ppm (by weight) of impurity content (5N, i.e. 99.999 % nominal purity) will present a decrease of 10 mK in relation to the freezing point of the ideally pure material.

In figure 2, one can identify the aforementioned parts of a typical freezing curve. To give a feel for the dimensions, parameters and values of a given real aluminium freezing curve are given on this schematic diagram.

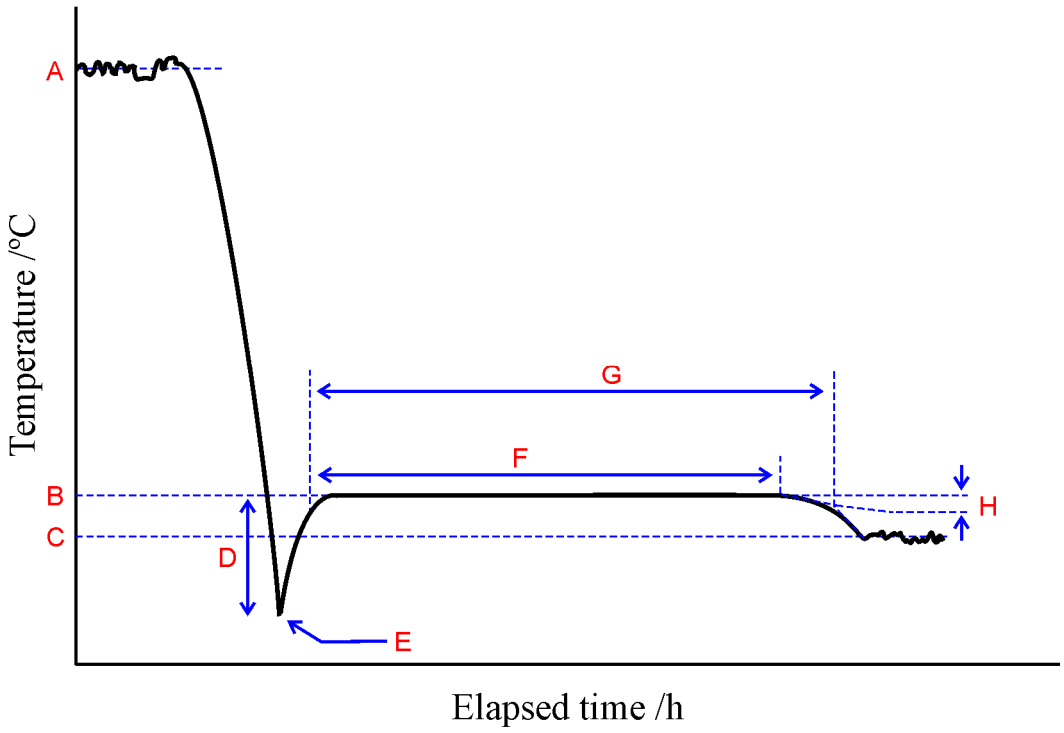

Figure 2: Structure of a typical aluminium freezing curve where: A – is the furnace temperature after the previous melt, typically adjusted 5 °C above the melting point (the oscillation in the readings is representative of the stabilisation regime of the furnace which, given its specification, would be approximately 0.1 °C); B – the freezing temperature of the cell; C – the furnace temperature adjusted to maintain the freezing plateau for a reasonable length and verified after the end of the freeze; D – is the maximum undercool (for the aluminium cells constructed, this is typically < 1.5 °C); E – nucleation, followed by recalescence; F – freezing plateau; G – total freezing time and H – the freezing range.

When a real Al freeze is established, it is essential to set up a solid-liquid interface, adjacent to the re-entrant well. This interface is established through the introduction of cold rods into the re-entrant well causing the measurements (around nucleation) to be disrupted. This is illustrated in figure 3, where a curve with two segments is depicted: the first one, A, shows the temperature decrease below the expected freezing value, followed by nucleation and recalescence. As soon as the latter is observed, the thermometer is withdrawn to allow for the induction of the inner solid-liquid interface

through the introduction of cold rods. The second segment, B, shows the measurements after the induction of the inner interface, in which the recording of data is resumed when the thermometer is about to reach thermal equilibrium with the cell, usually a few degrees lower than the material freezing temperature. Segment B is the one in which most of the interest of this study resides.

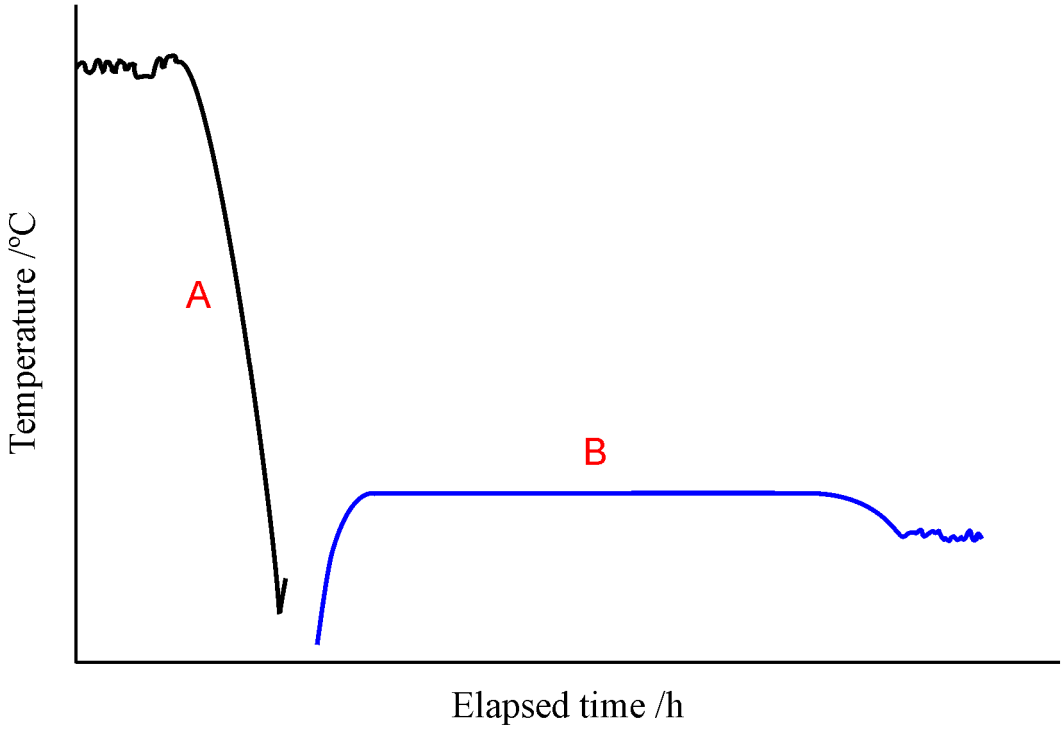

Figure 3: Discontinuity in measurements due to the withdrawal of the thermometer and the introduction of a cold rod into the re-entrant well to initiate the formation of the inner solid-liquid interface in the aluminium freezing cell.

2.2.3. Essential technical requirements to establish reproducible experimental conditions for fixed point cells

In order to start the freezing of the reference material, the temperature of its surroundings has to be decreased to approximately 1 °C below its freezing point, under-cooling the material (for the aluminium cells investigated in this thesis, the furnace was adjusted to 2 °C below the aluminium freezing point temperature). After undercool, nucleation and recalescence, the temperature in the re-entrant well becomes

constant during the freezing plateau. After a while, the temperature starts decreasing and finally, all material becomes solid. The duration of this process depends on the cooling rate, the mass of reference material present and its purity. The formation of solid demands the presence of liquid in the undercooled state, nucleation and crystal growth (the latent heat of fusion liberated by crystal nucleation and growth provokes recalescence) [35].

As the reference material freezes dissolved trace impurities tend to be expelled and remain in the liquid layer – indeed, this fact promotes uniform plateau reproducibility every time a freezing is realised. However, the presence of impurities usually results in the decrease of the fixed point temperature and leads to a shortening of the phase transition duration [35].

The effect of pressure variations during the phase transition of metal reference materials is of low significance to their temperature: generally less than 0.1 µK. (according to observations of the pressure inside the cells during the measurements for this study). Nevertheless, in accurate realisations of the ITS-90 the pressure effect is mitigated for by determining freezing point temperatures at a pressure value of 101 325 Pa (1 atm) [35].

The furnace must be able to provide an isothermal region (< 50 mK over the height of the fixed point metal) to obtain a long and uniform freezing plateau, allowing for the calibration of several thermometers on the same plateau [35].

The fixed point cell must contain enough reference material to realise such plateaus and also provide enough immersion depth for the thermometer, usually a volume of 100 cm^3 to 150 cm^3, depending on the exact design of the fixed point cell [32]. In addition, the cell (and its enclosure) must be constructed in such a way as to guarantee the reference material is not contaminated during construction or repeated use. For safety purposes, the cell must allow for expansion and contraction of the reference material up to 10 °C above its freezing point [35].

It is essential that the solid-liquid interface is induced in the re-entrant well right after the onset of recalescence. This is usually performed by withdrawing the thermometer and inserting one or two cool rods in the well, following a procedure

referred to as *inside nucleation*. This results in a thin layer of solid adjacent to the well, the inner solid-liquid interface [35].

Concerning errors when using fixed point cells, a major source is related to the failure of the thermometer being measured to reach thermal equilibrium with the reference temperature due to unwanted heat flow. This kind of error is minimised by ensuring that a sufficient immersion depth for the thermometer is established. Another source of error is related to the immersion of the cell in the furnace. It has to be adequately immersed in order to avoid heat loss from the furnace, allowing for a better thermal equilibrium and homogenisation (figure 4). This last characteristic is of great importance for the realisation of fixed points for temperature calibration as the furnace has to provide an environment that enforces the phase transition of the reference material simultaneously along its whole longitudinal axis.

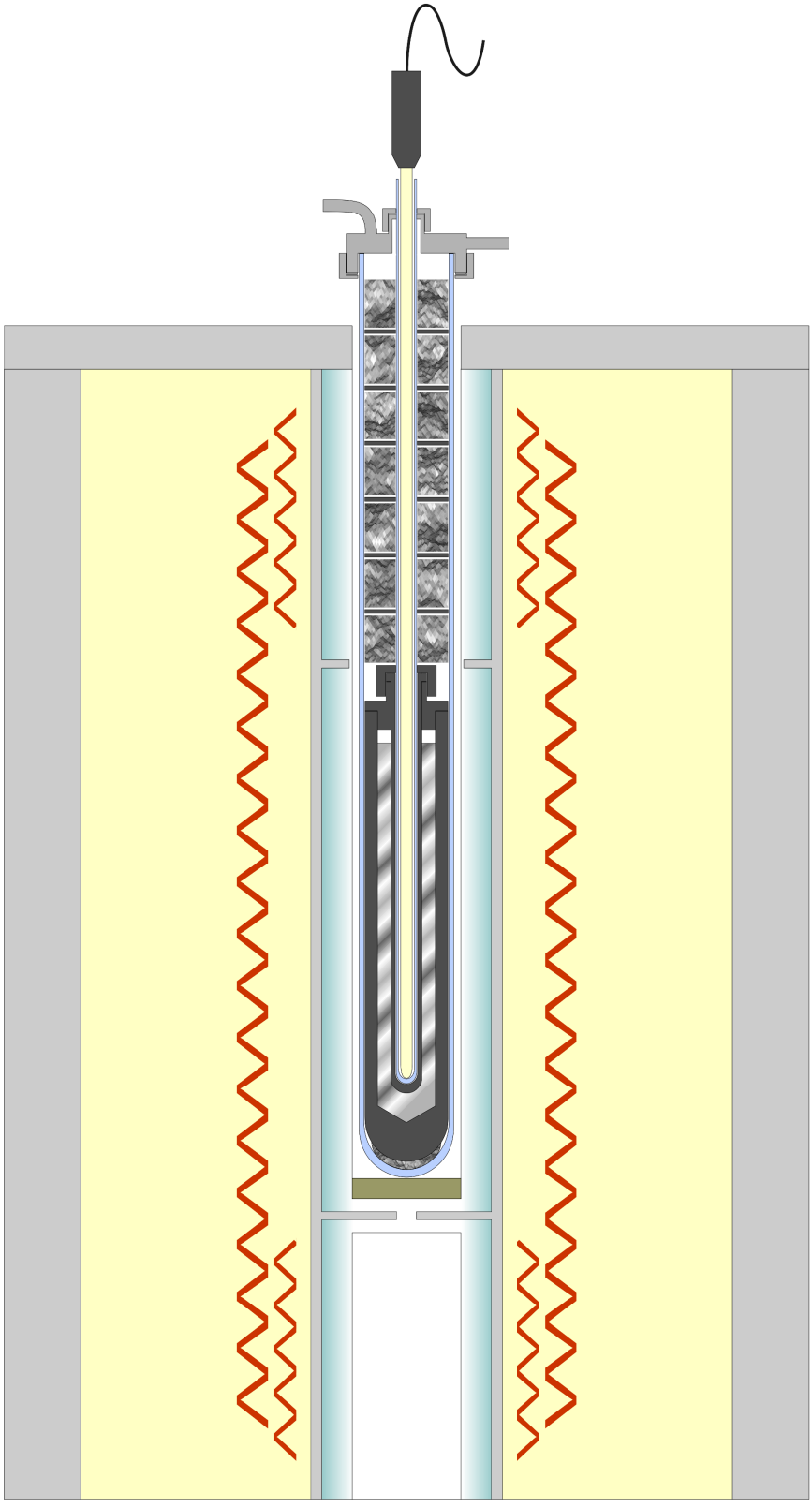

Figure 4: Position of an aluminium fixed point cell in the three-zone furnace used for the research reported here. The fixed point metal is conveniently located in the main zone so that it benefits from improved temperature homogeneity.

The freezing point temperature of the pure substance, as described in the ITS-90, can be assigned to the cell if these requirements are met: if the purity of the original material is sufficient (and assembly of the cell did not contaminate it) and if the evaluation tests confirm its performance [35]. However, there would be an uncertainty attributed to the reference temperature, which would be related to the actual impurity content of the reference material. This is why materials of the highest purity are used, minimising (but not eliminating) the uncertainty contribution to the temperature arising from the remaining impurities. The state of the art calibration of SRTs is now, in many cases, limited by the effect of the residual impurities and so this topic, which forms the research of this thesis, will be discussed below.

2.3. Addressing the impurity-related aspects and effects

Materials to be used as temperature fixed points of the ITS-90 have to be of suitable purity [32, 35]. For most of them, the nominal purity is usually 99.999 9 % (6N), the exceptions being mercury and gallium (currently being used predominantly at grades 8N+). The reason for this is that the ITS-90 is based upon phase transformations of ideally pure substances and the best approach to achieve this is to make use of materials of the highest purity available. However, in spite of all efforts and improvements in high purity metal refinery, constructing fixed point cells containing slightly purer metal than the usual (6N) might not lead to the expected better performance [25]. The hindrance to better performance could be due to contamination during construction caused by improper handling but more likely attributable to the level of purity of the other materials employed during the construction of the cells: i.e. the graphite parts for the crucible and the argon gas for maintaining the pressure at 1 atm are likely to be the main sources of long term contamination, as they are in intimate contact with the fixed point material. Apart from this extraneous contamination, that is almost impossible to be avoided, the residual impurity of the fixed point metals themselves (0.000 1 % for a nominal 6N pure sample) could result in a temperature departure from the behaviour expected for the phase transition of an ideal 100 % pure system [11]. This temperature shift provoked by the presence of impurities yields an additional uncertainty component in fixed point realisations. In

the case of the high temperature fixed points, namely aluminium and silver, the uncertainty due to these impurities is the major source of uncertainty [20].

2.3.1. Fundamentals of the behaviour of impurities in phase transitions

In order to characterise the behaviour and influence of impurities in fixed point materials, it is important to acquire knowledge of the equilibrium distribution coefficient, k_0^i, which is a measure of the solubility (distribution) of impurities in the solid $\left(c_s^i\right)$ and liquid $\left(c_l^i\right)$ phases of the host material. This is characterised by equation 14 [10, 11, 36]:

$$k_0^i = \frac{c_s^i}{c_l^i} \tag{14}$$

Also needed for these analyses is the knowledge of the liquidus slope, m_l^i, for each impurity *i*, given by the derivative (equation 15)

$$m_l^i = \frac{\partial T_l}{\partial c_l^i} \tag{15}$$

The liquidus slope represents the concentration-dependence of the fixed point temperature for each impurity, where T_l is the temperature of the liquidus line with respect to concentration of impurity *i*, deduced from equilibrium phase diagrams at low concentrations.

When all impurities are insoluble in the solid phase of the host material and the ideal solution law is valid, the impurities remain in the liquid solution. Then, considering there is no concentration gradient as the freezing front advances, the depression in the temperature of the remaining liquid (in which the impurities are concentrated and uniformly distributed), relative to the freezing-point temperature of the pure material, is directly proportional to the impurity concentration divided by the first cryoscopic constant, given by (equation 16)

$$T_{pure} - T_{obs} = \frac{c_l}{A} \tag{16}$$

Where T_{pure} is the freezing-point temperature of the pure material, T_{obs} is the observed equilibrium temperature of the sample; c_l is the mole fraction impurity concentration in the liquid and A is the first cryoscopic constant. The equation above (16) is known as Raoult's law. The first cryoscopic constant, A, is given by equation 13 (given in section 2.2.1).

Values of k for all fixed point metals (considering from hydrogen to plutonium as individual impurities) were only compiled recently, after thorough examination of the related literature. These values are available in [12]. The first cryoscopic constants for the ITS-90 metal fixed points are documented in [37].

The equilibrium distribution coefficient and the liquidus slope are related by Van't Hoff's law (equation 17) [12, 38]:

$$\frac{\partial T_l}{c_l^i} = \frac{RT^2}{\Delta H}(k-1) \tag{17}$$

Where H is the enthalpy of fusion (or also referred to as 'molar heat of fusion', L). Van't Hoff's relation (equation 17) seems to be valid at the limit of zero impurity concentration in the liquid and hence it is applicable for fixed points (total impurity concentration of 0.1 ppm or less) and can be used to describe the effect of individual impurities in the fixed points of the ITS-90 [38].

When impurities form solid solutions with the fixed point material, during the freezing of the material the impurities can be segregated in three different conditions [10]:

1- *Complete equilibrium mixing in the liquid*

This is based on the assumption that the freezing occurs so slowly that it allows for complete and uniform mixing of impurities in the liquid phase by convection and diffusion, eliminating concentration gradients in the liquid. This represents the possibility of maximum segregation of impurities. This condition, however, can only be achieved with very slow freezing rates.

2- *Partial mixing in the liquid*

Assuming that the distribution of impurities in the liquid is affected by both diffusion and convection, the segregation of impurities will depend strongly on the freezing conditions, being governed by an effective distribution coefficient, k_{eff}^{i} , which has a value between that of k_0^i and 1 (the value of k_{eff}^{i} approaches 1 if the rate of freezing is high). The higher the rate of freezing, the less segregation of impurities will occur.

3- *No mixing in the liquid*

This takes into account the fact that the impurity distribution in the liquid phase is affected only by diffusion, i.e. assuming that there is no convection. In this case, as freezing advances, the impurities in the liquid layer adjacent to the liquid/solid interface increases ($k_0^i < 1$; i.e. impurities rejected by the solid) or decreases ($k_0^i > 1$; i.e. impurities gathered by the solid phase). The impurity distribution in the solid phase will depend strongly on the equilibrium distribution coefficient, the rate of freezing (speed in which the liquid/solid interface advances), the diffusion coefficient of the impurity in the liquid and the sample geometry. It is generally assumed that convection plays a relatively minor role in fixed point cells used in thermometry (due to the very small temperature gradients present, which is a condition commonly encountered in thermometry).

2.3.2. Current methodologies for estimating the effect of impurities in fixed point cells

Considering the above fundamental aspects, the CCT recommends a number of techniques to account for the influence of impurities in fixed points. The main methods are: the Sum of Individual Estimates (SIE), the Overall Maximum Estimate (OME), the Hybrid SIE/OME, the Scheil model, the gradient method, the thermal analysis (or '1/F method') and the direct comparison of cells. These are all summarised below in the context of the current study.

2.3.2.1. Sum of Individual Estimates (SIE)

The SIE method [10] relies on the assumption that the effect of each impurity in the metal is independent of the others [38] so that the effect of all the impurities on the freezing temperature can be summed over all impurities. It is currently the method recommended by the CCT [11]. It also relies on a knowledge of the amount of each impurity present, provided by the GDMS analysis, and reliable knowledge of the liquidus slope in the limit of low concentration. The change in the freezing temperature caused by the impurities is given by equation 18

$$\Delta T_{\mathrm{SIE}} = T_{\mathrm{pure}} - T_{\mathrm{liq}} = -\sum_{i} c_{l1}^{i} \cdot m_{l}^{i} \qquad (18)$$

Where T_{pure} is the freezing temperature of the ideally pure material and T_{liq} is the observed freezing temperature of the material. Both T_{pure} and T_{liq} represent the liquidus point. c_{l1}^{i} is the concentration of impurity i when the material is completely molten and m_{l}^{i} is its liquidus slope, which is the concentration dependence of the fixed point temperature in relation to each impurity i, given by equation 15 (previously given in section 2.3.1).

The liquidus slopes used in this investigation are given as a function of atomic number Z up to Z = 94 in table 4 [13].

The uncertainty in the value of ΔT_{SIE} is given by equation 19:

$$u^2(\Delta T_{SIE}) = \sum_i \left[u(c_{l1}^i) \cdot m_l^i\right]^2 + \left[c_{l1}^i \cdot u(m_l^i)\right]^2 \qquad (19)$$

Atomic No	Element	m_l^i µK/ppbw	$u(m_l^i)$ µK/ppbw
1	H	– 17.873	0.106
2	He	– 4.527	0.001
3	Li	– 1.319	1.030
4	Be	– 1.832	0.111
5	B	– 1.858	0.774
6	C	– 1.131	0.870
7	N	– 1.276	0.020
8	O	– 0.396	0.119
9	F	0.000	0.000
10	Ne	– 0.898	0.000
11	Na	– 0.724	0.150
12	Mg	– 0.450	0.116
13	Al	Matrix	Matrix
14	Si	– 0.623	0.093
15	P	– 0.834	0.576
16	S	– 0.511	0.131
17	Cl	0.000	0.000
18	Ar	– 0.453	0.000
19	K	– 0.277	0.263
20	Ca	– 0.470	0.088
21	Sc	– 0.223	0.517
22	Ti	4.607	1.895
23	V	3.321	1.789
24	Cr	1.051	0.634
25	Mn	0.115	0.264
26	Fe	– 0.311	0.024
27	Co	– 0.297	0.016
28	Ni	– 0.309	0.056
29	Cu	– 0.252	0.095
30	Zn	– 0.037	0.156
31	Ga	– 0.150	0.083
32	Ge	– 0.208	0.033
33	As	– 0.235	0.014
34	Se	– 0.288	0.134
35	Br	– 0.227	0.068
36	Kr	– 0.216	0.065
37	Rb	– 0.160	0.069
38	Sr	– 0.196	0.014
39	Y	– 0.192	0.011

Atomic No	Element	m_l^i µK/ppbw	$u(m_l^i)$ µK/ppbw
40	Zr	1.233	1.016
41	Nb	5.478	1.697
42	Mo	1.155	0.901
43	Tc	0.045	0.317
44	Ru	– 0.143	0.044
45	Rh	0.068	0.437
46	Pd	– 0.057	0.194
47	Ag	0.010	0.184
48	Cd	– 0.112	0.038
49	In	– 0.157	0.024
50	Sn	– 0.142	0.003
51	Sb	– 0.081	0.072
52	Te	– 0.116	0.050
53	I	0.000	0.000
54	Xe	– 0.137	0.002
55	Cs	– 0.104	0.041
56	Ba	– 0.079	0.071
57	La	– 0.121	0.018
58	Ce	– 0.128	0.002
59	Pr	– 0.127	0.002
60	Nd	– 0.125	0.002
61	Pm	0.000	0.000
62	Sm	– 0.110	0.017
63	Eu	– 0.119	0.036
64	Gd	– 0.115	0.003
65	Tb	– 0.107	0.010
66	Dy	– 0.101	0.017
67	Ho	– 0.099	0.017
68	Er	– 0.098	0.017
69	Tm	– 0.104	0.004
70	Yb	– 0.046	0.054
71	Lu	– 0.104	0.031
72	Hf	2.391	2.522
73	Ta	5.443	1.253
74	W	0.488	0.873
75	Re	0.095	0.131
76	Os	0.400	0.657
77	Ir	0.376	0.622
78	Pt	0.017	0.190

Atomic No	Element	m_l^i µK/ppbw	$u(m_l^i)$ µK/ppbw	Atomic No	Element	m_l^i µK/ppbw	$u(m_l^i)$ µK/ppbw
79	Au	– 0.010	0.074	87	Fr	0.000	0.000
80	Hg	– 0.030	0.059	88	Ra	0.000	0.000
81	Tl	– 0.059	0.028	89	Ac	0.000	0.000
82	Pb	– 0.052	0.056	90	Th	– 0.052	0.034
83	Bi	– 0.039	0.013	91	Pa	– 0.079	0.024
84	Po	0.000	0.000	92	U	– 0.060	0.027
85	At	0.000	0.000	93	Np	– 0.077	0.023
86	Rn	– 0.081	0.000	94	Pu	– 0.049	0.039

Table 4: Values of the liquidus slopes of impurities in aluminium in the low concentration limit [13].

There are significant problems with this approach; e.g. uncertainty in chemical analysis, irreproducibility in such analysis between different laboratories, large uncertainties associated with liquidus slope estimates.

In 2003, the CCT Working Group 1 (CCT-WG1) realised that uncertainties of chemical analyses can be as high as 300% of the specified value. Then they decided that when such uncertainties exceed 100% of the measured value, a correction should not be made to the temperature of the fixed point cell, but rather, what would be the possible correction should be used as the uncertainty due to impurities of the matrix substance. Beside this, insufficient knowledge of impurity distribution and reproducibility in the chemical analysis by different laboratories causes issues. To exemplify the lack of reproducibility in chemical analysis, samples of the same batch of material were analysed by GDMS in two different laboratories and according to the results, the total impurity content of the sample was 0.990 ppm (laboratory 1) and 0.074 ppm (laboratory 2), showing a 1350 % difference in between them [39]. Consequently, corrections should not be applied if based on a single analysis (especially one that has been provided by the supplier of the material). Indeed, it is stated that in order to improve results in thermometry more extensive proofs of the purity of fixed point materials are mandatory because not only it is necessary to know the impurity content but also each impurity influence on the phase transition temperature of the matrix substance. A quantitative approach (based on doped samples with well-known impurity content, directly traceable to SI units) was proposed. The

procedure described is reported to be the most accurate one, yielding small uncertainties. Such reliability comes from the work with doping experiments in ppb levels. Other analysis methods, which could be complementary to GDMS were suggested [39]:

1- For metals: inductively coupled plasma mass spectrometry (ICP-MS); atomic absorption spectrometry (AAS) and instrumental neutron activation analysis (INAA).

2- For non-metals: carrier gas hot extraction (CGHE) and photon activation analysis (PAA).

However, it is acknowledged that the detection limits of these techniques cannot reach the expected level of impurities present in the samples (total amount < 1 ppm for a 6N pure sample), and in reality GDMS is the most suitable type of chemical analysis for ITS-90 fixed point metallic samples.

The impurities with the highest content within high-purity metals are thought to be dissolved gases. However, their role is thought to be insignificant as they are extracted when the cell is evacuated at high temperatures (i.e. when molten) [39].

2.3.2.2. Overall Maximum Estimate (OME)

Whenever there is not sufficient knowledge of the impurity concentrations or their liquidus slopes, the CCT recommends the use of the OME method [11], which only requires a knowledge of the overall mole fraction impurity concentration and the first cryoscopic constant [37] for the fixed point material. This method does not provide a correction to the freezing temperature; instead, it yields a value that can be used to represent the uncertainty in the temperature. This is given by equation 20:

$$\Delta T_{\mathrm{OME}} = \frac{c_l}{A} \tag{19}$$

where c_l is the overall impurity concentration (in mole fractions) in the liquid, and A is the first cryoscopic constant.

The uncertainty in ΔT_{OME} is given by equation 21:

$$u^2(\Delta T_{\mathrm{OME}}) = \frac{\left[\frac{c_l}{A}\right]^2}{3} \tag{20}$$

As the GDMS analyses in this study are rather complete, and the published list of common impurities is well represented in the analyses [40], the overall concentration of impurities can be estimated by summing the results of the GDMS analyses of the aluminium samples under study.

2.3.2.3. Hybrid SIE/Modified-OME

This method combines the SIE method for the dominant impurities and the OME method for the remaining impurities [11]. If the equilibrium distribution coefficients *k* of all relevant impurities are known, which is now the case for aluminium [12, 13], a simpler, modified OME method can be used. The change in the liquidus-point temperature for impurities with *k* less than 0.1 can be reliably estimated by fitting the expression (equation 22) to the freezing curve over an appropriate range, typically within the first half of the freeze (unless there is a substantial amount of high *k* impurities in the material) [11]:

$$T_{pure} - T_{liq} = \frac{c}{FA} \tag{21}$$

where *c* is the mole fraction concentration of all impurities with *k* less than 0.1 and *F* is the liquid fraction. Alternatively, it is acceptable to determine the correction for impurities with $k > 0.1$ by parameterisation using a least-squares fit of (equation 23) to the measured freezing curve, setting the value of *k* as 0 (assuming these impurities are insoluble in the solid phase). Then, for the remaining impurities not covered by the OME analysis (those with $k \geq 0.1$), the SIE method (equation 18) is applied to determine ΔT_{SIE}. The two estimates are then summed.

In this investigation, the OME component was estimated by fitting data at the beginning of the freezing curve over a narrow range ($0.05 < F_s < 0.20$) using (equation 23), as described above. To perform the fitting, it is necessary for the

freezing curve abscissa to be in terms of solid fraction, F_s, ($F_s = 1 - F$), and the ordinate to be in terms of temperature. The peak in the freezing plateau is defined as occurring at $F_s = 0$, and ΔT is specified as zero at this point. To convert the elapsed time to solid fraction, it is necessary to define an end point. This is taken to be the point of inflection in the curve after the steep drop in temperature following the end of the flat part of the curve, prior to the approach to the furnace temperature; this has been found to coincide with the disappearance of the liquid-solid interface [22]. The point of inflection is taken as the maximum value calculated through the derivative of temperature over time ($^{\partial T}/_{\partial t}$) of the freezing curve.

The uncertainty in this hybrid method may be determined by combining the uncertainty of the two individual corrections in quadrature.

2.3.2.4. Scheil model

The Scheil model of solidification makes the assumption that diffusion processes are very fast compared with the velocity of the liquid-solid interface [22, 24]. In practical terms, this means freezing durations of greater than about 12 hours. In the Scheil model the temperature is related to the liquid fraction F by (equation 23)

$$T = T_0 + mc_0 F^{k-1} \tag{23}$$

where T is the temperature of the interface for one solute, T_0 is the melting temperature of the pure material, m is the liquidus slope, c_0 is the overall concentration of impurities and k is the distribution coefficient. By fitting this expression to the freezing curve using least-squares methods, the quantity mc_0 can be obtained, which is the change in temperature due to the impurities corresponding to F = 1. Note that m and c_0 cannot be parameterised independently because of their linear interdependence during the fitting process.

The main drawback of this method is the degeneracy associated with the existence of several impurities having different values of k. In this case, different combinations of impurities can all give rise to the same value of mc_0, which means that in some cases the model is not able to uniquely identify the temperature correction.

Nonetheless, this method provides useful additional information on the impurity effects, and, importantly, does not rely on the GDMS analysis. In this study, the uncertainty attributed to the correction yielded by the Scheil method was obtained from the uncertainty in the value of the fitted parameter *mc* arising from the least-squares fit. Care should be taken to perform the fitting only in the region of the freezing curve where the shape is dominated by impurity effects, i.e. towards the early parts of the freeze. Towards the end of the freeze, the shape gradually becomes dominated by thermal effects as the liquid-solid interface approaches the re-entrant well and the corresponding immersion of the SPRT sensing element deteriorates. Figure 5 shows a typical fit of the Scheil model.

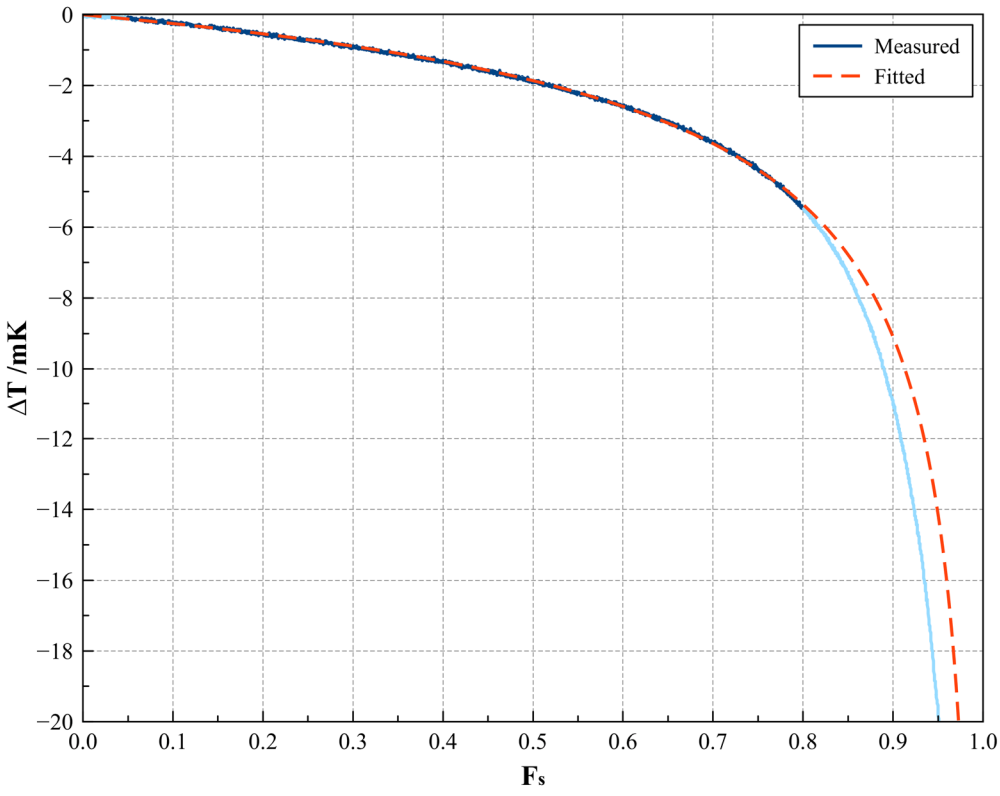

Figure 5: Fit of the Scheil expression (equation 23) to experimentally measured freezing curve. T_0, *mc*, and *k* are free parameters. In this example, the least-square fitting returned the parameters: T_0 = 5.298 mK; *mc* = – 5.306 mK and *k* = 0.567.

2.3.2.5. Gradient method

The gradient method is derived from the Scheil method [23]. It is a fast way of estimating the impurity correction. The gradient of the freezing curve at F = 0.50 is determined by fitting a tangent to the freezing curve at that point (over the range $0.45 < F < 0.55$), and extrapolating it to F = 0. The estimate is given by (equation 24)

$$T_0 = T_T + \frac{T_T - T_{F_s=1}}{(1-k)} \tag{24}$$

where T_T is the temperature at F = 0.50. The method is only applicable for systems where $k = 0$. The uncertainty in the correction is taken to be the uncertainty associated with the fitting process. This is illustrated in figure 6.

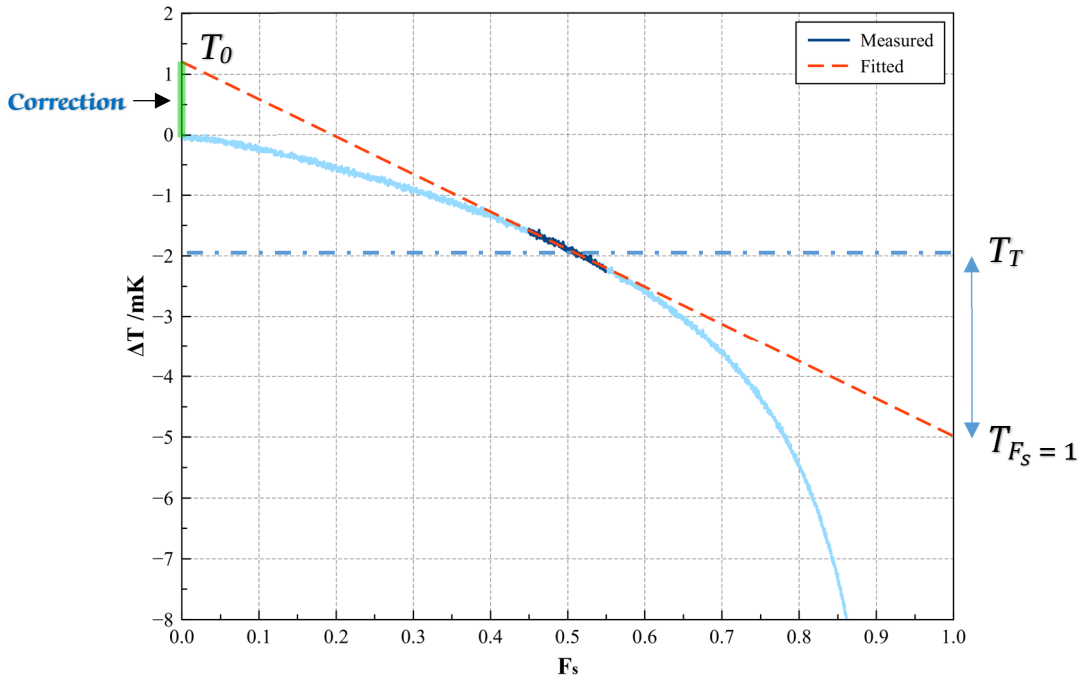

Figure 6: The same freezing curve (as figure 5) now analysed by the gradient method. The ordinate is plotted as a temperature difference (from the peak temperature), in order to find the correction for the cell. In this example, the coefficients from the linear fit were: $a = -6.186$ and $b = 1.202$. The result of this estimate was $T_0 = 1.14$ mK.

2.3.2.6. Thermal analysis

One of the biggest criticisms of the SIE approach came from [17, 19]. It is advocated that the thermal analysis method (also known as the '1/F method'), which is one of the methods based on the actual performance of the cell, portrays the actual state of the metal, after (and possibly whilst) some reactions between the metal and the other cell materials occur. On the contrary, the SIE method is based on the analysis of the fixed point material prior to its use on the cell and hence whatever happens to the material during or after handling will not be included in the calculations. Consequently, the SIE does not represent the real situation in real fixed points.

It has been stated that the maximum value of the freezing curve is a very good approximation of the liquidus temperature: it is almost not influenced by homogeneity or furnace stability [11, 39, 41]. The depression of the freezing point is assumed as the effect of the existence of impurities within the fixed point metal. So, as a reference, the value equivalent to the extrapolated 1/F=0 point is considered as the hypothetical freezing point of the 100 % pure fixed point material [19]. To use the method, temperature is plotted as a function of 1/F, which allows a straight line to be fitted to the linear portion of the data in the early part of the freeze (from 1/F=1 to 1/F=1.5) (figure 7), where the shape of the freezing curve is dominated by impurity effects. The gradient of this line can then be used to yield a parameter $dT / d(1/F)_{1/F=1}$ [20], which is taken to represent the correction at F=1. This method can be considered as a variation of the Scheil method, with *k* assumed to be zero [17, 19, 20]. The uncertainty associated with the correction was obtained from the uncertainty in the value of the fitted gradient arising from the least-squares fit.

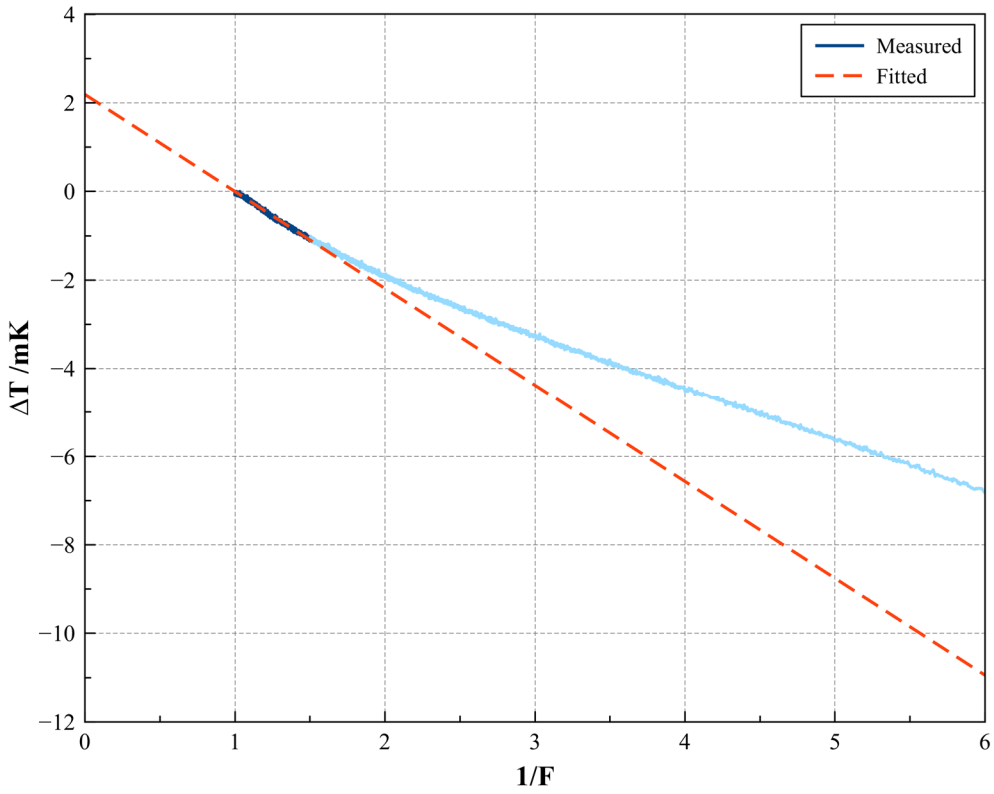

Figure 7: Example of thermal analysis of a freeze plateau. The coefficients returned by the fit are: a = – 2.189 mK and b = 2.188 mK. The correction for the cell according to the thermal analysis method performed on this freeze is 2.19 mK.

Even though, as a limitation of the method, it has been reported that the thermal analysis method is dependent on the experimental apparatus and conditions (e.g. due to the existence of heat flux in the furnaces as phase transitions occur; the rate of solidification; the possibility of an inaccurate determination of the fraction of molten/frozen metal) [11]. Considering this, the magnitude of a freezing slope could be erroneously attributed to the influence of impurities when instead it would mainly be due to thermal effects. Indeed, investigations at PTB (*Physikalisch-Technische Bundesanstalt*), in Germany, have shown that the temperature profile of furnaces can influence the freezing slopes: some experiments were performed with different rates of solidification and the outcome was that the lower the furnace set-point was in relation to the fixed point temperature, the larger the slope was [39].

2.3.2.7. Direct cell comparison

The direct comparison of freezing curves is a widely used *de-facto* standard method of comparing the freezing temperatures. This method cannot be used to determine absolute corrections for impurity effects, but can be used to examine relative differences between cells. To achieve the most reliable results it is essential that the SPRT used for the comparison is stable, and that the thermal environment of the cells is reproducible. In this investigation the same furnace was used for all five cells, which were compared against the NPL national reference standard cells. The SPRT was carefully quenched and measured at the triple point of water between measurements to express the comparison in terms of the ratio of the resistance at the aluminium freezing temperature and the resistance at the triple point of water, namely *W*. In addition, all measurements were corrected for self-heating, hydrostatic head, and pressure differences. As with all measurements performed in this investigation, the cell was held in the molten state for 24 hours prior to beginning the freeze. This allowed for all the impurities in the molten state to homogenise by diffusion throughout the metal matrix. The uncertainty budget for the comparison measurements is shown in Table 5.

Component	Description	Standard Uncertainty	Sensitivity Coefficient	Uncertainty Contribution mK
Al – A1	Repeatability of readings (0 mA)	0.4 x 10^{-7} Ω/Ω	1250 K	0.080
Al – B1	Uncertainty of Al reference cell	0.858 mK	1	0.858
Al – B2	Hydrostatic pressure correction	10 mm (÷ √3)	1.6 mK/m	0.009
Al – B3	Perturbing heat exchanges	0.7 mK (÷ √3)	1	0.214
Al – B4	Self-heating extrapolation: bridge current ratio	2% of S.H. (3 mK)	1	0.035
Al – B5	Bridge linearity	0.5 x 10^{-7} Ω/Ω (÷ √3)	1250 K	0.036
Al – B6	Temperature of standard resistor	20 mK (÷ √3)	1.05 mK/ppm	0.022
Al – B7	AC/DC, frequency, etc	0.7 x 10^{-7} Ω/Ω (÷ √3)	1250 K	0.051
Al – B8	Argon pressure in cell	2.6 kPa (÷ √3)	7.0 x 10^{-8} K/Pa	0.106
	Sub-total at FP Al			**0.897**
TPW – A1	Repeatability of readings (0 mA)	0.05 x 10^{-7} Ω/Ω	1000 K	0.008
TPW – B1	Uncertainty of TPW cell	0.034 mK	1	0.034
TPW – B2	Hydrostatic pressure correction	5 mm (÷ √3)	0.73 mK/m	0.002
TPW – B3	Perturbing heat exchanges	0.01 mK (÷ √3)	1	0.006
TPW – B4	Self-heating extrapolation: bridge current ratio	2% of S.H. (3 mK)	1	0.035
TPW – B5	Bridge linearity	0.5 x 10^{-7} Ω/Ω (÷ √3)	1000 K	0.029
TPW – B6	Temperature of standard resistor	20 mK (÷ √3)	0.25 mK/ppm	0.005
TPW – B7	AC/DC, frequency, etc	0.27 x 10^{-7} Ω/Ω (÷ √3)	1000 K	0.016
	Sub-total at TPW			**0.059**
	Equivalent at FP Al	0.059 mK	4.2	**0.250**
			Combined uncertainty (*k* = 1)	**0.931**

Table 5: Uncertainty budget for the direct comparison of cells.

2.3.2.8. Difficulties in applying the methodologies

There are a few problems concerning applying these corrections because a number depend on reliable chemical analyses of the materials used for the construction and characterisation of fixed point cells. Such analyses are hard to obtain for the following reasons:

- The measurement uncertainty of the impurity, which in most cases can be in excess of 100%;
- The uncertainty component of the measurement of impurities in a sample is usually based only on the suppliers' purity claims (often batch analysis as well);
- Another problem is that commercially available cells generally do not have detailed (and sufficient) information about impurity;
- Finally, some suppliers provide assays saying no impurities were detected (usually because the analytical technique employed lacks resolution for the required level of purity). In these situations, it is essential that additional measurements be made, involving extra time and expense.

It is recognised the necessity to improve GDMS analysis in order to allow comparability and traceability to the technique so that the results are more reliable (which includes the reduction of uncertainties and detection limits for the elements analysed) [14].

For thermometry one major issue related to impurities is whether or not these impurities *actually* change the temperature of the fixed point materials. Impurity concentrations of less than 0.01 ppb would result in temperature changes no greater than 0.2 µK [42]. By 2011, data on the influence of each impurity on the phase-transition temperature of fixed point materials were rare [42]. In addition, the information derived from phase diagrams were not reliably extrapolated to low concentrations (< 1 ppm). These issues triggered the study of doping experiments at low concentrations considering binary systems (i.e. fixed point substance + impurity x_i). Over 20 years of research on doping showed that *some* impurities do not change the phase-transition temperature of fixed point materials – a discovery totally dismissed at

first. For example, studies have shown that impurities that are gaseous at the fixed point material phase-transition temperature are largely extracted from the cell by the process of 'flushing and argon filling'. Though there may, in some circumstances, be some exceptions to this [30, 31].

Since those initial studies more impurities were discovered not to have any temperature effect on certain fixed point materials, which could be explained as suggested below [42]:

- the impurity is either insoluble or presents very small maximum solubility. If the impurity suffers a reaction (i.e. oxidation), the result is also insoluble;
- the impurity dissolves but later reacts with other components to form an insoluble compound, precipitating out;
- the dissolution of the impurity is inhibited or takes longer than the experiment;
- the temperature change due to the impurity sample in unnoticeable;
- the impurity is volatile;
- the impurity dissolves at first and subsequently reacts with other substances to form a volatile compound.

For example, it is obvious that fixed point cells contain oxides, mostly formed with the fixed point metal. This oxide is not dissolved hence not changing the temperature of the cell but being a potential reservoir for oxygen for other reactions (formation of insoluble impurity oxides, which precipitate out of the metal, and consequently no longer affecting its temperature) [43].

2.3.2.9. Controversy around the topic

Regardless of all methodologies developed to deal with the issues of impurities (whether endorsed or not by the CCT), as observed in [15], there is disagreement between the National Metrology Institutes (NMIs) with respect to which methodology to employ. Each institute seems to back a given methodology. Historically the German institute *Physikalisch-Technische Bundesanstalt* (PTB) would support the use of the SIE and OME methods, discouraging the analysis of freezing curves for the evaluation of impurities. The French institute, at that time named *Bureau National de*

Métrologie – BNM, backed the use of estimates based on representative comparisons of cells (ERC) whereas the Italian institute INRIM (*Istituto Nazionale di Ricerca Metrologica*) considered that the values assigned for the fixed point cells should be that of the ideally pure materials. The US NIST (*National Institute for Standards and Technology*) would use a set of methods based on chemical assays (and application of Raoult's law) along with analysis of freezing curves and comparisons of cells made from the same batch of metal.

More controversy arose at the 22nd meeting of the CCT in 2003: it was stated that the methodologies were not very reliable. Yet, it was claimed by one member that there should be no correction for the cells due to impurities but their effect should be included as an uncertainty component. The idea behind it is that the national standard cells are compared to one another during key comparisons, usually run by the CCT, meaning that what matters is the difference in between these 'real' standards, not the comparison of each individual cell to an imaginary ideal cell. "The reference cell of a National Standard should bear the reference temperature, which is equal to that defined in the ITS-90, and the information about possible difference between this cell and the reference cells of other countries, obtained through key comparisons" [16]. This assumption is in accordance with [35] in that every cell made with the required pure reference materials should be assigned with the value defined in the ITS-90. Finally, when the ITS-90 fixed point values were defined, metals and filling techniques were probably not as refined as they are now, so modern cells should have better performance in relation to 20+ years old cells. In view of these continued issues and controversies it is clear the thermometry community would benefit from a consensus related to the influence of impurities on fixed point cells. It is in this context that this work on Al has been performed.

2.3.3. Previous investigations at the freezing point of aluminium

Among the fixed point metals in the temperature range applicable to a long-stem SPRT, aluminium is known to be the most sensitive to oxidation, and that its uncertainty due to its impurities is known to be of order of a few millikelvins. Several

studies attempted at finding a solution to this matter. Findings from the main investigations are summarised below.

According to [19], one of the main sources of contamination is using the metal in form of pellets and casting the cell in steps: more exposure of the metal to the environment will occur due to the shape and the surface area of the pellets (in total, greater surface area will be exposed). In addition, the use of pellets requires more fillings steps (usually four or more, as reported, but in regular practice it could be as low as only two). Instead, there is a recommendation to use cylinders/ingots or rods in order to fit in the internal volume of crucible, but with a central hole to allow for graphite well placement [18]. The main reason for this is the high affinity aluminium has with oxygen, which would form the oxide Al_2O_3 (although some other researchers seem to benefit from this reaction as they consider it forms a protective layer around the pure aluminium material [25]). Nonetheless, one should be concerned about the manufacturing of the customised-size cylinder as it would probably cause contamination during the casting as well.

In [19] a novel technique was proposed for pushing the graphite re-entrant well while the aluminium was molten during the casting of the aluminium ingot. It consisted of the addition of balancing weights on top of the graphite well so that once the metal became liquid, the pressure added by the weights would force the well to its intended position, without having to open the cell during the procedure. According to this, the cell made from aluminium rods showed better results than the cell made with pellets, while the balancing weights method proved to be effective [19].

In order to acquire more knowledge on the behaviour of impurities in high purity aluminium, a myriad of doping experiments was carried out. In [26] an aluminium cell was doped, in series, with a total of 13 impurities (Ag, Ca, Cd, Cu, Fe, In, Mn, Ni, Sb, Si, Ti, Zn and quartz), chosen according to the results obtained through chemical analysis (major contaminants found) and the ones widely known to considerably influence the phase transition temperature of aluminium. The cell was installed in a high temperature calorimeter and the temperature measurements were performed using a PRT. It was observed that the presence of impurities could lead to uncertainty in determining the total melting time (hence the deduced liquidus point) and poor

immersion profiles (10 mK over the bottommost 10 cm of the well). According to the results, among the dopants tested, the most significant influence came from titanium (3.30 ± 0.09) mK/ppm.

The possible permeability of quartz glass to some gases at high temperature (including the phase transition temperature of aluminium) was studied by [27]. This assumption was based on the observation on a constant decrement of pressure inside the cell. Some (very unusual) gases were tested for use with fixed point cells: argon, nitrogen, helium, air and carbon dioxide, from which only nitrogen did not leak (or was not absorbed by the aluminium inside the crucible) over eight days. It suggests the realisation of aluminium triple point instead of the ITS-90 defined freezing point in order to eliminate the pressure dependence.

In 2008 a project was established, coordinated by LNE-INM/CNAM (France), under the auspices of EUROMET, in order to mainly improve European temperature standards and reduce the uncertainty of primary fixed points (by a factor of two or three). This was started after the conclusion that there were unexplained discrepancies in results (alongside a relatively large spread of the uncertainty components) of comparisons carried out in the previous decade [25]. As part of this project, a new generation aluminium cell was developed at LNE-INM/CNAM, accounting for all the following issues: effect of impurities, chemical analysis, cell material, protocol to clean the container, filling process, control of the thermal process and the effect of pressure. In addition, it was highlighted that thermal disturbances could affect the phase transition, leading to a non-uniform displacement of the solid-liquid interface (if it moves at different rates in different places, it could cause a thermal short circuit between the sensing element of the SPRT and the furnace in that area). The cell constructed during the investigations contained aluminium of 6N5 purity, with a maximum impurity concentration of 445 ppb, according to the assay. These impurities would amount to 0.30 mK (0.15 mK due to the impurities whose liquidus slope is known, yielded by SIE; and 0.15 mK calculated by OME method for the other impurities, as in the hybrid method). If the impurity effect was determined via OME only (considering that the liquidus slope of some impurities are not known), this estimate would be 0.59 mK.

Observations on an old aluminium ingot indicated that a possible reaction (physical or chemical) between aluminium and carbon could have occurred: the aluminium surface was granular and not bright [25]. Accounting for this, when they constructed the cell studied in the paper, they took advantage of the aluminium oxide film formed after the exposure of the metal to air/oxygen (as opposed to [19]), which is unavoidable considering the high affinity high purity aluminium presents for oxygen. It was based on the assumption that this oxide does not mix with neither liquid nor solid aluminium phases (consequently not affecting the temperature of the phase transition of the material). This oxide film is then intended to protect the pure aluminium, avoiding its contact with the graphite surface and the possible sticking reaction with carbon. This measure turned out to be very successful as they inspected the new ingot and it seemed not to have reacted with carbon. However, the new cell had a few craters (in some the re-entrant well was even visible) along the side of the ingot, which suggests it was due to the presence of a gas, but it still has to be studied in depth. Even though they used the best materials and were very meticulous when constructing the cell, the outcome did not match their efforts: the new cell (6N5) presented a freezing curve slope equivalent to 3 mK, while the older cell (6N, constructed in 1997) presented a slope of 1.1 mK.

In [28], it is addressed that some pollution could be brought to the fixed point ingot by the cell surroundings (especially the furnace tube, heat pipes and heating elements). This was based on the same cell reported in [25]. The cell was filled with 3 cylinders of aluminium (one with diameter 32.5 mm and height 9 mm; the other two had diameter 32.5 mm and height 104 mm, but with a clear well of diameter 16.4 mm). After some measurements, the ingot was extracted to be inspected and it was discovered that after the degassing that could have provoked the craters, they disappeared but the ingot presented some yellow reflections on its surface. The chemical analysis detected important contaminants: Na, Mg, S, Fe, W. A fast decrease of pollution in the thickness of metal was observed but sodium still remained up to 100 µm depth. The origin of these pollutants is supposed to be: Na (diffusing from Inconel, silica and graphite walls); Fe (the Inconel envelope of the heat pipe); W (the furnace heating resistance); Mg (furnace thermal insulators). The author assumes the

silica envelope of the cell presents a porosity in some areas that allows the contaminant vapours penetration.

Another research [29] investigated how the time spent in the liquid phase (after the completion of a melt) could impact the behaviour of a subsequent freezing plateau. They studied both the time spent and the temperature above the phase transition. The time spent varied from 30 min up to 61 h. The temperatures were 0.5 °C and 3.8 °C above the melting point. The freezing points were all carried out in the same manner: i.e. induced nucleation in both the outer and inner surroundings of the ingot; the furnace set 0.2 °C below the phase transition temperature. The freezing plateau was considered finished when the SPRT read a variation $\geq 50\ \mu K \cdot min^{-1}$. Their conclusion was that, for aluminium, the metal should remain molten for at least 25 h before the freezing point induction, irrespective of the temperature at which the metal was kept liquid. Optimal freezing range was obtained with the cell left for around 38.5 h in the liquid phase before inducing nucleation. This time duration is of course impractical for repeated measurements. After around 300 h at a temperature close or equal to its phase transition, the cell was opened and its ingot was inspected. They observed some yellow reflections, black zones and disturbed zones on the outer surface of the ingot. Several analyses were carried out so as to detect the possible impurities. The material was sampled in seven different regions. The main impurities were Na, S, P and Mg. The upper part of the ingot was the most affected area, possibly due to gravitational segregation (difference in density). The impurities Na and Mg are attributed to furnace materials. The purest aluminium was found close to the thermometer well.

Doping aluminium cells was also performed by [30]. They tested different concentrations of the impurities copper, silicon and titanium, considering each of them to form a binary system with the aluminium matrix. The conditions at which the investigation was done were the same as regularly set for conventional measurements and calibration services. After each doping, the cells were kept at 5 °C above the phase transition temperature for several days to ensure a proper mixing of the impurities. In ideal conditions, the purer the metal is, the flatter the plateau will be. For comparison purposes, the maximum value of the freezing plateaux was used in order to qualify and compare the cells. According to the results obtained, the aluminium freezing point was

shifted at the ratios –0.43 mK/ppmw[1], –0.85 mK/ppmw and +3.2 mK/ppmw, as polluted by copper, silicon and titanium, respectively. It was stressed that SPRT stability is still a major problem at this temperature. Due to the high ratio at which titanium changed the aluminium phase transition temperature, a few years later, its influence was investigated again [31]. They doped 6N aluminium with 99.8 % titanium, with two concentrations: 0.9 ppmw and 1.8 ppmw. However, according to the experimental data, the temperature change caused by titanium was found to be (+5.1 ± 3.0) mK·ppmw^{-1}. Subsequently an offset to the GDMS analyser was found and when taken into account, this impurity sensitivity would be +3.4 mK·ppmw^{-1}, similar to other studies.

The methodology for measurements applied in [20] focused in the furnace set-points being changed in small steps: the aluminium ingot was melted by increasing the furnace temperature from –1 °C to +1 °C above the phase transition temperature. Afterwards, the temperature was increased by 2 °C and the metal was left for 1 h for homogenisation in order to promote uniform impurity distribution. Then, the furnace was brought back to +1 °C above the phase transition temperature and left for 2 h so as to have the metal annealed at a temperature as close to the fixed point temperature as possible. Their conclusions included: ready-to-use cylinders produces better results than pellets; the 6N5 cylinder cell was better than the 6N cylinder cell. Indeed, to date, the highest purity available at sufficient amount to produce a fixed point cell was 6N5, which is quite difficult to obtain commercially and in addition, the cost of 6N5 aluminium is 5-10x higher compared to the widely available 6N. However, the conclusions from investigations with 6N5 aluminium are mixed and therefore the use of aluminium with this level of purity does not seem justifiable given its cost and doubtful performance.

[1] Parts per million by weight (mass fraction)

2.3.4. Delimitation of the study

In this section, I describe the limits of the research. I focus on the fixed point of aluminium and in particular the freezing behaviour of different samples of pure aluminium.

Melting plateaus are not used for cell evaluation due to their lower stability in comparison to freezing plateau and also the difficulty on defining the melt-off point (the end of the melting curve) and hence the determination of the liquid fraction *F* (and its inverse) with great accuracy.

At the early stages of investigations of impurity effects on fixed point cells, an approach based on Raoult's Law was proposed. It assumes that the transition temperature of the pure substance can be determined by suitable extrapolation of the measured temperature as a function of the molten fraction of the sample (as if the impurities were colligative, i.e. dependent on the amount rather than the nature/type of impurities). This method is also used to determine the purity of materials in Chemistry by means of calorimetry. It was even considered by the BIPM Consultative Committee for Quantity of Substance (CCQM) as a potential primary method for the amount of substance measurement. However, its main drawback is that it assumes all impurities to be soluble in the liquid but not in the solid phase of the matrix, whilst some well-documented systems were reported to exhibit significant solubility of impurities in the solid state, or even presenting greater solubility in the solid rather than in the liquid phase. This would mean a completely different behaviour of the impurities: instead of decreasing the temperature as assumed, impurities soluble in the solid state will increase the fixed point temperature [14]. Indeed, other references [10, 11, 44], as mentioned before, explain that it is of major importance knowing the specific effect of a given impurity, as some can either change or have no effect at all on the phase transition temperature of the matrix material. Taking into consideration these issues, methodologies based on the Raoult's law should be applied with caution (which probably is the reason why estimates yielded according to the OME methodology should not be applied to correct temperatures due to the effect of impurities). Furthermore, methodologies described in [45] were not accounted for this research due to their lack of consistency.

This study specifically investigates the application of the main methodologies used to correct the freezing point temperatures of fixed point cells for impurity effects – the SIE, the OME, the Hybrid SIE/Modified OME, the Scheil model, the gradient method, the thermal analysis (or '1/F method') and the direct comparison of cells. In order to better characterise the impurity distribution in the aluminium samples utilised to construct the cells for this study, samples were prepared and additional GDMS analyses were performed by three independent laboratories. The ultimate objective is to be able to determine the correction methodologies that are more consistent across the cells that were studied.

Chapter 3

Construction of the aluminium cells

The research in this thesis centred on the construction of aluminium fixed point cells from different batches of aluminium provided by different suppliers. As such meticulous care had to be taken to ensure that all the cells were constructed in a similar way, avoiding contamination. Initially the first cell constructed was intended as a prototype, by means of which the construction process was tested. However, once the construction of this cell was completed and its construction deemed successful (and hence the construction procedure was satisfactory, without requiring amendments), the first cell was kept as the first to be tested. The other four cells were constructed following the same process. This process including the selection of materials employed to the assembly of the five cells is described in this chapter.

3.1. Selection of materials

The intent of this study was to investigate possible changes in the phase transition temperature of high purity aluminium due to the effect of residual impurities. As such it was of paramount importance to restrict the variability of the system (chief of which was the fixed points themselves but of course included the measurement systems as well) to the different samples of the metal alone. Consequently, all other components of the fixed point were of the best quality available and identical in all cells, handled and prepared rigorously according to the same procedure before being used for the assembly of the cells.

3.1.1. Description of the Aluminium samples

In order to achieve some variability in both the quantity and nature of impurities present in the aluminium used for construction of the suite of fixed point cells, batches of aluminium were obtained from five different suppliers: one from the UK (New Metals and Chemicals), one from Japan (Sumitomo Corporation) and three from the USA (Alfa Aesar, ESPI Metals and Honeywell).

Despite not being commercially available yet, aluminium can currently be purified to the level of 99.999 99 % (7N), as reported in [46]. The purest it can be procured at is 99.999 95 % (6N5), although at the time of sourcing the materials for this research only one supplier was verifiably able to produce it. However, the purification of aluminium at these levels of purity is an extremely time consuming and expensive process. Due to this, the purity of the aluminium samples studied here was 99.999 9 % (6N). This decision was also reinforced by the fact that the vast majority (if not the totality) of aluminium cells which constitute ensembles of national standards for the realisation of the ITS-90 have been constructed using 6N aluminium for decades. Still, using purer aluminium than 6N might not effectively produce purer cells because it is possible that some impurities could be introduced by the interaction with the argon and graphite (currently not available purer than 6N) at this temperature.

It was decided that the metal samples should be supplied in the form of shots/slugs, mainly because of ease of sample handling. The exception being the sample material from Japan, which was supplied as a 3 kg monolithic block (from which the required portion of the material was extracted) (figure 8). This was because the supplier specialised in bulk sales only and 3 kg was the minimum that it could provide (and in fact generously donated to this study).

Figure 8: Metal samples supplied to this study: Alfa Aesar cylinders (top left), ESPI shots (top centre), Honeywell shots (bottom left), New Metals slugs (bottom centre) and the Sumitomo monolithic block (measuring 200 mm x 140 mm x 43 mm).

3.1.2. Description of the graphite components

The graphite crucible, re-entrant well, crucible cap and heat shunt discs were manufactured by the SGL Carbon Group. They were made with specialty graphite (fine grained, isostatically pressed), grade SIGRAFINE® R6300-P5, whose ash content is stated as being below 5 parts per million, ppm. This corresponds to a nominal purity of 99.999 5 %. After the machining of the graphite components (by the manufacturer) was complete, they were subjected to both a purification process and a final ultrasonic cleaning. They came supplied as separate sets, each set containing the required parts to construct one cell (figure 9).

Figure 9: A set of specialty graphite components (SIGRAFINE R6300-P5, purity 99.999 5 %), supplied in vacuum sealed bags, selected and ready to be baked.

Apart from these components, the cell was insulated by adding layers of high purity graphite felt on top of the assembled crucible. The felt was also supplied by SGL Carbon Group. The grade of the felt was SIGRATHERM® GFA5, with nominal purity of 99.998 % (ash content below 20 ppm) (figure 10).

Figure 10: Graphite felt discs (SIGRATHERM® GFA5, purity 99.998 %) cut to fit the internal diameter of the quartz envelope, also allowing the insertion of quartz re-entrant tube.

3.1.3. Description of the quartz tubes

The cell was encapsulated in a quartz envelope with a re-entrant well inserted in the graphite thermometer well. These tubes were manufactured by Cambridge Glassblowing, a company which NPL has used for many years. Each fixed point crucible had its own quartz envelope and re-entrant well. The dimensions of the re-entrant well were 470 mm (length) x 10.5 mm (outside diameter, wall thickness 1 mm). The dimensions of the envelope were 480 mm x 50 mm (outside diameter, wall thickness 2.2 mm). Furthermore, three dedicated longer envelopes (750 mm) were used: one for the baking of the machined graphite parts, one for the baking of the graphite felt discs and one for the casting of the ingots inside the graphite crucibles.

The tubes were supplied in a clean state. The cleaning procedure adopted by the supplier consisted of a hydrofluoric acid soak followed by a deionised water rinse. After this, the tubes were rinsed with acetone and oven dried at 120 °C. The tube of the re-entrant well and the envelope both had their external surfaces partly sandblasted (in the region to where temperature gradients form between the furnace core and the ambient). It has been shown that sandblasting is required because it promotes better temperature homogeneity throughout the cell (through the scattering of thermal radiation) and helps to control overheating of the portion of the cell which protrudes from the upper part of the furnace.

3.1.4. Details of the argon gas

Argon gas was used to maintain the pressure inside the quartz envelope atmospheric at the melting point. It is common practice to realise metallic ITS-90 fixed points at atmospheric pressure (101 325 Pa) at their melting point (as recommended by CCT) as the melting/freezing temperature is affected by the pressure of the surrounding gas[2]. The argon used within the cell was 99.999 9 % pure (N6.0 grade), contained in a dedicated cylinder, supplied by Air Products and Chemicals. The gas

[2] At the freezing point of aluminium, the temperature variation with pressure is equivalent to 70 nK/Pa.

was employed to initially flush and purge the system and to set the pressure inside the quartz envelope. When in use, the argon protects the graphite and metal from oxidation. Furthermore, the use of inert gas improves the thermal contact between the fixed point metal inside the crucible and the thermometer.

3.1.5. Other materials

Apart from those components, other materials used for the construction of the cells were:

- Room temperature vulcanisation (RTV) silicone, manufactured by Raytech (working temperature up to 200 °C), for the casting of a specially designed gasket to seal the cap onto the quartz tube;
- Quartz rod used to push/position the pieces inside the quartz envelopes and to push the graphite re-entrant well to be fitted to the graphite cap (resisting buoyancy until the metal solidifies);
- Lint-free cleanroom laundered wiper Microseal® 1200 (made of polyester knit fabric) used when cleaning quartz parts;
- Lint-free cleanroom nonwoven wiper Durx® 770 (made of a blend of cellulose and polyester) used for general cleaning and lining of benches before handling the parts and for sliding the crucibles inside the quartz envelopes;
- Kaowool ceramic fibre for insulation of the furnace;
- Rubber o-rings;
- Disposable powder-free latex gloves;
- Disposable polystyrene weighing dishes;
- 3M Wetordry Tri-M-ite sanding paper, series 734 P800;
- Expanded polyethylene rigid plastic foam blocks;
- Vacuum storage bags and
- Jeweller's saw – for cutting the samples off the Japanese supplied Al block.

3.2. Preparation of materials

In order to cast the fixed point ingots inside the graphite crucibles, parts were inspected and a regular procedure established to prepare the materials for use. They are described as follows.

3.2.1. Handling and inspection of parts

All parts were kept in their original packaging until they were used. The materials were handled using disposable latex powder-free gloves in order to guarantee their cleanliness. The graphite and quartz parts were inspected to check for faults (especially cracks) and if the dimensions matched the specifications in the drawings.

3.2.2. Auxiliary equipment

The auxiliary equipment used in the construction of the cells comprised:

- A laminar flow workstation manufactured by Bassaire Limited, model K2V;
- A Pfeiffer HiCube 80 Eco turbomolecular pump;
- Calibrated scales from Fisher Scientific, model SG-402;
- A Carbolite three-zone furnace, model TZF 12/75/700;
- Cooling fans;
- A water circulator coupled with a water bath, manufactured by Grant, model Optima TC120-R4;
- Gas handling system with a calibrated pressure gauge manufactured by GE model Druck DPI 104;
- A leak detector manufactured by Oerlikon Leybold Vacuum, model PhoeniXL300, equipped with a turbomolecular pump, a mass spectrometer and a helium sensor and
- A cylinder containing high purity helium (99.999 %, supplied by BOC Industrial Gases) used in conjunction with the leak detector.

3.2.3. Further cleaning of quartz parts

Even though the quartz pieces (envelopes, rods and re-entrant tubes) were supplied cleaned, individually sealed in plastic sleeves, they were rinsed with analytical grade acetone before use. For pieces that aided the construction of the aluminium cells (rods and the dedicated envelopes for baking the graphite and the one for casting the ingots) this procedure was repeated whenever one of these parts was used again.

3.2.4. Furnace tests

Firstly, the tree-zone furnace used for the construction of the fixed point cells was tested in order to measure the controller offset from the melting temperature of aluminium. After that, its temperature profile and stability were determined using two thermocouples. These measurements were used to minimise the thermal gradient within the furnace. This was very important especially because a minimal temperature gradient is required when melting the metal to cast the ingots. The furnace was set up so that the graphite crucible was positioned at the most homogenous temperature profile of the furnace, which after some adjustments in the zone controllers, became the central zone (which had a uniformity of 2 °C over 24 cm, tested at 660 °C). The measured gradient was acceptable for the manufacture of the fixed points because the aluminium ingots would be cast at 10 °C above its melting temperature. The homogeneity tests were not performed at higher temperatures as rigid control of temperature was not required for baking the graphite parts.

3.2.5. Manufacture of gaskets

When testing the seal of the metal cap with the quartz envelopes, it was observed that the o-rings were not able to completely seal the system. This was an issue because oxygen could harm the graphite pieces at high temperatures, especially while baking them. However, operation with fixed point cells needed to occur at a set pressure (101 325 Pa). A series of different things were attempted to solve this issue

and eventually a gasket made with RTV silicone, using the metal cap itself as a mould, made the system sufficiently airtight (best vacuum around 0.3 Pa; leak rate below minimum level, 1 x 10^{-10} Pa·l/s).

The manufacture of the silicone gasket consisted of weighing both of the RTV silicone components (at the ratio 1:1) and mixing until they formed a homogeneous viscous liquid. Then, this mixture was poured into the mould, which consisted of the metal cap (placed upside down on top of a brass stand) with a stainless steel cylinder of 50 mm diameter at the centre. After around 10 minutes, the vulcanisation of the silicone was complete and the gasket extracted from the mould (figure 11).

Figure 11: Highlights of the manufacture of the gasket made with two-part RTV silicone. From top-left: weighing and mixing the components; pouring the mixture into the mould; vulcanisation of the silicone and extraction of the gasket from the mould.

3.2.6. Baking of graphite pieces

Prior to casting the aluminium ingots, the machined graphite pieces needed to be baked at a high temperature (1100 °C), in vacuum, in order to clean it from any residual impurities arising from the machining of the pieces. Any impurities still present in the material would be volatilised at that temperature and extracted by the vacuuming. When the graphite pieces were subsequently used at the intended temperature (660 °C), impurities that would have been volatile up to this temperature (which could potentially migrate to the high purity metal) would have been extracted from the graphite, hence preventing contamination of the aluminium samples. For the construction of any fixed point in a graphite crucible this procedure is generally realised at a much higher temperature than the intended use.

The fitting of the graphite pieces was checked before the baking procedure so that, if required, any adjustments were made before they were baked. If needed, the pieces were adjusted by gentle abrasion with sanding paper (3M wetordry Tri-M-ite). The pieces were baked as a set, which contained all parts required for the construction of one cell. They were inserted in the quartz envelope dedicated for the baking of the machined graphite parts. After that, the quartz tube was inserted in the furnace so that 15 cm of the tube protruded from the furnace to prevent overheating of the rubber gaskets in the cap. Some insulation (kaowool ceramic fibre) was also placed in between the upmost part of the furnace alumina tube and the quartz tube. The quartz envelope metal cap was fixed at the top with all connections already in place (silicone hoses for water cooling and gas hose for gas extraction). The water circulator (connected to the cap via the silicone hoses) was turned on. Then, the central hole in the cap (originally designed for the re-entrant well) was blocked by a 10 mm quartz rod and rubber o-rings. The set-up is shown in figure 12.

Figure 12: Set-up for the bake of the graphite pieces and casting of the ingots.

The turbo pump was turned on and the system left to be evacuated until the pressure was below 1 Pa. After that, before turning the temperature up, the seals between the metal cap and the quartz parts were leak tested with the leak detector (figure 13).

Figure 13: Testing the seals in the metal cap with the leak detector.

In order to prevent over-heating of the protruding section of the quartz envelope, two cooling fans were directed at the tube. The furnace was turned on and set to 1100 °C at a ramp rate of 10 °C/min (which decreased gradually as the furnace temperature increased, especially above 600 °C). Once it reached the set-point, it was left baking for a period of 48 hours (figure 14).

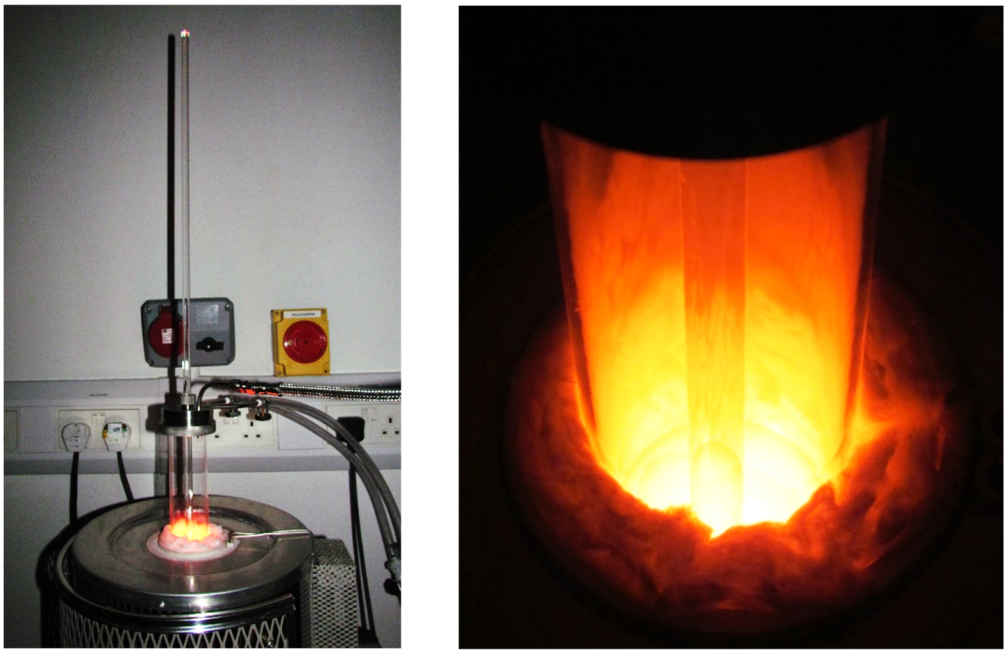

Figure 14: Graphite crucible assembly during bake at 1100 °C.

The cooling fans proved to be efficient as the temperature of the tube region close to the cap was around room temperature. After the 48 hour baking cycle, the furnace was set to 20 °C. It was important to leave the furnace running because although the controller would cut the power of the main heater, the auxiliary ones (top and bottom zones) would continue to equalise the temperatures, preventing the build-up of large temperature gradients (> 100 °C). Once the furnace reached ambient temperature, the turbo pump was switched off and the pieces extracted from the quartz envelope. All five sets of machined graphite pieces were baked according to this procedure.

After all five sets were baked, the graphite felt discs were cut and also baked, following a similar procedure, in a separate tube at around 1000 °C for 40 hours. The lower temperature used for the felt discs was due to the softening of the quartz tube, noticed after the first bake of the discs attempted at 1100 °C. Approximately 60 discs were baked at a time as it was the maximum that could fit in the bottommost 50 cm of the quartz envelope which was required to guarantee all discs were exposed to approximately the same temperature.

3.3. Construction of the cells

After the above preparatory steps, the metal samples were cast in the baked crucibles. To preserve the purity of the samples, the construction followed the same procedure in order to guarantee that the fixed point cells would be constructed in a manner as systematic and reproducible as possible. The main aspects of this stage are described below.

3.3.1. Design of the fixed point crucibles

The fixed point cell design was based on one in long standing use by the thermometry team at NPL. Only a few minor design details were adapted for the purpose of this research. It was considered that it would be advantageous to keep most of the common practice of the NPL. Taking into account that the equipment and the realisation procedures employed in numerous NMIs (notably the world leading institutes) are similar, the results of this study could be directly applicable to standards in other institutes. The fixed point cells from NPL have successfully shown their performance through key comparisons [47, 48], with the results registered on the BIPM key comparison database (KCDB) [49] and are listed in the BIPM calibration and measurement capabilities (CMC) database. The main design modifications for this study were related to the quartz envelope, whose dimensions had to be changed because of the diameter of the furnace worktube used with the fixed points (52 mm). In addition, the design of the quartz re-entrant well of the cell was modified (limited to 470 mm in length and 8.5 mm in inner diameter) in order to allow for the insertion of a wide range (almost all types) of long-stem SPRTs (figure 15).

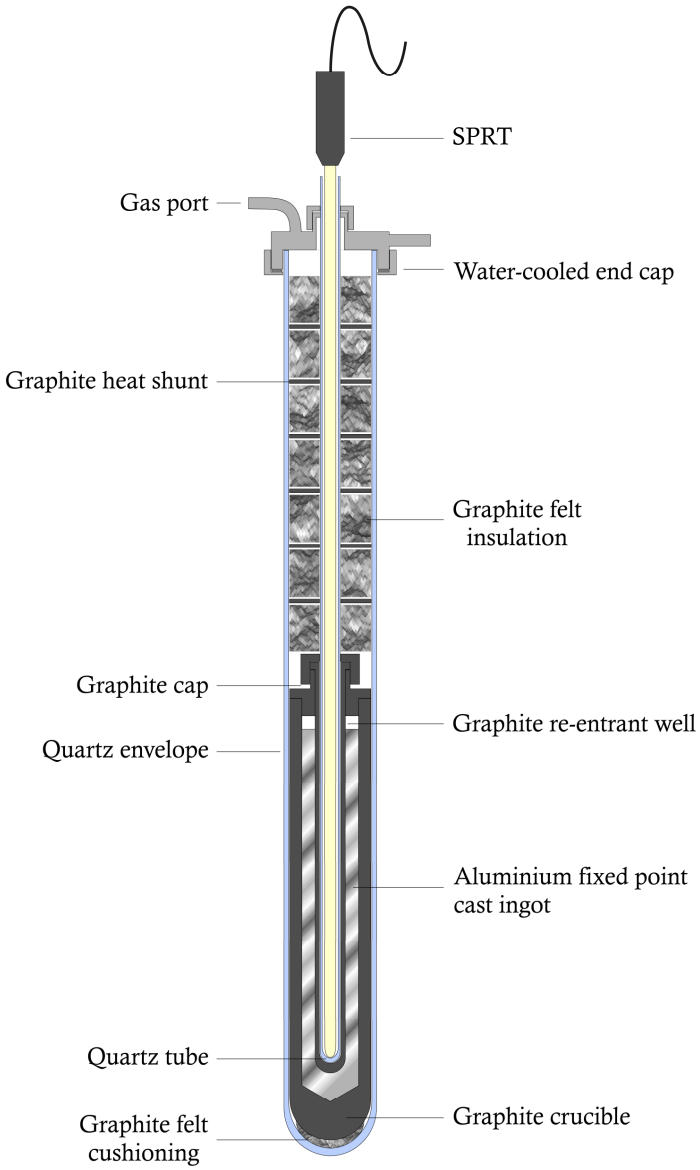

Figure 15: Schematic diagram of the aluminium fixed point open cell design used in this study (drawn to size to check the fitting of the assembly, scale 1:4).

The fixed point system in figure 15 consists of a high purity aluminium ingot contained in a graphite crucible. The casting of the ingot will be described later in this chapter. Above the crucible assembly, there is insulation (graphite felt discs) interspersed with graphite heat shunts. The fixed point system is enclosed in a quartz envelope and has a quartz re-entrant well for the insertion of the temperature sensors into the fixed point ingot. The whole system is sealed with a water-cooled metal cap.

The crucible assembly was intended to accommodate enough metal to provide adequate immersion depth for the sensors to be used in the finalised cell. For illustrative purposes only, the relevant dimensions of the crucible and graphite re-entrant well are shown in figure 16.

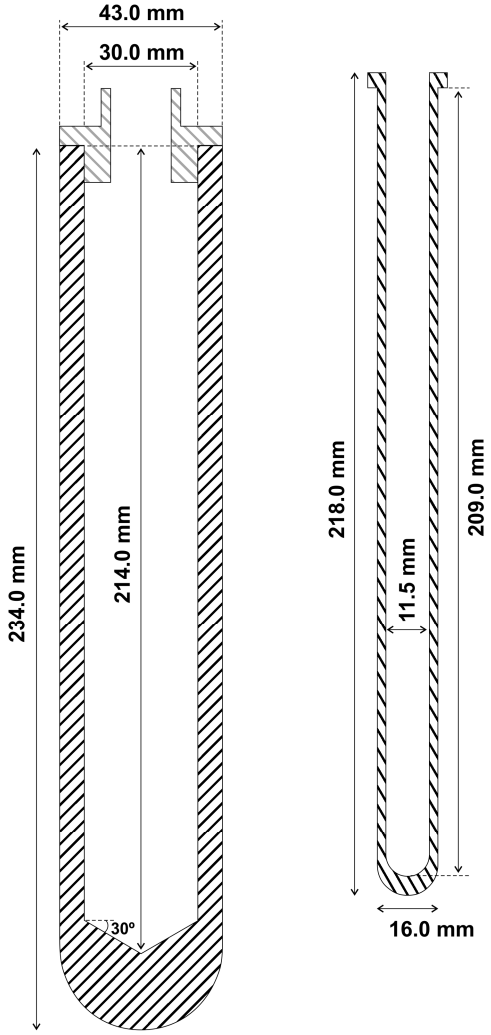

Figure 16: Dimensions of the crucible and re-entrant well (scale 1:2).

The internal volume of the crucible is 97.64 cm^3. Considering that the density of liquid aluminium is 2.71 g/cm^3 [50, 51], the mass of aluminium required to fill each cell should be 231.91 g. This gives an immersion depth for the thermometers, into the ingot, equivalent to 172 mm inside the thermometric well (figure 17).

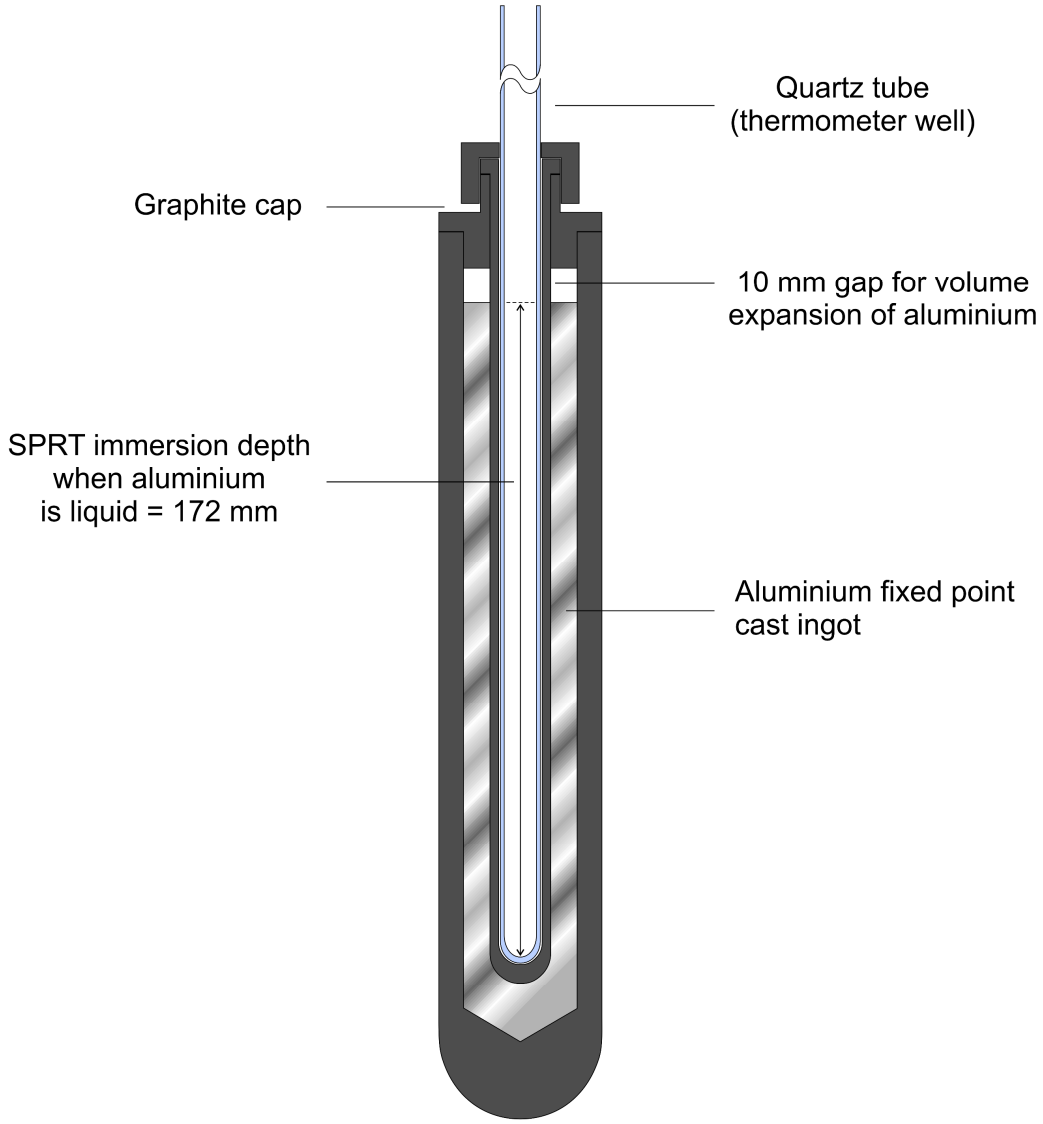

Figure 17: Fixed point crucible assembly (scale 1:2).

These volume calculations include a total of 10 mm gap in between the surface of aluminium (in the liquid phase) and the crucible cap. This gap allows the equivalent thermal expansion of the molten ingot for a temperature increment of around 10 °C above the melting point. This is a safety measure to prevent breakage of the cells in the event of overheating. Preventative care in this regard also includes: melting the cells only at 5 °C above the melting point (so that the gap still allows some expansion) and setting the furnace controller to cut the furnace power off if it ever accidentally reaches 10 °C above the melting point.

3.3.2. Procedure for casting the aluminium ingots

In order to ensure the purity of the metal, during the whole process, the metal shot was never handled, not even by gloved hands. They were poured in small portions from the shot containers to polystyrene weighing dishes and then after the shot was weighed the shot was transferred directly to the crucible. All this handling, from opening the containers of the aluminium samples to pouring them into the graphite crucibles, occurred inside the laminar flow cabinet in an attempt to prevent particulate contamination. The exception for this was the block of aluminium supplied by Sumitomo, whose handling was more complex: it required extracting small portions of the metal with a jeweller's saw. In order to do it, the block of aluminium had to be secured by a vice (figure 18). During the process, the metal was only handled by gloved hands and the section that would be in contact with the vice was wrapped in multiple layers of cleanroom wiper Durx® 770 (also to protect the material from indentation caused by the serrated jaws of the vice).

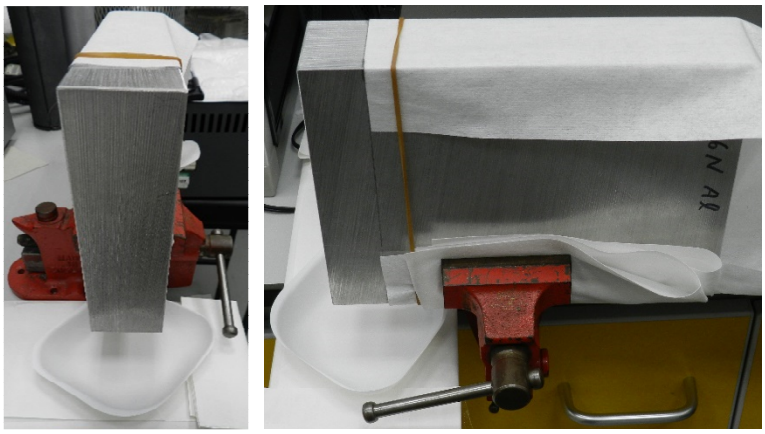

Figure 18: Block of aluminium supplied by Sumitomo ready to be cut.

Due to the high affinity aluminium has for oxygen, especially at this level of purity, oxidation at the surface of the metal shot was inevitable. However, it has been reported that, for aluminium, this oxide layer, instead of being a source of contamination that would affect the phase transition temperature of aluminium, it actually protects the core metal from being contaminated. This happens because the oxide formed, Al_2O_3,

is immiscible (not dissolved) in the pure aluminium matrix, hence precipitates out [25, 42, 43].

Due to the interstices between the shot, the total mass of the ingot could not be put into the crucible in a single fill, instead two fillings were required to completely charge the crucible with the required amount of aluminium. The first filling consisted of approximately 200 g of aluminium shot, weighed in small portions with the aid of weighing dishes (figure 19). From the polystyrene dishes, the metal was then poured directly into the crucible (figure 20).

Figure 19: Weighing the portions of aluminium to transfer to the crucible. The first four cells were constructed with metal samples in the form of shot or slugs (left). The last cell (Al-S) was made using aluminium blocks cut from the larger sample sent by the supplier (right).

Figure 20: Crucible containing 200 g of aluminium shot, ready to be melted.

After the crucible was filled with the aluminium sample it was covered with its cap and carefully inserted into the quartz envelope. After that, the quartz tube was inserted in the furnace and the metal top cap added. A quartz rod was also inserted in the central hole of the metal cap to make the system airtight by locking the rod through a retaining nut. The turbo pump was started and the system allowed to be evacuated until the highest achievable vacuum was reached (around 0.3 Pa). This step from switching on the pump to achieving the highest vacuum took around 40 minutes.

The furnace was then turned on and its controller was set to 650 °C. Once this temperature was reached (approximately 2 hours later), a preparatory process was carried out before proceeding to melt the aluminium sample. This process was started by closing the vacuum valve and slowly filling the quartz envelope with pure argon up to a pressure around 103 kPa (slightly overpressurisation). Then, the gas valve was locked and the system was gradually evacuated again, until the pressure went below 1 Pa. At this point, the process of filling the system with argon and purging it was executed again. The final step, before initiating the melt, was refilling the system with argon up to a pressure close to 101 325 Pa. This procedure is necessary as it eliminates any impurities before the actual melt, avoiding these contaminants from mixing with the pure material once it becomes liquid. As soon as the system was pressurised to the intended pressure at which the phase transition occurs, the furnace controller was set to 670 °C (nearly 10 °C above the melting point of aluminium) to melt the samples and cast a solid aluminium ingot inside the graphite crucible. After about 3 hours of melting, the furnace was turned down to 20 °C and allowed to cool naturally (aided by the zone controllers to avoid the formation of massive temperature gradients along the furnace tube). Once at room temperature, the system was dismantled and the crucible extracted from the quartz envelope and inspected inside the laminar flow cabinet (figure 21).

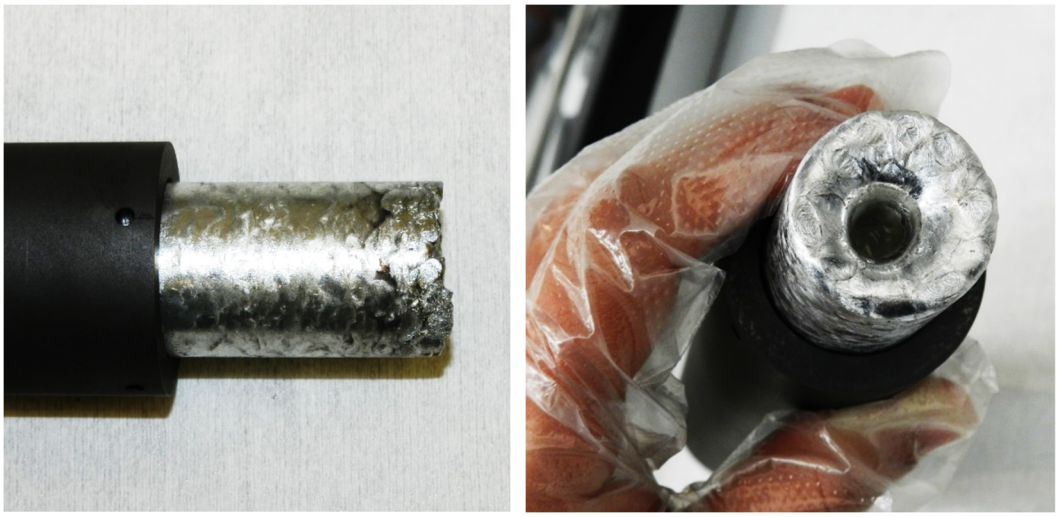

Figure 21: Inspection of the ingot formed from the first load of metal.

To complete the process the second filling was performed as follows. The remaining required mass of metal (around 32 g, from the same batch) was weighed and poured on top of the already cast ingot. In addition, the crucible cap was placed in position and this time, the graphite re-entrant well was inserted among the metal shot. After that, a quartz rod was introduced in the graphite re-entrant well to assist the correct final positioning and fitting of the graphite crucible assembly. The height of the re-entrant well that was yet to be inserted in the metal ingot was measured and transferred to the portion of the quartz rod immediately external to the envelope assembly (figure 22). This height was typically around 130 mm.

Figure 22: Measurement of the height of the re-entrant well to be pushed through the metal once it becomes liquid (left). Height transferred to the quartz rod to indicate when the insertion was complete.

In order to complete the crucible assembly, the extra sample of metal must be melted and the graphite re-entrant well inserted into the molten metal ingot. For melting the aluminium, the same procedure was adopted as for the first filling, from initially increasing the furnace temperature to actually setting the furnace temperature above the metal melting point temperature. Approximately two hours after the initiation of the melt, the retainer nut on the gas tight metal cap was loosened and the quartz rod carefully pushed until a solid portion of metal ingot was encountered. Once it was not possible to move the quartz rod further in, the retainer nut was then tightened, securing the quartz rod at its new immersion depth. The pressure in the system was checked and adjusted. Results varied but, generally, each attempt at pushing the rod caused it to move 35 mm inwards on average. This process was repeated at every 40 min or so until the re-entrant well was fully inserted into the crucible. The furnace was then turned down to room temperature and allowed to cool naturally. Once cold, the system was disassembled and the crucible inspected again (figure 23). If the procedure was successful, the re-entrant well was locked by a graphite retainer cap because future melts could cause the well to float upwards due to the effect of buoyancy of aluminium. At this stage assembly of the graphite crucible was complete.

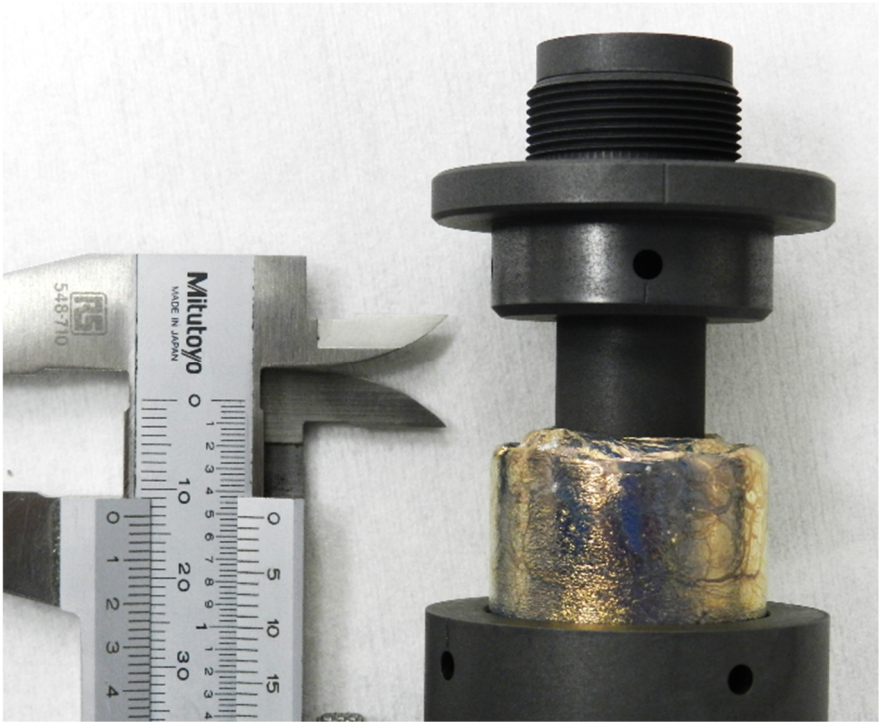

Figure 23: Inspection of the ingot after insertion of the re-entrant well is complete. The gap allows for the expansion of aluminium on melting (caused by the difference in the density of aluminium, from solid to liquid).

3.3.3. Final assembly of the cells

For the final assembly of the cell, insulation and so forth, the graphite crucible was inserted in its permanent 480 mm quartz envelope, on top of one disc of graphite felt that served as cushioning. After that, above the crucible assembly, some graphite felt discs (6.7 mm in thickness) interspersed with graphite shunt discs (2.0 mm in thickness) were inserted. The felt discs acted as thermal insulation of the crucible (to prolong the phase transition curves) while the solid graphite discs served as thermal links between the furnace temperature and the thermometer inside the cell (to compensate to some extent for heat losses along the SPRT stem). The arrangement of these discs was: 6 sets consisting of 4 felt discs topped by one shunt disc. Above the last set, other three felt discs were used to complete the insulation, the total length of which was around 185 mm. The discs were pushed into position with the aid of a clean quartz rod. After this stage was finished, in order to complete the assembly, a quartz

tube was introduced through the insulation until it reached the bottom of the graphite re-entrant well. A complete crucible, insulation, quartz envelope and metal cap assembly is shown in (figure 24).

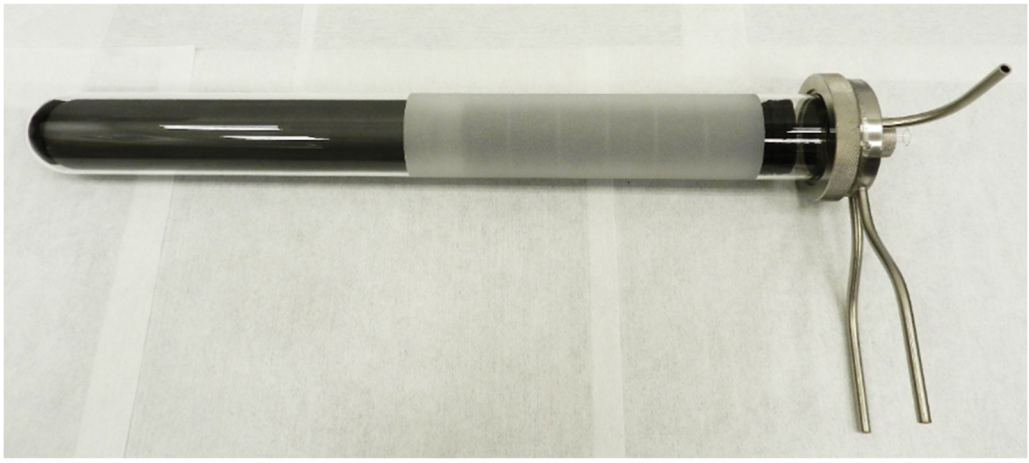

Figure 24: An assembled aluminium cell ready for testing.

Given the way the water-cooled metal cap was designed, it was not advisable to disconnect the gas and water hoses every time a cell was used. It was decided to use the metal cap as a fixed part of the system: the assembled cell would be inserted in the vertical furnace tube and then the metal cap (already connected to the system) would be attached to it. While not in use, the crucible assembly was protected using a piece of clean plastic foam fitted at the top and the cells were individually stored inside a vacuum storage bag (figure 25).

Figure 25: All five cells stored after the construction stage.

3.3.4. Basic characteristics of each cell after the construction

The main difference among the cells is the mass of aluminium in the crucible. This varied slightly mainly due to the different shape and weight of the metal samples and because of which it was unfeasible to fill the cells with the optimum 231.91 g of aluminium. There was also the special case of the cell Al-S, made from aluminium samples cut from the monolithic block supplied, which made it even more complicated to set the mass close to the target value. However, in the event when the crucibles were assembled, the final amount of aluminium in the crucibles was very similar leading to a similar immersion depth for each. These differences are stated in table 6.

Cell	Supplier	Shape of sample	Average weight (pellet) /g	Total mass (aluminium) /g	Immersion depth /mm
Al-H	Honeywell	shot	0.22	231.92	172.01
Al-E	ESPI	shot	0.22	231.88	171.98
Al-A	Alfa Aesar	cylinder	0.53	232.16	172.21
Al-N	New Metals	slug	0.81	232.09	172.15
Al-S	Sumitomo	block	—	231.44	171.61

Table 6: Basic characteristics concerning the mass of metal and immersion depth of each assembled aluminium crucible.

The preparation for casting the cell made with the Sumitomo block of aluminium required cutting the samples. This was done using a jeweller's saw and it was important to check post cutting whether this process had introduced any contamination. In order to perform the impurity analysis, two small samples were extracted from cell Al-S after the ingot was cast. In the end, it resulted in this cell having around 0.5 g less than the other cells. Nevertheless, the differences in immersion depth are negligible, and all cells were considered to have 172 mm of immersion. The results of the chemical analysis on the samples extracted from cell Al-S are given in the next chapter.

In this chapter I described the construction of the aluminium cells used in this investigation. Details were given of the high purity aluminium samples, the materials employed in the construction, the auxiliary equipment required to cast the ingot, the designs of the graphite crucible and the cell assembly. In addition, the procedure for the construction was also detailed. In the next chapter, I describe the measurement protocol (including the equipment employed in the measurements of the cells and the measurements performed), some corrections that need to be applied to the results (for cell comparisons), the preparation of samples for the GDMS analyses and the procedure for numerical conversions.

Chapter 4

Evaluation of aluminium cells

In the previous chapter I have described the construction of the aluminium cells to be used in the subsequent studies in this thesis. In this chapter I describe the experiments performed to investigate the effect of impurities on the phase transitions of the aluminium fixed points. Similar to the construction stage, a protocol was first established in order to ensure a standardised set of measurements were made. As the effect this study is investigating is likely to be small, the establishment of such a protocol was essential. The cells were tested in the sequence they were constructed. In this chapter, the equipment used for the experiments and the measurements performed are described. Furthermore, the preparation of the samples for additional GDMS analyses is also detailed.

4.1. Equipment

In order to accurately apply the various impurity correction methodologies proposed, the phase transition curves of the cells had to be determined using equipment of the best kind currently available, in accordance with the guidelines and procedures set by the ITS-90 and related literature. The apparatus employed (figure 26) to induce and maintain the phase transitions with the fixed point cells as well as to measure and record the data of respective curves is detailed in the Sections below.

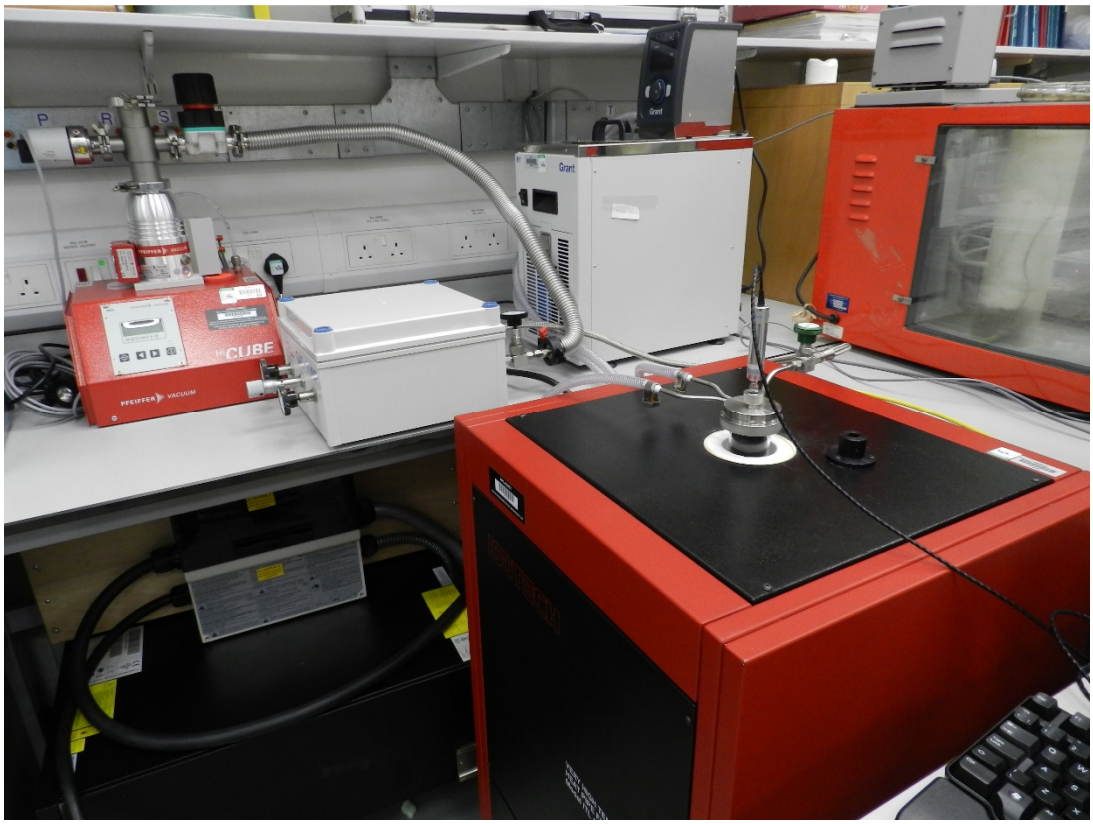

Figure 26: Apparatus for inducing and maintaining the freezing curves in the aluminium cells. Shown in the picture are a furnace, pressure control equipment, the cap of the quartz tube and the measurement platinum resistance thermometer.

4.1.1. Furnace

The furnace employed to induce and maintain the melting and freezing plateaus of the aluminium cells was a three zone furnace (model 9114, serial number A63118) manufactured by Fluke Corporation. It was connected to a dedicated water circulator (controlled at 20 °C) located close to the furnace. This preventative measure was required especially because the furnace was operating close to its upper temperature limit. In addition, in order to prevent overheating and damage of the system, the safety cut-out controller of the furnace was set to 670 °C.

This furnace was optimised for the use with the aluminium cells. This was done through a series of tests to identify the best controller parameters to achieve optimal

temperature stability and, in particular, temperature uniformity along the furnace tube. These tests were performed with the aid of a stable SPRT (Chino Corporation, model R800-2, serial number RS129-03).

The test for the long term stability of the furnace temperature was performed by measuring the SPRT after the completion of a freezing curve. Usually, unsatisfactory behaviour would be noticed a few hours after the set temperature was reached. If repetitive temperature spikes were observed on the SPRT showing that the furnace was unstable (at the level of > 50 mK) or the temperature display of the furnace could be seen to oscillate, either of these effects meant that the controller was allowing too much power to the heaters to maintain the furnace at the set point temperature. On the other hand, if it was not delivering enough power, the real temperature would drop over time. In either case, the parameter called proportional band should be adjusted in the controller menu and observations should be made over a few hours. This should be repeated until a proper adjustment was observed (i.e. the furnace display was steady and furnace oscillations were not observed by the SPRT). To confirm stability had been achieved the measurements were extended for a period spanning over 30 h. Such a long period is necessary to guarantee that the furnace performance would be maintained for a duration longer than that of the freezing curves of the aluminium cells (commonly 20 hours).

Satisfactory results were achieved when the controller proportional band was set to 4.71 °C. The long term stability of the furnace was optimised to 32 mK (maximum amplitude) over a period of over 50 hours (figure 27). This figure shows that the overall performance of the furnace is even better than required as the fluctuations are kept below 16 mK for most of the time.

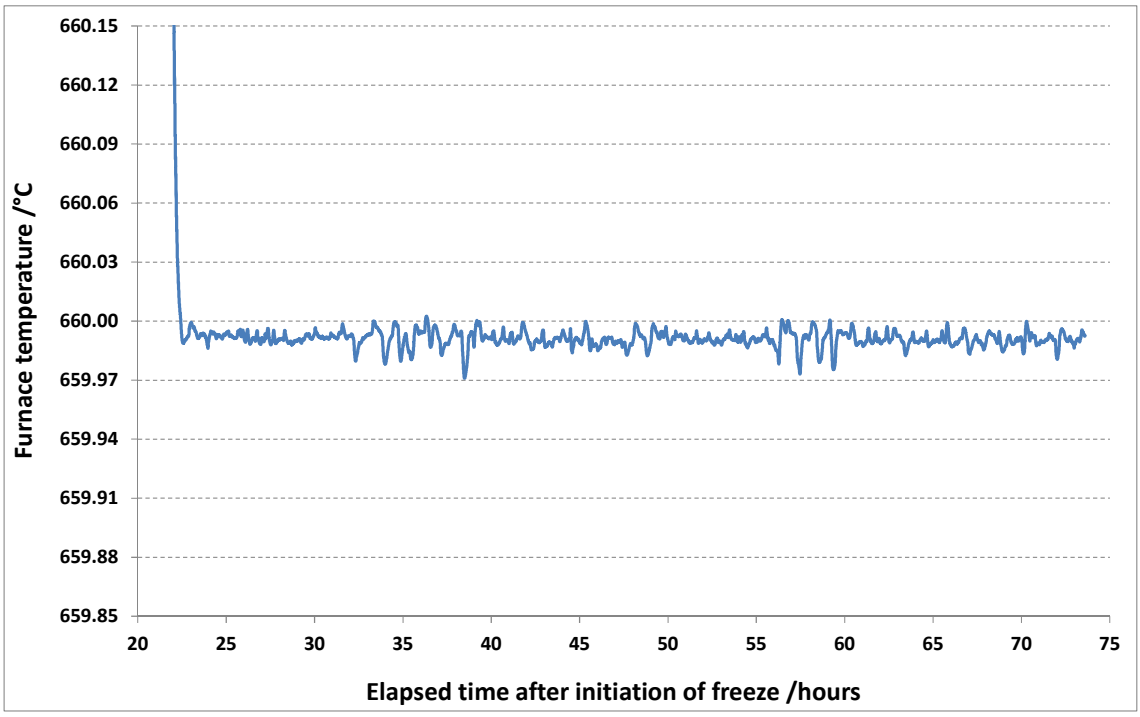

Figure 27: Set-point stability of furnace Fluke 9114 A63118 after freezing of cell Al-E (made from ESPI samples).

To determine the vertical temperature uniformity, the temperature of the furnace was measured inside the re-entrant well of the cell. These measurements were performed with the fixed point in its frozen state, at a temperature just below the melting point (~ 658 °C). The SPRT was fully immersed in the re-entrant well of the cell and measurements started when the sensor readings were stable. The thermometer was withdrawn 2 cm from the cell. At this new immersion, readings were taken for around 5 minutes until stability has been achieved and then the SPRT was lifted 2 cm again. This was repeated to a maximum height of 14 cm. This has to be done as quickly as possible because I am trying to compare all the measurements as if they were taken simultaneously (i.e. as if there was no temporal drift in the thermal gradient) – which in practice is not possible to do. Additionally, it is indispensable to have an ascending gradient in the cell (it should be colder at the bottom and hotter at the top of the ingot) in order to ensure that the top portion of the metal would, at the respective phase transitions, be the first to become liquid and last to freeze. This prevents damage to the cell due to the upward volume expansion of the liquefying metal being obstructed by a solid layer at the surface.

If the temperature uniformity profile was not satisfactory, a different adjustment of the furnace zone controllers was made by setting a different value at one of the controllers and new tests were done after two hours (waiting for the furnace to achieve new state of thermal equilibrium). This process was repeated until suitable results were achieved. As there is no set rule or correlation between the results and the adjustment to be made at the controllers, this is essentially a trial and error method (which can take up to several weeks to achieve the desired optimisation of the furnace). This procedure was adapted from [52], which states that the maximum temperature gradient should be 50 mK along the bottommost 20 cm of the re-entrant well of the cell.

Measurements were only done up to position 14 cm. Given the lower temperature observed after steady increments in temperature as the thermometer was withdrawn from the cell, it was concluded that measurements beyond that position would not be realistic (it can be seen in figure 28 that for most of the tests the temperature dropped beyond the 12 cm position). The sensing element of the thermometer is approximately 37 mm long and is positioned 10 mm away from the tip of the SPRT (totalling 187 mm). This means that at 14 cm and beyond the sensing element was no longer only measuring the temperature of the frozen ingot of the cell (equivalent to a total depth of approximately 158 mm, when solid, inside the re-entrant well), but the furnace surroundings as well. Another factor influencing the thermometer lower readings at the 14 cm position is heat loss caused by stem conduction, due to a substantial portion of the stem being exposed to ambient temperature.

The first measurements were done with the settings already at which the furnace had been operating (bottom zone at 0.0 °C and top zone at +0.4 °C). The resulting vertical gradient was 178 mK in 14 cm. In order to have only one of the parameters varying, the bottom zone controller was fixed at 0.0 °C for the other settings tested, while the values set at the top zone controller were chosen arbitrarily. The following tests were performed with the top zone set at – 0.5 °C, – 1.0 °C, – 0.8 °C and – 0.7 °C, which resulted in maximum vertical gradients of 43 mK, – 30 mK, 13 mK (dropping after 8 cm, reaching – 17 mK at 14 cm) and 13 mK, respectively (figure 28). Therefore, satisfactory results were achieved with the zone controllers set at 0.0 °C (bottom) and – 0.7 °C (top), whose results are also tabulated in table 7.

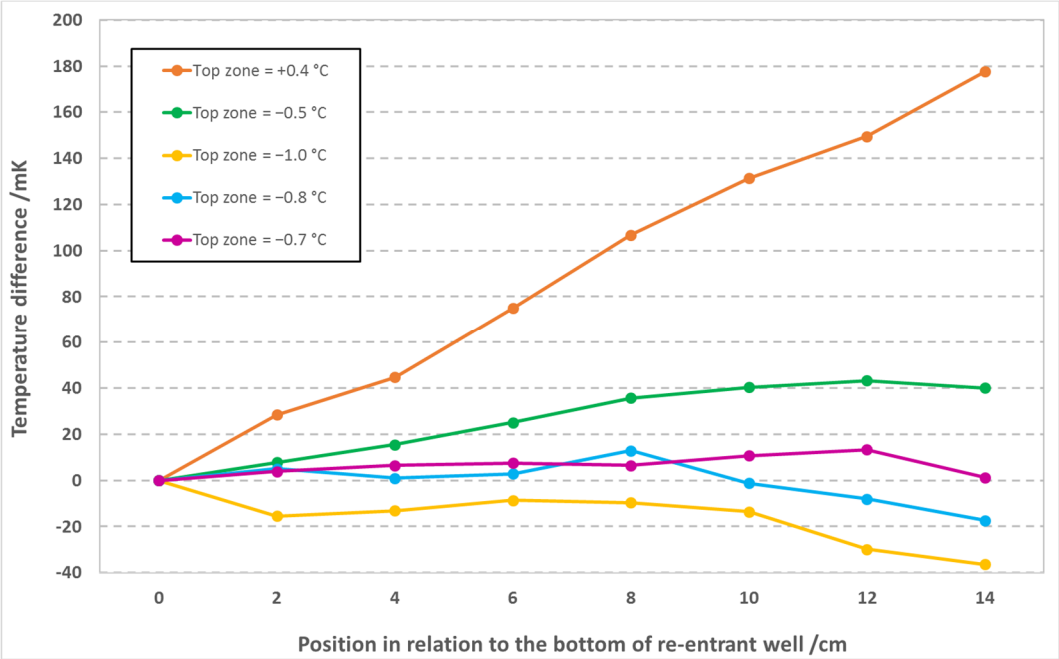

Figure 28: Results of the thermal profile measurements performed with various zone controller settings.

Position in relation to the bottom of the re-entrant well	**SPRT Resistance**	**Temperature difference in relation to the bottom**
cm	**Ω**	**mK**
0	86.477 414	0.0
2	86.477 423	3.9
4	86.477 636	6.5
6	86.477 711	7.5
8	86.477 634	6.5
10	86.477 971	10.7
12	86.478 181	13.3
14	86.477 215	1.3

Table 7: Thermal profile tests of furnace Fluke 9114 A63118 done with cell Al-H (Honeywell) and SPRT Chino RS129-03.

4.1.2. Standard platinum resistance thermometers

The measurements reported in this research were performed using two brand new 25.5 ohm standard platinum resistance thermometers, SPRTs. Before being used with the cells, they have been annealed according to a well-established procedure (described below) and were selected as the most stable ones from a suite of six sensors tested. The SPRTs were: one manufactured by Chino Corporation (model R800-2, serial number RS129-03) and the other made by Isotech Limited (model 670SQ, serial number 312), both designed to be used up to 670 °C. The measurements reported in this thesis are from the SPRT made by Chino (figure 29). The other SPRT was available as a backup in case of any damage occurring to the main thermometer during the measurements.

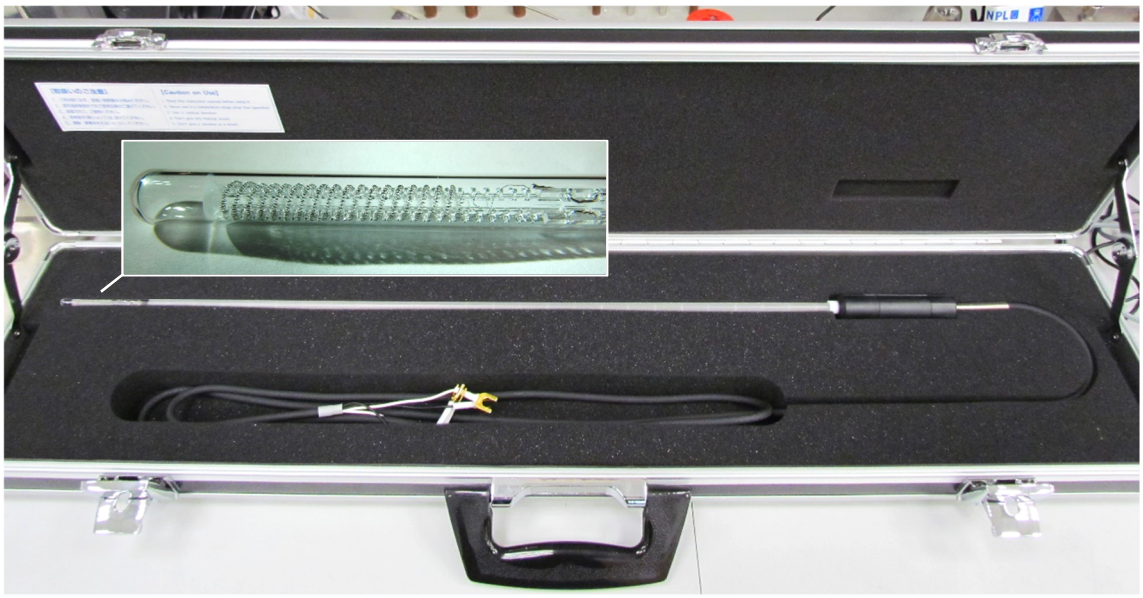

Figure 29: Details of the sensing element of the SPRT Chino RS-129-03, employed in the measurements.

SPRTs are extremely sensitive sensors, requiring a lot of care both while handling (as even mild mechanical vibrations could result in permanent damage to the structure of the sensing element due to the induced strain) and when exposing the sensor to temperatures above 450 °C (because platinum crystal growth becomes more

evident) [32]. As they were to be used above this temperature threshold, once they were delivered, the SPRTs had to be annealed so that they performed with the best stability. Initially they were checked at the triple point of water (TPW) in order to have a known resistance for comparison. The annealing procedure consisted of soaking the sensors for a period of 3 hours in an auxiliary furnace at 670 °C. After that, the annealing furnace was slowly cooled in a controlled way to 450 °C at a low cooling rate (approximately 85 °C/h). This slow cooling is performed in order to prevent the formation of crystal defects in the platinum wire due to a rapid quenching of the sensor. When the furnace reached the set temperature, the SPRTs were then withdrawn from the furnace and allowed to cool down to room temperature. Once cooled, the sensors were measured again at the TPW in order to compare the resistance values [32]. Whenever these sensors are exposed to temperature above 450 °C, they need to be cooled down following the aforementioned procedure.

Commonly, annealing an SPRT results in lowering its resistance (especially at lower temperatures) due to the fact it reduces the crystal defects in platinum [32]. An SPRT is considered stable if this downwards shift in the resistance measured at the TPW is ≤ 1 mK. The annealing should be repeated until this condition was satisfied. The SPRT Chino RS129-03 had to be annealed four times (total of 12 hours at 670 °C), while the SPRT Isotech 312 was only annealed twice (total of 6 hours at 670 °C). They both consistently presented variations equivalent to ≤ 0.1 mK for the last two annealings they were subjected to. After being properly annealed, the SPRTs were calibrated at the freezing point of aluminium by using the working standard of the laboratory as the reference cell (cell Al 10/09).

Whenever the SPRTs were used, prior to their insertion in the cells and/or exposure to high temperatures, the quartz sheaths were thoroughly rinsed with analytical grade acetone. This was done in order to clean it from any contaminants (especially organic ones which could be introduced by handling the sheath), so as to prevent devitrification (which is a process that causes the glass sheath to become gas-permeable due to the reactions of contaminants at the surface, contaminating the platinum sensing element).

4.1.3. Thermometry bridge

The instrument used as the indicator of the SPRT readings was an AC thermometry bridge manufactured by Automatic Systems Laboratories (ASL), model F900, serial number 009340/02. The bridge readings are in terms of resistance ratio, between the SPRT and the external resistor (a calibrated standard resistor).

The bridge was previously calibrated (January 2014) and adjusted in order to provide optimal performance. Any deviations in the linearity of the bridge were covered by the uncertainty of the bridge (50 ppb of resistance ratio) assigned in the uncertainty budget of the calibrations.

The bridge settings were:

- Source impedance: 100 ohm
- Gain: 10^5
- Frequency: 25 Hz
- Quadrature: 1
- Bandwidth: 0.2 Hz
- Current: 1 mA

With these settings, the bridge was capable of providing a new reading at every 10 seconds.

4.1.4. Standard resistor

In conjunction with the thermometry bridge and SPRTs, a standard resistor was used for the measurements. It was a Wilkins type 100 ohm resistor (model 5685A, serial number 268167) manufactured by Tinsley Instrumentation Ltd. In order to ensure its stability, it was constantly kept at 20 °C in an oil bath especially designed to maintain resistors at stable working temperatures. The resistor was calibrated under similar conditions. According to the most recent calibration, dated 28 April 2014, the value assigned to the resistor is 99.999 540 Ω ± 0.000 005 Ω (k = 2).

4.1.5. Pre-heat furnace

A three-zone furnace (manufactured by Elite Thermal Systems Ltd, model TSV 12/70/750, serial number 2795/07/10) was used as an auxiliary furnace to set the thermometers at 670 °C during the annealing stage. The same furnace was also employed during the measurements: when the SPRT was inserted in the cell during a freezing plateau for the cell comparison, it needed to be pre-heated to around 660 °C for 30 min in order to avoid shortening of the plateau through excessive heat extraction. When the sensor was not to be cooled down to room temperature with the fixed point cell (i.e. by setting the furnace to 20 °C), it was transferred to the pre-heat furnace to cool down at a controlled rate until it reached approximately 450 °C and then immediately withdrawn to room temperature (as described in section 4.1.2).

4.1.6. Triple point of water reference cells

After the exposure of the SPRTs at the aluminium freezing point, they needed to be measured at the triple point of water to check their stability. These measurements were also used when comparing the aluminium cells with the reference cell because the comparison is done in terms of resistance ratios, W(660.323 °C), as given by equation 2.

In total, four TPW cells (that are part of the NPL working standard batch) were used throughout the measurements, from the annealing of the SPRTs to the final tests with the cells. Their serial numbers were 767, 768, 1147 and 1148. There is no correction to be applied to these cells because the difference in their realisation temperatures was negligible, below the uncertainty of the calibration with the NPL national standard batch (± 70 µK, k = 2). These cells were only used after their mantles were given the time required for the ice crystals to anneal (typically 3 days) in order to at least guarantee a satisfactory performance, i.e. that their reproducibility would be below the uncertainty declared. It has been reported, however, that optimal performance is achieved after the ice mantle of the TPW cells has been annealed for 10 days, when the reproducibility of the cells reaches the level of just 10 µK [53, 54].

4.1.7. Reference aluminium cell

One of the methodologies used to estimate the effect of impurities in fixed point cells is comparison of the phase transition of the cells. The cell used as reference for the aluminium freezing point was the working Al standard of the laboratory, cell Al 10/09, which was set up in a dedicated Carbolite single-zone furnace (model CTF 12/100/700, serial number 12/96/3233), coupled with a potassium heat pipe to promote better temperature homogeneity. This furnace was also checked for its longitudinal temperature uniformity, similar to the tests previously described in section 4.1.1. However in this case, no controller adjustments would be possible to improve the profile as it was a single zone furnace. The results are shown in table 8.

Position in relation to the bottom of the re-entrant well	**SPRT Resistance**	**Temperature difference in relation to the bottom**
cm	**Ω**	**mK**
0	85.549 149	0.0
2	85.549 424	3.4
4	85.550 004	10.7
6	85.550 276	14.1
8	85.549 914	9.6
10	85.550 012	10.8

Table 8: Thermal profile tests of furnace Carbolite CTF 12/100/700, serial number 12/96/3233.

It is clear that the potassium heatpipe is working satisfactory and a uniform zone in the NPL Al cell furnace is established.

This cell is periodically compared to the national standard cell for this temperature, named ‘Al sealed’. According to the results of the last comparison (July 2014), the correction for cell Al 10/09 was 3.18 mK ± 1.72 mK (k = 2).

4.1.8. Auxiliary equipment

Apart from the standards and devices described above, other pieces of equipment were necessary for the measurements. These were:

- A Pfeiffer HiCube 80 Eco turbomolecular pump;
- Gas handling system with a calibrated pressure gauge manufactured by GE model Druck DPI 104;
- A dedicated cylinder containing 6N argon gas, supplied by Air Products and Chemicals;
- A water circulator coupled to a water bath, manufactured by Grant, model Optima TC120-R1;
- Cooling fans;
- A Carbolite single-zone furnace fitted with a potassium heat pipe, model CTF 12/100/700 (serial number 12/96/3233), used to induce and maintain the freezing plateaus with the aluminium *reference* cell;
- An oil bath (manufactured by Fluke, model 7108) used to maintain the standard resistor at 20.000 °C (long term stability of 0.004 °C);
- A dewar flask filled with ice for the maintenance of the ice mantles of the triple point of water (TPW) cells;
- A copper rod inside a quartz tube to create an inner solid-liquid interface on the re-entrant well in the solidifying ingot.

4.1.9. Data acquisition

The data was recorded via bespoke software written to communicate with the thermometry bridge (controlling the bridge, acquiring and plotting the data generated). The computer was connected to the bridge via IEEE-488 parallel interface. This software, written in a LabVIEW environment, was capable of automatically performing some of the calculations and recording all data in a comprehensive database. The recorded unprocessed data was later processed in Microsoft Excel spreadsheets.

4.2. Measurement of phase transition curves

The cells were measured in sequence. For each cell, the following measurement protocol was followed:

- Initial measurement of the TPW with the main SPRT;
- Four sets of melting and freezing point realisations (of the test cell);
- Melting point followed by freezing point (for the cell comparison);
- Measurement at TPW to check stability and calculate W (660.323 °C);
- Initial measurement at TPW with the backup SPRT;
- Measurement of backup SPRT at the freezing curve (cell comparison);
- Four sets of melting and freezing point realisations (backup);
- Measurement at TPW to check stability and calculate W (660.323 °C).

The description of the procedures for the realisation of these curves is given below.

4.2.1. Melting curves

In order to perform the melting plateaux, the furnace was adjusted to 665.32 °C (5 °C above the melting temperature of aluminium). For the first melt, the cell was installed and fully evacuated (highest vacuum around 0.3 Pa) while still at room temperature. After approximately 40 min, the furnace was turned on and set to 650 °C (at 5 °C/min heating rate). The main SPRT was inserted in the re-entrant well, whilst the cell was cold, to monitor the heating process. When the furnace reached the set-point temperature (and was left to stabilise for 30 min), the cell was filled with argon and purged in the same manner as when the ingots were cast. This was performed twice and when the cell was refilled for the third time, the pressure of argon inside the cell was adjusted to 101 325 Pa. Once the pressure was stabilised, the furnace controller was adjusted to 665.32 °C in order to initiate the melt of the aluminium fixed point cell. As soon as the melt was complete, the aluminium ingot was left at that temperature for around 20 hours in order to diffuse the impurities throughout the fixed point, with the furnace temperature adjusted to 5 °C above the melting point (figures 30 and 31).

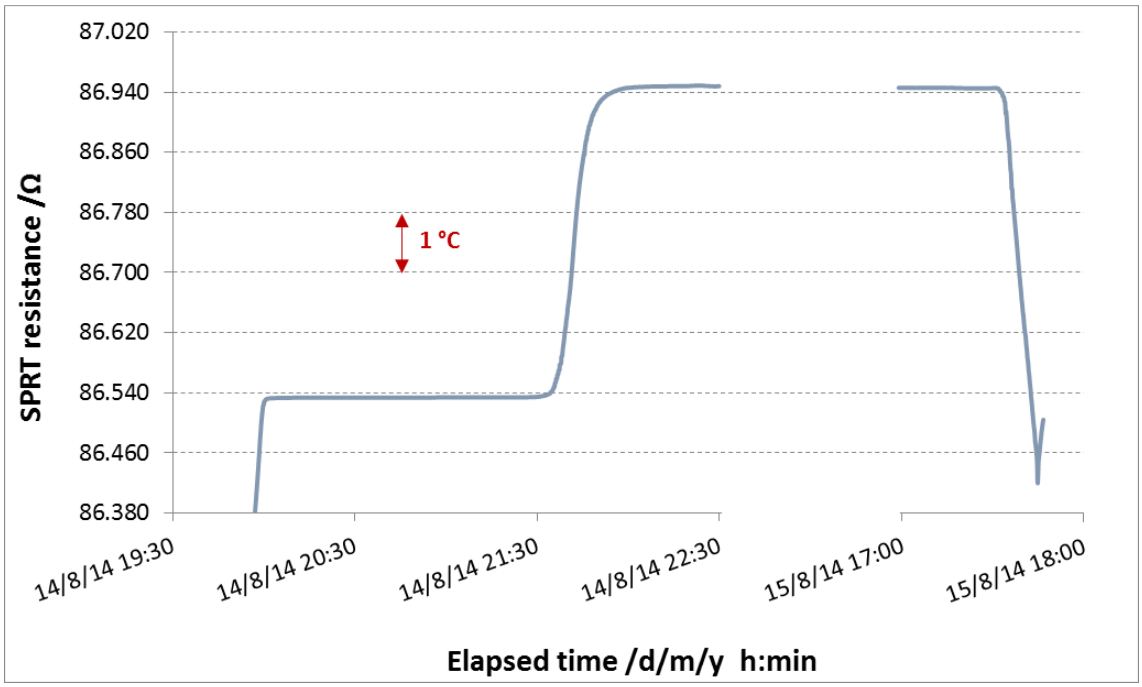

Figure 30: Melting of cell Al-E in 14 August 2014. SPRT Chino RS129-03 monitoring the process until the subsequent freezing was initiated (after 20 hours at 5 °C above the melting point). Measurements stopped right after nucleation and the recalescence were confirmed (by observing the rise out of the undercool).

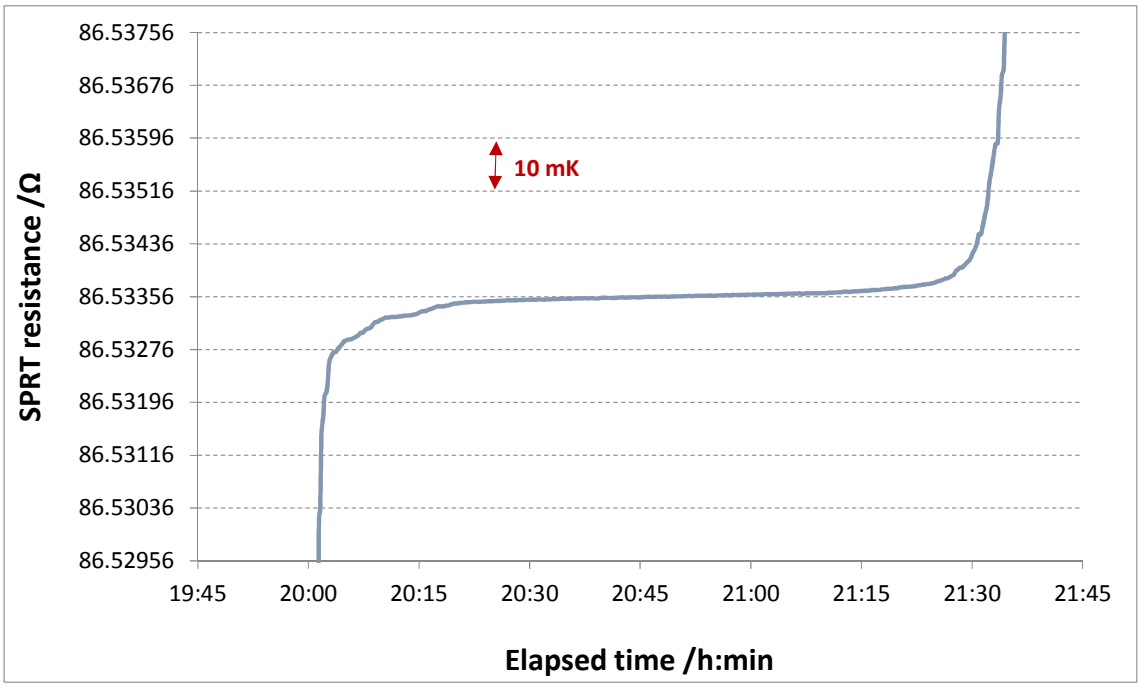

Figure 31: Detailed melting of cell Al-E (ESPI metals) with SPRT Chino RS129-03, in 14 August 2014.

During this process, the thermometry bridge was adjusted to supply a 1 mA excitation current to the SPRT to measure its resistance. This study focused on a detailed examination of the freezing curves. Melting curves were not accounted for in the application of the methodologies and analysis in the present study. This is primarily due to the fact that the ITS-90 defines the freezing point of aluminium as the realisation fixed point. This resides mostly in the following observations: freezing curves usually present flatter plateaus and, for materials with nominal purity < 7N, melting curves result in less accurate/reproducible realisations in comparison to freezing realisations (the slope of a melting curve is sensitive to its previous freeze as the result of the distribution of the residual impurities). In general, more accuracy could be obtained by operating a fast freeze (< 30 min) prior to every melting curve intended to be analysed. This creates a homogeneous mixture of impurities in the metal but it is not recommended because it requires an extremely risky procedure that may include the extraction of the cell from the furnace leaving it to freeze at room temperature, which in turn can result in the cell and SPRT being destroyed.

4.2.2. Freezing curves

In order to initiate the freeze of the metal inside the cell, two liquid/solid interfaces have to be induced: one external (adjacent to the crucible wall) and one internal (adjacent to the re-entrant well). Both interfaces must be uniform throughout the column of liquid metal in the ingot. As the metal transfers heat, through the graphite crucible walls, to the slightly colder surroundings (the furnace tube), the external interface advances progressively towards the re-entrant well, progressively thickening the solid layer in the liquid material. While the external interface progresses, it protects and stabilise the inner interface, which is essentially static [55]. It is of paramount importance that the SPRT be surrounded as far as possible by the solid-liquid interface because it improves the accuracy of the measurements. If there are gaps along this interface, the SPRT readings will be affected by the temperature of these zones (which is highly influenced by the furnace temperature) [56]. The external mantle is induced by setting the furnace to a temperature lower than the temperature of nucleation of the material. Establishing the internal interface requires a specific procedure, described in the next paragraph.

After the required time for establishing a uniform distribution of impurities (by diffusion) in the liquid metal ingot has elapsed, the furnace was set to freeze the cell by adjusting the controller to 658.32 °C (2 °C below the freezing point). The thermometer was kept inside the cell to monitor the decrease in temperature until nucleation occurred followed by the onset of recalescence. The actual nucleation temperature varied from one cell to another, but was usually around 1.6 °C below the freezing point. After a few thermometer readings confirmed the recalescence of the liquid aluminium, the thermometer was carefully withdrawn from the cell and held vertically, at room temperature. Then, a cold copper rod (encapsulated by a quartz tube) was inserted in the re-entrant well of the cell and held there for one minute. Meanwhile, the temperature of the furnace was increased by 1 °C. After this, the rod was replaced by the thermometer, which was reinserted in the cell. This process was carried out to create the inner solid-liquid interface.

When the thermometer was again inside the cell, the measurements were resumed and the temperature of the furnace increased by 0.6 °C (and then in order to maintain

a low rate of solidification, the temperature of the furnace was adjusted to only 0.4 °C below the freezing point). The gradual increases of the furnace temperature to the desired temperature were to avoid overshooting the temperature in the cell as that could cause the cell to re-melt instead of progressing the freezing front into the molten metal (note this is a potential danger because only a very small portion of the liquid metal at this point had been solidified).

As the SPRT (and the ingot/furnace arrangement) was approaching thermal equilibrium, the pressure inside the cell was checked and, if needed, adjusted to 101 325 Pa. In order to ensure optimum measurements, the procedure demanded constant monitoring of the freeze as some interventions were necessary. After approximately 24 hours, the cell was completely solidified (figure 32). If the cell was to be melted again, the furnace was simply adjusted back to 5 °C above the melting temperature of aluminium.

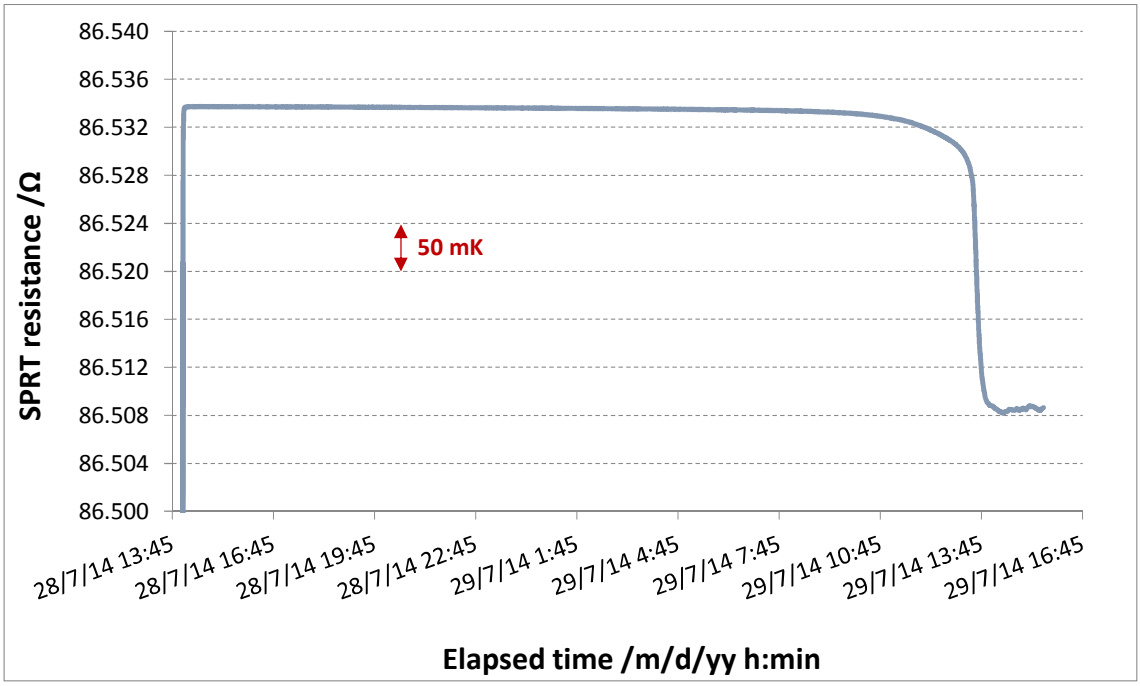

Figure 32: Typical raw data of the freezing of cell Al-H (Honeywell) in 28 July 2014 as measured with the SPRT Chino RS129-03.

4.2.2.1. Cell comparisons

The comparison of the aluminium cells was made in terms of the resistance measured with an SPRT at the NPL reference Al cell and the Al cells constructed for this study. However, in order to account for any drifts that could be caused during and/or after the exposure of the thermometer to the temperature of the aluminium freezing point, subsequent measurements at the triple point of water were also required. This measurement is signified by the ratio W of the resistance measured by the SPRT at the freezing point of aluminium and the triple point of water, as given by equation 2 (in chapter 2). Considering that SPRTs are highly susceptible to drifts, the comparison of cells has to be done in terms of W because any variation in the resistance measured by the SPRT at a given fixed point (which is attributed to the sensor itself) would be proportionally apparent at subsequent measurements at the triple point of water as well. This means that this type of error would be considerably minimised (*cancelled*) when the resistance ratio was obtained. Resistance values measured at a given fixed point $R(T_{90})$, on their own, are not appropriate for cell comparisons because the drifts are not accounted for. This means that any changes in the SPRT resistance (due to handling, heating/cooling of the sensor from one cell to another) will be mistakenly accounted as the difference in the temperatures realised with the cells. In addition to this precaution the measurements should also be corrected for: the self-heating effect of the SPRT sensing element (applied to measurements at both the aluminium and water cell temperature) and the differences in the height of the column of the fixed point material in the liquid phase (only applied to the aluminium cells). These corrections are discussed below in dedicated topics.

In order to collect the required data, a given aluminium cell was melted according to the procedure given in Section 4.2.1 and had the freezing plateau induced as described in Section 4.2.2. After around 60 min past the onset of recalescence, the software was set to control the thermometry bridge and automatically measure and calculate the self-heating effect (described below). Once enough results had been obtained to apply the self-heating correction, the thermometer (supplied with 1 mA) was left in the cell measuring the freezing plateau. After the end of the plateau was observed, the thermometer was withdrawn from the cell and transferred to the pre-heat furnace to proceed with the cooling of the SPRT according to the previously described

process. When at room temperature, the thermometer was measured at the triple point of water, including determining the self-heating effect of the thermometer at 0.01 °C.

Considering that the TPW cells used for all measurements had similar heights of the column of water (immersions varying from 272 mm to 285 mm), the necessary corrections were very small. As for the aluminium cells, all the cells (the reference and the constructed ones) had around 174 mm of immersion.

Usually this type of comparison is made simultaneously, with both the reference and the test cells being initiated at almost the same time, to guarantee that the measurements are made in the same region of the plateaus (the same solid fraction). However, as this comparison involved a total of six aluminium cells, simultaneous measurements were not possible. It was decided to proceed with the measurements of each cell at a certain time, as it best suits the schedule of the measurements (around four weeks for each successive cell).

4.2.2.1.1. Determination of the Self-heating effect

The working principle of SPRTs is based on the variation of electrical resistance with temperature of the platinum wires used in the sensing element. However, the resistance can only be measured if the sensing element is supplied with an electrical current, which in turn, causes heat to be dissipated, increasing the temperature readings of the thermometer (Joule effect). This effect varies according to the temperature being measured and the characteristics of both the SPRT and the thermal medium (the fixed point cell). For a 25.5 ohm SPRT (nominal resistance at the TPW), this effect can be equivalent to several millikelvins (which is large compared to the effect being measured). With regards to calibration of SPRTs and comparison of cells, the values assigned must be corrected for this effect. This correction is as if the resistance measurements were made without the flow of electrical current in the circuit (0 mA).

When evaluating this effect, adequate accuracy and reliability can be achieved by measuring the resistance of the SPRT in two different currents, i_1 and i_2. Virtually any pair of currents can be selected in the range from 0.10 mA to 2.82 mA (especially in

AC bridges, for which the options are restricted). However, given the fact that the majority of ordinary SPRT measurements are done with 1 mA, the pair of currents 1 mA and 1.414 mA (which is effectively $\sqrt{2}$ mA) is widely used in resistance thermometry and proven to yield accurate results. The measurements are performed in the sequence $i_1 - i_2 - i_1$. The current i_1 is repeated at the end in order to check the stability of the readings, ensuring there were no substantial changes in the measurements after supplying the thermometer with i_2 (for a 25.5 ohm SPRT at the freezing point of aluminium, the allowed tolerance is of order 2 μΩ, which is equivalent to 25 μK). To determine the correction, the i_1 mean value is obtained from both initial and final sets of readings. Once in possession of the mean values measured with both currents, the results are extrapolated to 0 mA, as if there were no self-heating effect (equation 25).

$$R_{(0\ mA)} = \frac{R_{(i_1)} \cdot R_{(i_2)}}{\left(2 \cdot R_{(i_2)}\right) - R_{(i_1)}} \tag{25}$$

Equation 25 yields the resistance value already corrected for the self-heating effect, without requiring prior quantification of the effect itself. However, if required, the self-heating effect (*S.H.*) could be obtained from the equation below (equation 26):

$$S.H. = R_{(i_1)} - R_{(0\ mA)} \tag{26}$$

In order to obtain the data for the calculation of the extrapolation, an automated procedure was adopted. During the beginning of the freezing plateau, the bridge was set to automatically supply the thermometer with the selected currents (1 mA, 1.414 mA and 1 mA), while recording all the resistance readings from the SPRT (figure 33). At each current, a total of 40 readings were taken. For calculations, the first 20 readings of each of the currents selected were discarded as they account for the time the thermometer requires to become stable at the new current. This procedure is performed to provide the required data to calculate the self-heating effect of the SPRT in a given cell.

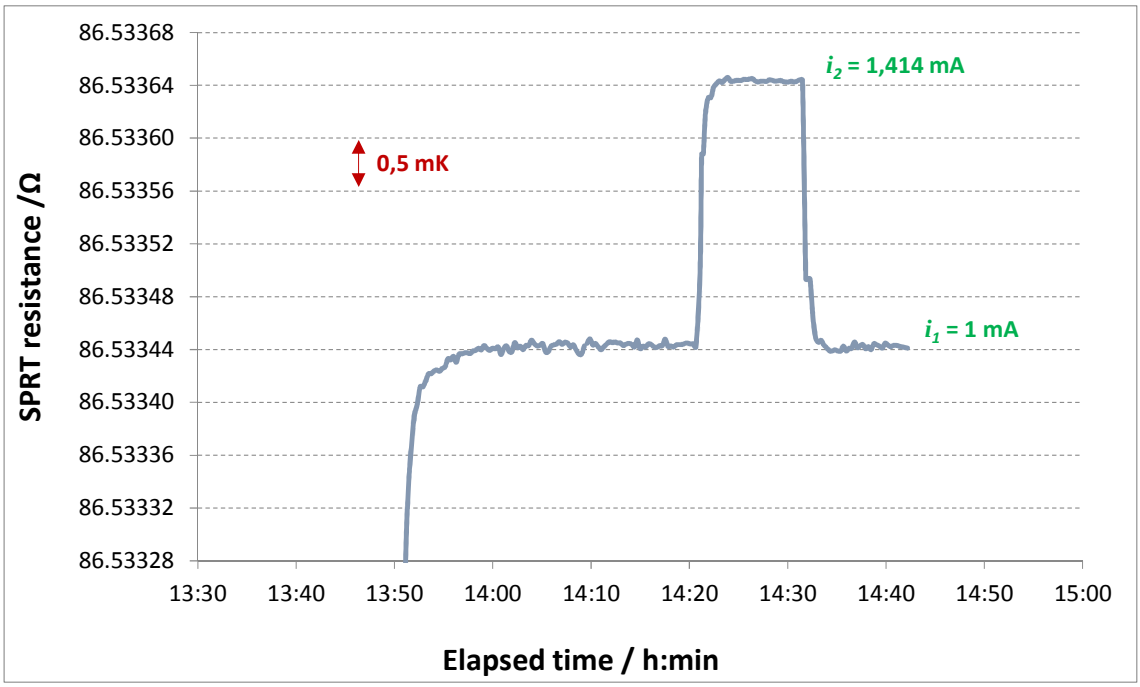

Figure 33: A sequence of automatic measurements to calculate the self-heating effect of the SPRT Chino RS129-03 in the cell Al-E. 26 August 2014. The mean value at 1 mA was 86.533 443 0 Ω while at 1.414 mA it was 86.533 643 4 Ω (standard deviations < 20 μK). Application of equation 25 yields the extrapolated mean, R_{0mA}, of 86.533 242 5 Ω, being the self-heating effect equivalent to 200.5 μΩ (2.5 mK).

4.2.2.1.2. Hydrostatic head correction

The temperature of realisation of a freezing point material, by definition, is realised only at the surface of the material. An infinitesimal portion at the surface of the material adjacent to the re-entrant well contains the contact point where both liquid and solid phases of the material coexist. Nevertheless, during these measurements, the sensing element of the SPRT is actually located close to the bottom of the re-entrant well because of immersion requirements for these measurements. This causes a departure from the fixed point temperature defined in the ITS-90 and a correction has to be applied for SPRT calibrations and for comparison of fixed point cells, if they have different immersion depths [57]. Corrections for this effect are calculated by determining the height of the liquid column above the mid-point of the sensing element of the SPRT being used and the coefficient of variation of temperature in relation to

depth (table 9). However, these corrections were not required for the comparison of aluminium cells described here because they all had approximately the same immersion depth, around 172 mm. The maximum difference among the immersion of the cells was 2.4 mm, which yields a value no greater than 4 μK (which is sufficiently covered by the respective uncertainty). Similarly, no corrections were applied to the measurements at the triple point of water because the maximum difference in the immersion depth of the cells was 11 mm (equivalent to 8 μK).

Substance	**Equilibrium Temperature**	**Temperature variation**		**First Cryoscopic Constant**
		with pressure	**with depth**	
	°C	**nK/Pa**	**mK/m**	**K^{-1}**
Water $_{(TP)}$	0.01	- 75	- 0.73	0.009684
Gallium $_{(MP)}$	29.7646	- 20	- 1.2	0.007321
Indium	156.5985	+ 49	+ 3.3	0.002143
Tin	231.928	+ 33	+ 2.2	0.003377
Zinc	419.527	+ 43	+ 2.7	0.001772
Aluminium	660.323	+ 70	+ 1.6	0.001489
Silver	961.78	+ 60	+ 5.4	0.000890
Gold	1064.18	+ 61	+ 10.0	0.000855
Copper	1084.62	+ 33	+ 2.6	0.000843

Table 9: Properties of materials used as ITS-90 fixed points in the range above 0 °C. All materials are defined as freezing points, except for water (triple point) and gallium (melting point) [8].

4.3. Chemical analyses

In order to implement the corrections proposed according to some of the methodologies investigated in this thesis (SIE, OME, Hybrid SIE/Modified OME), it was necessary to have a chemical analysis performed of the metal used for each cell. Given the purity of the samples (stated total impurity concentration of 1 part per

million, ppm), the technique selected should be capable of detecting trace impurities at the level of parts per billion (ppb) otherwise the results would be inconclusive. Techniques that require dissolution of the solid samples are not suitable because they present serious limitations: they yield an incomplete assay due to the dilution of the solid samples (at rates of 1:500) and the fact that only a fraction of the resulting solution can be analysed at a time. In addition, even if they could provide suitable resolution, single element analysis techniques would be too expensive and time consuming, considering that the samples would be scanned for 70+ elements. To date, the best multi-elemental technique currently available that can provide this resolution is known as glow discharge mass spectrometry (GDMS), which is capable of directly analysing solid samples. These spectrometers are so sensitive that a few elements can even be detected at parts per trillion (ppt) levels. Unfortunately, there are only very few providers of this technique in the world.

Each aluminium sample was supplied with a chemical analysis; however, only three were performed with GDMS, the other two having been performed with inductively coupled plasma (ICP) spectrometry. The ICP results revealed no impurities detected in one material sample, and only one contaminant in the other. In all cases, no information was provided on the uncertainty associated with the analysis. Given these very incomplete results, and the aim of this study, it was essential to have more comprehensive assays performed.

4.3.1. Sample preparation

Samples from each of the five metals were prepared and sent to three different laboratories: AQura GmbH in Germany, the National Research Council (NRC) in Canada and the National Institute of Metrology (NIM) in China. Each of these laboratories had a particular requirement concerning the sample shape and size. AQura was the only one to accept a collection of randomly sized pellets from each material and prepare the samples by pressing the pellets to form a thick coin (diameter 20 mm, height 3 mm). The NRC requested a parallelepiped pin (square base with 2.3 mm, height 20 mm). The laboratory at NIM requested a flat cylinder (diameter 20 mm,

height 5 mm). In order to produce the required geometries of the samples for NRC and NIM, graphite moulds were produced so that the pellets could be cast into the shapes required. However, because of the amount of aluminium required to produce the samples for NRC, a bigger sample had to be cast (square base 7.5 mm x 30 mm in height) and further prepared by being cut with a clean jewellers saw and chemically etched (to remove surface contamination) prior to being analysed (figure 34). Before the graphite moulds were used they were, after manufacture, thoroughly cleaned and baked in vacuum at 900 °C for around 15 hours. One mould was produced for each metal batch, totalling five moulds. Care was taken to identify the samples appropriately and to avoid cross-contamination of the samples. The casting was performed under vacuum in a graphite single zone furnace (manufactured by Webb, model RD-G) at 700 °C. The system was held at this temperature for two hours, then cooled to room temperature at a rate of about 3 °C per minute.

Figure 34: Preparation of the samples for GDMS analysis. Samples positioned in the furnace to be melted into the moulds (top left). Sample of aluminium supplied by New Metal made for NIM and NRC (top right). Collection of samples to be sent to NIM (bottom left). Pin after being cast and cut to the right size for NRC (bottom right).

Concerning the possible contamination of the samples that had to be cut, it is a procedure of the laboratories to chemically etch the samples and to disregard the first measurements (readings are taken after the sample has been sputtered for around 30 min, so that the measurements performed correspond to a few microns inside the sample). Nevertheless, to provide extra confidence that no contamination by iron was present, scanning electron microscopy (SEM) and x-ray photoelectron spectroscopy (XRS) analyses on the samples prepared for NRC confirm that there was no significant contamination of the samples from the saw used to cut the pins (figure 35).

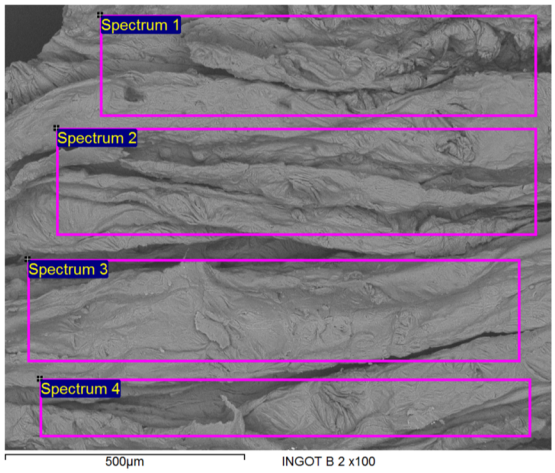

Spectrum	C	O	Al	Total
Spectrum 1	16.09	21.53	62.38	100.00
Spectrum 2	12.26	22.01	65.72	100.00
Spectrum 3	9.51	24.60	65.90	100.00
Spectrum 4	11.26	23.84	64.90	100.00
Mean	12.28	23.00	64.72	100.00
Std. deviation	2.78	1.46	1.63	
Max.	16.09	24.60	65.90	
Min.	9.51	21.53	62.38	

All results in weight %

Figure 35: SEM results (both image and table) showing principal constituents corresponding to the regions 1, 2, 3 and 4 on the image.

4.4. Numerical conversions and calculations

Application of the correction methodologies under investigation in this thesis required the conversion of the data and the selection of a specific part of the freezing plateau so that the methodologies could be systematically applied to all freezing curves.

4.4.1. Converting elapsed time into solid fraction

The evaluation of the freezing plateaux required that the temperature readings were correlated to the progression of the freeze, from the state of virtually 0 % solid (100 % liquid) to 100 % solid (0 % liquid). To achieve this, the elapsed time of the readings was transformed into solid fraction, F_s. Considering that a freezing curve presents a region of super-cooled liquid before the nucleation of the metal occurs and, that subsequently, the thermometer is withdrawn from the cell so that the inner solid-liquid interface can be induced, the peak in the freezing plateau is taken as the initial point in the curve ($F_s=0$). ΔT is specified as zero at this point. The end point, corresponding to the temperature measured when $F_s=1$, is taken as the inflection in the curve after the steep drop in temperature following the end of the flat portion of the curve, prior to the approach to the furnace temperature. This is a measure of the maximum variation of temperature in time (dT/dt) (figure 36) and has been found to coincide with the disappearance of the liquid-solid interface determined with more rigorous methods [22]. After determining these extremes, the elapsed time of each reading was transformed into solid fraction by the simple calculation of proportions.

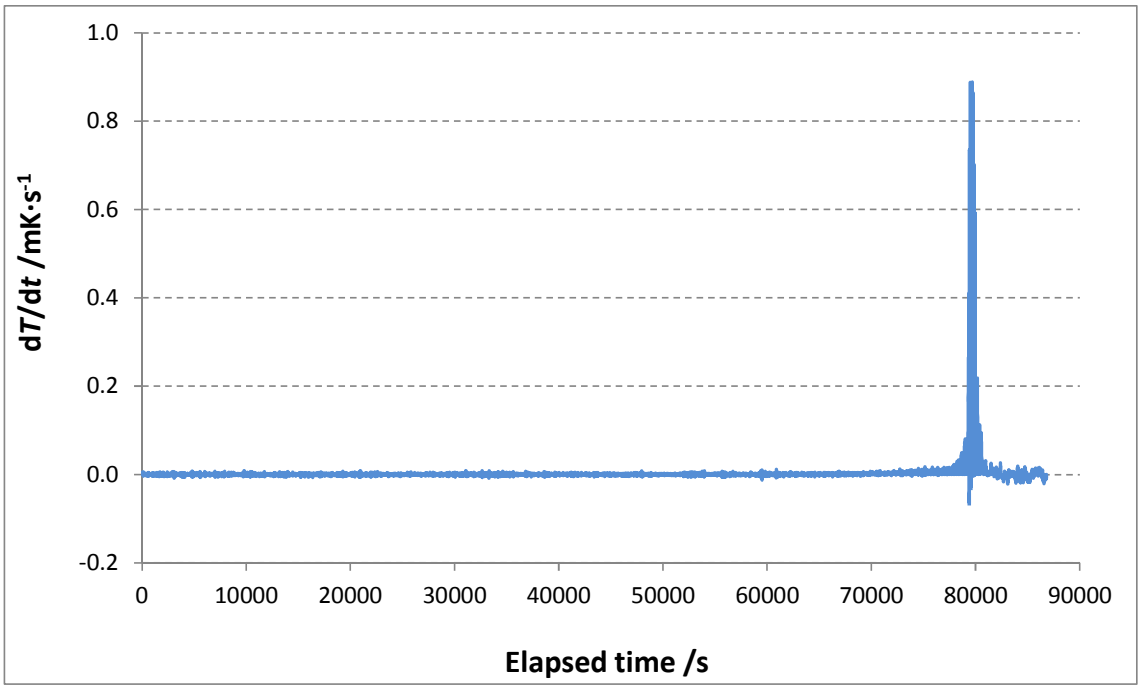

Figure 36: Identification of the end of the freezing curve in cell Al-H (Honeywell) in 28 July 2014 (as in figure 31) after calculation of the variation of temperature with time d*T*/d*t*. The point of inflection (F_s=1) in this curve occurred at 79495 seconds past the peak of the freezing curve (F_s=0).

4.4.2. Converting resistance ratio into temperature

In order to transform the SPRT readings into temperature, a series of transformations are necessary. The thermometry bridge output is the ratio of the resistance measured by the thermometer divided by the resistance value supplied by the calibrated standard resistor. The first conversion to be made is to retrieve the resistance value of the SPRT by multiplying the ratio readings by the value declared in the certificate of calibration of the standard resistor.

The conversion of absolute values of resistance to temperature requires the application of the ITS-90 reference or deviation functions described in chapter 2 (equations 4 – 11). However, taking into account that the methodologies applied would yield a small temperature difference in relation to the value assigned to the freezing of the 100 % pure material (in the order of up to few millikelvins), it is

sufficient to use the coefficient of variation of the resistance in relation to the temperature measured, d*R*/d*T*. This coefficient is used only for small temperature differences. For temperatures near 660 °C, this value is equivalent to 0.08 Ω/°C.

After having determined the readings that correspond to the 0 % and 100 % solid fractions of the curve, all resistance values were subtracted from the peak of the curve, each yielding a variation of resistance, Δ*R*. Values of Δ*R* were transformed into temperature difference by simply multiplying them by the coefficient d*R*/d*T* (0.08 Ω/°C). Examples of the end point of this process are shown in figures 37 and 38 below.

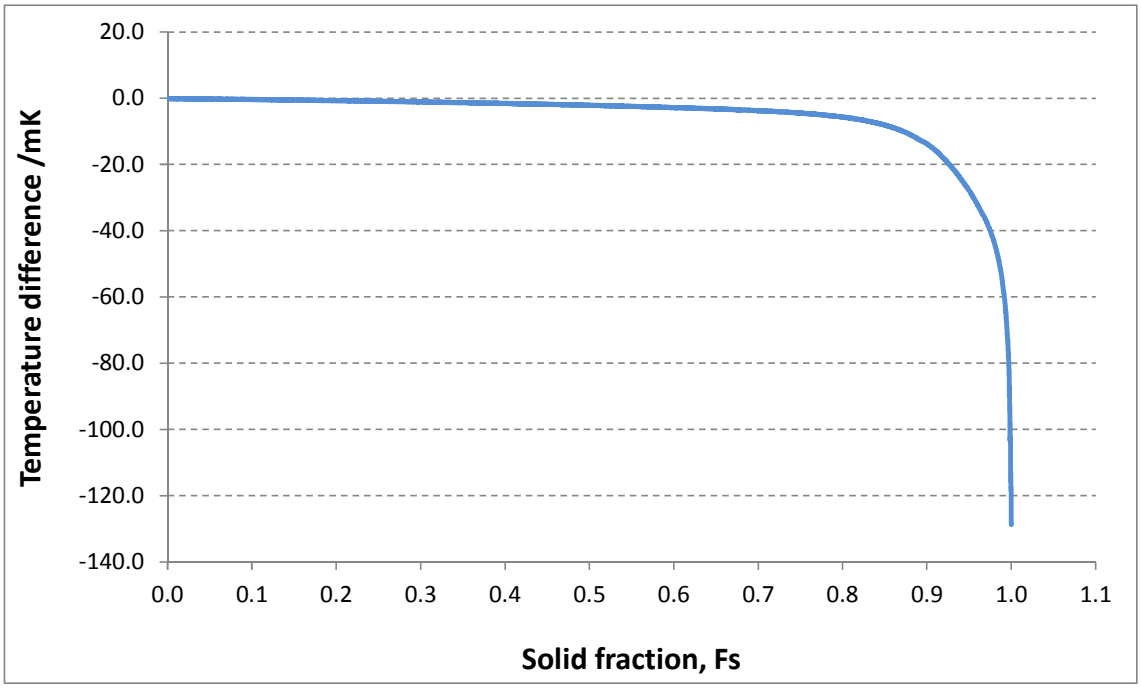

Figure 37: Graph of the freezing of cell Al-H (28 July 2014) after the required data conversions.

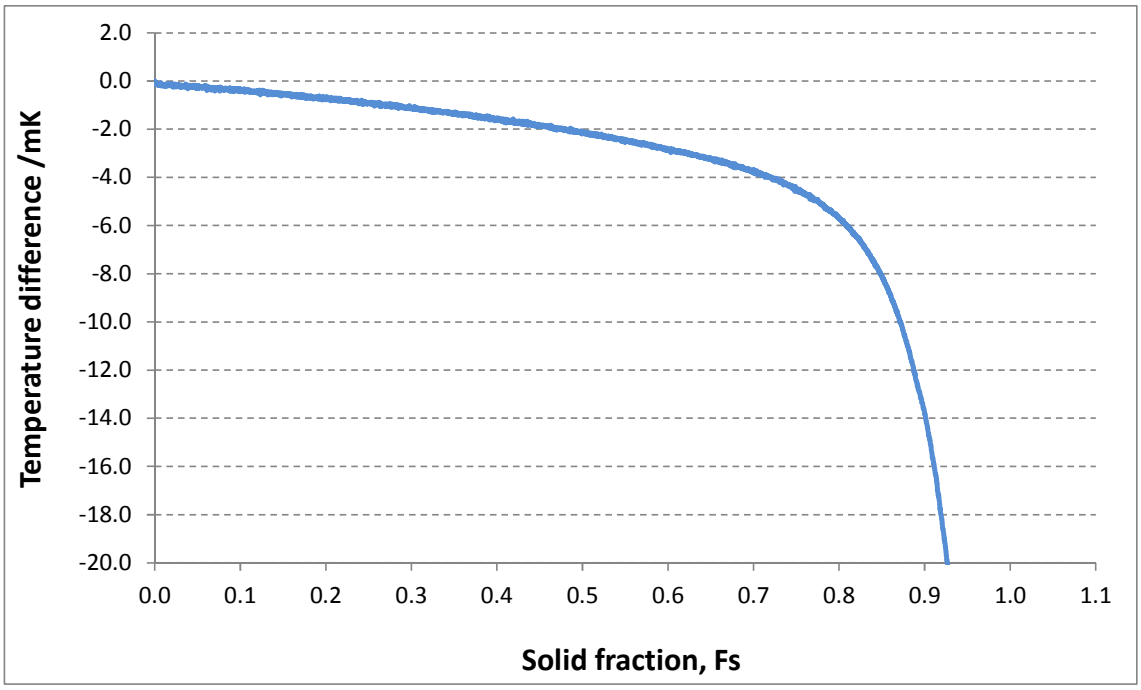

Figure 38: Detail of the graph of the freezing of cell Al-H (28 July 2014) after the required data conversions.

In this chapter I described the set of measurements that comprised the protocol adopted for evaluating the constructed aluminium cells, including a detailed description of the procedures, equipment used and the measurements that were performed. It also included the preparation of the samples for extra GDMS analyses and the procedure required for numerical conversions. In the next chapter, the results of the GDMS analyses are given together with the results of the freezing curve measurements. In addition, the results obtained from the application of the seven methodologies investigated are provided in chapter 6, which includes the analysis and discussion of these results.

Chapter 5

Results of chemical assays and measurements of freezing curves

In chapter 4, I described the measurements required to investigate the effect of impurities on the phase transitions of the aluminium fixed points, including a detailed description of the equipment utilised and the adjustments needed in order to achieve the best performance from the measuring system. Furthermore, an account of the numerical conversions and calculations was also provided. In this chapter, I start by describing the results for the GDMS. The assays provided by each supplier are compared with those of independent GDMS analysis providers. Then the measured freezing curves for each of the five cells are given. In the subsequent chapter, these results are combined to obtain the correction and uncertainty estimates for each cell, according to the correction methodologies introduced in chapter 2.

A summary of the results presented here is also available in [58] (Appendix A).

5.1. Chemical assays provided by the metal suppliers

High purity metals are commonly supplied with an impurity assay for the corresponding batch, as a default. Considering the fact that the higher the purity of the metal the lower the total impurity concentration will be, it is expected that the chemical analysis utilised has the capability of detecting trace elements in levels much lower than the overall concentration of impurities (for 6N samples, the nominal total concentration of impurities should be equivalent to 1 ppm). This is essential for a proper characterisation of the fixed point material used in the construction of an ITS-90

fixed point cell. However, not all samples procured for this study was supplied with a chemical assay that could be used in the calculations of the correction methodologies. Examples were the samples supplied by ESPI and Honeywell, where the analysis was performed by ICP (inductively coupled plasma spectrometry) a technique of lower resolution (mainly because it requires dissolution of the samples). The assay supplied by Honeywell specifies that the technique was ICP-AES (inductively coupled plasma atomic emission spectrometry) whereas the one provided by ESPI just states that the analysis performed was ICP. A summary of these assays, showing the impurities detected in each of the samples, is presented in table 10. Note that no other impurities were reportedly detected outside of these reported here.

Atomic No	Element symbol	Impurity concentration, ng/g				
		Alfa Aesar	ESPI	Honeywell	New Metals	Sumitomo
11	Na					4
12	Mg	78			88	45
14	Si	186	900		154	270
15	P	10				
22	Ti	37			58	10
23	V	24			17	65
24	Cr	35			37	15
25	Mn	34			24	3
26	Fe	14			7	55
28	Ni					10
29	Cu					57
40	Zr					7
41	Nb					3
42	Mo					24

Table 10: Summary of the chemical assays provided by the metal suppliers.

According to those assays, the metal supplied by Alfa Aesar presented a total impurity concentration of 418 ppb. The analysis for the ESPI material detected solely 900 ppb of Silicon. The analysis provided by Honeywell has not detected any impurities in the 6N matrix of aluminium. The analysis for the New Metals samples detected a total of 385 ppb of impurities, while the analysis for the Sumitomo material resulted in a 568 ppb total impurity concentration. There was no information regarding the laboratories that performed those chemical assays or any statement of the measurement uncertainty for the results (for each individual element scanned).

In situations such as when the chemical analysis for the metal does not retrieve results (because impurities were below the level of detection of the technique employed), the CCT initially recommended applying half of the detection limits stated in the assay for each element scanned in order to calculate the estimates for the proposed methodologies [11]. However, this recommendation was subsequently modified based upon a collection of assays from various sources and a list of common impurities found in high purity metals used as ITS-90 fixed points has been established [40]. According to that list, only the impurities commonly found in pure ITS-90 metal matrices should be accounted for in cases where no impurities were detected by the chemical analysis employed. The concept of employing half of these values is based on the assumption that if a given element concentration was greater than or equal to half its detection limit ($\geq 0.5x$), the value would be rounded up to the detection limit itself and hence be detected. Therefore, in order not to be detected, the maximum its concentration could be was less than half ($< 0.5x$). The impurities commonly found in pure aluminium samples are shown in figure 39 [40].

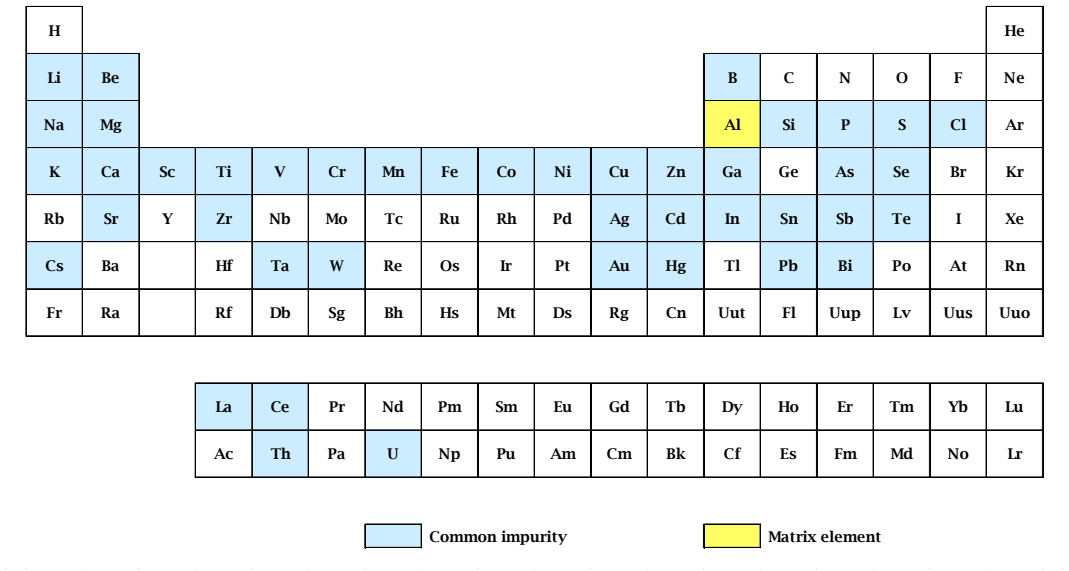

Figure 39: Elements commonly found in trace amounts in high purity aluminium.

5.2. GDMS analyses provided by third party laboratories

The results from the GDMS analyses based on the samples prepared during the construction of the cells helped to better characterise the actual metal samples employed in each cell, which was especially useful for the samples from Honeywell and ESPI. In order to facilitate the comparison of the results from the different chemical assays supplied, tables 11-15 give the results of the initial assays (provided with the metal samples) in conjunction with the results of the GDMS analyses for each of the five metal samples employed in this thesis, being organised by sample. Elements that were not scanned for during the analysis correspond to an empty cell in the tables, whereas if an element was scanned for but no quantity was detected above the detection limit of the analyser, the value given corresponds to the detection limit itself, being preceded by a < sign.

Atomic No	Element symbol	Impurity concentration, ng/g			
		Supplier	AQura	NRC	NIM
1	H				
2	He				
3	Li	< 5	0.6	< 2	< 1
4	Be	< 5	< 6	< 0.9	< 1
5	B	< 5	20	12	11.30
6	C				
7	N				
8	O				
9	F	< 100		< 3	1230.75
10	Ne				
11	Na	< 5	40	< 1	268.50
12	Mg	78	100	30	10.55
13	Al	Matrix	Matrix	Matrix	Matrix
14	Si	186	400	780	2421.60
15	P	10	100	39	124.35
16	S	< 100	100	< 3	
17	Cl	< 100		5	3 073.55
18	Ar				
19	K	< 100	90	< 4	40.45
20	Ca	< 20	100	< 20	83.25
21	Sc		40	64	61.30
22	Ti	37	600	640	479.15
23	V	24	20	28	21.30
24	Cr	35	40	69	111.95
25	Mn	34	40	47	25.35
26	Fe	14	200	830	99.25
27	Co	< 5	30	540	56.15
28	Ni	< 5	100	440	443.75
29	Cu	< 200	100	49	2946.45
30	Zn	< 50	50	26	321.80
31	Ga	< 5	7	< 5	8.15
32	Ge	< 40	< 20	< 9	1332.50
33	As	< 5	50	< 5	264.30
34	Se		< 40	< 30	112 751.9
35	Br		< 40	< 11	833.00
36	Kr				
37	Rb		< 2	< 1	3.10
38	Sr		0.7	< 0.9	2.45
39	Y		< 0.7	< 0.8	1.50
40	Zr	< 5	4	280	7.65
41	Nb		3	13	15.60
42	Mo	< 2	10	< 5	104.35
43	Tc				
44	Ru		0.4		12.35
45	Rh		3		13.20
46	Pd	< 100	6		< 1
47	Ag	< 5	40	< 6	333.85
48	Cd	< 50	50	< 20	449.30
49	In	< 5	30	< 3	6.35
50	Sn	< 50	30	48	7.45

Atomic No	Element symbol	Impurity concentration, ng/g			
		Supplier	AQura	NRC	NIM
51	Sb	< 5	< 10	< 5	11.90
52	Te		10	26	36.35
53	I		< 2	< 2	1.40
54	Xe				
55	Cs	< 10	< 1	< 0.8	1.40
56	Ba	< 5	0.6	< 0.9	< 1
57	La	< 5	0.5	< 0.7	2.65
58	Ce	< 5	0.9	< 0.9	1.20
59	Pr		< 0.9		< 1
60	Nd	< 5	< 4		< 1
61	Pm				
62	Sm		5		< 1
63	Eu		< 2		3.45
64	Gd		< 3		12.75
65	Tb		< 1		1.15
66	Dy		< 4		< 1
67	Ho		< 0.9		2.25
68	Er		< 5		< 1
69	Tm		< 0.9		< 1
70	Yb		3		5.10
71	Lu		< 0.8		< 1
72	Hf		3	15	12.15
73	Ta				< 1
74	W	< 25	10	4	< 1
75	Re		6		3.55
76	Os		< 10		95.20
77	Ir		< 3		3.70
78	Pt	< 100	< 8	< 9	< 1
79	Au	< 10	2	< 1 400	< 1
80	Hg	< 100	< 20	< 25	20.45
81	Tl		< 7	< 6	6.00
82	Pb	< 5	4	6	2 488.25
83	Bi	< 5	6	< 3	6.45
84	Po				
85	At				
86	Rn				
87	Fr				
88	Ra				
89	Ac				
90	Th	< 700	< 0.1	< 0.9	1.30
91	Pa				
92	U	< 700	0.2	< 0.9	1.40
93	Np				
94	Pu				

Table 11: Results of the GDMS analyses for batch of metal from Alfa Aesar.

Atomic No	Element symbol	Impurity concentration, ng/g			
		Supplier	AQura	NRC	NIM
1	H				
2	He				
3	Li		< 0.3	< 3	< 1
4	Be		5	< 1	4.88
5	B		40	77	6.32
6	C				
7	N				
8	O				
9	F			< 2	185.32
10	Ne				
11	Na		20	< 1	27.05
12	Mg		300	73	35.95
13	Al	Matrix	Matrix	Matrix	Matrix
14	Si	900	800	920	813.50
15	P		50	18	13.25
16	S		100	< 4	
17	Cl			6	366.02
18	Ar				
19	K		30	< 4	8.95
20	Ca		< 30	< 20	23.58
21	Sc		30	69	60.40
22	Ti		30	71	85.70
23	V		30	49	62.60
24	Cr		50	57	66.70
25	Mn		50	33	38.15
26	Fe		200	220	54.58
27	Co		1	< 0.7	1.48
28	Ni		4	8	5.65
29	Cu		100	46	406.88
30	Zn		20	35	59.78
31	Ga		5	< 6	8.10
32	Ge		< 20	< 10	253.90
33	As		40	< 6	70.50
34	Se		< 40	< 40	13 306.42
35	Br		< 40	< 12	108.82
36	Kr				
37	Rb		< 2	< 2	0.52
38	Sr		< 0.9	< 0.9	0.82
39	Y		< 0.8	< 1	0.40
40	Zr		7	180	15.75
41	Nb		< 0.9	4	0.62
42	Mo		10	< 2	27.08
43	Tc				
44	Ru		1		12.72
45	Rh		2		2.92
46	Pd		< 10		16.50
47	Ag		10	< 7	84.12
48	Cd		30	27	53.00
49	In		20	41	0.60
50	Sn		70	< 43	4.05

Atomic No	Element symbol	Impurity concentration, ng/g			
		Supplier	AQura	NRC	NIM
51	Sb		20	< 9	3.35
52	Te		< 20	18	8.20
53	I		< 1	< 3	0.38
54	Xe				
55	Cs		< 1	< 1	0.80
56	Ba		< 1	< 1	< 1
57	La		8	9	0.50
58	Ce		10	20	0.18
59	Pr		1		0.30
60	Nd		10		2.98
61	Pm				
62	Sm		< 4		6.20
63	Eu		< 2		1.00
64	Gd		< 4		0.92
65	Tb		< 1		< 1
66	Dy		< 5		1.65
67	Ho		< 1		0.65
68	Er		< 3		1.30
69	Tm		< 1		0.45
70	Yb		< 4		0.78
71	Lu		< 1		0.15
72	Hf		0.3	< 4	2.78
73	Ta				0.95
74	W		20	< 3	1.20
75	Re		7		1.02
76	Os		< 20		4.38
77	Ir		< 3		0.70
78	Pt		< 10	< 11	5.90
79	Au		4	< 920	1.88
80	Hg		< 20	< 32	11.32
81	Tl		< 8	< 8	4.65
82	Pb		10	8	129.15
83	Bi		1 700	21	0.92
84	Po				
85	At				
86	Rn				
87	Fr				
88	Ra				
89	Ac				
90	Th		0.5	< 1	0.38
91	Pa				
92	U		0.1	< 1	0.20
93	Np				
94	Pu				

Table 12: Results of the GDMS analyses for batch of metal from ESPI Metals. The technique employed in the analysis provided by the supplier of the metal batch was ICP. No information was given about detection limits for the other elements scanned.

Atomic No	Element symbol	Impurity concentration, ng/g			
		Supplier	AQura	NRC	NIM
1	H				
2	He				
3	Li		0.5	< 2	13.10
4	Be	< 100	5	< 0.9	1.25
5	B	< 100	9	22	11.88
6	C				
7	N				
8	O				
9	F			< 2	428.50
10	Ne				
11	Na		20	< 1	60.05
12	Mg	< 100	200	270	135.73
13	Al	Matrix	Matrix	Matrix	Matrix
14	Si	< 500	400	500	1116.85
15	P	< 5 000	30	7	54.03
16	S		50	< 3	
17	Cl			7	927.68
18	Ar				
19	K		30	< 4	16.93
20	Ca	< 500	< 30	< 17	56.20
21	Sc		30	53	34.03
22	Ti	< 100	50	52	95.13
23	V	< 100	20	29	30.18
24	Cr	< 100	20	25	17.45
25	Mn	< 100	20	14	20.78
26	Fe	< 100	100	220	130.17
27	Co	< 100	< 2	< 0.4	4.25
28	Ni	< 300	5	4	5.65
29	Cu	< 100	70	23	781.70
30	Zn	< 500	40	24	40.20
31	Ga	< 100	5	< 5	4.43
32	Ge	< 1 000	< 20	< 8	394.13
33	As	< 2 000	40	< 5	96.18
34	Se		< 60	< 70	19 056.03
35	Br		< 30	< 10	122.03
36	Kr				
37	Rb		< 2	< 1	0.85
38	Sr	< 100	< 0.9	< 0.6	0.30
39	Y		< 0.8	< 0.8	0.13
40	Zr	< 100	20	130	23.93
41	Nb		< 0.9	3	0.45
42	Mo	< 500	6	< 2	32.73
43	Tc				
44	Ru		0.5		3.40
45	Rh		2		1.60
46	Pd	< 200	< 9		7.95
47	Ag	< 100	10	< 6	89.05
48	Cd	< 100	80	26	70.43
49	In	< 500	10	15	0.35
50	Sn	< 1 000	300	290	2.58

Atomic No	Element symbol	Impurity concentration, ng/g			
		Supplier	AQura	NRC	NIM
51	Sb	< 1 000	< 10	< 7	6.40
52	Te	< 5 000	< 20	21	51.98
53	I		< 1	< 2	< 1
54	Xe				
55	Cs		< 1	< 0.8	0.98
56	Ba	< 100	< 1	< 0.9	5.88
57	La		< 0.9	< 0.6	< 1
58	Ce		< 1	< 0.6	9.13
59	Pr		< 1		1.00
60	Nd		< 5		< 1
61	Pm				
62	Sm		< 4		3.93
63	Eu		< 2		0.95
64	Gd		< 4		1.15
65	Tb		< 1		0.60
66	Dy		< 4		3.13
67	Ho		< 1		< 1
68	Er		< 3		0.80
69	Tm		< 1		0.38
70	Yb		< 4		2.70
71	Lu		< 1		0.33
72	Hf		1	< 3	31.18
73	Ta				0.93
74	W		10	< 2	61.40
75	Re		< 2		< 1
76	Os		< 20		7.67
77	Ir		3		1.28
78	Pt	< 1 000	< 10	< 8	1.73
79	Au	< 100	3	< 1 300	0.58
80	Hg	< 500	< 20	< 25	5.00
81	Tl	< 1 000	< 8	< 6	1.73
82	Pb	< 2 000	4	8	114.43
83	Bi	< 3 000	20	< 3	1.68
84	Po	< 100			
85	At	< 500			
86	Rn	< 1 000			
87	Fr	< 1 000			
88	Ra	< 5 000			
89	Ac				
90	Th		0.1	< 0.8	0.93
91	Pa				
92	U	< 100	0.1	< 0.8	0.48
93	Np				
94	Pu				

Table 13: Results of the chemical analyses for batch of metal from Honeywell. The technique employed in the analysis provided by the supplier of the metal batch was ICP-AES.

Atomic No	Element symbol	Impurity concentration, ng/g			
		Supplier	AQura	NRC	NIM
1	H				
2	He				
3	Li	< 5	0.4	< 3	17.90
4	Be	< 5	< 8	< 1	2.17
5	B	< 5	10	< 2	6.97
6	C				
7	N				
8	O				
9	F			< 4	301.07
10	Ne				
11	Na	< 5	20	< 1	170.60
12	Mg	88	100	37	3.67
13	Al	Matrix	Matrix	Matrix	Matrix
14	Si	154	200	180	562.13
15	P		30	< 3	15.80
16	S		50	< 4	
17	Cl			< 2	528.20
18	Ar				
19	K	< 100	10	< 4	9.30
20	Ca	< 20	50	< 16	48.57
21	Sc		40	52	54.33
22	Ti	58	30	49	44.73
23	V	17	10	23	22.97
24	Cr	37	40	40	65.00
25	Mn	24	30	37	50.63
26	Fe	7	100	260	34.90
27	Co	< 5	< 2	< 0.6	1.33
28	Ni	< 5	5	< 2	19.93
29	Cu	< 200	30	25	494.43
30	Zn	< 50	30	23	52.03
31	Ga	< 5	4	< 5	< 0.01
32	Ge	< 40	< 30	< 9	386.13
33	As	< 5	30	< 3	86.40
34	Se		50	< 70	33 655.10
35	Br		< 30	< 10	258.57
36	Kr				
37	Rb		< 2	< 1	1.67
38	Sr		< 1	< 0.8	0.10
39	Y		< 0.8	< 0.9	0.23
40	Zr	< 5	1	110	2.83
41	Nb		< 1	5	0.30
42	Mo	< 5	9	< 2	5.00
43	Tc				
44	Ru		0.4		5.80
45	Rh		2		1.77
46	Pd	< 100	10		13.97
47	Ag	< 5	6	< 7	124.40
48	Cd	< 50	30	< 22	958.27
49	In	< 5	9	< 2	0.67
50	Sn	< 50	40	150	2.30

Atomic No	Element symbol	Impurity concentration, ng/g			
		Supplier	AQura	NRC	NIM
51	Sb	< 5	10	< 5	< 0.01
52	Te		< 20	23	13.57
53	I		< 2	< 3	1.30
54	Xe				
55	Cs	< 10	< 2	< 0.9	0.43
56	Ba	< 5	< 1	< 1	4.30
57	La	< 5	1	< 0.7	0.53
58	Ce	< 5	< 1	< 0.7	0.73
59	Pr		< 1		0.33
60	Nd	< 5 000	< 6		< 0.01
61	Pm				
62	Sm		< 4		< 0.01
63	Eu		< 2		< 0.01
64	Gd		< 4		3.97
65	Tb		< 1		0.73
66	Dy		< 5		1.80
67	Ho		< 1		0.70
68	Er		< 4		1.43
69	Tm		< 1		0.67
70	Yb		< 4		1.57
71	Lu		< 1		0.60
72	Hf		0.7	< 4	1.27
73	Ta				< 0.01
74	W	< 25	9	5	< 0.01
75	Re		10		1.10
76	Os		< 20		< 0.01
77	Ir		< 3		0.73
78	Pt	< 100	20	< 8	3.10
79	Au	< 10	3	< 1 300	2.07
80	Hg	< 50	< 20	< 29	< 0.01
81	Tl		< 9	< 7	4.03
82	Pb	< 5	< 3	< 3	440.40
83	Bi	< 5	6	< 3	2.03
84	Po				
85	At				
86	Rn				
87	Fr				
88	Ra				
89	Ac				
90	Th	< 0.7	0.1	< 0.8	0.40
91	Pa				
92	U	< 0.7	< 0.1	< 1	< 0.01
93	Np				
94	Pu				

Table 14: Results of the GDMS analyses for batch of metal from New Metals.

Atomic No	Element symbol	Impurity concentration, ng/g			
		Supplier	AQura	NRC	NIM
1	H				
2	He				
3	Li	< 1	< 1	< 2	71.75
4	Be	< 1	7	< 0.8	1.75
5	B	< 10	60	< 1	125.80
6	C				
7	N				
8	O				
9	F			< 3	374.45
10	Ne				
11	Na	4	30	< 1	118.98
12	Mg	45	50	76	2.43
13	Al	Matrix	Matrix	Matrix	Matrix
14	Si	270	400	330	735.05
15	P		30	12	11.65
16	S		100	< 3	
17	Cl			9	1 204.83
18	Ar				
19	K	< 100	20	< 4	21.10
20	Ca	< 50	90	< 16	20.90
21	Sc		40	57	34.45
22	Ti	10	40	10	19.65
23	V	65	40	61	58.93
24	Cr	15	40	15	32.45
25	Mn	3	10	4	10.25
26	Fe	55	200	70	98.70
27	Co	< 1	2	< 0.5	0.38
28	Ni	10	20	9	8.03
29	Cu	57	400	18	516.87
30	Zn	< 2	20	27	141.53
31	Ga	< 1	10	< 4	12.20
32	Ge	< 50	< 30	< 7	467.50
33	As	< 5	50	< 4	137.00
34	Se	< 30	70	< 60	25 090.53
35	Br	< 50	< 30	< 10	193.90
36	Kr				
37	Rb		2	< 1	1.73
38	Sr		< 1	< 0.6	3.48
39	Y		< 0.8	< 0.7	0.58
40	Zr	7	5	62	3.83
41	Nb	3	0.7	2	0.93
42	Mo	24	40	< 2	32.13
43	Tc				
44	Ru		0.7		7.83
45	Rh		2		0.95
46	Pd		< 10		103.48
47	Ag	< 1	10	< 6	891.08
48	Cd	< 10	50	89	55.80
49	In	< 1	8	74	< 1
50	Sn	< 20	300	< 32	1.83

Atomic No	Element symbol	Impurity concentration, ng/g			
		Supplier	AQura	NRC	NIM
51	Sb	< 5	< 10	< 9	14.83
52	Te		10	22	7.30
53	I		< 2	< 2	1.05
54	Xe				
55	Cs	< 1	< 2	< 0.6	0.38
56	Ba	< 1	1	< 0.7	6.90
57	La	< 1	< 1	< 0.6	0.68
58	Ce	< 1	< 1	< 0.6	0.60
59	Pr		< 1		1.10
60	Nd	< 3	< 6		3.58
61	Pm				
62	Sm		< 4		3.78
63	Eu		< 2		0.43
64	Gd		< 5		4.80
65	Tb		< 1		0.85
66	Dy		< 5		2.85
67	Ho		< 1		0.28
68	Er		< 4		1.15
69	Tm		< 1		1.05
70	Yb		< 4		1.28
71	Lu		< 1		0.25
72	Hf	< 1	7	< 3	< 1
73	Ta				0.43
74	W	< 1	70	< 2	2.13
75	Re		< 2		0.90
76	Os		< 20		< 1
77	Ir		< 4		1.20
78	Pt	< 2	< 10	< 8	7.48
79	Au		5	< 1 100	0.83
80	Hg	< 10	< 20	< 24	5.08
81	Tl	< 1	< 9	< 6	4.83
82	Pb	< 1	5	8	173.85
83	Bi	< 1	30	< 3	2.08
84	Po				
85	At				
86	Rn				
87	Fr				
88	Ra				
89	Ac				
90	Th	< 0.3	< 0.1	< 0.6	1.90
91	Pa				
92	U	< 0.3	0.1	< 0.8	0.73
93	Np				
94	Pu				

Table 15: Results of the GDMS analyses for batch of metal from Sumitomo.

It is important to observe that extreme care was taken during the preparation of the samples, which included cleaning and baking of the graphite moulds and use of vacuum during the casting. Furthermore, according to the GDMS providers, the samples are generally chemically etched before analysis. Once inside the analyser, readings are only taken into account after the sample has been through an initial period of 30 min of sputtering (guaranteeing that valid readings are taken only after the beam reached several microns inside the sample so that possible contaminants in the outer surface are ignored). Nevertheless, considerable variation in the quality of the chemical analyses was observed. This could be due to the fact that the samples were not good representatives of the batches, then samples from the same batch presented very different characteristics because the batch lacks homogeneity in impurity distribution among the pellets as the process of forming the pellets could cause segregation of impurities so that different pellets would have different residual impurity compositions.

Another hypothesis would be that the technique itself needs improvements and the analysers need to be calibrated (hence traceable) so that results from different analysers provide more agreeable results for a given sample.

The first hypothesis is very likely to happen as it is very difficult to establish an adequate sampling to represent the metal portion used to cast the fixed point ingot (maybe adding more samples to be sent to each GDMS supplier but it would increase the costs of production considerably). However, that does not exclude the fact that chemical analyses at this level of resolution still require improvement to achieve comparability of results [39]. This is especially valid for the discrepancies observed in the NIM results, which presented several peaks for a number of elements (F, Si, Cl, Cu, Ge, Se, Br and Pb) while the results from the other providers were, in most of the cases, either below the detection limits or in comparatively much lower concentrations. This could be an indication that there was some contamination present in the NIM GDMS device. Further concerning the values in the tables 11 – 15 corresponding to NIM measurements, it is important to note that they do not represent the real resolution of the analyser (0.01 ppb) but were actually truncated since most values were expressed with too many significant figures in the assays.

In general, very little information was given with respect to the uncertainty of the measurements. For example, incomplete (as just percentages were provided without declaration of coverage factors and/or degrees of freedom) uncertainty statements were provided only by two of the chemical analyses providers (AQura and NRC). Assays provided by the metal suppliers contained no information about uncertainties either.

Due to its semi-quantitative capabilities, uncertainties declared by NRC were expressed as ‘a factor of two’ (one-half to two-fold) of the values indicated for all 54 elements scanned. This tends to be the standard practice, if uncertainties are declared at all. The vast majority of assays supplied with high purity metals do not come with a declaration of uncertainties.

AQura uncertainties varied from ± 20 % to ‘a factor of five’ (figure 40 / table 16). The smaller uncertainties were achieved for some elements due to a self-calibration capability of the analyser for these elements.

For the purpose of making the calculations, uncertainties declared as ‘factor of two’ were translated into the value of the concentration itself and ‘factor of five’ was considered as four times its concentration. In all other cases where uncertainties were not stated, the uncertainty was assumed to be equal in magnitude to the amount of impurity stated in the assays (as if they were declared as a ‘factor of two’).

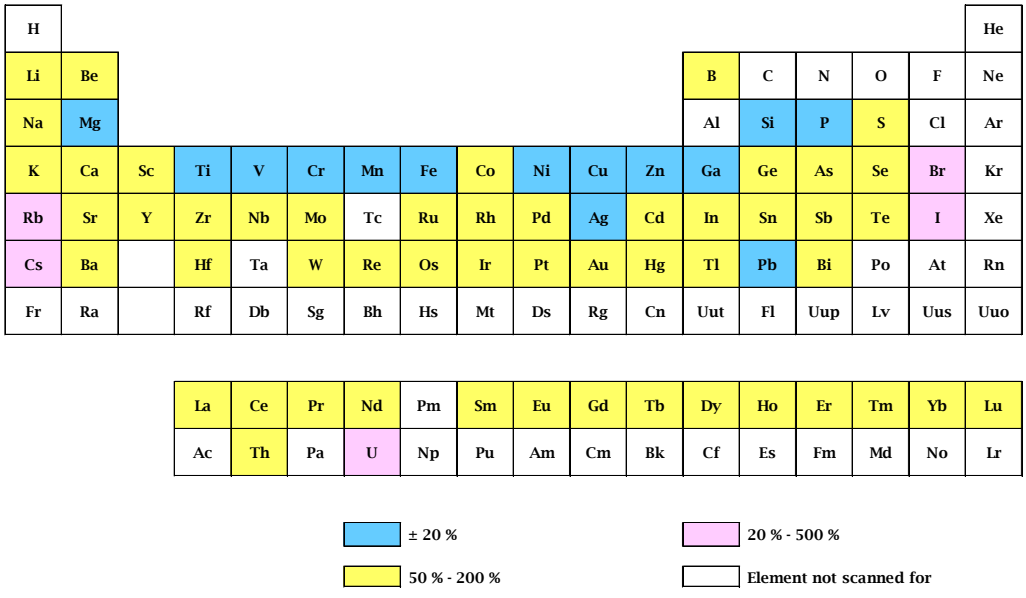

Figure 40: Uncertainties declared by AQura for the 70 elements scanned.

Atomic No	Element	$u(c_l^i)$ %
1	H	
2	He	
3	Li	50 - 200
4	Be	50 - 200
5	B	50 - 200
6	C	
7	N	
8	O	
9	F	
10	Ne	
11	Na	50 - 200
12	Mg	± 20
13	Al	Matrix
14	Si	± 20
15	P	± 20
16	S	50 - 200
17	Cl	
18	Ar	
19	K	50 - 200
20	Ca	50 - 200
21	Sc	50 - 200
22	Ti	± 20
23	V	± 20
24	Cr	± 20
25	Mn	± 20
26	Fe	± 20
27	Co	50 - 200
28	Ni	± 20
29	Cu	± 20
30	Zn	± 20
31	Ga	± 20
32	Ge	50 - 200
33	As	50 - 200
34	Se	50 - 200
35	Br	20 - 500
36	Kr	
37	Rb	20 - 500
38	Sr	50 - 200
39	Y	50 - 200
40	Zr	50 - 200
41	Nb	50 - 200
42	Mo	50 - 200
43	Tc	
44	Ru	50 - 200
45	Rh	50 - 200
46	Pd	50 - 200
47	Ag	± 20

Atomic No	Element	$u(c_l^i)$ %
48	Cd	50 - 200
49	In	50 - 200
50	Sn	50 - 200
51	Sb	50 - 200
52	Te	50 - 200
53	I	20 - 500
54	Xe	
55	Cs	20 - 500
56	Ba	50 - 200
57	La	50 - 200
58	Ce	50 - 200
59	Pr	50 - 200
60	Nd	50 - 200
61	Pm	
62	Sm	50 - 200
63	Eu	50 - 200
64	Gd	50 - 200
65	Tb	50 - 200
66	Dy	50 - 200
67	Ho	50 - 200
68	Er	50 - 200
69	Tm	50 - 200
70	Yb	50 - 200
71	Lu	50 - 200
72	Hf	50 - 200
73	Ta	
74	W	50 - 200
75	Re	50 - 200
76	Os	50 - 200
77	Ir	50 - 200
78	Pt	50 - 200
79	Au	50 - 200
80	Hg	50 - 200
81	Tl	50 - 200
82	Pb	± 20
83	Bi	50 - 200
84	Po	
85	At	
86	Rn	
87	Fr	
88	Ra	
89	Ac	
90	Th	50 - 200
91	Pa	
92	U	20 - 500
93	Np	
94	Pu	

Table 16: Uncertainties declared by AQura for the 70 elements scanned.

5.3. Freezing curve measurements

The five aluminium fixed point cells used in this study were measured rigorously following the protocol described in chapter 4. For each of the cells, a total of four complete freezing curves was obtained to be used as input to calculate the correction and uncertainty estimates according to the Scheil, gradient and thermal methodologies. The freezing curves obtained with the fixed point cells for the calculations are shown in figures 41-45.

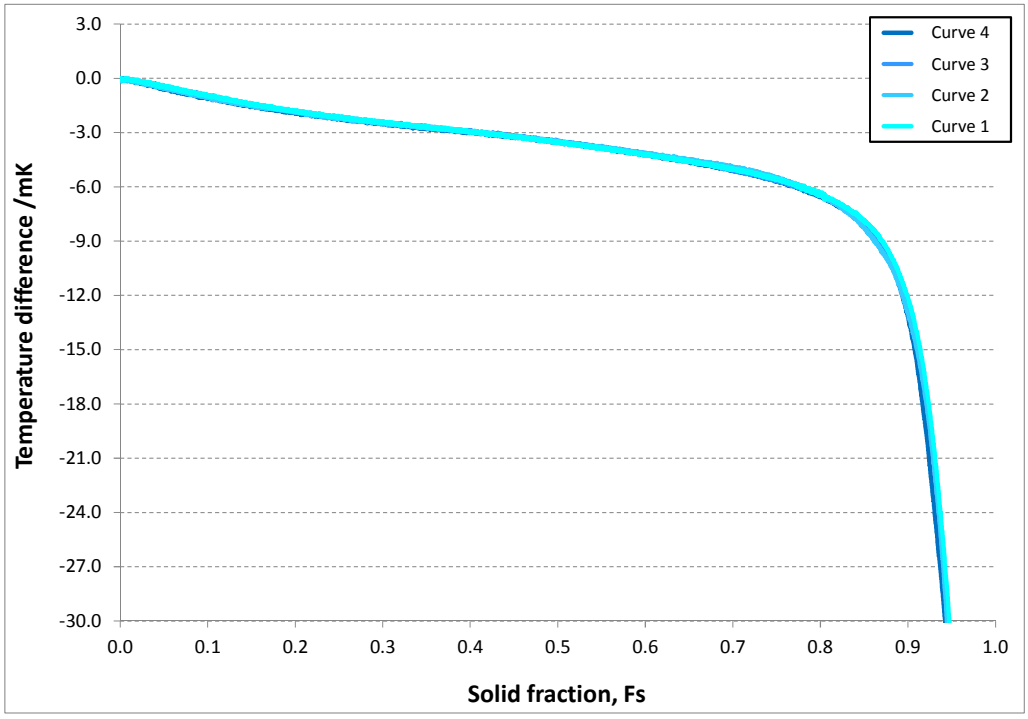

Figure 41: The four freezing curves measured for the cell using aluminium from Alfa Aesar (cell Al-A).

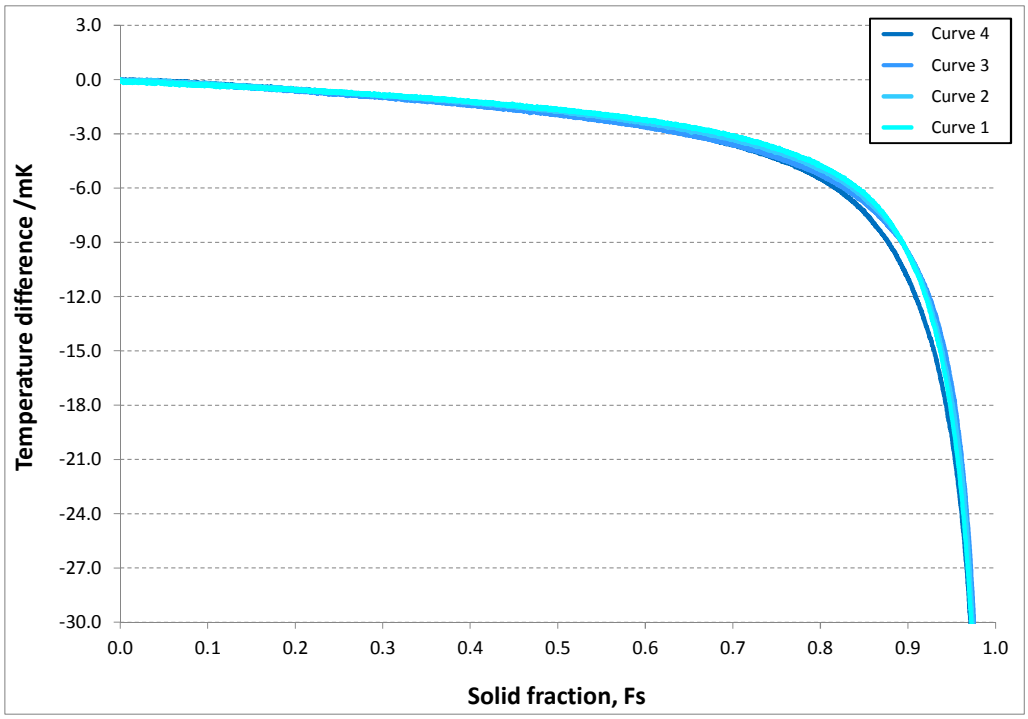

Figure 42: The four freezing curves measured for the cell using aluminium from ESPI (cell Al-E).

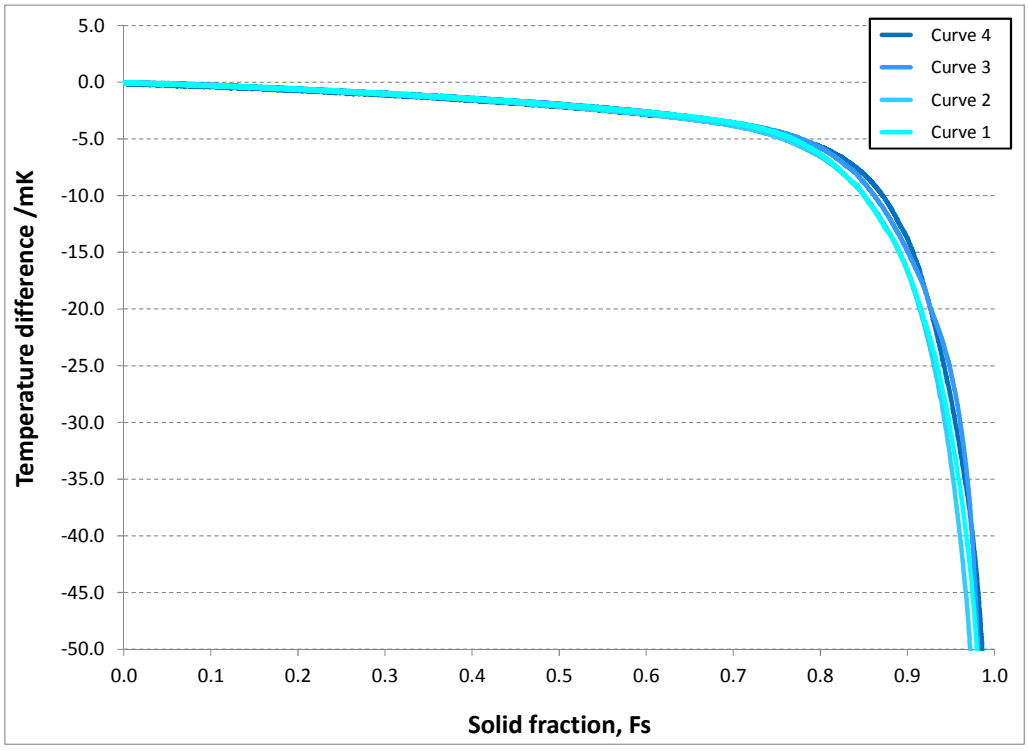

Figure 43: The four freezing curves measured for the cell using aluminium from Honeywell (cell Al-H).

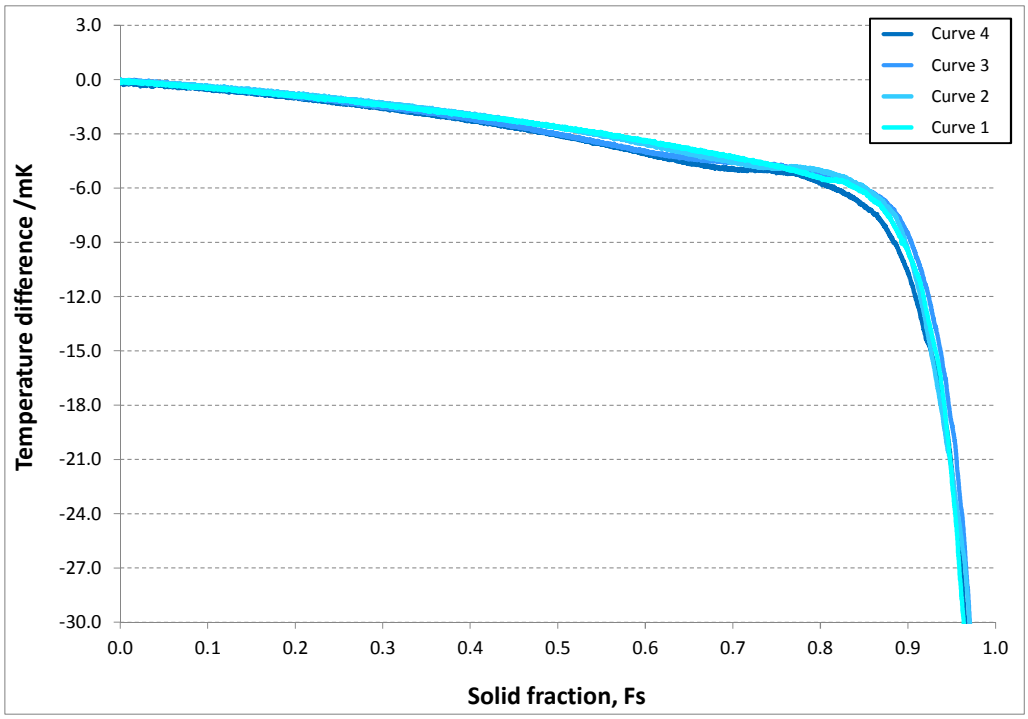

Figure 44: The four freezing curves measured for the cell using aluminium from New Metals (cell Al-N).

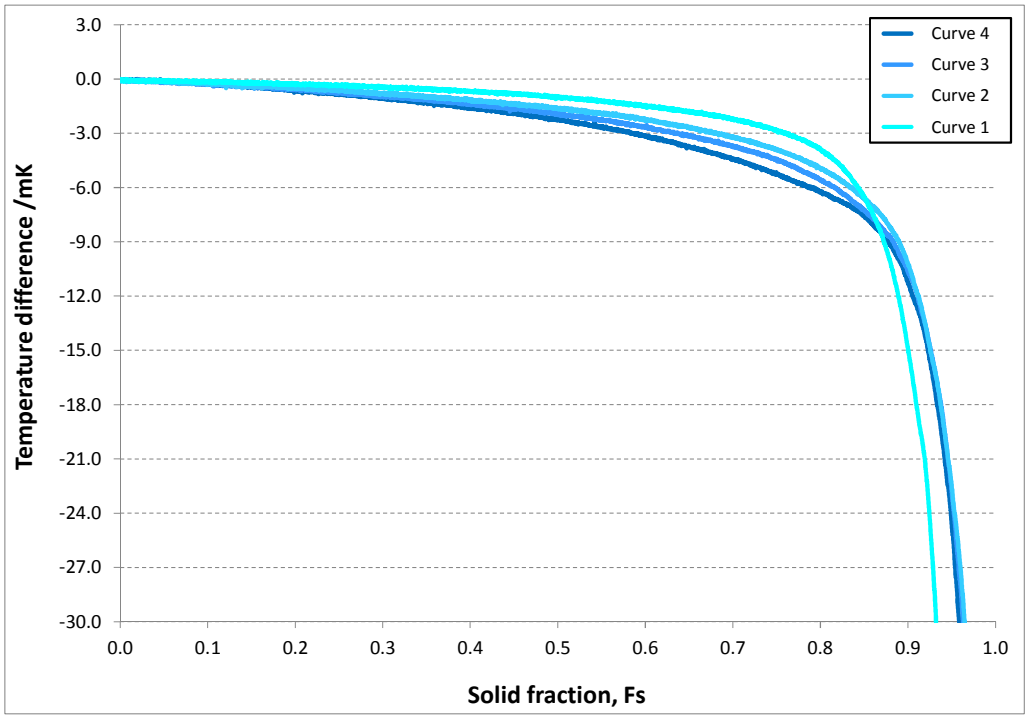

Figure 45: The four freezing curves measured for the cell using aluminium from Sumitomo (cell Al-S).

Overall, the four curves measured with each cell show great reproducibility, especially at the first half of the freezing, even though the freezing curves measured in cells Al-A and Al-N have unexpected shapes. The cell produced with samples from Alfa Aesar (Al-A) exhibited an abnormal steep beginning (equivalent to about 2.2 mK, present up to F_s 0.20). This was possibly caused by the increased concentration of high *k* impurities (whose effect causes the elevation of the freezing temperature of the material), as were also detected in the GDMS analyses.

The cell constructed using samples supplied by New Metals (Al-N) generated curves with a discontinuity in the slope range towards the end of the freezing plateau (varying from curve to curve, overall from F_s 0.65 onwards) marked by a sudden decrease in the freezing rate as if the freeze was being delayed. No changes in the furnace controllers or measurement system was observed during this phenomenon. This result is most certainly due to the effect of impurities, probably resulting from impurities that were kept immiscible and somehow, after a reaction was triggered, they were gradually aggregated in the solution in the later stage of the freezing. It is speculated that high *k* impurities could also be the cause of this reaction, but contrary to what occurred with cell Al-A, in this case they would only prevail later in the freezing, towards the end of the phase transition.

An alternative explanation of the behaviour in cell Al-N could be that low *k* impurities that were dissolved in the liquid metal started to solidify shortly after the beginning of the freeze, becoming apparent right after 10% of the freezing occurred. Due to the build up of the concentration of these impurities in the solid-solid solution, they increased the slope of the freezing curve, forcing the plateau downwards as the freezing progressed (hence resulting in an increased freezing range). This effect would then continue until these impurities were all frozen. The later part (flatter section) could be explained as either the system (once free from those impurities) recovering and then compensating for this at the end of the freezing or high *k* impurities being dissolved later in the freeze, counterbalancing the initial effect of those low *k* impurities. It must be noted that neither of these hypotheses were confirmed by the GDMS results for the samples supplied by New Metals, since no clear relation could be established between the impurity content and the behaviour of the freezing curve, as it was the case for cell Al-A.

To illustrate the differences between the freezing behaviour of the cells, figure 46 shows a representative curve from each of them.

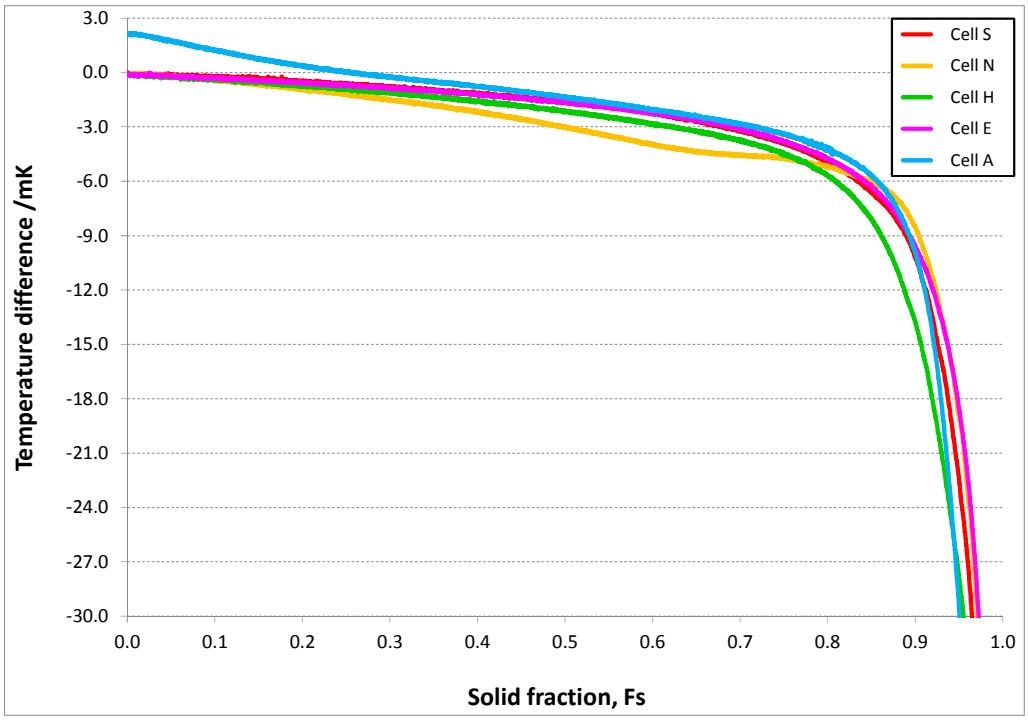

Figure 46: Detail of representative freezing curves for each of the five cells.

Since the curve from cell Al-A exhibited a steep beginning, to facilitate comparison, its freezing curve was shifted up by 2.2 mK. Furthermore, it is important to note that all curves are normalised, which implies that the origin of each curve derives independently from each particular freezing curve that was measured. This is because the application of the correction methodologies for which these curves were intended does not require absolute temperatures but temperature differences in relation to the maximum measured. Due to the nature of these measurements, comparisons in terms of absolute temperatures are neither applicable nor possible: these are only relevant for the last methodology applied, the direct cell comparison. If so required, these curves would have to be plotted and compared in terms of $W(T_{90})$ (equation 2) with the application of the necessary corrections, as previously described in section 4.2.2.1 (cell comparisons). Measurements of $W(T_{90})$ (from which one would derive T_{90}) would demand the withdrawal and annealing of the SPRT after every

freezing curve realisation (section 4.1.2), which would expose the sensor to unnecessary risks and be considerably more time consuming.

In this chapter I described the results of the chemical analyses provided by the metal suppliers and compared them with the GDMS analyses supplied by the third party laboratories AQura, NRC and NIM. These results are briefly discussed (including the uncertainties of the assays). Subsequently, the freezing curves obtained with the five cells are provided. The analysis of these results, including the application of the methodologies proposed is given in chapter 6, together with a discussion of the findings.

Chapter 6

Results for the calculations of the various impurity correction methodologies investigated

In this chapter the impurity assays and the freezing curve measurements given in the previous chapter were used to investigate the various proposed correction methods. In brief, the GDMS results were the main input for the calculation of both the Sum of Individual Estimates (SIE) and the Overall Maximum Estimate (OME) methodologies and also contributed for the calculations of the hybrid SIE/modified OME approach. The other methodologies relied on the measurement of freezing curves from the fixed point cells. The estimates calculated according to the Scheil, the gradient and the thermal analysis methods required that the freezing curves were parameterised through least square fitting. The results of the calculations are given in the sections to follow.

6.1. Sum of Individual Estimates (SIE) correction and uncertainty calculation

The calculations for the Sum of Individual Estimates were performed through the application of equations 18 and 19 (in chapter 2) to the impurity concentrations (c_{l1}^{i}) given by the GDMS analyses together with the corresponding values for the liquidus slopes (m_l^i), given in table 4. The uncertainties for the liquidus slopes, $u(m_l^i)$, were also taken from table 4 (in chapter 2). The uncertainties for the impurity concentrations ($u(c_{l1}^{i})$) given by the GDMS in the assays were obtained according to the percentages assigned for the individual elements:

- for the analyses provided by AQura, they were calculated according to the percentages given in table 16 (in chapter 5);

- for the analyses provided by NRC, as per declaration in the certificates of analyses, the uncertainties were taken as equivalent in magnitude to the value of the impurity concentration itself;
- for the assays provided by the metal suppliers as well as NIM, the uncertainty for all elements was assumed to be the same case as NRC, since no declaration of uncertainties was provided.

To facilitate the comparison of the calculations, the corrections and uncertainties performed according to the SIE methodology for the cell Al-S (Sumitomo) are given in tables 17 – 20. Subsequently, a summary of the SIE results for all five cells is shown in table 21.

Atomic No	Element symbol	c_{l1}^{i}	$u(c_{l1}^{i})$	m_l^i	$u(m_l^i)$	Individual Correction	Uncertainty Contribution
		ng/g	ng/g	µK/ppbw	µK/ppbw	µK	μK^2
1	H			– 17.873	0.106		
2	He			– 4.527	0.001		
3	Li	< 1	0.50	– 1.319	1.030	—	0.70
4	Be	< 1	0.50	– 1.832	0.111	—	0.84
5	B	< 10	5.00	– 1.858	0.774	—	101.30
6	C			– 1.131	0.870		
7	N			– 1.276	0.020		
8	O			– 0.396	0.119		
9	F			0.000	0.000		
10	Ne			– 0.898	0.000		
11	Na	4	4.00	– 0.724	0.150	– 2.89	8.74
12	Mg	45	45.00	– 0.450	0.116	– 20.23	436.45
13	Al	Matrix	Matrix	Matrix	Matrix	Matrix	Matrix
14	Si	270	270.00	– 0.623	0.093	– 168.16	28 916.42
15	P			– 0.834	0.576		
16	S			– 0.511	0.131		
17	Cl			0.000	0.000		
18	Ar			– 0.453	0.000		
19	K	< 100	50.00	– 0.277	0.263	—	363.97
20	Ca	< 50	25.00	– 0.470	0.088	—	142.72
21	Sc			– 0.223	0.517		
22	Ti	10	10.00	4.607	1.895	46.07	2 481.91
23	V	65	65.00	3.321	1.789	215.86	60 125.35
24	Cr	15	15.00	1.051	0.634	15.77	339.09
25	Mn	3	3.00	0.115	0.264	0.34	0.75
26	Fe	55	55.00	– 0.311	0.024	– 17.10	294.23
27	Co	< 1	0.50	– 0.297	0.016	—	0.02
28	Ni	10	10.00	– 0.309	0.056	– 3.09	9.84
29	Cu	57	57.00	– 0.252	0.095	– 14.34	235.08
30	Zn	< 2	1.00	– 0.037	0.156	—	0.03
31	Ga	< 1	0.50	– 0.150	0.083	—	0.01
32	Ge	< 50	25.00	– 0.208	0.033	—	27.68
33	As	< 5	2.50	– 0.235	0.014	—	0.35
34	Se	< 30	15.00	– 0.288	0.134	—	22.74
35	Br	< 50	25.00	– 0.227	0.068	—	35.01
36	Kr			– 0.216	0.065		
37	Rb			– 0.160	0.069		
38	Sr			– 0.196	0.014		
39	Y			– 0.192	0.011		
40	Zr	7	7.00	1.233	1.016	8.63	125.10
41	Nb	3	3.00	5.478	1.697	16.43	295.98
42	Mo	24	24.00	1.155	0.901	27.72	1 236.33
43	Tc			0.045	0.317		
44	Ru			– 0.143	0.044		
45	Rh			0.068	0.437		
46	Pd			– 0.057	0.194		
47	Ag	< 1	0.50	0.010	0.184	—	0.01
48	Cd	< 10	5.00	– 0.112	0.038	—	0.35
49	In	< 1	0.50	– 0.157	0.024	—	0.01
50	Sn	< 20	10.00	– 0.142	0.003	—	2.02
51	Sb	< 5	2.50	– 0.081	0.072	—	0.07
52	Te			– 0.116	0.050		
53	I			0.000	0.000		
54	Xe			– 0.137	0.002		
55	Cs	< 1	0.50	– 0.104	0.041	—	0.00

Atomic No	Element symbol	c_{l1}^{i}	$u(c_{l1}^{i})$	m_l^i	$u(m_l^i)$	Individual Correction	Uncertainty Contribution
		ng/g	ng/g	µK/ppbw	µK/ppbw	µK	μK^2
56	Ba	< 1	0.50	– 0.079	0.071	—	0.00
57	La	< 1	0.50	– 0.121	0.018	—	0.00
58	Ce	< 1	0.50	– 0.128	0.002	—	0.00
59	Pr			– 0.127	0.002		
60	Nd	< 3	1.50	– 0.125	0.002	—	0.03
61	Pm			0.000	0.000		
62	Sm			– 0.110	0.017		
63	Eu			– 0.119	0.036		
64	Gd			– 0.115	0.003		
65	Tb			– 0.107	0.010		
66	Dy			– 0.101	0.017		
67	Ho			– 0.099	0.017		
68	Er			– 0.098	0.017		
69	Tm			– 0.104	0.004		
70	Yb			– 0.046	0.054		
71	Lu			– 0.104	0.031		
72	Hf	< 1	0.50	2.391	2.522	—	3.02
73	Ta			5.443	1.253		
74	W	< 1	0.50	0.488	0.873	—	0.25
75	Re			0.095	0.131		
76	Os			0.400	0.657		
77	Ir			0.376	0.622		
78	Pt	< 2	1.00	0.017	0.190	—	0.04
79	Au			– 0.010	0.074		
80	Hg	< 10	5.00	– 0.030	0.059	—	0.11
81	Tl	< 1	0.50	– 0.059	0.028	—	0.00
82	Pb	< 1	0.50	– 0.052	0.056	—	0.00
83	Bi	< 1	0.50	– 0.039	0.013	—	0.00
84	Po			0.000	0.000		
85	At			0.000	0.000		
86	Rn			– 0.081	0.000		
87	Fr			0.000	0.000		
88	Ra			0.000	0.000		
89	Ac			0.000	0.000		
90	Th	< 0.3	0.15	– 0.052	0.034	—	0.00
91	Pa			– 0.079	0.024		
92	U	< 0.3	0.15	– 0.060	0.027	—	0.00
93	Np			– 0.077	0.023		
94	Pu			– 0.049	0.039		

SIE correction	**– 0.11 mK**
u^2 (Σ contributions)	**95 206.55 μK^2**
u (ΔT_{SIE})	**± 0.31 mK**

Table 17: Calculation of SIE correction and uncertainty for Al metal sample from Sumitomo based on the assay provided by the metal supplier.

Atomic No	Element symbol	c_{l1}^{i}	$u(c_{l1}^{i})$	m_l^i	$u(m_l^i)$	Individual Correction	Uncertainty Contribution
		ng/g	ng/g	µK/ppbw	µK/ppbw	µK	μK^2
1	H			– 17.873	0.106		
2	He			– 4.527	0.001		
3	Li	< 1	0.50	– 1.319	1.030	—	0.70
4	Be	7	7.00	– 1.832	0.111	– 12.83	165.09
5	B	60	60.00	– 1.858	0.774	– 111.50	14 587.66
6	C			– 1.131	0.870		
7	N			– 1.276	0.020		
8	O			– 0.396	0.119		
9	F			0.000	0.000		
10	Ne			– 0.898	0.000		
11	Na	30	30.00	– 0.724	0.150	– 21.71	491.48
12	Mg	50	10.00	– 0.450	0.116	– 22.48	53.71
13	Al	Matrix	Matrix	Matrix	Matrix	Matrix	Matrix
14	Si	400	80.00	– 0.623	0.093	– 249.13	3 881.38
15	P	30	6.00	– 0.834	0.576	– 25.03	323.56
16	S	100	100.00	– 0.511	0.131	– 51.13	2 786.18
17	Cl			0.000	0.000		
18	Ar			– 0.453	0.000		
19	K	20	20.00	– 0.277	0.263	– 5.53	58.24
20	Ca	90	90.00	– 0.470	0.088	– 42.26	1 849.71
21	Sc	40	40.00	– 0.223	0.517	– 8.93	508.09
22	Ti	40	8.00	4.607	1.895	184.30	7 103.27
23	V	40	8.00	3.321	1.789	132.84	5 829.04
24	Cr	40	8.00	1.051	0.634	42.05	714.22
25	Mn	10	2.00	0.115	0.264	1.15	7.04
26	Fe	200	40.00	– 0.311	0.024	– 62.20	177.06
27	Co	2	2.00	– 0.297	0.016	– 0.59	0.35
28	Ni	20	4.00	– 0.309	0.056	– 6.17	2.78
29	Cu	400	80.00	– 0.252	0.095	– 100.63	1 856.35
30	Zn	20	4.00	– 0.037	0.156	– 0.74	9.77
31	Ga	10	2.00	– 0.150	0.083	– 1.50	0.78
32	Ge	< 30	15.00	– 0.208	0.033	—	9.96
33	As	50	50.00	– 0.235	0.014	– 11.75	138.69
34	Se	70	70.00	– 0.288	0.134	– 20.18	495.25
35	Br	< 30	60.00	– 0.227	0.068	—	186.07
36	Kr			– 0.216	0.065		
37	Rb	2	8.00	– 0.160	0.069	– 0.32	1.67
38	Sr	< 1	0.50	– 0.196	0.014	—	0.01
39	Y	< 0.8	0.40	– 0.192	0.011	—	0.01
40	Zr	5	5.00	1.233	1.016	6.17	63.82
41	Nb	0.7	0.70	5.478	1.697	3.83	16.11
42	Mo	40	40.00	1.155	0.901	46.20	3 434.25
43	Tc			0.045	0.317		
44	Ru	0.7	0.70	– 0.143	0.044	– 0.10	0.01
45	Rh	2	2.00	0.068	0.437	0.14	0.78
46	Pd	< 10	5.00	– 0.057	0.194	—	1.02
47	Ag	10	2.00	0.010	0.184	0.10	3.37
48	Cd	50	50.00	– 0.112	0.038	– 5.61	35.00
49	In	8	8.00	– 0.157	0.024	– 1.25	1.60
50	Sn	300	300.00	– 0.142	0.003	– 42.66	1 821.06
51	Sb	< 10	5.00	– 0.081	0.072	—	0.29
52	Te	10	10.00	– 0.116	0.050	– 1.16	1.60
53	I	< 2	4.00	0.000	0.000	—	0.00
54	Xe			– 0.137	0.002		
55	Cs	< 2	4.00	– 0.104	0.041	—	0.18

Atomic No	Element symbol	c_{l1}^{i}	$u(c_{l1}^{i})$	m_l^i	$u(m_l^i)$	Individual Correction	Uncertainty Contribution
		ng/g	ng/g	µK/ppbw	µK/ppbw	µK	μK^2
56	Ba	1	1.00	– 0.079	0.071	– 0.08	0.01
57	La	< 1	0.50	– 0.121	0.018	—	0.00
58	Ce	< 1	0.50	– 0.128	0.002	—	0.00
59	Pr	< 1	0.50	– 0.127	0.002	—	0.00
60	Nd	< 6	3.00	– 0.125	0.002	—	0.14
61	Pm			0.000	0.000		
62	Sm	< 4	2.00	– 0.110	0.017	—	0.05
63	Eu	< 2	1.00	– 0.119	0.036	—	0.02
64	Gd	< 5	2.50	– 0.115	0.003	—	0.08
65	Tb	< 1	0.50	– 0.107	0.010	—	0.00
66	Dy	< 5	2.50	– 0.101	0.017	—	0.07
67	Ho	< 1	0.50	– 0.099	0.017	—	0.00
68	Er	< 4	2.00	– 0.098	0.017	—	0.04
69	Tm	< 1	0.50	– 0.104	0.004	—	0.00
70	Yb	< 4	2.00	– 0.046	0.054	—	0.02
71	Lu	< 1	0.50	– 0.104	0.031	—	0.00
72	Hf	7	7.00	2.391	2.522	16.73	591.66
73	Ta			5.443	1.253		
74	W	70	70.00	0.488	0.873	34.18	4 902.94
75	Re	< 2	1.00	0.095	0.131	—	0.03
76	Os	< 20	10.00	0.400	0.657	—	59.14
77	Ir	< 4	2.00	0.376	0.622	—	2.11
78	Pt	< 10	5.00	0.017	0.190	—	0.91
79	Au	5	5.00	– 0.010	0.074	– 0.05	0.14
80	Hg	< 20	10.00	– 0.030	0.059	—	0.43
81	Tl	< 9	4.50	– 0.059	0.028	—	0.09
82	Pb	5	1.00	– 0.052	0.056	– 0.26	0.08
83	Bi	30	30.00	– 0.039	0.013	– 1.16	1.51
84	Po			0.000	0.000		
85	At			0.000	0.000		
86	Rn			– 0.081	0.000		
87	Fr			0.000	0.000		
88	Ra			0.000	0.000		
89	Ac			0.000	0.000		
90	Th	< 0.1	0.05	– 0.052	0.034	—	0.00
91	Pa			– 0.079	0.024		
92	U	0.1	0.40	– 0.060	0.027	– 0.01	0.00
93	Np			– 0.077	0.023		
94	Pu			– 0.049	0.039		

SIE correction	**0.34 mK**
u^2 (Σ contributions)	**52 176.70 μK^2**
u (ΔT_{SIE})	**± 0.23 mK**

Table 18: Calculation of SIE correction and uncertainty for Al metal sample from Sumitomo based on the chemical analysis supplied by AQura.

Atomic No	Element symbol	c_{l1}^{i}	$u(c_{l1}^{i})$	m_l^i	$u(m_l^i)$	Individual Correction	Uncertainty Contribution
		ng/g	ng/g	µK/ppbw	µK/ppbw	µK	μK^2
1	H			– 17.873	0.106		
2	He			– 4.527	0.001		
3	Li	< 2	1.00	– 1.319	1.030	—	2.80
4	Be	< 0.8	0.40	– 1.832	0.111	—	0.54
5	B	< 1	0.50	– 1.858	0.774	—	1.01
6	C			– 1.131	0.870		
7	N			– 1.276	0.020		
8	O			– 0.396	0.119		
9	F	< 3	1.50	0.000	0.000	—	0.00
10	Ne			– 0.898	0.000		
11	Na	< 1	0.50	– 0.724	0.150	—	0.14
12	Mg	76	76.00	– 0.450	0.116	– 34.17	1 244.89
13	Al	Matrix	Matrix	Matrix	Matrix	Matrix	Matrix
14	Si	330	330.00	– 0.623	0.093	– 205.53	43 196.14
15	P	12	12.00	– 0.834	0.576	– 10.01	147.97
16	S	< 3	1.50	– 0.511	0.131	—	0.63
17	Cl	9	9.00	0.000	0.000	0.00	0.00
18	Ar			– 0.453	0.000		
19	K	< 4	2.00	– 0.277	0.263	—	0.58
20	Ca	< 16	8.00	– 0.470	0.088	—	14.62
21	Sc	57	57.00	– 0.223	0.517	– 12.72	1 031.73
22	Ti	10	10.00	4.607	1.895	46.07	2 481.91
23	V	61	61.00	3.321	1.789	202.58	52 953.00
24	Cr	15	15.00	1.051	0.634	15.77	339.09
25	Mn	4	4.00	0.115	0.264	0.46	1.33
26	Fe	70	70.00	– 0.311	0.024	– 21.77	476.60
27	Co	< 0.5	0.25	– 0.297	0.016	—	0.01
28	Ni	9	9.00	– 0.309	0.056	– 2.78	7.97
29	Cu	18	18.00	– 0.252	0.095	– 4.53	23.44
30	Zn	27	27.00	– 0.037	0.156	– 0.99	18.76
31	Ga	< 4	2.00	– 0.150	0.083	—	0.12
32	Ge	< 7	3.50	– 0.208	0.033	—	0.54
33	As	< 4	2.00	– 0.235	0.014	—	0.22
34	Se	< 60	30.00	– 0.288	0.134	—	90.96
35	Br	< 10	5.00	– 0.227	0.068	—	1.40
36	Kr			– 0.216	0.065		
37	Rb	< 1	0.50	– 0.160	0.069	—	0.01
38	Sr	< 0.6	0.30	– 0.196	0.014	—	0.00
39	Y	< 0.7	0.35	– 0.192	0.011	—	0.00
40	Zr	62	62.00	1.233	1.016	76.45	9 813.67
41	Nb	2	2.00	5.478	1.697	10.96	131.55
42	Mo	< 2	1.00	1.155	0.901	—	2.15
43	Tc			0.045	0.317		
44	Ru			– 0.143	0.044		
45	Rh			0.068	0.437		
46	Pd			– 0.057	0.194		
47	Ag	< 6	3.00	0.010	0.184	—	0.30
48	Cd	89	89.00	– 0.112	0.038	– 9.98	110.88
49	In	74	74.00	– 0.157	0.024	– 11.58	137.22
50	Sn	< 32	16.00	– 0.142	0.003	—	5.18
51	Sb	< 9	4.50	– 0.081	0.072	—	0.24
52	Te	22	22.00	– 0.116	0.050	– 2.56	7.75
53	I	< 2	1.00	0.000	0.000	—	0.00
54	Xe			– 0.137	0.002		
55	Cs	< 0.6	0.30	– 0.104	0.041	—	0.00

Atomic No	Element symbol	c_{l1}^{i}	$u(c_{l1}^{i})$	m_l^i	$u(m_l^i)$	Individual Correction	Uncertainty Contribution
		ng/g	ng/g	µK/ppbw	µK/ppbw	µK	μK^2
56	Ba	< 0.7	0.35	– 0.079	0.071	—	0.00
57	La	< 0.6	0.30	– 0.121	0.018	—	0.00
58	Ce	< 0.6	0.30	– 0.128	0.002	—	0.00
59	Pr			– 0.127	0.002		
60	Nd			– 0.125	0.002		
61	Pm			0.000	0.000		
62	Sm			– 0.110	0.017		
63	Eu			– 0.119	0.036		
64	Gd			– 0.115	0.003		
65	Tb			– 0.107	0.010		
66	Dy			– 0.101	0.017		
67	Ho			– 0.099	0.017		
68	Er			– 0.098	0.017		
69	Tm			– 0.104	0.004		
70	Yb			– 0.046	0.054		
71	Lu			– 0.104	0.031		
72	Hf	< 3	1.50	2.391	2.522	—	27.17
73	Ta			5.443	1.253		
74	W	< 2	1.00	0.488	0.873	—	1.00
75	Re			0.095	0.131		
76	Os			0.400	0.657		
77	Ir			0.376	0.622		
78	Pt	< 8	4.00	0.017	0.190	—	0.58
79	Au	< 1100	550.00	– 0.010	0.074	—	1 703.99
80	Hg	< 24	12.00	– 0.030	0.059	—	0.63
81	Tl	< 6	3.00	– 0.059	0.028	—	0.04
82	Pb	8	8.00	– 0.052	0.056	– 0.42	0.37
83	Bi	< 3	1.50	– 0.039	0.013	—	0.00
84	Po			0.000	0.000		
85	At			0.000	0.000		
86	Rn			– 0.081	0.000		
87	Fr			0.000	0.000		
88	Ra			0.000	0.000		
89	Ac			0.000	0.000		
90	Th	< 0.6	0.30	– 0.052	0.034	—	0.00
91	Pa			– 0.079	0.024		
92	U	< 0.8	0.40	– 0.060	0.027	—	0.00
93	Np			– 0.077	0.023		
94	Pu			– 0.049	0.039		

SIE correction	**– 0.04 mK**
u^2 (Σ contributions)	**113 979.14 μK^2**
u (ΔT_{SIE})	**± 0.34 mK**

Table 19: Calculation of SIE correction and uncertainty for Al metal sample from Sumitomo based on the chemical analysis supplied by NRC.

Atomic No	Element symbol	c_{l1}^{i}	$u(c_{l1}^{i})$	m_l^i	$u(m_l^i)$	Individual Correction	Uncertainty Contribution
		ng/g	ng/g	µK/ppbw	µK/ppbw	µK	μK^2
1	H			– 17.873	0.106		
2	He			– 4.527	0.001		
3	Li	71.75	71.75	– 1.319	1.030	– 94.61	14 416.68
4	Be	1.75	1.75	– 1.832	0.111	– 3.21	10.32
5	B	125.80	125.80	– 1.858	0.774	– 233.79	64 127.50
6	C			– 1.131	0.870		
7	N			– 1.276	0.020		
8	O			– 0.396	0.119		
9	F	374.45	374.45	0.000	0.000	0.00	0.00
10	Ne			– 0.898	0.000		
11	Na	118.98	118.98	– 0.724	0.150	– 86.08	7729.84
12	Mg	2.43	2.43	– 0.450	0.116	– 1.09	1.27
13	Al	Matrix	Matrix	Matrix	Matrix	Matrix	Matrix
14	Si	735.05	735.05	– 0.623	0.093	– 457.81	214314.12
15	P	11.65	11.65	– 0.834	0.576	– 9.72	139.47
16	S			– 0.511	0.131		
17	Cl	1 204.83	1 204.83	0.000	0.000	0.00	0.00
18	Ar			– 0.453	0.000		
19	K	21.10	21.10	– 0.277	0.263	– 5.84	64.82
20	Ca	20.90	20.90	– 0.470	0.088	– 9.81	99.75
21	Sc	34.45	34.45	– 0.223	0.517	– 7.69	376.87
22	Ti	19.65	19.65	4.607	1.895	90.54	9 583.19
23	V	58.93	58.93	3.321	1.789	195.69	49 411.73
24	Cr	32.45	32.45	1.051	0.634	34.11	1 586.94
25	Mn	10.25	10.25	0.115	0.264	1.18	8.73
26	Fe	98.70	98.70	– 0.311	0.024	– 30.69	947.53
27	Co	0.38	0.38	– 0.297	0.016	– 0.11	0.01
28	Ni	8.03	8.03	– 0.309	0.056	– 2.48	6.33
29	Cu	516.87	516.87	– 0.252	0.095	– 130.02	19 329.71
30	Zn	141.53	141.53	– 0.037	0.156	– 5.21	515.43
31	Ga	12.20	12.20	– 0.150	0.083	– 1.83	4.38
32	Ge	467.50	467.50	– 0.208	0.033	– 97.15	9 677.78
33	As	137.00	137.00	– 0.235	0.014	– 32.21	1 041.21
34	Se	25 090.53	25 090.53	– 0.288	0.134	– 7232.18	6.36×10^7
35	Br	193.90	193.90	– 0.227	0.068	– 43.96	2 106.34
36	Kr			– 0.216	0.065		
37	Rb	1.73	1.73	– 0.160	0.069	– 0.28	0.09
38	Sr	3.48	3.48	– 0.196	0.014	– 0.68	0.47
39	Y	0.58	0.58	– 0.192	0.011	– 0.11	0.01
40	Zr	3.83	3.83	1.233	1.016	4.72	37.35
41	Nb	0.93	0.93	5.478	1.697	5.07	28.14
42	Mo	32.13	32.13	1.155	0.901	37.10	2 215.13
43	Tc			0.045	0.317		
44	Ru	7.83	7.83	– 0.143	0.044	– 1.12	1.37
45	Rh	0.95	0.95	0.068	0.437	0.06	0.18
46	Pd	103.48	103.48	– 0.057	0.194	– 5.86	438.57
47	Ag	891.08	891.08	0.010	0.184	9.13	26 853.96
48	Cd	55.80	55.80	– 0.112	0.038	– 6.26	43.58
49	In	< 1	0.50	– 0.157	0.024	—	0.01
50	Sn	1.83	1.83	– 0.142	0.003	– 0.26	0.07
51	Sb	14.83	14.83	– 0.081	0.072	– 1.20	2.58
52	Te	7.30	7.30	– 0.116	0.050	– 0.85	0.85
53	I	1.05	1.05	0.000	0.000	0.00	0.00
54	Xe			– 0.137	0.002		
55	Cs	0.38	0.38	– 0.104	0.041	– 0.04	0.00

Atomic No	Element symbol	c_{l1}^{i}	$u(c_{l1}^{i})$	m_l^i	$u(m_l^i)$	Individual Correction	Uncertainty Contribution
		ng/g	ng/g	µK/ppbw	µK/ppbw	µK	μK^2
56	Ba	6.90	6.90	– 0.079	0.071	– 0.54	0.54
57	La	0.68	0.68	– 0.121	0.018	– 0.08	0.01
58	Ce	0.60	0.60	– 0.128	0.002	– 0.08	0.01
59	Pr	1.10	1.10	– 0.127	0.002	– 0.14	0.02
60	Nd	3.58	3.58	– 0.125	0.002	– 0.45	0.20
61	Pm			0.000	0.000		
62	Sm	3.78	3.78	– 0.110	0.017	– 0.42	0.18
63	Eu	0.43	0.43	– 0.119	0.036	– 0.05	0.00
64	Gd	4.80	4.80	– 0.115	0.003	– 0.55	0.30
65	Tb	0.85	0.85	– 0.107	0.010	– 0.09	0.01
66	Dy	2.85	2.85	– 0.101	0.017	– 0.29	0.09
67	Ho	0.28	0.28	– 0.099	0.017	– 0.03	0.00
68	Er	1.15	1.15	– 0.098	0.017	– 0.11	0.01
69	Tm	1.05	1.05	– 0.104	0.004	– 0.11	0.01
70	Yb	1.28	1.28	– 0.046	0.054	– 0.06	0.01
71	Lu	0.25	0.25	– 0.104	0.031	– 0.03	0.00
72	Hf	< 1	0.50	2.391	2.522	—	3.02
73	Ta	0.43	0.43	5.443	1.253	2.31	5.63
74	W	2.13	2.13	0.488	0.873	1.04	4.52
75	Re	0.90	0.90	0.095	0.131	0.09	0.02
76	Os	< 1	0.50	0.400	0.657	—	0.15
77	Ir	1.20	1.20	0.376	0.622	0.45	0.76
78	Pt	7.48	7.48	0.017	0.190	0.13	2.04
79	Au	0.83	0.83	– 0.010	0.074	– 0.01	0.00
80	Hg	5.08	5.08	– 0.030	0.059	– 0.15	0.11
81	Tl	4.83	4.83	– 0.059	0.028	– 0.28	0.10
82	Pb	173.85	173.85	– 0.052	0.056	– 9.09	175.79
83	Bi	2.08	2.08	– 0.039	0.013	– 0.08	0.01
84	Po			0.000	0.000		
85	At			0.000	0.000		
86	Rn			– 0.081	0.000		
87	Fr			0.000	0.000		
88	Ra			0.000	0.000		
89	Ac			0.000	0.000		
90	Th	1.90	1.90	– 0.052	0.034	– 0.10	0.01
91	Pa			– 0.079	0.024		
92	U	0.73	0.73	– 0.060	0.027	– 0.04	0.00
93	Np			– 0.077	0.023		
94	Pu			– 0.049	0.039		

SIE correction	**8.13 mK**
u^2 (Σ contributions)	**6.40 x 10^7 μK^2**
u (ΔT_{SIE})	**± 8.00 mK**

Table 20: Calculation of SIE correction and uncertainty for Al metal sample from Sumitomo based on the chemical analysis supplied by NIM.

Metal sample	GDMS supplier	SIE correction mK	SIE uncertainty mK
Alfa Aesar	Metal supplier	– 0.13	0.25
	AQura	– 2.19	1.27
	NRC	– 2.43	3.28
	NIM	33.37	35.97
ESPI Metals	Metal supplier	0.56	0.57
	AQura	0.70	0.21
	NRC	0.08	0.79
	NIM	3.93	4.29
Honeywell	Metal supplier	2.97	2.60
	AQura	0.20	0.15
	NRC	0.08	0.50
	NIM	6.08	6.12
New Metals	Metal supplier	– 0.23	0.45
	AQura	0.13	0.10
	NRC	– 0.26	0.35
	NIM	10.33	10.71
Sumitomo	Metal supplier	– 0.11	0.31
	AQura	0.34	0.23
	NRC	– 0.04	0.34
	NIM	8.13	8.00

Table 21: Summary of SIE results.

In these tables, the concentrations of impurities were expressed as given by the assays (possibly an indicative of the resolution of the detection limits for each element). Figures greater than 10^6 were expressed in scientific notation. Concentrations preceded by a < sign denotes the detection limit of the analyser for that element since it was scanned for but not detected in the sample. Whenever the detection limit was given instead of a measured value, the corresponding correction was null but half of the detection limit was accounted in the uncertainty calculation for that element. Again, it is relevant to highlight that the NIM figures do not correspond to the resolution of the analyser (0.01 ppb) and needed to be truncated.

The calculations based on the assay provided by Honeywell followed the criteria specified in [11], which states that when the concentration of key elements are not identified in the sample, half the detection limit should be used to calculate the estimates. This was applied only for impurities that are more commonly detected in pure aluminium sample [40]. Since the technique employed in the analysis did not have enough resolution, it could not detect any trace elements in the high purity

sample. Once the application of this rule was made, it returned an excessive result (2.97 mK) when compared to the estimates based on the assays supplied by AQura and NRC.

Apart from the results based on NIM data and a few differences, it was possible to observe some consistency among the SIE corrections. The correction based on the assay provided by Alfa Aesar was much lower than the results based on the AQura and NRC analyses because comparatively the GDMS assay provided by the metal supplier presented a total impurity concentration equivalent to 0.4 ppm (while according to the assay from AQura the sample presented approximately 2.4 ppm of total impurity concentration and according to NRC, about 4 ppm). Besides this, impurities such as Si and Ti (dominant in the samples) were detected in much lower concentrations in the analysis provided by Alfa Aesar (table 11).

The unexpected peaks detected in the NIM analyses caused the largest discrepancies across the results. Even though they presented high levels of individual impurity concentrations in general (several of them in ppm levels), it was the presence of unrealistically high selenium peaks that caused those large differences. For illustrative purposes only, if the peaks of Selenium found in all analyses made by NIM were to be excluded from the estimates, the corresponding SIE results would be:

- Alfa Aesar (0.87 mK ± 2.99 mK)
- ESPI (0.09 mK ± 0.73 mK)
- Honeywell (0.58 mK ± 0.90 mK)
- New Metals (0.63 mK ± 0.50 mK)
- Sumitomo (0.90 mK ± 0.65 mK).

In order to be more conservative, the estimates will be kept as initially calculated, without filtering the elements that should be accounted for.

6.2. Overall Maximum Estimate (OME) uncertainty calculation

The calculations of the Overall Maximum Estimate were performed through the application of equation 20, in chapter 2. However, the overall impurity concentration (c_l) used in this equation has to be included as the mole fraction sum of impurities. In order to achieve this, each individual impurity concentration detected by the chemical analyses was transformed from mass fractions (ng/g) into mole fractions using equation 27:

$$n_i = \frac{m_i}{M_i} \tag{27}$$

where n_i is the amount of substance (number of atoms) of impurity i, obtained by the quotient of the mass of impurity i (m_i) by the atomic weight of impurity i (M_i). Similarly, the number of atoms of aluminium was also calculated using equation 27 above. However, in order to differentiate it from the impurities, the subscript index i is replaced by Al since it refers to the matrix element (solvent). The mass of aluminium, m_{Al} , was determined by equation 28

$$m_{Al} = 1 - \sum_i m_i \tag{28}$$

Finally, the overall impurity concentration c_l was obtained through equation 29

$$c_l = \frac{\sum_i n_i}{\left(\frac{m_{Al}}{M_{Al}} + \sum_i n_i\right)} \tag{29}$$

Although not the conversion method used in this study, the impurity concentrations can be equivalently converted from ppm weight to ppm atomic through equation 30, with just a negligible error (equivalent to a few microkelvins)

$$ppm_{atomic} = ppm_{weight} * \frac{atomic\ weight\ of\ aluminium}{atomic\ weight\ of\ impurity} \tag{30}$$

The value for the first cryoscopic constant for aluminium is given in table 9. The uncertainties for the OME calculations were obtained through the application of equation 21. For the OME methodology, the uncertainty of the individual impurity

concentrations are not relevant when assigning the uncertainty of the estimates since the OME is a calculation of a maximum limit, that is there is no correction assigned to the temperature of the cell but the value should instead be treated as an uncertainty. The temperature of the cell is considered to be the one assigned to the fixed point, as per the definition of the ITS-90 and the OME provides an upper limit uncertainty to the defined value due to the trace impurities present in the metal sample.

In order to illustrate the calculations, the corrections and uncertainties performed according to the OME methodology for the cell Al-S (Sumitomo) are given in tables 22 – 25. The values of the atomic weights M_i used in this study were defined by the International Union of Pure and Applied Chemistry (IUPAC) [50, 51]. Some elements could not have their atomic weight assigned because they had no stable isotopes; presented wide variability in isotopic composition or were completely absent in nature [51]. In these cases (10 elements in total), the mass number of the longest-lived isotope of these elements was given instead, in square parenthesis []. Nevertheless, since none of them was scanned for in any of the chemical analyses, this substitution caused no loss to the calculated estimates.

Similarly as it was applied to the SIE methodology, the OME calculations were performed in accordance with the criteria specified in [11] and [40]: elements which are considered common impurities in samples of high purity aluminium, when scanned for but not detected in the analyses, had half of their respective detection limits accounted for in the estimates.

For comparison reasons, the uncertainties calculated via equation 21 were not added to the bounds calculated (OME estimates). A summary of the OME results for all five cells is shown in table 26.

Atomic No	Element symbol	c_l^i ng/g	Atomic weight g/mol	Mole fraction
1	H		1.008	
2	He		4.003	
3	Li	< 1	6.938	7.20×10^{-11}
4	Be	< 1	9.012	5.55×10^{-11}
5	B	< 10	10.806	4.62×10^{-10}
6	C		12.011	
7	N		14.007	
8	O		15.999	
9	F		18.998	
10	Ne		20.180	
11	Na	4	22.990	1.74×10^{-10}
12	Mg	45	24.306	1.85×10^{-09}
13	Al	Matrix	26.982	Matrix
14	Si	270	28.085	9.61×10^{-09}
15	P		30.974	
16	S		32.068	
17	Cl		35.452	
18	Ar		39.948	
19	K	< 100	39.098	1.28×10^{-09}
20	Ca	< 50	40.078	6.24×10^{-10}
21	Sc		44.956	
22	Ti	10	47.867	2.09×10^{-10}
23	V	65	50.942	1.28×10^{-09}
24	Cr	15	51.996	2.88×10^{-10}
25	Mn	3	54.938	5.46×10^{-11}
26	Fe	55	55.845	9.85×10^{-10}
27	Co	< 1	58.933	8.48×10^{-12}
28	Ni	10	58.693	1.70×10^{-10}
29	Cu	57	63.546	8.97×10^{-10}
30	Zn	< 2	65.380	1.53×10^{-11}
31	Ga	< 1	69.723	7.17×10^{-12}
32	Ge	< 50	72.630	—
33	As	< 5	74.922	3.34×10^{-11}
34	Se	< 30	78.971	1.90×10^{-11}
35	Br	< 50	79.901	—
36	Kr		83.798	
37	Rb		85.468	
38	Sr		87.620	
39	Y		88.906	
40	Zr	7	91.224	7.67×10^{-11}
41	Nb	3	92.906	3.23×10^{-11}
42	Mo	24	95.950	2.50×10^{-10}
43	Tc		[98]	
44	Ru		101.070	
45	Rh		102.906	
46	Pd		106.420	
47	Ag	< 1	107.868	4.64×10^{-12}
48	Cd	< 10	112.414	4.45×10^{-11}
49	In	< 1	114.818	4.35×10^{-12}
50	Sn	< 20	118.710	8.42×10^{-11}
51	Sb	< 5	121.760	2.05×10^{-11}
52	Te		127.600	
53	I		126.904	
54	Xe		131.293	
55	Cs	< 1	132.905	3.76×10^{-12}

Atomic No	Element symbol	c_l^i ng/g	Atomic weight g/mol	Mole fraction
56	Ba	< 1	137.327	—
57	La	< 1	138.905	3.60×10^{-12}
58	Ce	< 1	140.116	3.57×10^{-12}
59	Pr		140.908	
60	Nd	< 3	144.242	—
61	Pm		[145]	
62	Sm		150.360	
63	Eu		151.964	
64	Gd		157.250	
65	Tb		158.925	
66	Dy		162.500	
67	Ho		164.930	
68	Er		167.259	
69	Tm		168.934	
70	Yb		173.054	
71	Lu		174.967	
72	Hf	< 1	178.490	—
73	Ta		180.948	
74	W	< 1	183.840	2.72×10^{-12}
75	Re		186.207	
76	Os		190.230	
77	Ir		192.217	
78	Pt	< 2	195.084	—
79	Au		196.967	
80	Hg	< 10	200.592	2.49×10^{-11}
81	Tl	< 1	204.384	—
82	Pb	< 1	207.200	2.41×10^{-12}
83	Bi	< 1	208.980	2.39×10^{-12}
84	Po		[210]	
85	At		[210]	
86	Rn		[222]	
87	Fr		[223]	
88	Ra		[226]	
89	Ac		[227]	
90	Th	< 0.3	232.038	6.46×10^{-13}
91	Pa		231.036	
92	U	< 0.3	238.029	6.30×10^{-13}
93	Np		[237]	
94	Pu		[244]	

Total atoms of impurities	**1.87×10^{-08} mol**
Atoms of aluminium	**3.71×10^{-02} mol**
Mole fraction sum of impurities	**5.03×10^{-07}**
1st cryoscopic constant for Al	**0.001489 K^{-1}**
OME	**0.34 mK**
$u(\Delta T_{OME})$	**± 0.20 mK**

Table 22: Calculation of OME estimate and uncertainty for Al metal sample from Sumitomo based on the assay provided by the metal supplier.

Atomic No	Element symbol	c_l^i ng/g	Atomic weight g/mol	Mole fraction
1	H		1.008	
2	He		4.003	
3	Li	< 1	6.938	7.20×10^{-11}
4	Be	7	9.012	7.77×10^{-10}
5	B	60	10.806	5.55×10^{-09}
6	C		12.011	
7	N		14.007	
8	O		15.999	
9	F		18.998	
10	Ne		20.180	
11	Na	30	22.990	1.30×10^{-09}
12	Mg	50	24.306	2.06×10^{-09}
13	Al	Matrix	26.982	Matrix
14	Si	400	28.085	1.42×10^{-08}
15	P	30	30.974	9.69×10^{-10}
16	S	100	32.068	3.12×10^{-09}
17	Cl		35.452	
18	Ar		39.948	
19	K	20	39.098	5.12×10^{-10}
20	Ca	90	40.078	2.25×10^{-09}
21	Sc	40	44.956	8.90×10^{-10}
22	Ti	40	47.867	8.36×10^{-10}
23	V	40	50.942	7.85×10^{-10}
24	Cr	40	51.996	7.69×10^{-10}
25	Mn	10	54.938	1.82×10^{-10}
26	Fe	200	55.845	3.58×10^{-09}
27	Co	2	58.933	3.39×10^{-11}
28	Ni	20	58.693	3.41×10^{-10}
29	Cu	400	63.546	6.29×10^{-09}
30	Zn	20	65.380	3.06×10^{-10}
31	Ga	10	69.723	1.43×10^{-10}
32	Ge	< 30	72.630	—
33	As	50	74.922	6.67×10^{-10}
34	Se	70	78.971	8.87×10^{-10}
35	Br	< 30	79.901	—
36	Kr		83.798	
37	Rb	2	85.468	2.34×10^{-11}
38	Sr	< 1	87.620	5.71×10^{-12}
39	Y	< 0.8	88.906	—
40	Zr	5	91.224	5.48×10^{-11}
41	Nb	0.7	92.906	7.53×10^{-12}
42	Mo	40	95.950	4.17×10^{-10}
43	Tc		[98]	
44	Ru	0.7	101.070	6.93×10^{-12}
45	Rh	2	102.906	1.94×10^{-11}
46	Pd	< 10	106.420	—
47	Ag	10	107.868	9.27×10^{-11}
48	Cd	50	112.414	4.45×10^{-10}
49	In	8	114.818	6.97×10^{-11}
50	Sn	300	118.710	2.53×10^{-09}
51	Sb	< 10	121.760	4.11×10^{-11}
52	Te	10	127.600	7.84×10^{-11}
53	I	< 2	126.904	—
54	Xe		131.293	
55	Cs	< 2	132.905	7.52×10^{-12}

Atomic No	Element symbol	c_l^i ng/g	Atomic weight g/mol	Mole fraction
56	Ba	1	137.327	7.28×10^{-12}
57	La	< 1	138.905	3.60×10^{-12}
58	Ce	< 1	140.116	3.57×10^{-12}
59	Pr	< 1	140.908	—
60	Nd	< 6	144.242	—
61	Pm		[145]	
62	Sm	< 4	150.360	—
63	Eu	< 2	151.964	—
64	Gd	< 5	157.250	—
65	Tb	< 1	158.925	—
66	Dy	< 5	162.500	—
67	Ho	< 1	164.930	—
68	Er	< 4	167.259	—
69	Tm	< 1	168.934	—
70	Yb	< 4	173.054	—
71	Lu	< 1	174.967	—
72	Hf	7	178.490	3.92×10^{-11}
73	Ta		180.948	
74	W	70	183.840	3.81×10^{-10}
75	Re	< 2	186.207	—
76	Os	< 20	190.230	—
77	Ir	< 4	192.217	—
78	Pt	< 10	195.084	—
79	Au	5	196.967	2.54×10^{-11}
80	Hg	< 20	200.592	4.99×10^{-11}
81	Tl	< 9	204.384	—
82	Pb	5	207.200	2.41×10^{-11}
83	Bi	30	208.980	1.44×10^{-10}
84	Po		[210]	
85	At		[210]	
86	Rn		[222]	
87	Fr		[223]	
88	Ra		[226]	
89	Ac		[227]	
90	Th	< 0.1	232.038	2.15×10^{-13}
91	Pa		231.036	
92	U	0.1	238.029	4.20×10^{-13}
93	Np		[237]	
94	Pu		[244]	

Total atoms of impurities	**5.10×10^{-08} mol**
Atoms of aluminium	**3.71×10^{-02} mol**
Mole fraction sum of impurities	**1.38×10^{-06}**
1st cryoscopic constant for Al	**0.001489 K^{-1}**
OME	**0.92 mK**
$u(\Delta T_{OME})$	**± 0.53 mK**

Table 23: Calculation of OME estimate and uncertainty for Al metal sample from Sumitomo based on the assay provided by AQura.

Atomic No	Element symbol	c_l^i ng/g	Atomic weight g/mol	Mole fraction
1	H		1.008	
2	He		4.003	
3	Li	< 2	6.938	1.44×10^{-10}
4	Be	< 0.8	9.012	4.44×10^{-11}
5	B	< 1	10.806	4.62×10^{-11}
6	C		12.011	
7	N		14.007	
8	O		15.999	
9	F	< 3	18.998	—
10	Ne		20.180	
11	Na	< 1	22.990	2.17×10^{-11}
12	Mg	76	24.306	3.13×10^{-09}
13	Al	Matrix	26.982	Matrix
14	Si	330	28.085	1.17×10^{-08}
15	P	12	30.974	3.87×10^{-10}
16	S	< 3	32.068	4.68×10^{-11}
17	Cl	9	35.452	2.54×10^{-10}
18	Ar		39.948	
19	K	< 4	39.098	5.12×10^{-11}
20	Ca	< 16	40.078	2.00×10^{-10}
21	Sc	57	44.956	1.27×10^{-09}
22	Ti	10	47.867	2.09×10^{-10}
23	V	61	50.942	1.20×10^{-09}
24	Cr	15	51.996	2.88×10^{-10}
25	Mn	4	54.938	7.28×10^{-11}
26	Fe	70	55.845	1.25×10^{-09}
27	Co	< 0.5	58.933	4.24×10^{-12}
28	Ni	9	58.693	1.53×10^{-10}
29	Cu	18	63.546	2.83×10^{-10}
30	Zn	27	65.380	4.13×10^{-10}
31	Ga	< 4	69.723	2.87×10^{-11}
32	Ge	< 7	72.630	—
33	As	< 4	74.922	2.67×10^{-11}
34	Se	< 60	78.971	3.80×10^{-10}
35	Br	< 10	79.901	—
36	Kr		83.798	
37	Rb	< 1	85.468	—
38	Sr	< 0.6	87.620	3.42×10^{-12}
39	Y	< 0.7	88.906	—
40	Zr	62	91.224	6.80×10^{-10}
41	Nb	2	92.906	2.15×10^{-11}
42	Mo	< 2	95.950	—
43	Tc		[98]	
44	Ru		101.070	
45	Rh		102.906	
46	Pd		106.420	
47	Ag	< 6	107.868	2.78×10^{-11}
48	Cd	89	112.414	7.92×10^{-10}
49	In	74	114.818	6.44×10^{-10}
50	Sn	< 32	118.710	1.35×10^{-10}
51	Sb	< 9	121.760	3.70×10^{-11}
52	Te	22	127.600	1.72×10^{-10}
53	I	< 2	126.904	—
54	Xe		131.293	
55	Cs	< 0.6	132.905	2.26×10^{-12}

Atomic No	Element symbol	c_l^i ng/g	Atomic weight g/mol	Mole fraction
56	Ba	< 0.7	137.327	—
57	La	< 0.6	138.905	2.16×10^{-12}
58	Ce	< 0.6	140.116	2.14×10^{-12}
59	Pr		140.908	
60	Nd		144.242	
61	Pm		[145]	
62	Sm		150.360	
63	Eu		151.964	
64	Gd		157.250	
65	Tb		158.925	
66	Dy		162.500	
67	Ho		164.930	
68	Er		167.259	
69	Tm		168.934	
70	Yb		173.054	
71	Lu		174.967	
72	Hf	< 3	178.490	—
73	Ta		180.948	
74	W	< 2	183.840	5.44×10^{-12}
75	Re		186.207	
76	Os		190.230	
77	Ir		192.217	
78	Pt	< 8	195.084	—
79	Au	< 1 100	196.967	2.79×10^{-09}
80	Hg	< 24	200.592	5.98×10^{-11}
81	Tl	< 6	204.384	—
82	Pb	8	207.200	3.86×10^{-11}
83	Bi	< 3	208.980	7.18×10^{-12}
84	Po		[210]	
85	At		[210]	
86	Rn		[222]	
87	Fr		[223]	
88	Ra		[226]	
89	Ac		[227]	
90	Th	< 0.6	232.038	1.29×10^{-12}
91	Pa		231.036	
92	U	< 0.8	238.029	1.68×10^{-12}
93	Np		[237]	
94	Pu		[244]	

Total atoms of impurities	**2.71×10^{-08} mol**
Atoms of aluminium	**3.71×10^{-02} mol**
Mole fraction sum of impurities	**7.31×10^{-07}**
1st cryoscopic constant for Al	**0.001489 K^{-1}**
OME	**0.49 mK**
$u(\Delta T_{OME})$	**± 0.28 mK**

Table 24: Calculation of OME estimate and uncertainty for Al metal sample from Sumitomo based on the assay provided by NRC.

Atomic No	Element symbol	c_l^i ng/g	Atomic weight g/mol	Mole fraction
1	H		1.008	
2	He		4.003	
3	Li	71.75	6.938	1.03×10^{-08}
4	Be	1.75	9.012	1.94×10^{-10}
5	B	125.80	10.806	1.16×10^{-08}
6	C		12.011	
7	N		14.007	
8	O		15.999	
9	F	374.45	18.998	1.97×10^{-08}
10	Ne		20.180	
11	Na	118.98	22.990	5.18×10^{-09}
12	Mg	2.43	24.306	9.98×10^{-11}
13	Al	Matrix	26.982	Matrix
14	Si	735.05	28.085	2.62×10^{-08}
15	P	11.65	30.974	3.76×10^{-10}
16	S		32.068	
17	Cl	1 204.83	35.452	3.40×10^{-08}
18	Ar		39.948	
19	K	21.10	39.098	5.40×10^{-10}
20	Ca	20.90	40.078	5.21×10^{-10}
21	Sc	34.45	44.956	7.66×10^{-10}
22	Ti	19.65	47.867	4.11×10^{-10}
23	V	58.93	50.942	1.16×10^{-09}
24	Cr	32.45	51.996	6.24×10^{-10}
25	Mn	10.25	54.938	1.87×10^{-10}
26	Fe	98.70	55.845	1.77×10^{-09}
27	Co	0.38	58.933	6.36×10^{-12}
28	Ni	8.03	58.693	1.37×10^{-10}
29	Cu	516.87	63.546	8.13×10^{-09}
30	Zn	141.53	65.380	2.16×10^{-09}
31	Ga	12.20	69.723	1.75×10^{-10}
32	Ge	467.50	72.630	6.44×10^{-09}
33	As	137.00	74.922	1.83×10^{-09}
34	Se	25 090.53	78.971	3.18×10^{-07}
35	Br	193.90	79.901	2.43×10^{-09}
36	Kr		83.798	
37	Rb	1.73	85.468	2.02×10^{-11}
38	Sr	3.48	87.620	3.97×10^{-11}
39	Y	0.58	88.906	6.47×10^{-12}
40	Zr	3.83	91.224	4.19×10^{-11}
41	Nb	0.93	92.906	9.96×10^{-12}
42	Mo	32.13	95.950	3.35×10^{-10}
43	Tc		[98]	
44	Ru	7.83	101.070	7.74×10^{-11}
45	Rh	0.95	102.906	9.23×10^{-12}
46	Pd	103.48	106.420	9.72×10^{-10}
47	Ag	891.08	107.868	8.26×10^{-09}
48	Cd	55.80	112.414	4.96×10^{-10}
49	In	< 1	114.818	4.35×10^{-14}
50	Sn	1.83	118.710	1.54×10^{-11}
51	Sb	14.83	121.760	1.22×10^{-10}
52	Te	7.30	127.600	5.72×10^{-11}
53	I	1.05	126.904	8.27×10^{-12}
54	Xe		131.293	
55	Cs	0.38	132.905	2.82×10^{-12}

Atomic No	Element symbol	c_l^i ng/g	Atomic weight g/mol	Mole fraction
56	Ba	6.90	137.327	5.02×10^{-11}
57	La	0.68	138.905	4.86×10^{-12}
58	Ce	0.60	140.116	4.28×10^{-12}
59	Pr	1.10	140.908	7.81×10^{-12}
60	Nd	3.58	144.242	2.48×10^{-11}
61	Pm		[145]	
62	Sm	3.78	150.360	2.51×10^{-11}
63	Eu	0.43	151.964	2.80×10^{-12}
64	Gd	4.80	157.250	3.05×10^{-11}
65	Tb	0.85	158.925	5.35×10^{-12}
66	Dy	2.85	162.500	1.75×10^{-11}
67	Ho	0.28	164.930	1.67×10^{-12}
68	Er	1.15	167.259	6.88×10^{-12}
69	Tm	1.05	168.934	6.22×10^{-12}
70	Yb	1.28	173.054	7.37×10^{-12}
71	Lu	0.25	174.967	1.43×10^{-12}
72	Hf	< 1	178.490	—
73	Ta	0.43	180.948	2.35×10^{-12}
74	W	2.13	183.840	1.16×10^{-11}
75	Re	0.90	186.207	4.83×10^{-12}
76	Os	< 1	190.230	—
77	Ir	1.20	192.217	6.24×10^{-12}
78	Pt	7.48	195.084	3.83×10^{-11}
79	Au	0.83	196.967	4.19×10^{-12}
80	Hg	5.08	200.592	2.53×10^{-11}
81	Tl	4.83	204.384	2.36×10^{-11}
82	Pb	173.85	207.200	8.39×10^{-10}
83	Bi	2.08	208.980	9.93×10^{-12}
84	Po		[210]	
85	At		[210]	
86	Rn		[222]	
87	Fr		[223]	
88	Ra		[226]	
89	Ac		[227]	
90	Th	1.90	232.038	8.19×10^{-12}
91	Pa		231.036	
92	U	0.73	238.029	3.05×10^{-12}
93	Np		[237]	
94	Pu		[244]	

Total atoms of impurities	**4.64×10^{-07} mol**
Atoms of aluminium	**3.71×10^{-02} mol**
Mole fraction sum of impurities	**1.25×10^{-05}**
1st cryoscopic constant for Al	**0.001489 K^{-1}**
OME	**8.42 mK**
$u(\Delta T_{OME})$	**± 4.86 mK**

Table 25: Calculation of OME estimate and uncertainty for Al metal sample from Sumitomo based on the assay provided by NIM.

Metal sample	GDMS supplier	OME estimate mK	OME uncertainty mK
Alfa Aesar	Metal supplier	0.44	0.26
	AQura	1.09	0.63
	NRC	1.64	0.94
	NIM	32.92	19.01
ESPI Metals	Metal supplier	0.58	0.34
	AQura	1.31	0.76
	NRC	1.11	0.64
	NIM	4.46	2.58
Honeywell	Metal supplier	6.54	3.78
	AQura	0.72	0.42
	NRC	0.88	0.51
	NIM	6.82	3.94
New Metals	Metal supplier	0.32	0.18
	AQura	0.47	0.27
	NRC	0.45	0.26
	NIM	9.54	5.51
Sumitomo	Metal supplier	0.34	0.20
	AQura	0.92	0.53
	NRC	0.49	0.28
	NIM	8.42	4.86

Table 26: Summary of OME results.

Concentrations preceded by a < sign correspond to the detection limit of the analyser for that element. As directed by [11], for the OME calculations, undetected elements had half of their detection limit used for the estimates if those elements were regarded as a common impurity according to [40]. Were it not for this rule, it would not be possible to calculate the OME estimate for the Honeywell sample based on the assay provided by its supplier. However, due to the high detection limits, it returned an excessively high value when compared to the estimates based on the assays supplied by AQura and NRC.

Apart from this, the OME estimates give good agreement, the only exceptions being the calculations based upon the NIM analyses, which caused some discrepancies across the results. Even though the NIM results presented high levels of individual impurity concentrations in general (several of them in ppm levels), it was the presence of unrealistically high selenium peaks that caused the large differences in the estimates. For illustrative purposes only, if the peaks of Selenium found in all analyses

made by NIM were to be excluded from the estimates, the corresponding OME results would be:

- Alfa Aesar (7.04 mK ± 4.07 mK)
- ESPI (1.41 mK ± 0.81 mK)
- Honeywell (2.45 mK ± 1.42 mK)
- New Metals (1.82 mK ± 1.05 mK)
- Sumitomo (2.66 mK ± 1.53 mK).

In order to be more conservative, the estimates will be kept as initially calculated, without filtering the elements that should be accounted for.

6.3. Hybrid SIE / Modified OME correction and uncertainty calculation

The estimates for the Hybrid SIE/Modified OME methodology were obtained through the combination of both the SIE method (equation 18) applied to impurities with $k > 0.1$ and the OME method (via least-squares fit of equation 23) applied to the measured freezing curves over a narrow range (F_s 0.05 to F_s 0.20) to account for the remainder of the impurities ($k < 0.1$). The exception for this OME fitting range occurs when a substantial amount of high k impurities is present in the material, since it would be sensible to shift the range to a later part of the freezing plateau (an example is described in page 183). The impurities with $k > 0.1$ were identified through the application of equation 17 to the values of the liquidus slopes contained in table 4. According to the results obtained, a total of 43 impurities were accounted in the hybrid SIE component: Li, Be, C, O, Mg, K, Sc, Ti, V, Cr, Mn, Fe, Ni, Cu, Zn, Ga, Rb, Zr, Nb, Mo, Tc, Rh, Pd, Ag, Cd, In, Sb, Cs, Ba, Yb, Hf, Ta, W, Re, Os, Ir, Pt, Au, Hg, Tl, Pb, U and Pu.

As before, in order to illustrate the calculations, tables 27 – 30 show the corrections and uncertainties accounted for as the hybrid SIE component for the Sumitomo aluminium cell (Al-S). In these tables, the rows corresponding to the elements with $k > 0.1$ were shaded in light grey to identify these elements and to give them prominence since the hybrid component is only applied to this type of impurities. These calculations obeyed the same criteria as the SIE methodology discussed in 6.1 (especially the one concerning the inclusion of undetected common impurities in the uncertainty calculations).

Graphs featuring the fittings performed to implement the modified OME component are shown in figures 47 – 50. The results represent the estimated temperature difference caused by the impurities present in the fixed-point material. The correction calculated for the OME component (i.e. the additive inverse of the estimated temperature difference) is given in table 31, where a summary of the estimates for both components and the results obtained for this hybrid methodology for cell Al-S are presented.

Atomic No	Element symbol	c_{l1}^{i}	$u(c_{l1}^{i})$	m_l^i	$u(m_l^i)$	Individual Correction	Uncertainty Contribution
		ng/g	ng/g	µK/ppbw	µK/ppbw	µK	μK^2
1	H			– 17.873	0.106		
2	He			– 4.527	0.001		
3	Li	< 1	0.50	– 1.319	1.030	—	0.70
4	Be	< 1	0.50	– 1.832	0.111	—	0.84
5	B	< 10		– 1.858	0.774		
6	C			– 1.131	0.870		
7	N			– 1.276	0.020		
8	O			– 0.396	0.119		
9	F			0.000	0.000		
10	Ne			– 0.898	0.000		
11	Na	4		– 0.724	0.150		
12	Mg	45	45.00	– 0.450	0.116	– 20.23	436.45
13	Al	Matrix	Matrix	Matrix	Matrix	Matrix	Matrix
14	Si	270		– 0.623	0.093		
15	P			– 0.834	0.576		
16	S			– 0.511	0.131		
17	Cl			0.000	0.000		
18	Ar			– 0.453	0.000		
19	K	< 100	50.00	– 0.277	0.263	—	363.97
20	Ca	< 50		– 0.470	0.088		
21	Sc			– 0.223	0.517		
22	Ti	10	10.00	4.607	1.895	46.07	2 481.91
23	V	65	65.00	3.321	1.789	215.86	60 125.35
24	Cr	15	15.00	1.051	0.634	15.77	339.09
25	Mn	3	3.00	0.115	0.264	0.34	0.75
26	Fe	55	55.00	– 0.311	0.024	– 17.10	294.23
27	Co	< 1		– 0.297	0.016		
28	Ni	10	10.00	– 0.309	0.056	– 3.09	9.84
29	Cu	57	57.00	– 0.252	0.095	– 14.34	235.08
30	Zn	< 2	1.00	– 0.037	0.156	—	0.03
31	Ga	< 1	0.50	– 0.150	0.083	—	0.01
32	Ge	< 50		– 0.208	0.033		
33	As	< 5		– 0.235	0.014		
34	Se	< 30		– 0.288	0.134		
35	Br	< 50		– 0.227	0.068		
36	Kr			– 0.216	0.065		
37	Rb			– 0.160	0.069		
38	Sr			– 0.196	0.014		
39	Y			– 0.192	0.011		
40	Zr	7	7.00	1.233	1.016	8.63	125.10
41	Nb	3	3.00	5.478	1.697	16.43	295.98
42	Mo	24	24.00	1.155	0.901	27.72	1 236.33
43	Tc			0.045	0.317		
44	Ru			– 0.143	0.044		
45	Rh			0.068	0.437		
46	Pd			– 0.057	0.194		
47	Ag	< 1	0.50	0.010	0.184	—	0.01
48	Cd	< 10	5.00	– 0.112	0.038	—	0.35
49	In	< 1	0.50	– 0.157	0.024	—	0.01
50	Sn	< 20		– 0.142	0.003		
51	Sb	< 5	2.50	– 0.081	0.072	—	0.07
52	Te			– 0.116	0.050		
53	I			0.000	0.000		
54	Xe			– 0.137	0.002		
55	Cs	< 1	0.50	– 0.104	0.041	—	0.00

Atomic No	Element symbol	c_{l1}^{i}	$u(c_{l1}^{i})$	m_l^i	$u(m_l^i)$	Individual Correction	Uncertainty Contribution
		ng/g	ng/g	µK/ppbw	µK/ppbw	µK	μK^2
56	Ba	< 1	0.50	– 0.079	0.071	—	0.00
57	La	< 1		– 0.121	0.018		
58	Ce	< 1		– 0.128	0.002		
59	Pr			– 0.127	0.002		
60	Nd	< 3		– 0.125	0.002		
61	Pm			0.000	0.000		
62	Sm			– 0.110	0.017		
63	Eu			– 0.119	0.036		
64	Gd			– 0.115	0.003		
65	Tb			– 0.107	0.010		
66	Dy			– 0.101	0.017		
67	Ho			– 0.099	0.017		
68	Er			– 0.098	0.017		
69	Tm			– 0.104	0.004		
70	Yb			– 0.046	0.054		
71	Lu			– 0.104	0.031		
72	Hf	< 1	0.50	2.391	2.522	—	3.02
73	Ta			5.443	1.253		
74	W	< 1	0.50	0.488	0.873	—	0.25
75	Re			0.095	0.131		
76	Os			0.400	0.657		
77	Ir			0.376	0.622		
78	Pt	< 2	1.00	0.017	0.190	—	0.04
79	Au			– 0.010	0.074		
80	Hg	< 10	5.00	– 0.030	0.059	—	0.11
81	Tl	< 1	0.50	– 0.059	0.028	—	0.00
82	Pb	< 1	0.50	– 0.052	0.056	—	0.00
83	Bi	< 1		– 0.039	0.013		
84	Po			0.000	0.000		
85	At			0.000	0.000		
86	Rn			– 0.081	0.000		
87	Fr			0.000	0.000		
88	Ra			0.000	0.000		
89	Ac			0.000	0.000		
90	Th	< 0.3		– 0.052	0.034		
91	Pa			– 0.079	0.024		
92	U	< 0.3	0.15	– 0.060	0.027	—	0.00
93	Np			– 0.077	0.023		
94	Pu			– 0.049	0.039		

Hybrid SIE correction	**– 0.28 mK**
u^2 (Σ contributions)	**65 949.50 µK^2**
u ($\Delta T_{HYBRID\ SIE}$)	**± 0.26 mK**

Table 27: Calculation of the hybrid SIE correction and uncertainty for Al metal sample from Sumitomo based on the chemical analysis supplied by the metal supplier.

Atomic No	Element symbol	c_{l1}^{i}	$u(c_{l1}^{i})$	m_l^i	$u(m_l^i)$	Individual Correction	Uncertainty Contribution
		ng/g	ng/g	µK/ppbw	µK/ppbw	µK	μK^2
1	H			– 17.873	0.106		
2	He			– 4.527	0.001		
3	Li	< 1	0.50	– 1.319	1.030	—	0.70
4	Be	7	7.00	– 1.832	0.111	– 12.83	165.09
5	B	60		– 1.858	0.774		
6	C			– 1.131	0.870		
7	N			– 1.276	0.020		
8	O			– 0.396	0.119		
9	F			0.000	0.000		
10	Ne			– 0.898	0.000		
11	Na	30		– 0.724	0.150		
12	Mg	50	10.00	– 0.450	0.116	– 22.48	53.71
13	Al	Matrix	Matrix	Matrix	Matrix	Matrix	Matrix
14	Si	400		– 0.623	0.093		
15	P	30		– 0.834	0.576		
16	S	100		– 0.511	0.131		
17	Cl			0.000	0.000		
18	Ar			– 0.453	0.000		
19	K	20	20.00	– 0.277	0.263	– 5.53	58.24
20	Ca	90		– 0.470	0.088		
21	Sc	40	40.00	– 0.223	0.517	– 8.93	508.09
22	Ti	40	8.00	4.607	1.895	184.30	7 103.27
23	V	40	8.00	3.321	1.789	132.84	5 829.04
24	Cr	40	8.00	1.051	0.634	42.05	714.22
25	Mn	10	2.00	0.115	0.264	1.15	7.04
26	Fe	200	40.00	– 0.311	0.024	– 62.20	177.06
27	Co	2		– 0.297	0.016		
28	Ni	20	4.00	– 0.309	0.056	– 6.17	2.78
29	Cu	400	80.00	– 0.252	0.095	– 100.63	1 856.35
30	Zn	20	4.00	– 0.037	0.156	– 0.74	9.77
31	Ga	10	2.00	– 0.150	0.083	– 1.50	0.78
32	Ge	< 30		– 0.208	0.033		
33	As	50		– 0.235	0.014		
34	Se	70		– 0.288	0.134		
35	Br	< 30		– 0.227	0.068		
36	Kr			– 0.216	0.065		
37	Rb	2	8.00	– 0.160	0.069	– 0.32	1.67
38	Sr	< 1		– 0.196	0.014		
39	Y	< 0.8		– 0.192	0.011		
40	Zr	5	5.00	1.233	1.016	6.17	63.82
41	Nb	0.7	0.70	5.478	1.697	3.83	16.11
42	Mo	40	40.00	1.155	0.901	46.20	3 434.25
43	Tc			0.045	0.317		
44	Ru	0.7		– 0.143	0.044		
45	Rh	2	2.00	0.068	0.437	0.14	0.78
46	Pd	< 10	5.00	– 0.057	0.194		1.02
47	Ag	10	2.00	0.010	0.184	0.10	3.37
48	Cd	50	50.00	– 0.112	0.038	– 5.61	35.00
49	In	8	8.00	– 0.157	0.024	– 1.25	1.60
50	Sn	300		– 0.142	0.003		
51	Sb	< 10	5.00	– 0.081	0.072	—	0.29
52	Te	10		– 0.116	0.050		
53	I	< 2		0.000	0.000		
54	Xe			– 0.137	0.002		
55	Cs	< 2	4.00	– 0.104	0.041	—	0.18

Atomic No	Element symbol	c_{l1}^{i}	$u(c_{l1}^{i})$	m_l^i	$u(m_l^i)$	Individual Correction	Uncertainty Contribution
		ng/g	ng/g	µK/ppbw	µK/ppbw	µK	µK^2
56	Ba	1	1.00	– 0.079	0.071	– 0.08	0.01
57	La	< 1		– 0.121	0.018		
58	Ce	< 1		– 0.128	0.002		
59	Pr	< 1		– 0.127	0.002		
60	Nd	< 6		– 0.125	0.002		
61	Pm			0.000	0.000		
62	Sm	< 4		– 0.110	0.017		
63	Eu	< 2		– 0.119	0.036		
64	Gd	< 5		– 0.115	0.003		
65	Tb	< 1		– 0.107	0.010		
66	Dy	< 5		– 0.101	0.017		
67	Ho	< 1		– 0.099	0.017		
68	Er	< 4		– 0.098	0.017		
69	Tm	< 1		– 0.104	0.004		
70	Yb	< 4	2.00	– 0.046	0.054	—	0.02
71	Lu	< 1		– 0.104	0.031		
72	Hf	7	7.00	2.391	2.522	16.73	591.66
73	Ta			5.443	1.253		
74	W	70	70.00	0.488	0.873	34.18	4 902.94
75	Re	< 2	1.00	0.095	0.131	—	0.03
76	Os	< 20	10.00	0.400	0.657	—	59.14
77	Ir	< 4	2.00	0.376	0.622	—	2.11
78	Pt	< 10	5.00	0.017	0.190	—	0.91
79	Au	5	5.00	– 0.010	0.074	– 0.05	0.14
80	Hg	< 20	10.00	– 0.030	0.059	—	0.43
81	Tl	< 9	4.50	– 0.059	0.028	—	0.09
82	Pb	5	1.00	– 0.052	0.056	– 0.26	0.08
83	Bi	30		– 0.039	0.013		
84	Po			0.000	0.000		
85	At			0.000	0.000		
86	Rn			– 0.081	0.000		
87	Fr			0.000	0.000		
88	Ra			0.000	0.000		
89	Ac			0.000	0.000		
90	Th	< 0.1		– 0.052	0.034		
91	Pa			– 0.079	0.024		
92	U	0.1	0.40	– 0.060	0.027	– 0.01	0.00
93	Np			– 0.077	0.023		
94	Pu			– 0.049	0.039		

Hybrid SIE correction	**– 0.24 mK**
u^2 (Σ contributions)	**25 601.80 µK^2**
u ($\Delta T_{HYBRID\ SIE}$)	**± 0.16 mK**

Table 28: Calculation of the hybrid SIE correction and uncertainty for Al metal sample from Sumitomo based on the chemical analysis supplied by AQura.

Atomic No	Element symbol	c_{l1}^{i}	$u(c_{l1}^{i})$	m_l^i	$u(m_l^i)$	Individual Correction	Uncertainty Contribution
		ng/g	ng/g	µK/ppbw	µK/ppbw	µK	μK^2
1	H			– 17.873	0.106		
2	He			– 4.527	0.001		
3	Li	< 2	1.00	– 1.319	1.030	—	2.80
4	Be	< 0.8	0.40	– 1.832	0.111	—	0.54
5	B	< 1		– 1.858	0.774		
6	C			– 1.131	0.870		
7	N			– 1.276	0.020		
8	O			– 0.396	0.119		
9	F	< 3		0.000	0.000		
10	Ne			– 0.898	0.000		
11	Na	< 1		– 0.724	0.150		
12	Mg	76	76.00	– 0.450	0.116	– 34.17	1 244.89
13	Al	Matrix	Matrix	Matrix	Matrix	Matrix	Matrix
14	Si	330		– 0.623	0.093		
15	P	12		– 0.834	0.576		
16	S	< 3		– 0.511	0.131		
17	Cl	9		0.000	0.000		
18	Ar			– 0.453	0.000		
19	K	< 4	2.00	– 0.277	0.263	—	0.58
20	Ca	< 16		– 0.470	0.088		
21	Sc	57	57.00	– 0.223	0.517	– 12.72	1 031.73
22	Ti	10	10.00	4.607	1.895	46.07	2 481.91
23	V	61	61.00	3.321	1.789	202.58	52 953.00
24	Cr	15	15.00	1.051	0.634	15.77	339.09
25	Mn	4	4.00	0.115	0.264	0.46	1.33
26	Fe	70	70.00	– 0.311	0.024	– 21.77	476.60
27	Co	< 0.5		– 0.297	0.016		
28	Ni	9	9.00	– 0.309	0.056	– 2.78	7.97
29	Cu	18	18.00	– 0.252	0.095	– 4.53	23.44
30	Zn	27	27.00	– 0.037	0.156	– 0.99	18.76
31	Ga	< 4	2.00	– 0.150	0.083	—	0.12
32	Ge	< 7		– 0.208	0.033		
33	As	< 4		– 0.235	0.014		
34	Se	< 60		– 0.288	0.134		
35	Br	< 10		– 0.227	0.068		
36	Kr			– 0.216	0.065		
37	Rb	< 1	0.50	– 0.160	0.069	—	0.01
38	Sr	< 0.6		– 0.196	0.014		
39	Y	< 0.7		– 0.192	0.011		
40	Zr	62	62.00	1.233	1.016	76.45	9 813.67
41	Nb	2	2.00	5.478	1.697	10.96	131.55
42	Mo	< 2	1.00	1.155	0.901	—	2.15
43	Tc			0.045	0.317		
44	Ru			– 0.143	0.044		
45	Rh			0.068	0.437		
46	Pd			– 0.057	0.194		
47	Ag	< 6	3.00	0.010	0.184	—	0.30
48	Cd	89	89.00	– 0.112	0.038	– 9.98	110.88
49	In	74	74.00	– 0.157	0.024	– 11.58	137.22
50	Sn	< 32		– 0.142	0.003		
51	Sb	< 9	4.50	– 0.081	0.072	—	0.24
52	Te	22		– 0.116	0.050		
53	I	< 2		0.000	0.000		
54	Xe			– 0.137	0.002		
55	Cs	< 0.6	0.30	– 0.104	0.041	—	0.00

Atomic No	Element symbol	c_{l1}^{i}	$u(c_{l1}^{i})$	m_l^i	$u(m_l^i)$	Individual Correction	Uncertainty Contribution
		ng/g	ng/g	µK/ppbw	µK/ppbw	µK	μK^2
56	Ba	< 0.7	0.35	– 0.079	0.071	—	0.00
57	La	< 0.6		– 0.121	0.018		
58	Ce	< 0.6		– 0.128	0.002		
59	Pr			– 0.127	0.002		
60	Nd			– 0.125	0.002		
61	Pm			0.000	0.000		
62	Sm			– 0.110	0.017		
63	Eu			– 0.119	0.036		
64	Gd			– 0.115	0.003		
65	Tb			– 0.107	0.010		
66	Dy			– 0.101	0.017		
67	Ho			– 0.099	0.017		
68	Er			– 0.098	0.017		
69	Tm			– 0.104	0.004		
70	Yb			– 0.046	0.054		
71	Lu			– 0.104	0.031		
72	Hf	< 3	1.50	2.391	2.522	—	27.17
73	Ta			5.443	1.253		
74	W	< 2	1.00	0.488	0.873	—	1.00
75	Re			0.095	0.131		
76	Os			0.400	0.657		
77	Ir			0.376	0.622		
78	Pt	< 8	4.00	0.017	0.190	—	0.58
79	Au	< 1 100	550.00	– 0.010	0.074	—	1 703.99
80	Hg	< 24	12.00	– 0.030	0.059	—	0.63
81	Tl	< 6	3.00	– 0.059	0.028	—	0.04
82	Pb	8	8.00	– 0.052	0.056	—	0.37
83	Bi	< 3		– 0.039	0.013		
84	Po			0.000	0.000		
85	At			0.000	0.000		
86	Rn			– 0.081	0.000		
87	Fr			0.000	0.000		
88	Ra			0.000	0.000		
89	Ac			0.000	0.000		
90	Th	< 0.6		– 0.052	0.034		
91	Pa			– 0.079	0.024		
92	U	< 0.8	0.40	– 0.060	0.027	—	0.00
93	Np			– 0.077	0.023		
94	Pu			– 0.049	0.039		

Hybrid SIE correction	**– 0.25 mK**
u^2 (Σ contributions)	**70 512.55 μK^2**
u ($\Delta T_{HYBRID\ SIE}$)	**± 0.27 mK**

Table 29: Calculation of the hybrid SIE correction and uncertainty for Al metal sample from Sumitomo based on the chemical analysis supplied by NRC.

Atomic No	Element symbol	c_{l1}^{i}	$u(c_{l1}^{i})$	m_l^i	$u(m_l^i)$	Individual Correction	Uncertainty Contribution
		ng/g	ng/g	µK/ppbw	µK/ppbw	µK	μK^2
1	H			– 17.873	0.106		
2	He			– 4.527	0.001		
3	Li	71.75	71.75	– 1.319	1.030	– 94.61	14 416.68
4	Be	1.75	1.75	– 1.832	0.111	– 3.21	10.32
5	B	125.80		– 1.858	0.774		
6	C			– 1.131	0.870		
7	N			– 1.276	0.020		
8	O			– 0.396	0.119		
9	F	374.45		0.000	0.000		
10	Ne			– 0.898	0.000		
11	Na	118.98		– 0.724	0.150		
12	Mg	2.43	2.43	– 0.450	0.116	– 1.09	1.27
13	Al	Matrix	Matrix	Matrix	Matrix	Matrix	Matrix
14	Si	735.05		– 0.623	0.093		
15	P	11.65		– 0.834	0.576		
16	S			– 0.511	0.131		
17	Cl	1 204.83		0.000	0.000		
18	Ar			– 0.453	0.000		
19	K	21.10	21.10	– 0.277	0.263	– 5.84	64.82
20	Ca	20.90		– 0.470	0.088		
21	Sc	34.45	34.45	– 0.223	0.517	– 7.69	376.87
22	Ti	19.65	19.65	4.607	1.895	90.54	9 583.19
23	V	58.93	58.93	3.321	1.789	195.69	49 411.73
24	Cr	32.45	32.45	1.051	0.634	34.11	1 586.94
25	Mn	10.25	10.25	0.115	0.264	1.18	8.73
26	Fe	98.70	98.70	– 0.311	0.024	– 30.69	947.53
27	Co	0.38		– 0.297	0.016		
28	Ni	8.03	8.03	– 0.309	0.056	– 2.48	6.33
29	Cu	516.87	516.87	– 0.252	0.095	– 130.02	19 329.71
30	Zn	141.53	141.53	– 0.037	0.156	– 5.21	515.43
31	Ga	12.20	12.20	– 0.150	0.083	– 1.83	4.38
32	Ge	467.50		– 0.208	0.033		
33	As	137.00		– 0.235	0.014		
34	Se	25 090.53		– 0.288	0.134		
35	Br	193.90		– 0.227	0.068		
36	Kr			– 0.216	0.065		
37	Rb	1.73	1.73	– 0.160	0.069	– 0.28	0.09
38	Sr	3.48		– 0.196	0.014		
39	Y	0.58		– 0.192	0.011		
40	Zr	3.83	3.83	1.233	1.016	4.72	37.35
41	Nb	0.93	0.93	5.478	1.697	5.07	28.14
42	Mo	32.13	32.13	1.155	0.901	37.10	2 215.13
43	Tc			0.045	0.317		
44	Ru	7.83		– 0.143	0.044		
45	Rh	0.95	0.95	0.068	0.437	0.06	0.18
46	Pd	103.48	103.48	– 0.057	0.194	– 5.86	438.57
47	Ag	891.08	891.08	0.010	0.184	9.13	26 853.96
48	Cd	55.80	55.80	– 0.112	0.038	– 6.26	43.58
49	In	< 1	0.50	– 0.157	0.024	—	0.01
50	Sn	1.83		– 0.142	0.003		
51	Sb	14.83	14.83	– 0.081	0.072	– 1.20	2.58
52	Te	7.30		– 0.116	0.050		
53	I	1.05		0.000	0.000		
54	Xe			– 0.137	0.002		
55	Cs	0.38	0.38	– 0.104	0.041	– 0.04	0.00

Atomic No	Element symbol	c_{l1}^{i}	$u(c_{l1}^{i})$	m_l^i	$u(m_l^i)$	Individual Correction	Uncertainty Contribution
		ng/g	ng/g	µK/ppbw	µK/ppbw	µK	μK^2
56	Ba	6.90	6.90	– 0.079	0.071	– 0.54	0.54
57	La	0.68		– 0.121	0.018		
58	Ce	0.60		– 0.128	0.002		
59	Pr	1.10		– 0.127	0.002		
60	Nd	3.58		– 0.125	0.002		
61	Pm			0.000	0.000		
62	Sm	3.78		– 0.110	0.017		
63	Eu	0.43		– 0.119	0.036		
64	Gd	4.80		– 0.115	0.003		
65	Tb	0.85		– 0.107	0.010		
66	Dy	2.85		– 0.101	0.017		
67	Ho	0.28		– 0.099	0.017		
68	Er	1.15		– 0.098	0.017		
69	Tm	1.05		– 0.104	0.004		
70	Yb	1.28	1.28	– 0.046	0.054	– 0.06	0.01
71	Lu	0.25		– 0.104	0.031		
72	Hf	< 1	0.50	2.391	2.522	—	3.02
73	Ta	0.43	0.43	5.443	1.253	2.31	5.63
74	W	2.13	2.13	0.488	0.873	1.04	4.52
75	Re	0.90	0.90	0.095	0.131	0.09	0.02
76	Os	< 1	0.50	0.400	0.657	—	0.15
77	Ir	1.20	1.20	0.376	0.622	0.45	0.76
78	Pt	7.48	7.48	0.017	0.190	0.13	2.04
79	Au	0.83	0.83	– 0.010	0.074	– 0.01	0.00
80	Hg	5.08	5.08	– 0.030	0.059	– 0.15	0.11
81	Tl	4.83	4.83	– 0.059	0.028	– 0.28	0.10
82	Pb	173.85	173.85	– 0.052	0.056	– 9.09	175.79
83	Bi	2.08		– 0.039	0.013		
84	Po			0.000	0.000		
85	At			0.000	0.000		
86	Rn			– 0.081	0.000		
87	Fr			0.000	0.000		
88	Ra			0.000	0.000		
89	Ac			0.000	0.000		
90	Th	1.90		– 0.052	0.034		
91	Pa			– 0.079	0.024		
92	U	0.73	0.73	– 0.060	0.027	– 0.04	0.00
93	Np			– 0.077	0.023		
94	Pu			– 0.049	0.039		

Hybrid SIE correction	**– 0.08 mK**
u^2 (Σ contributions)	**126 076.21 μK^2**
u ($\Delta T_{HYBRID\ SIE}$)	**± 0.36 mK**

Table 30: Calculation of the hybrid SIE correction and uncertainty for Al metal sample from Sumitomo based on the chemical analysis supplied by NIM.

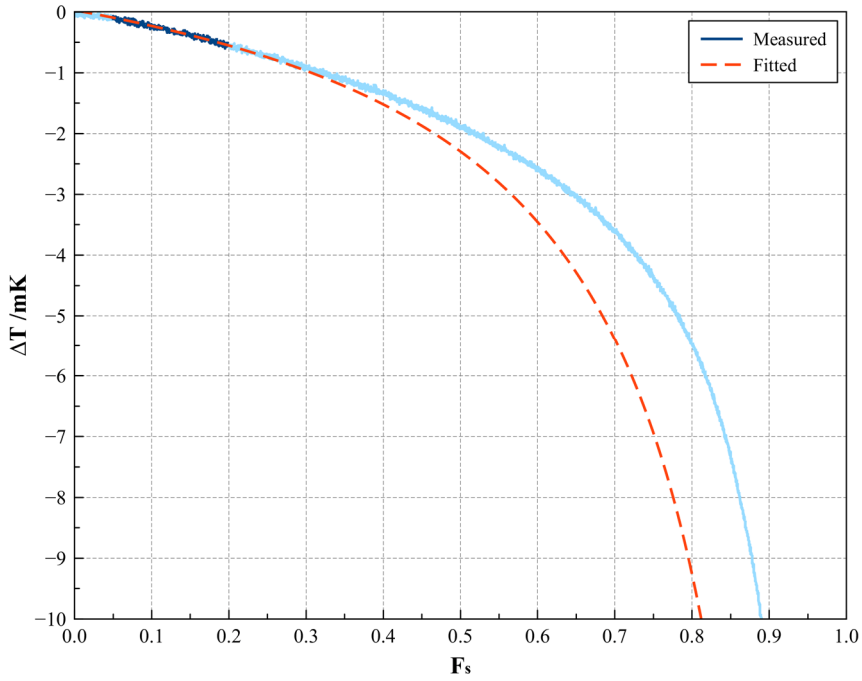

Figure 47: Hybrid OME component for cell Al-S (Sumitomo) freezing curve 1 (08/11/2014). Result of the fitting: – 2.32 mK.

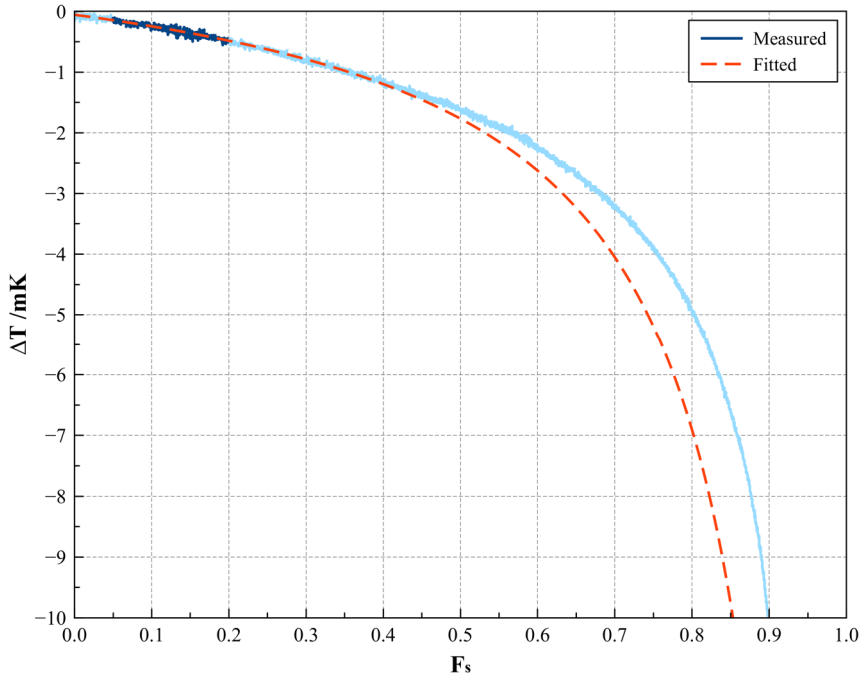

Figure 48: Hybrid OME component for cell Al-S (Sumitomo) freezing curve 2 (11/11/2014). Result of the fitting: – 1.70 mK.

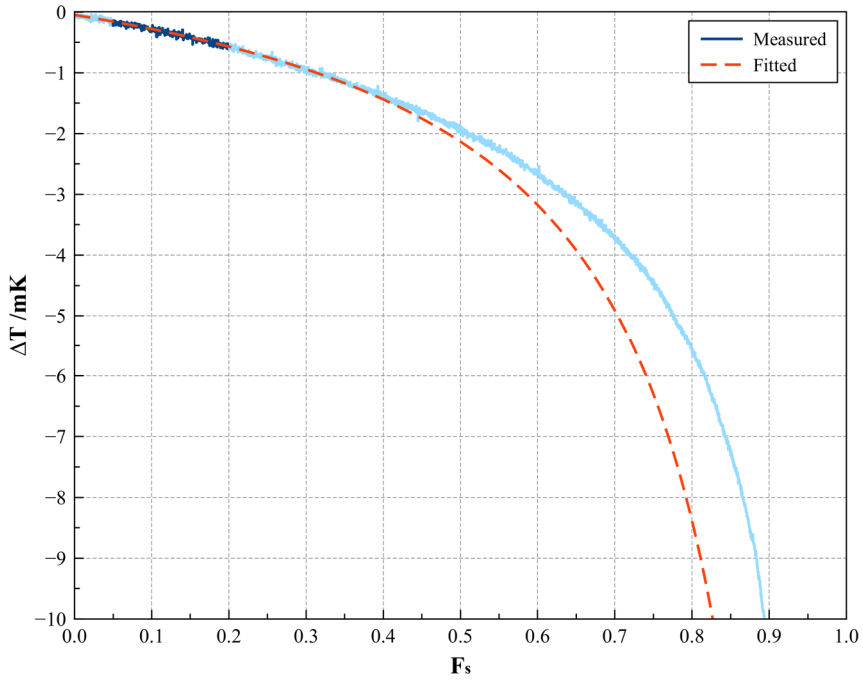

Figure 49: Hybrid OME component for cell Al-S (Sumitomo) freezing curve 3 (13/11/2014). Result of the fitting: – 2.08 mK.

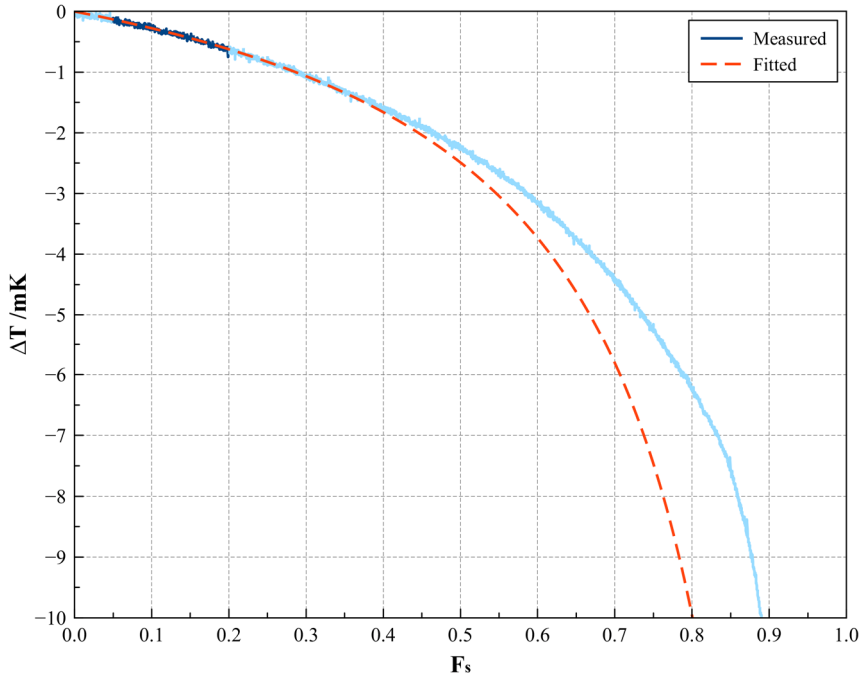

Figure 50: Hybrid OME component for cell Al-S (Sumitomo) freezing curve 4 (16/11/2014). Result of the fitting: – 2.48 mK.

GDMS supplier	Hybrid SIE correction mK	Hybrid SIE uncertainty mK
Metal supplier	– 0.28	0.26
AQura	– 0.24	0.16
NRC	– 0.25	0.27
NIM	– 0.08	0.36

Freezing curve	Modified OME correction mK
# 1	2.32
# 2	1.70
# 3	2.08
# 4	2.48
OME Mean	**2.15 mK**
Std. Deviation	**0.34 mK**

GDMS supplier	Hybrid SIE/Modified OME	
	Correction mK	Uncertainty mK
Metal supplier	1.87	0.43
AQura	1.91	0.38
NRC	1.90	0.43
NIM	2.07	0.49

Table 31: Results of Hybrid SIE/Modified OME methodology for cell Al-S.

For the modified OME component, the fitted values of the four freezing curves were averaged and the result used in conjunction with each individual hybrid SIE estimate to generate the corrections according to the hybrid SIE / modified OME methodology. As for the uncertainty calculations, the uncertainty for the SIE component corresponds to the value calculated according to equation 19, as displayed in the tables above (27 – 30). The uncertainty for the OME component was taken as the standard deviation of the values fitted for the freezing curves. The uncertainties calculated for the hybrid SIE and the modified OME were combined in quadrature in order to assign the uncertainty value for the hybrid SIE / modified OME methodology.

The fittings performed for the freezing curves of cell Al-A are given in figure 51, while the hybrid SIE results together with the results for the hybrid SIE/modified OME methodology are shown in table 32. The results for cell Al-E are given in figure 52 and table 33. Figure 53 and table 34 provide the results for cell Al-H while the results for cell Al-N are shown in figure 54 and table 35.

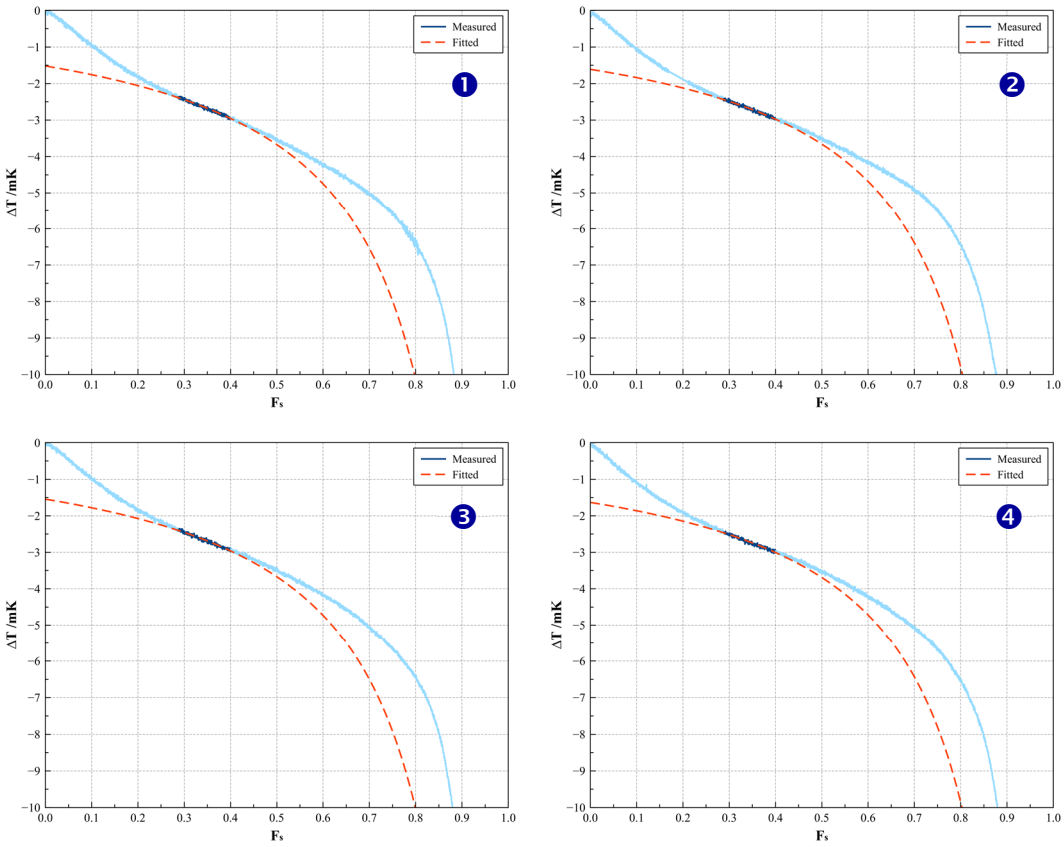

Figure 51: Modified OME fittings of four freezing curves with cell Al-A (Alfa Aesar).

GDMS supplier	Hybrid SIE correction mK	Hybrid SIE uncertainty mK
Metal supplier	– 0.25	0.22
AQura	– 2.71	1.27
NRC	– 3.14	3.24
NIM	– 1.55	2.54

Freezing curve	Modified OME correction mK
# 1	2.15
# 2	2.05
# 3	2.12
# 4	2.06
OME Mean	**2.10 mK**
Std. Deviation	**0.05 mK**

GDMS supplier	Hybrid SIE/Modified OME	
	Correction mK	Uncertainty mK
Metal supplier	1.85	0.22
AQura	– 0.61	1.27
NRC	– 1.04	3.24
NIM	0.55	2.54

Table 32: Results of the hybrid SIE/modified OME methodology for cell Al-A.

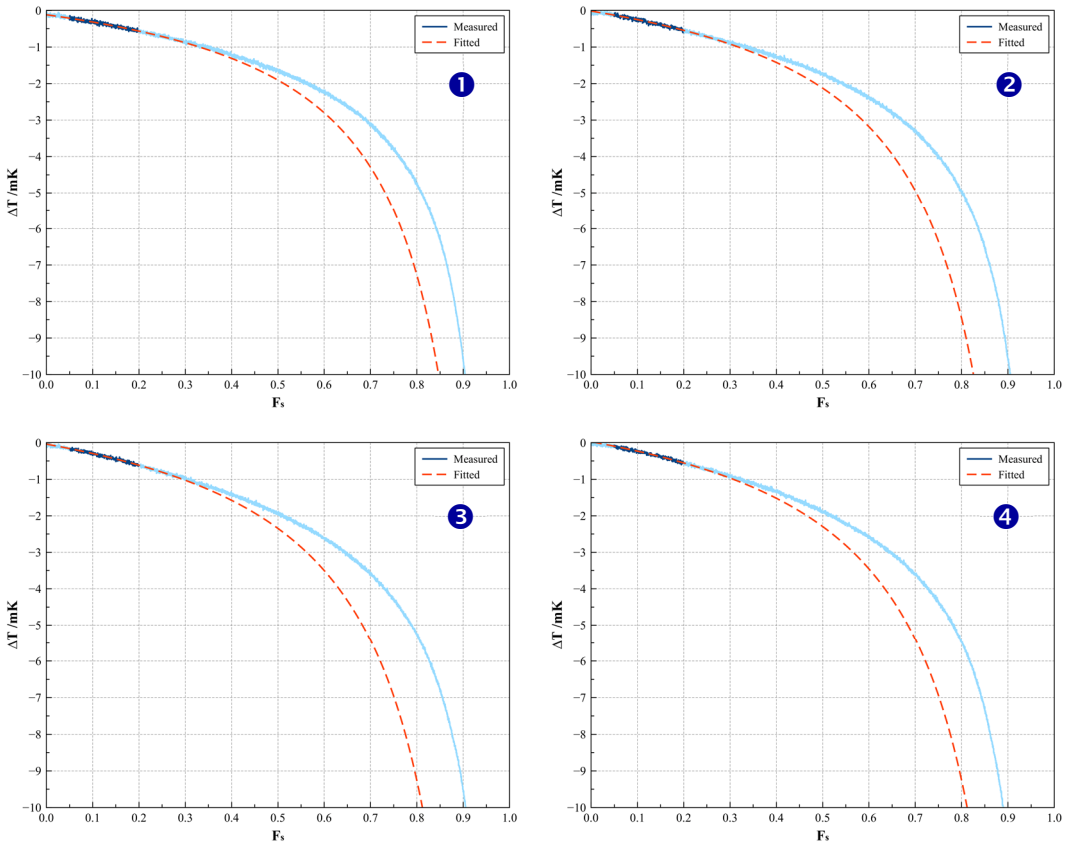

Figure 52: Modified OME fittings of four freezing curves with cell Al-E (ESPI).

GDMS supplier	Hybrid SIE correction mK	Hybrid SIE uncertainty mK
Metal supplier	0.00	0.00
AQura	– 0.07	0.11
NRC	– 0.66	0.51
NIM	– 0.57	0.51

Freezing curve	Modified OME correction mK
# 1	1.79
# 2	2.11
# 3	2.31
# 4	2.32
OME Mean	**2.13 mK**
Std. Deviation	**0.25 mK**

GDMS supplier	Hybrid SIE/Modified OME	
	Correction mK	Uncertainty mK
Metal supplier	2.13	0.25
AQura	2.06	0.27
NRC	1.47	0.56
NIM	1.56	0.57

Table 33: Results of Hybrid SIE/Modified OME methodology for ESPI cell Al-E.

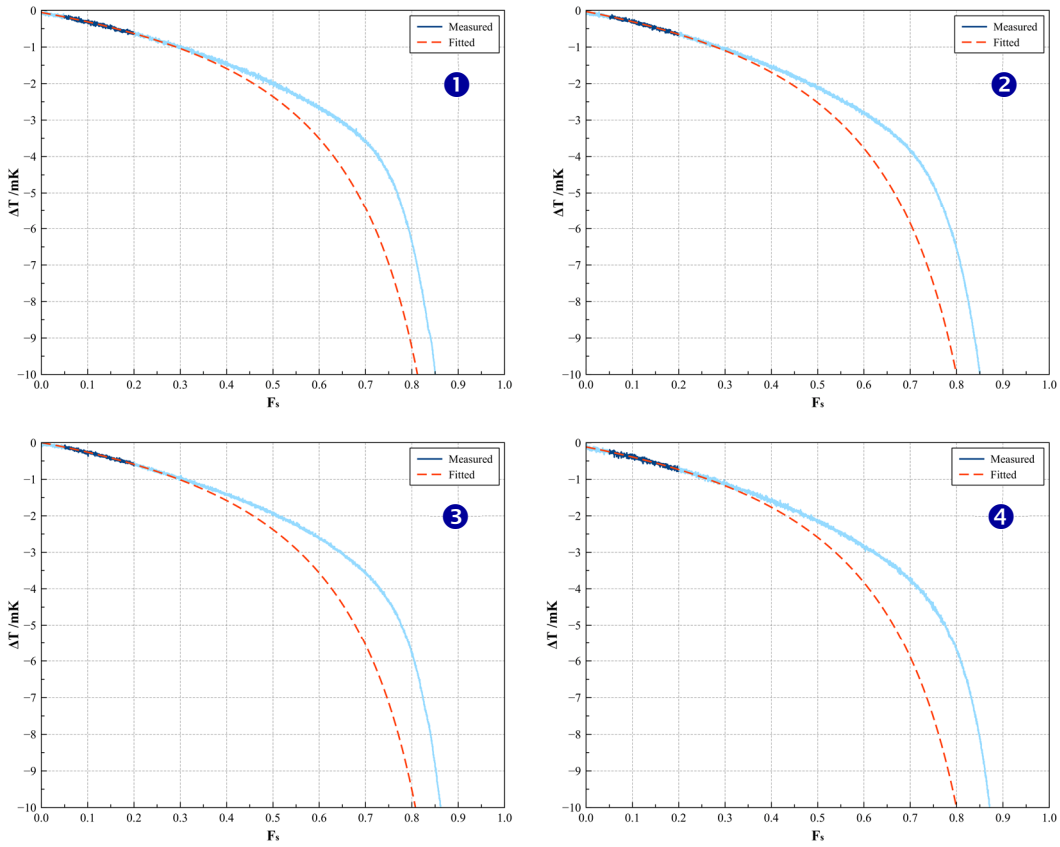

Figure 53: Modified OME fittings of four freezing curves with cell Al-H (Honeywell).

GDMS supplier	Hybrid SIE correction mK	Hybrid SIE uncertainty mK
Metal supplier	– 0.85	0.53
AQura	– 0.18	0.12
NRC	– 0.32	0.38
NIM	– 0.39	0.56

Freezing curve	Modified OME correction mK
# 1	2.30
# 2	2.50
# 3	2.38
# 4	2.48
OME Mean	**2.41 mK**
Std. Deviation	**0.09 mK**

GDMS supplier	Hybrid SIE/Modified OME	
	Correction mK	Uncertainty mK
Metal supplier	1.56	0.53
AQura	2.23	0.15
NRC	2.09	0.39
NIM	2.02	0.56

Table 34: Results of Hybrid SIE/Modified OME methodology for cell Al-H.

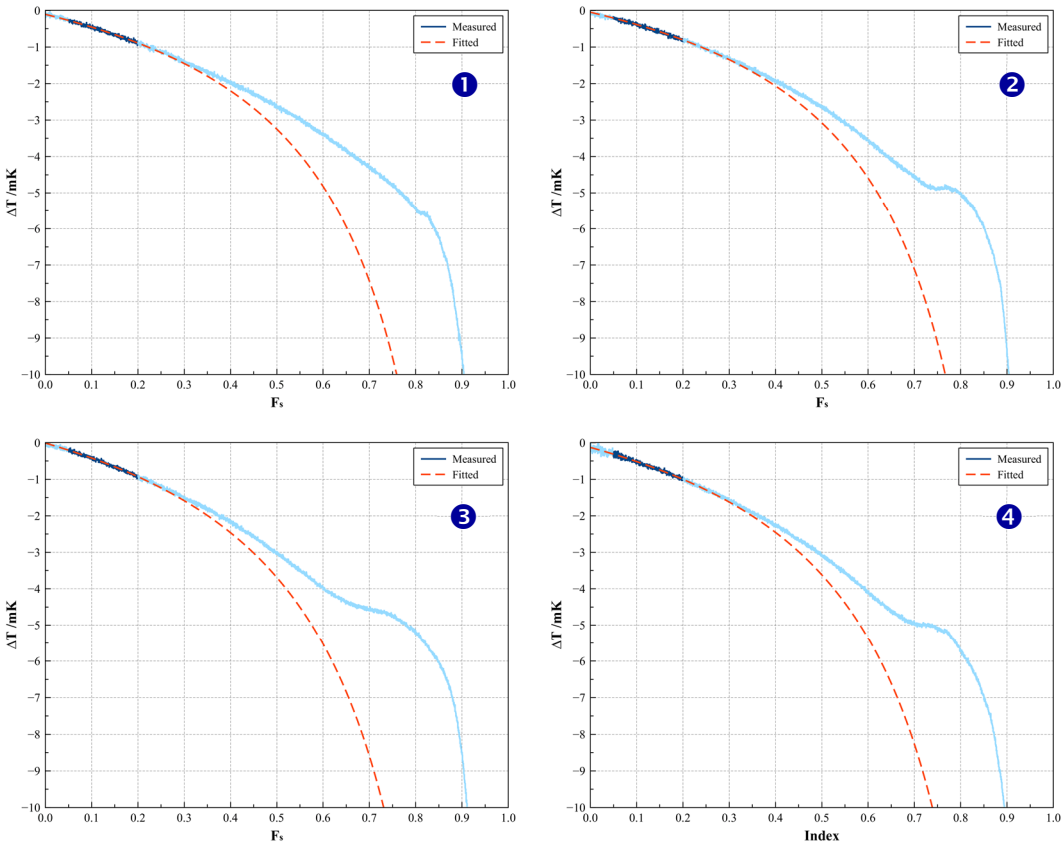

Figure 54: Modified OME fittings of four freezing curves with cell Al-N (New Metals).

GDMS supplier	Hybrid SIE correction mK	Hybrid SIE uncertainty mK
Metal supplier	– 0.32	0.30
AQura	– 0.13	0.08
NRC	– 0.40	0.60
NIM	– 0.05	0.31

Freezing curve	Modified OME correction mK
# 1	3.14
# 2	3.03
# 3	3.68
# 4	3.49
OME Mean	**3.34 mK**
Std. Deviation	**0.30 mK**

GDMS supplier	Hybrid SIE/Modified OME	
	Correction mK	Uncertainty mK
Metal supplier	3.02	0.43
AQura	3.21	0.31
NRC	2.94	0.68
NIM	3.29	0.43

Table 35: Results of Hybrid SIE/Modified OME methodology for cell Al-N.

It was observed that the freezing curve measurements made with cell Al-A (constructed using aluminium samples supplied by Alfa-Aesar) presented a high peak at the very beginning. In order to disregard this influence, the initial portion (equivalent to the first 25% of the curve) was not taken into consideration. Since this peak was assumed to be caused by high *k* impurities (most probably titanium, which was confirmed by the GDMS assays), it would be accounted as part of the hybrid SIE component. Once the valid data started at F_s 0.25, the interval at which the fitting of the modified OME was done for the other cells (F_s 0.05 to F_s 0.20) became (F_s 0.2875 to F_s 0.40) for cell Al-A. This transformation kept the proportionality in between the endpoints (the size of the interval) and the duration of the cropped freezing curves, since the curves were turned into 75% of the original solid fraction.

Even though the shape of the freezing curves measured with cell Al-N was also anomalous, it did not require any arrangements prior to the least square fitting because the depression on the freezing curve occurred at the end of the plateau, away from the region where the fitting would be performed. Nevertheless, application of this methodology for this cell resulted in the highest corrections, mainly because of the more noticeable departure of the fitted curve from the measured curve.

A summary of the results for the hybrid methodology for all cells is given in table 36.

Metal sample	GDMS supplier	Hybrid SIE/Modified OME	
		Correction mK	Uncertainty mK
Alfa Aesar	Metal supplier	1.85	0.22
	AQura	– 0.61	1.27
	NRC	– 1.04	3.24
	NIM	0.55	2.54
ESPI Metals	Metal supplier	2.13	0.25
	AQura	2.06	0.27
	NRC	1.47	0.56
	NIM	1.56	0.57
Honeywell	Metal supplier	1.56	0.53
	AQura	2.23	0.15
	NRC	2.09	0.39
	NIM	2.02	0.56
New Metals	Metal supplier	3.02	0.43
	AQura	3.21	0.31
	NRC	2.94	0.68
	NIM	3.29	0.43
Sumitomo	Metal supplier	1.87	0.43
	AQura	1.91	0.38
	NRC	1.90	0.43
	NIM	2.07	0.49

Table 36: Summary of hybrid SIE/modified OME results.

Overall, the results of cells Al-N and Al-S were more consistent between the different assays than the other cells. It is possible to observe that the effect caused by the variability in the GDMS results was minimised, as opposed to the result obtained with the application of the SIE method. This is because, in the hybrid methodology, impurities with the coefficient of distribution k less than 0.1 are not calculated via the SIE component but are accounted in the modified OME component. This is why the very high Se detected in the NIM analysis did not have much influence. Coincidently, the major discrepancies in the GDMS analyses for these two cells occurred with elements not accounted for individually (via SIE component). Concerning the impurities with $k > 0.1$, just a few differences were observed across the GDMS results, although not in levels that would produce significant variation in the final result.

6.4. Scheil model correction and uncertainty calculation

Once the freezing curve measurements were finished and the results recast in terms of temperature difference vs solid fraction (as described in section 4.4), the Scheil methodology could be applied to the freezing curves. The estimates assigned for the cells were determined through least-square fitting of equation 23. For this methodology, two types of configuration were tested: one in which the variables T_0, mc_0 and k in the equation are all set as free parameters (Scheil model – free k) and the other in which the coefficient of distribution k is fixed as zero (Scheil model – $k = 0$). In practical terms, the only difference in between these two configurations is the coefficient k either being determined by the fitting or being set as zero prior to the fitting. Application of the latter implies the condition that the impurities are insoluble in the solid phase. These particular configurations and the results obtained are described below.

6.4.1. Scheil model – free k

The method denominated 'Scheil model – free k' is the variation of the Scheil methodology in which the variables T_0, mc_0 and k are all set as free parameters. In order to obtain the temperature corrections according to this methodology, as an initial test, all freezing curves were fitted using ranges with the lower endpoint fixed at F_s 0.05 and the upper endpoint starting at F_s 0.15 (shortest data interval). The tests were repeated increasing the range in 0.05 (solid fraction) increments, up to the latest point in the curve which could yield estimates (F_s 0.85), even if the fitted curve was not a proper representative of the measured curve. It was decided to define the initial point of the fittings at F_s 0.05 to discard any possible issues at the very beginning of the curves (e.g. overshootings).

This initial test was performed to identify the consistency and dependence of the results upon the selected range, for all freezing curves. From this test, it was observed that only a few endpoints were suitable, from which two upper endpoints to proceed with the analyses were selected: F_s 0.50 and F_s 0.80. Apart from showing good consistency, there was a special interest in fitting the curves up to F_s 0.50 because it

would be valuable to have an estimate over just the first half of the curve, since this is generally the part of the curve which is more stable and less prone to thermal disturbances. Similarly, it would also be noteworthy to compare these estimates with ones obtained by performing the fitting over the whole freezing curve (or setting the upper endpoint as close to complete freezing, F_s 1.00, as possible), however it was not possible as the convergence of the fitted curve causes the estimates of the fitted variables to tend to infinity. Consequently, it was decided to proceed with the fittings by setting the upper endpoint to F_s 0.80, as it was the farthest point in the freezing curve that could be fitted and still provide a reasonable fitting over the original data (with low residuals).

The fitted curves and results obtained according to the Scheil method are given in the figures and tables to follow. The graphs for cell Al-S (Sumitomo) are given in figures 55 to 58 (for the lower limit, F_s 0.50) and figures 59 to 62 (for the upper limit, F_s 0.80). Furthermore, the estimates obtained from the fittings are tabulated in table 37, with the corresponding corrections and uncertainties being given in table 38.

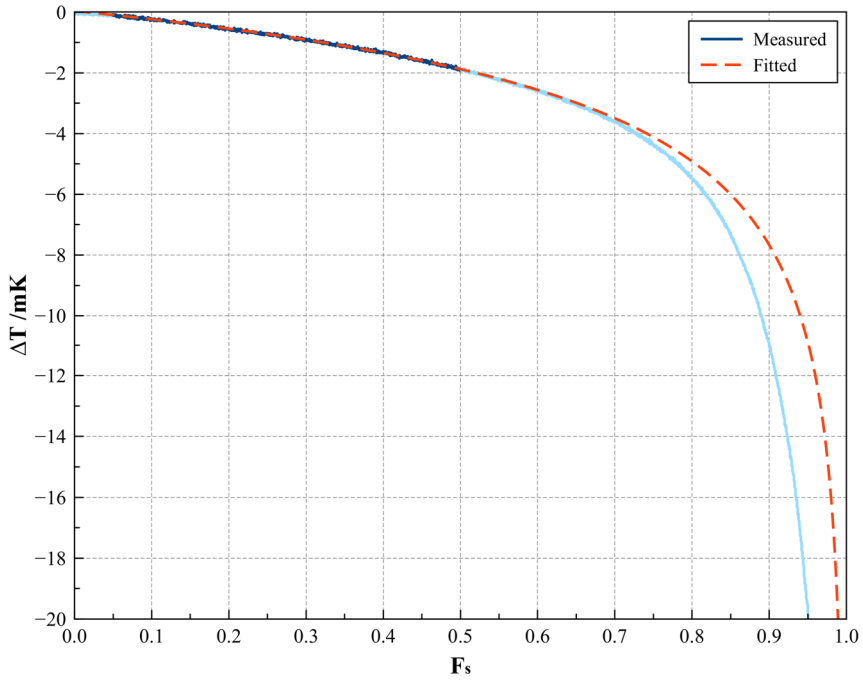

Figure 55: Scheil model applied to curve 1 measured in cell Al-S (Sumitomo). Fitting range from F_s 0.05 to F_s 0.50 (lower limit).

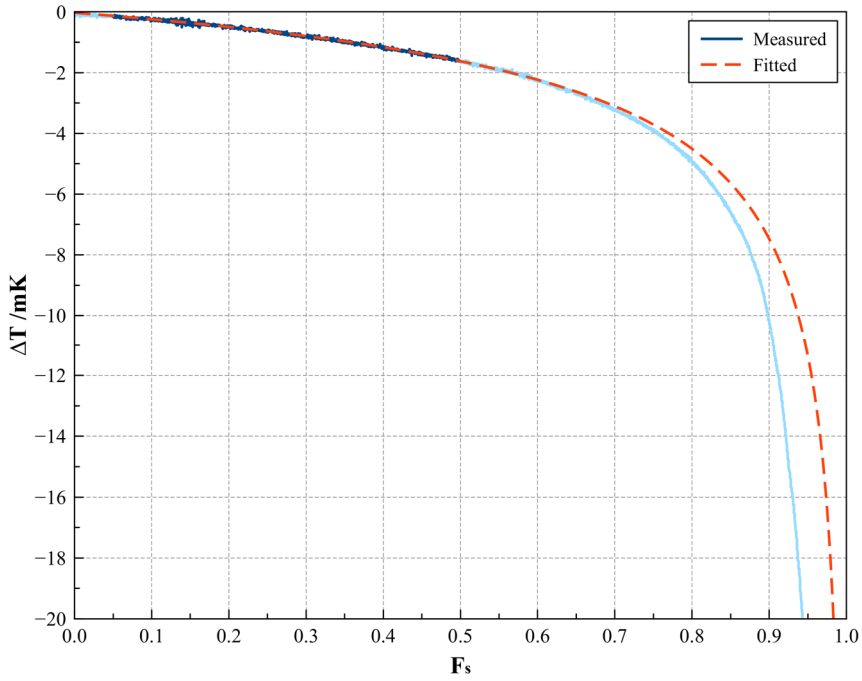

Figure 56: Scheil model applied to curve 2 measured in cell Al-S (Sumitomo). Fitting range from F_s 0.05 to F_s 0.50 (lower limit).

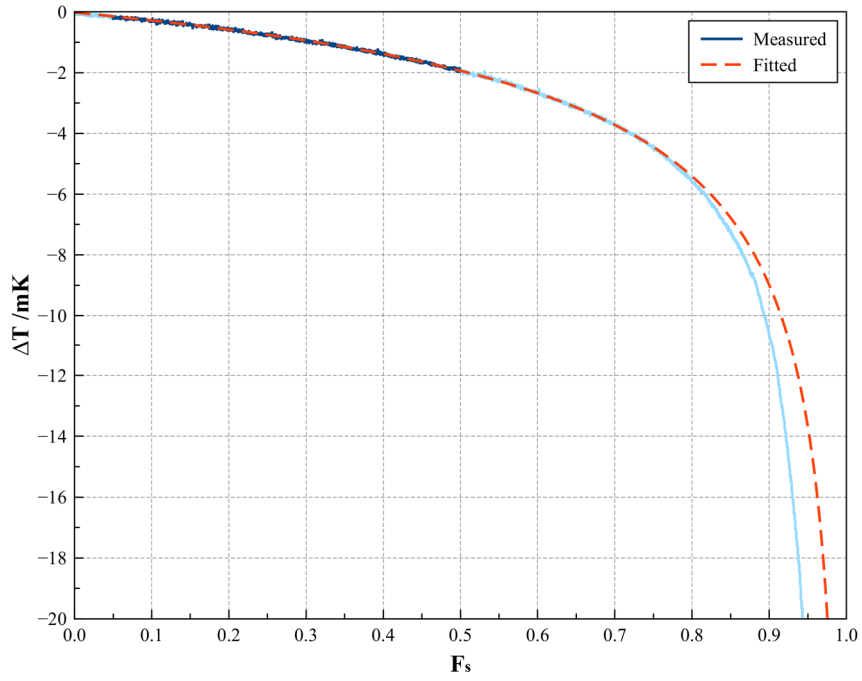

Figure 57: Scheil model applied to curve 3 measured in cell Al-S (Sumitomo). Fitting range from F_s 0.05 to F_s 0.50 (lower limit).

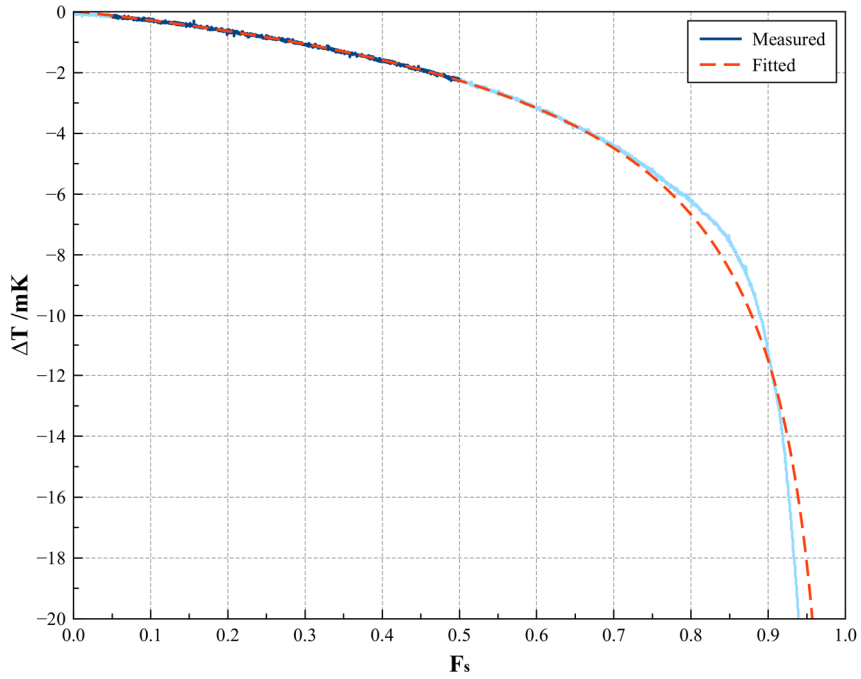

Figure 58: Scheil model applied to curve 4 measured in cell Al-S (Sumitomo). Fitting range from F_s 0.05 to F_s 0.50 (lower limit).

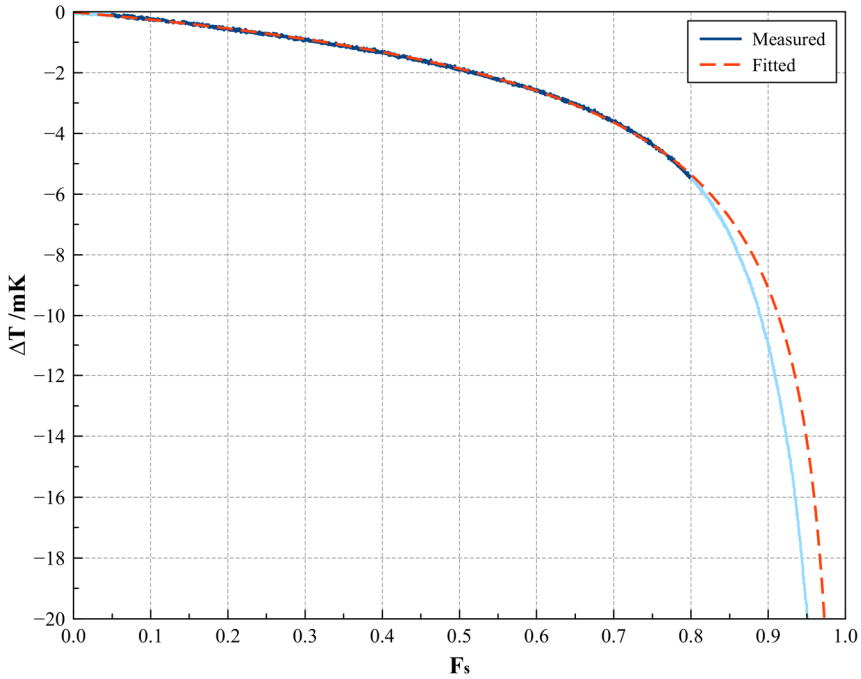

Figure 59: Scheil model applied to curve 1 measured in cell Al-S (Sumitomo). Fitting range from F_s 0.05 to F_s 0.80 (upper limit).

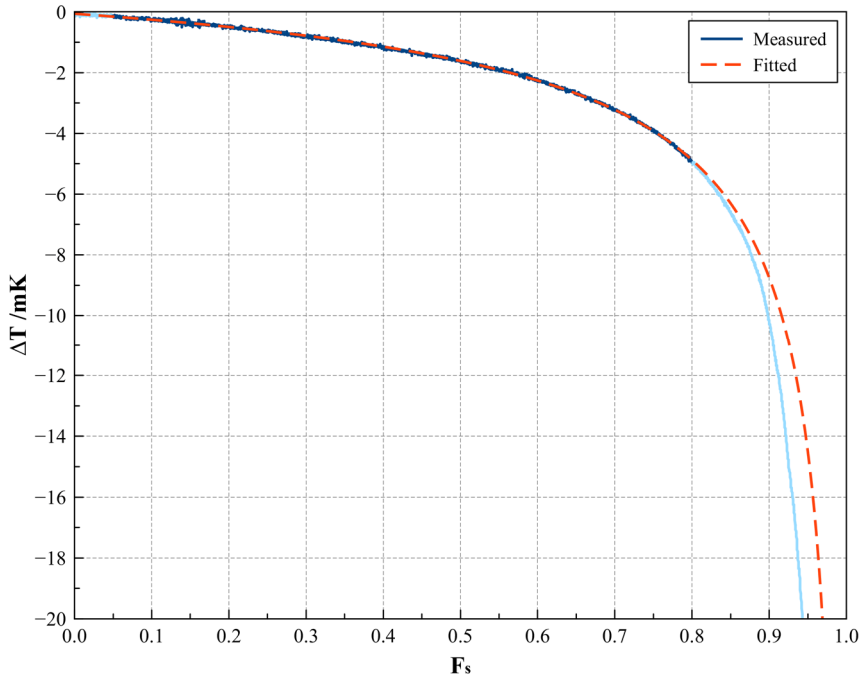

Figure 60: Scheil model applied to curve 2 measured in cell Al-S (Sumitomo). Fitting range from F_s 0.05 to F_s 0.80 (upper limit).

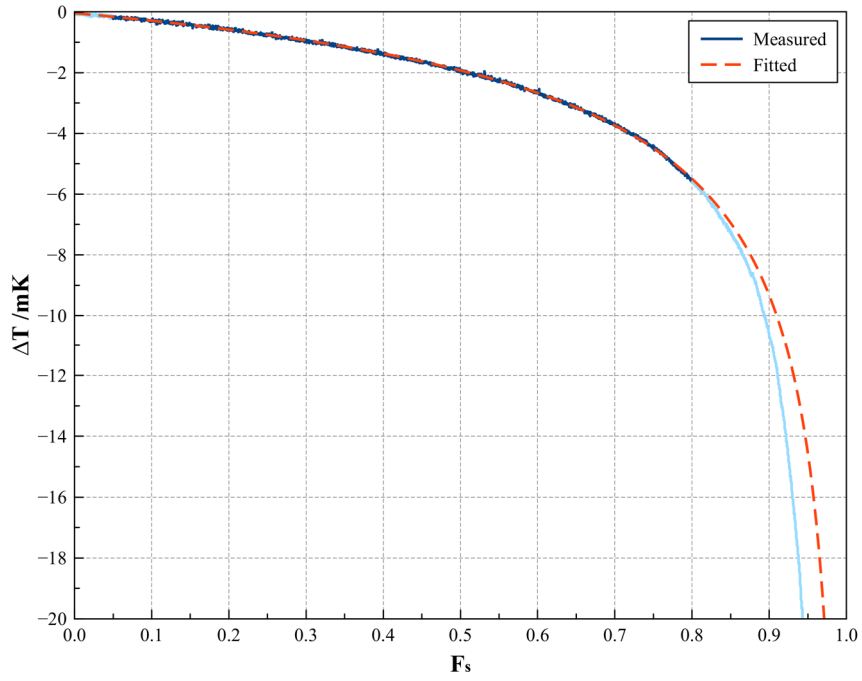

Figure 61: Scheil model applied to curve 3 measured in cell Al-S (Sumitomo). Fitting range from F_s 0.05 to F_s 0.80 (upper limit).

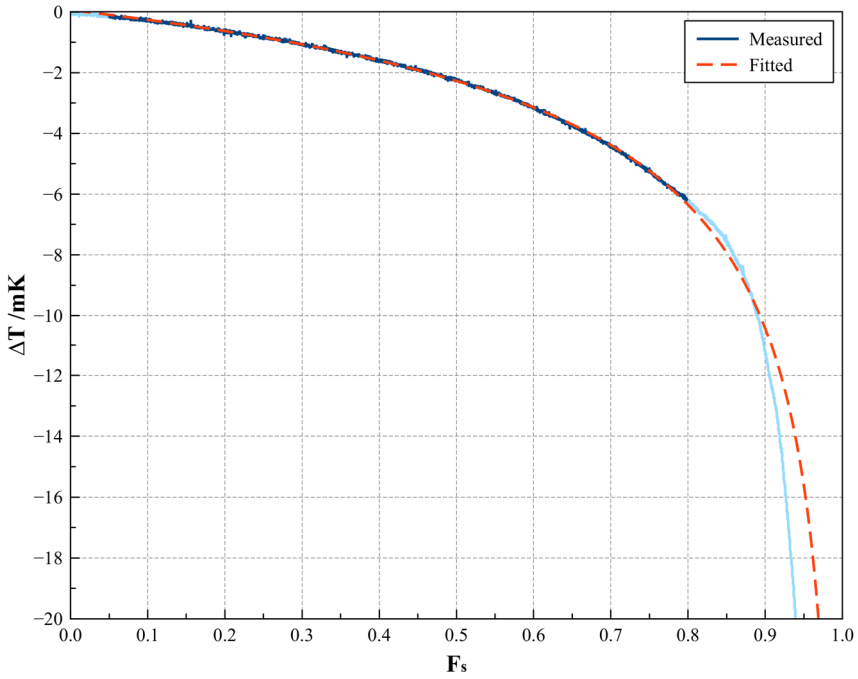

Figure 62: Scheil model applied to curve 4 measured in cell Al-S (Sumitomo). Fitting range from F_s 0.05 to F_s 0.80 (upper limit).

Fitting parameters		Curve #1 mK	Curve #2 mK	Curve #3 mK	Curve #4 mK
Free k	Range $F_{s\ 0.05-0.50}$	– 0.78	– 5.24	– 6.21	– 6.02
	Range $F_{s\ 0.05-0.80}$	– 0.98	– 3.23	– 5.28	– 8.55

Table 37: Estimates based on least square fitting of Scheil equation to the freezing curves measured with cell Al-S (Sumitomo).

Fitting parameters		Correction mK	Uncertainty mK
Free k	Range $F_{s\ 0.05-0.50}$	4.56	2.55
	Range $F_{s\ 0.05-0.80}$	4.51	3.22

Table 38: Results based on least square fitting of Scheil equation to the freezing curves measured with cell Al-S (Sumitomo).

In table 38, the corrections were calculated as the additive inverse of the averaged estimate for the four freezing curves. Uncertainties were given by the respective standard deviations. From the results for cell Al-S, it is possible to observe that the fitted curves provided good convergence over the measured curves, especially when the fitting was done with the upper endpoint (upper limit, F_s 0.80). As shown in figure 45, the first freezing curve measured had a slightly flatter slope in relation to the others, which in turn, resulted in a significant drop in the fitted estimates for curves 2 to 4. Observation of the results with F_s 0.80 indicates a decreasing trend in the values, possibly meaning it would keep on lowering if further measurements were to be done. This behaviour, however, is not as evident in the estimates resulting from the curves fitted with the lower endpoint F_s 0.50. Nevertheless, confirmation of this behaviour would demand a sequence of further measurements. This may indicate that given their impurity content, some cells would take several freezing curve realisations to stabilise their performance. Due to the variation observed in the estimates, the uncertainties were correspondingly large.

The fittings for the freezing curves measured with the other cells were performed similarly, following the same criteria and parameters. Nevertheless, due to constraints related to the shape of the curves obtained with cell Al-A (as per previous discussion), the ranges selected for the fittings had to be adapted accordingly. As shown in figure 63, it was attempted to maintain and apply the same parameters concerning the range of the fittings for this cell but the convergence of the fitted curves was not appropriate over the ranges selected, hence resulting in estimated corrections of approximately 310 mK, which is not consistent with the purity of the metal.

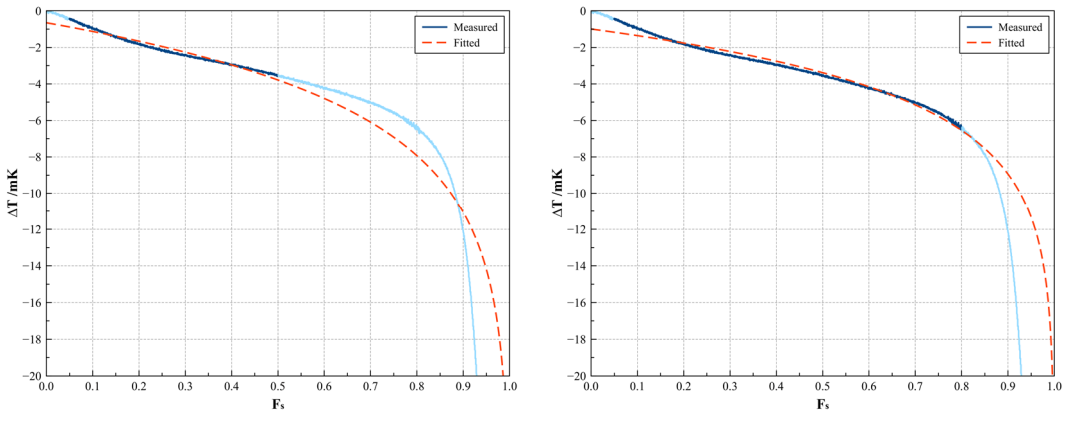

Figure 63: Scheil model applied to curve 1 measured with cell Al-A (Alfa Aesar).

Taking into consideration that the GDMS analyses indicated that the samples from Alfa Aesar contained a considerable concentration of titanium, an important high *k* impurity in aluminium, it was decided to try fitting the curves simulating a high *k* to account for this steep beginning of the curves. The fitting was then performed with an initial input (like a prediction) for the value for the coefficient *k* (equal to 5.0). Since it was set as a free parameter, the software would adjust this value as the least square fitting was done until optimum values for the parameters were achieved. Besides this, once the high *k* effect is predominantly observable at the beginning of the freezing curves, it was observed that fittings simulating a high *k* were compromised if done up to an upper endpoint approaching the completion of the freeze (F_s 1.00). Appropriate fittings could only be achieved up to F_s 0.50. In these circumstances, this was selected as the upper endpoint (upper limit) and F_s 0.25 was selected as the lower endpoint, restricting the fitting to just the region of the curve affected by the impurities with a high coefficient of distribution. These results can be seen in figures 64 and 65.

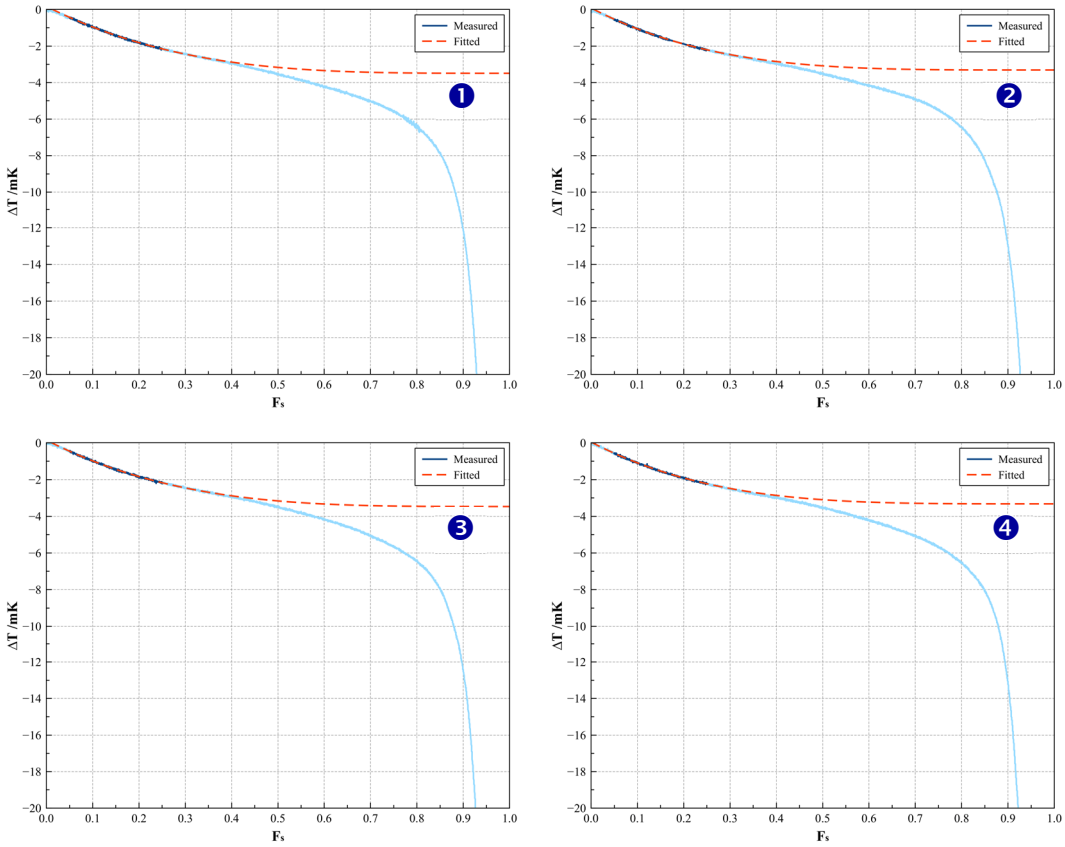

Figure 64: Curves for cell Al-A fitted with high *k* values (lower range, F_s 0.05 to F_s 0.25).

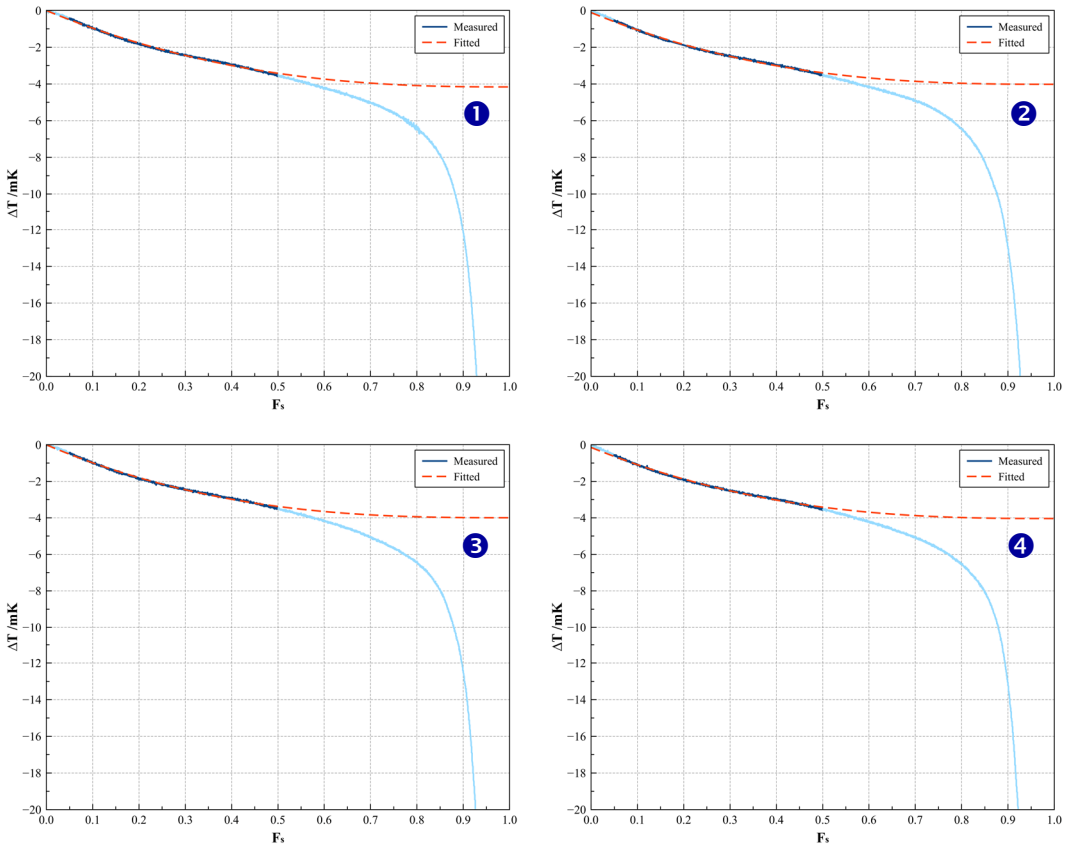

Figure 65: Curves for cell Al-A fitted with high *k* values (upper range, F_s 0.05 to F_s 0.50).

The estimates obtained from the fittings are tabulated in table 39, with the corresponding corrections and uncertainties being given in table 40. For illustration purposes only, the fitted values of *k* varied from 4.5 to 4.9 for the lower range and from 3.5 to 3.7 for the upper range.

Fitting parameters		Curve #1 mK	Curve #2 mK	Curve #3 mK	Curve #4 mK
Free k	**Range $F_{s\ 0.05-0.25}$**	3.67	3.40	3.62	3.37
	Range $F_{s\ 0.05-0.50}$	4.16	3.91	3.99	3.90

Table 39: Estimates based on least square fitting of Scheil equation to the freezing curves measured with cell Al-A (Alfa Aesar).

Fitting parameters		Correction mK	Uncertainty mK
Free k	**Range $F_{s\ 0.05-0.25}$**	– 3.51	0.15
	Range $F_{s\ 0.05-0.50}$	– 3.99	0.12

Table 40: Results based on least square fitting of Scheil equation to the freezing curves measured with cell Al-A (Alfa Aesar).

According to the calculations, the results of the fittings were consistent with the behaviour of the fixed point material which means that the temperature realised by the fixed point cell Al-A is at least 3.5 mK higher than the temperature of realisation defined in the ITS-90. Given the good reproducibility of the freezing curves, the uncertainties (standard deviations) were small, as opposed to cell Al-S.

Concerning the cell produced with aluminium samples from ESPI metals, cell Al-E, application of the Scheil methodology was straightforward in which no adaptations were imposed by the performance/behaviour of the cell. Consequently, it followed the parameters initially described which were applied for cell Al-S (F_s 0.50 defined as the upper endpoint for the lower range and F_s 0.80 the upper endpoint for the upper range). The fittings are shown in figures 66 (F_s 0.05 to F_s 0.50) and 67 (F_s 0.05 to F_s 0.80). The estimates produced by the least-square fittings are given in table 41. The corresponding corrections and uncertainties are shown in table 42.

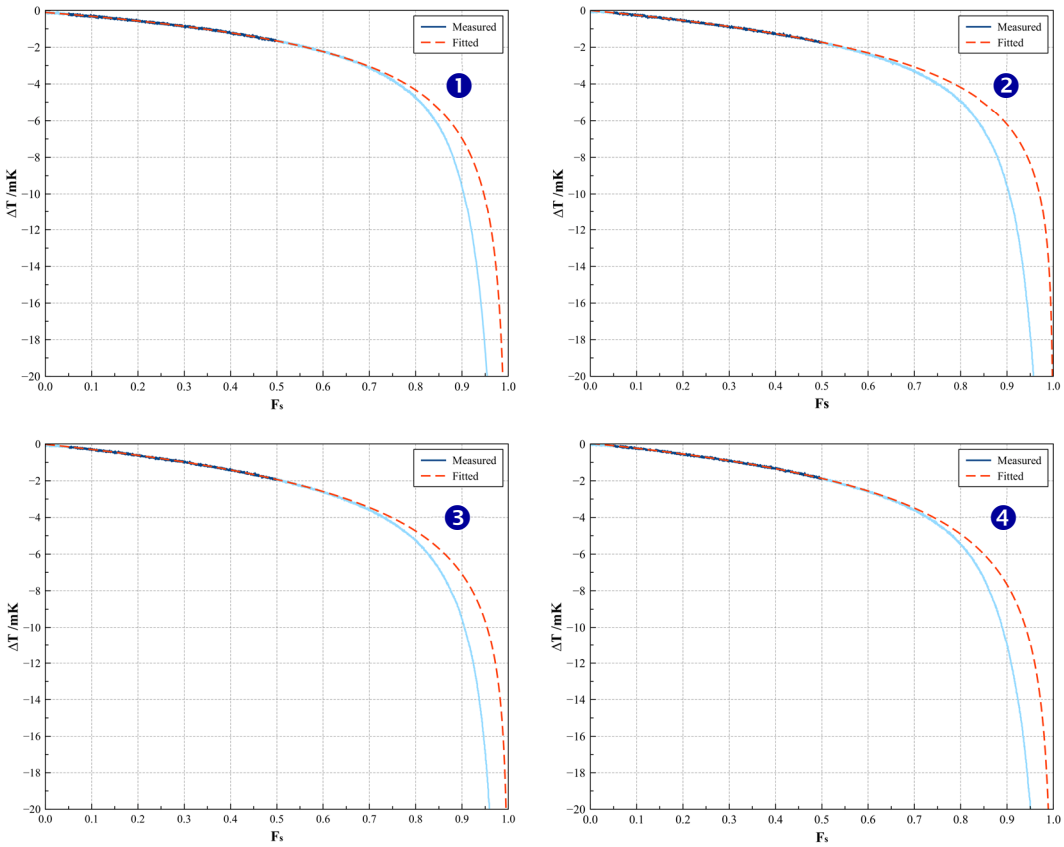

Figure 66: Fitting of the curves measured with cell Al-E (ESPI).

Range F_s 0.05 to F_s 0.50 with *k* being a free parameter.

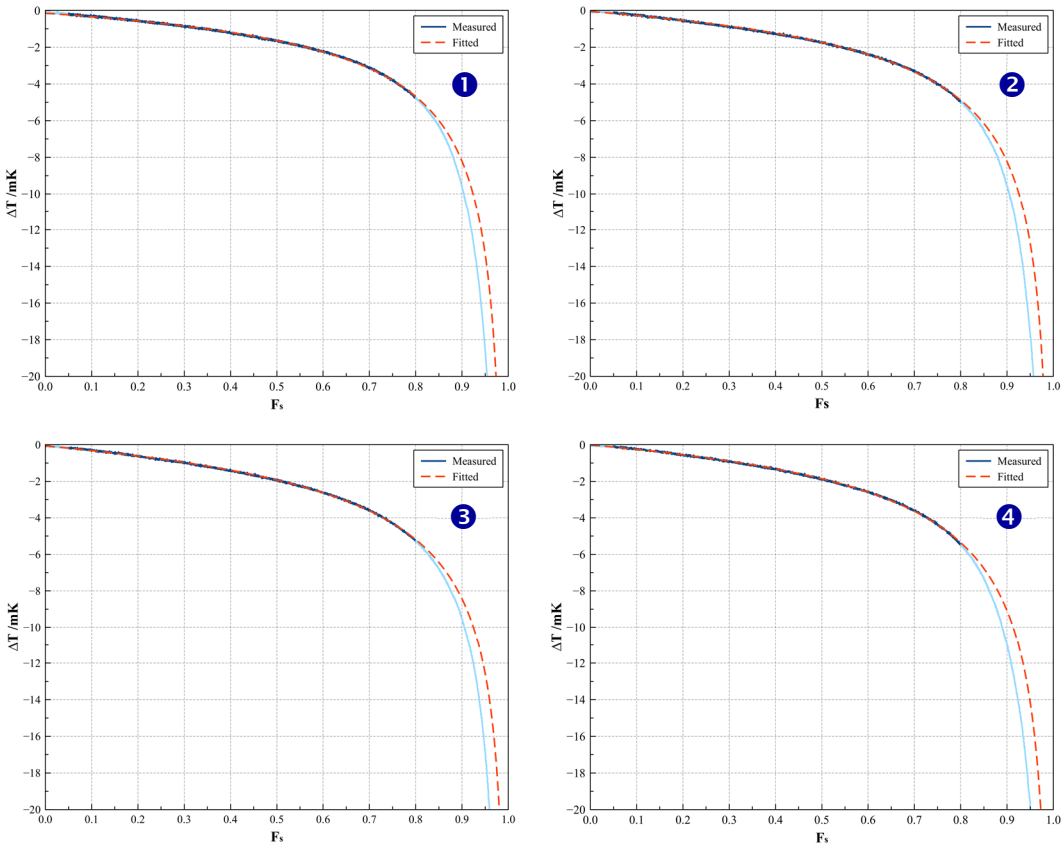

Figure 67: Fitting of the curves measured with cell Al-E (ESPI).

Range F_s 0.05 to F_s 0.80 with *k* being a free parameter.

Fitting parameters		Curve #1 mK	Curve #2 mK	Curve #3 mK	Curve #4 mK
Free k	**Range $F_{s\ 0.05-0.50}$**	– 6.10	– 26.70	– 21.09	– 11.36
	Range $F_{s\ 0.05-0.80}$	– 3.34	– 4.90	– 6.91	– 5.31

Table 41: Estimates based on least square fitting of Scheil equation to the freezing curves measured with cell Al-E (ESPI).

Fitting parameters		Correction mK	Uncertainty mK
Free k	**Range $F_{s\ 0.05-0.50}$**	16.31	9.30
	Range $F_{s\ 0.05-0.80}$	5.12	1.47

Table 42: Results based on least square fitting of Scheil equation to the freezing curves measured with cell Al-E (ESPI).

According to the results obtained with cell Al-E, it is observed that the fittings in the upper range presented more consistent results. In spite of the fact that there was good agreement in the shapes of the measured freezing curves and that the convergence of the fitted curves was optimal in both ranges tested, the results of the fittings in the lower range (to F_s 0.50) presented an unexpected and inexplicable variability.

The Scheil methodology was applied to cell Al-H (Honeywell) with the same parameters used with cells Al-S and Al-E. The resulting fittings are shown in figures 68 and 69. Then, the respective estimates are shown in table 43, with the corrections and uncertainties tabulated in table 44.

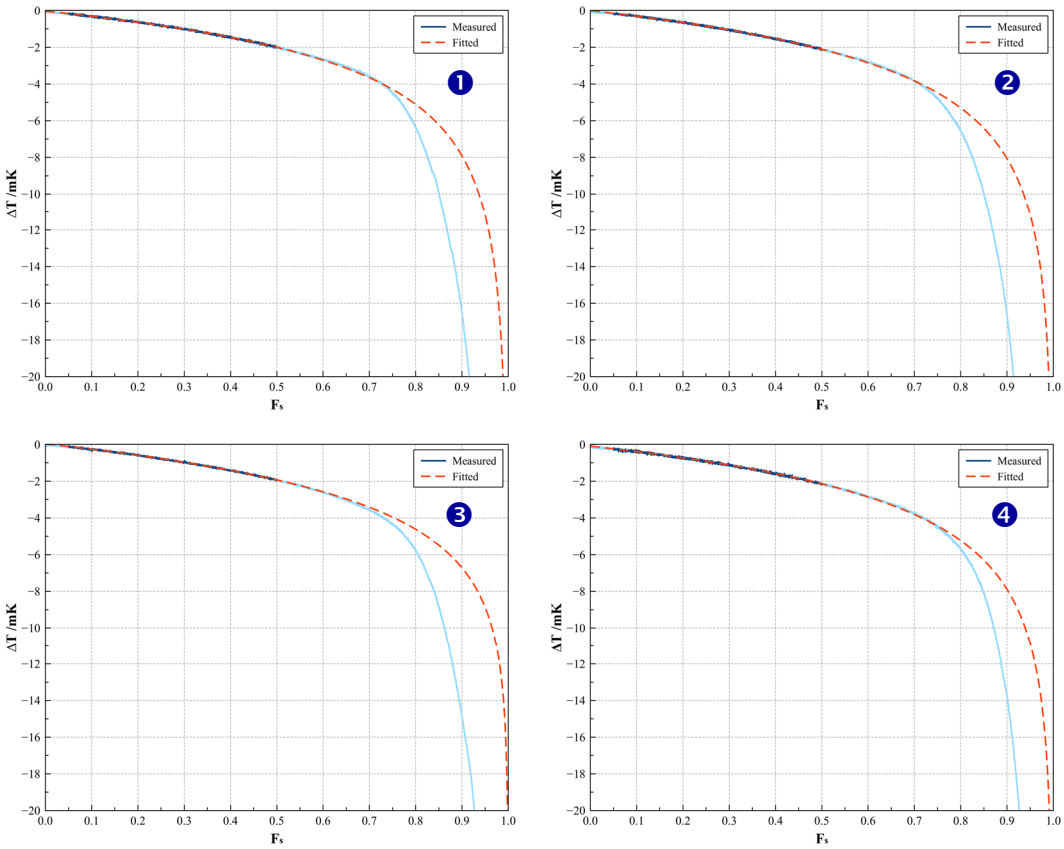

Figure 68: Fitting of the curves measured with cell Al-H (Honeywell).

Range F_s 0.05 to F_s 0.50 with *k* being a free parameter.

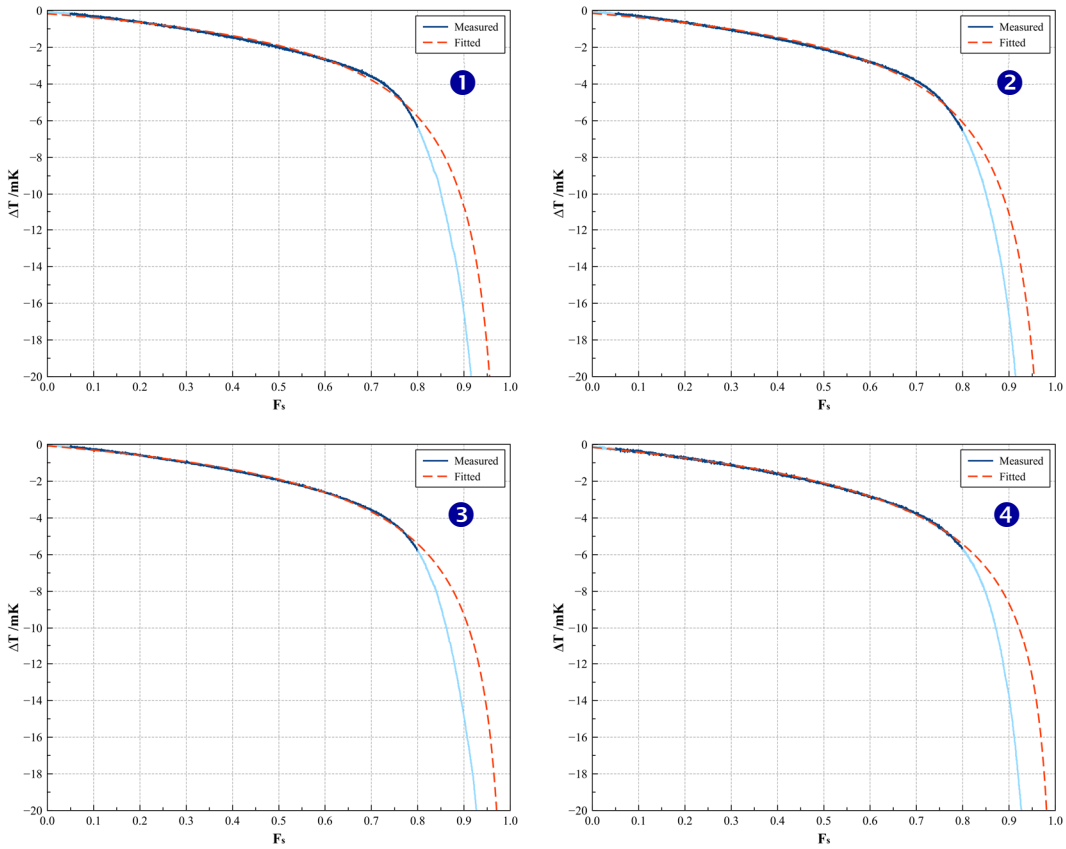

Figure 69: Fitting of the curves measured with cell Al-H (Honeywell).

Range F_s 0.05 to F_s 0.80 with *k* being a free parameter.

Fitting parameters		Curve #1 mK	Curve #2 mK	Curve #3 mK	Curve #4 mK
Free k	**Range $F_{s\ 0.05-0.50}$**	– 12.05	– 17.33	– 73.56	– 17.48
	Range $F_{s\ 0.05-0.80}$	– 3.05	– 3.54	– 4.77	– 8.06

Table 43: Estimates based on least square fitting of Scheil equation to the freezing curves measured with cell Al-H (Honeywell).

Fitting parameters		Correction mK	Uncertainty mK
Free k	**Range $F_{s\ 0.05-0.50}$**	30.11	29.08
	Range $F_{s\ 0.05-0.80}$	4.86	2.26

Table 44: Results based on least square fitting of Scheil equation to the freezing curves measured with cell Al-H (Honeywell).

Similarly to cell Al-E, it can be observed that the fittings performed with cell Al-H in the upper range presented reasonable consistency if compared to the results in the range up to F_s 0.50. Even though the curves showed good reproducibility, the fitted values for the four curves tested varied considerably in the lower range. Perhaps it was an isolated issue with curve 3, but that is not confirmed by the fitting in the upper range for that freezing curve.

Similarly to the issues with cell Al-A, the discontinuity in the shape of the freezing curves measured in cell Al-N (as discussed previously in this chapter) imposed some difficulties in the application of the Scheil methodology. This led to a few changes to the way the method was applied. From the beginning, it was noticed that it would be impossible to do the fittings up to F_s 0.80 since this part of the curve was impacted by the irregular behaviour of the cell observed. Indeed, it was only possible to apply the fitting up to F_s 0.65. In this case, the ranges applied were the same as for cell Al-A (F_s $0.05-0.25$ and F_s $0.05-0.50$). Even though it was due to different reasons, it would be important to restrict the variability in the ranges used (if not possible to employ the same parameters for all specimen tested). At least all cells were fitted in the range F_s 0.05 to F_s 0.50 (although for cells Al-E, Al-H and Al-S it represented the lower range and for cells Al-A and Al-N it marked the upper range instead). In theory, since the discontinuity appears only later in the freezing, it should not prevent the cell from presenting adequate fittings up to F_s 0.50.

The fittings applied to the freezing curves measured with cell Al-N are shown in figures 70 (lower range F_s $0.05-0.25$) and 71 (upper range F_s $0.05-0.50$). The values

of the estimates for the liquidus slopes are tabulated in table 45, with the corrections and uncertainties given in table 46.

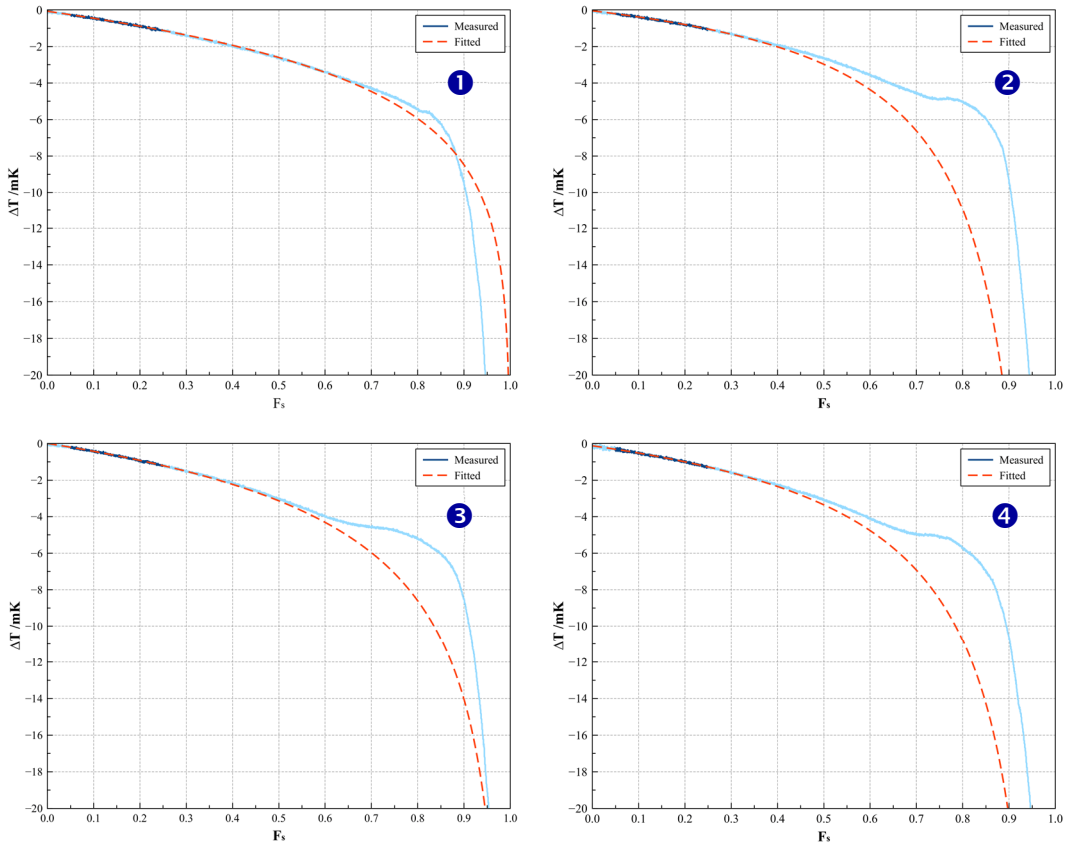

Figure 70: Fitting of the curves measured with cell Al-N (New Metals).
Range F_s 0.05 to F_s 0.25 with *k* being a free parameter.

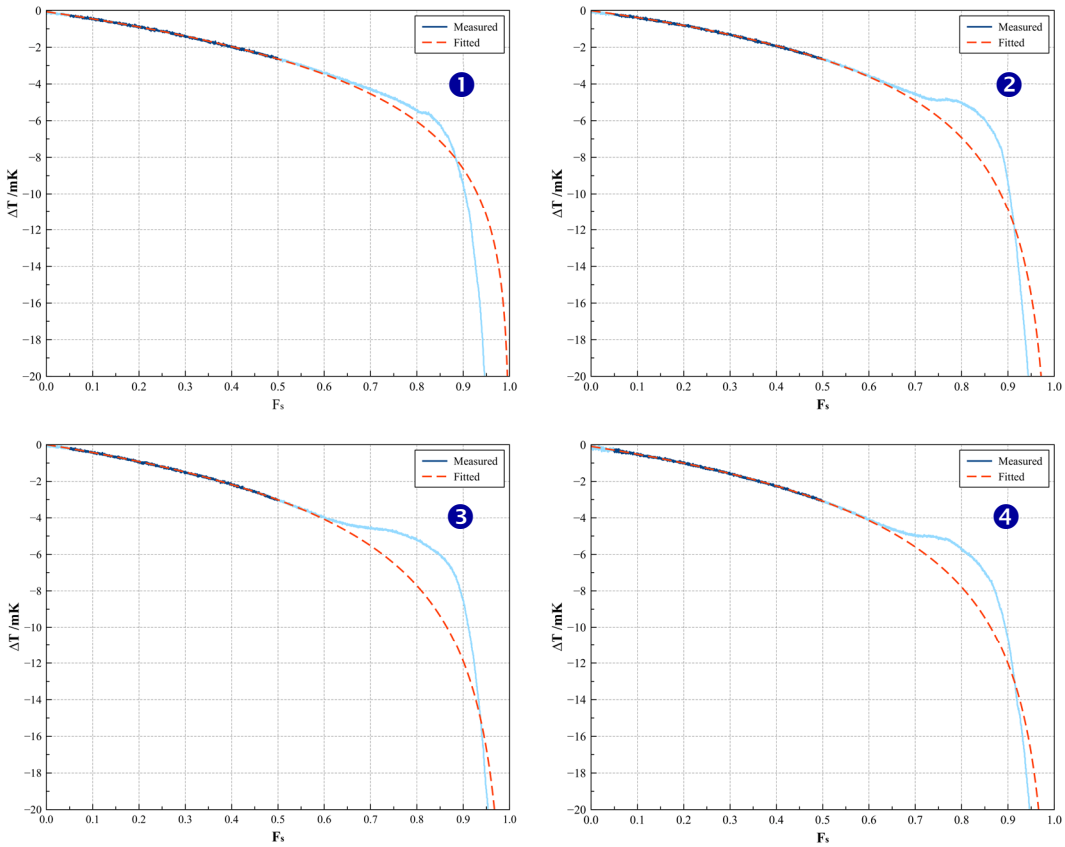

Figure 71: Fitting of the curves measured with cell Al-N (New Metals).

Range F_s 0.05 to F_s 0.50 with *k* being a free parameter.

	Fitting parameters	Curve #1 mK	Curve #2 mK	Curve #3 mK	Curve #4 mK
Free k	**Range $F_{s\ 0.05-0.25}$**	– 7.92	– 3.44	– 11.78	– 5.37
	Range $F_{s\ 0.05-0.50}$	—	– 14.21	– 20.24	– 18.85

Table 45: Estimates based on least square fitting of Scheil equation to the freezing curves measured with cell Al-N (New Metals).

Fitting parameters		Correction mK	Uncertainty mK
Free k	**Range $F_{s\ 0.05-0.25}$**	7.04	3.58
	Range $F_{s\ 0.05-0.50}$	17.77	3.16

Table 46: Results based on least square fitting of Scheil equation to the freezing curves measured with cell Al-N (New Metals).

Unfortunately, the fitting results were not as expected since they were large (most probably indicating that the issues at the end of the curve do indeed influence the earlier region of the curve, taking into account that even the fitting in the lower range presented substantial variation in the results).

As observed in table 46, no results could be obtained from the fitting of freezing curve 1 in the upper range. This was because it reached the maximum number of iterations permitted (10,000 iterations) without obtaining values for the fitted parameters within the deviation tolerance. Upon reaching the maximum number of iterations, the last value displayed for mc_0 was around 73 K, which is completely unrealistic: given the purity of the aluminium employed in the cells, the expected corrections should be in the order of a few milikelvins only.

6.4.2. Scheil model ($k = 0$)

The methodology referred to as 'Scheil model – $k = 0$' consists of the Scheil method being applied with the coefficient k being set as zero in the fittings. This variation of the method considers that the impurities are insoluble in the solid phase. Before applying this method, tests were also performed with the curves in order to check the most consistent ranges (better reproducibility across the freezing curves of a given cell) to apply the fittings. In general, the ranges that presented more consistency in this variation were F_s 0.05 – 0.50 and F_s 0.05 – 0.80, which coincide with the ranges used in the 'free k' variation for cells Al-E, Al-H and Al-S.

The fitted curves obtained according to the Scheil model are shown in the figures and tables to follow. To start with, the graphs for cell Al-S (Sumitomo) are given in figures 72 to 75 (for the lower limit, F_s 0.50) and figures 76 to 79 (for the upper limit, F_s 0.80). In addition, the estimates obtained from the fittings are provided in table 47, with the corresponding corrections and uncertainties being given in table 48.

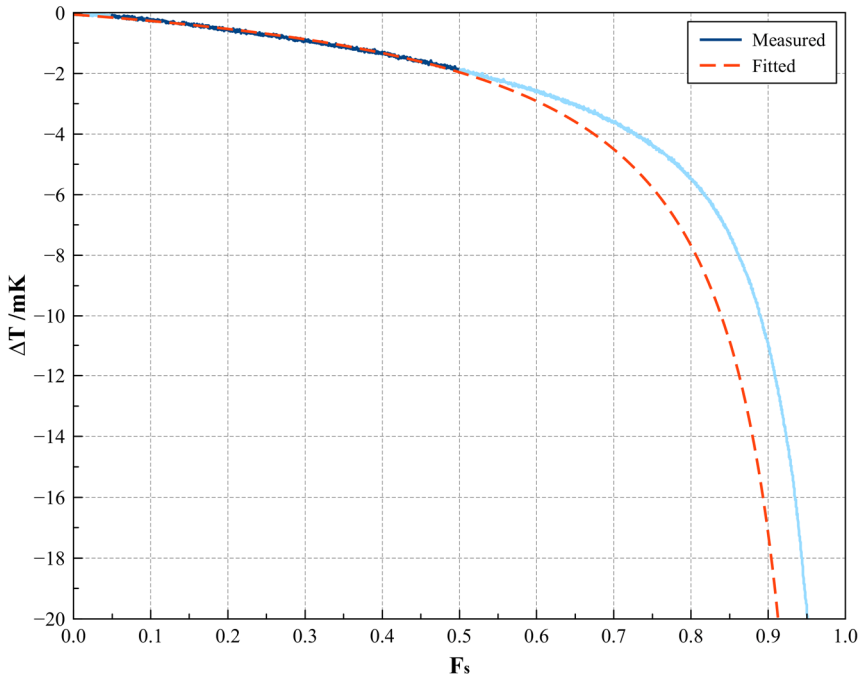

Figure 72: Scheil model applied to curve 1 measured in cell Al-S (Sumitomo). Fitting range from F_s 0.05 to F_s 0.50 (lower limit). Coefficient k fixed as 0.

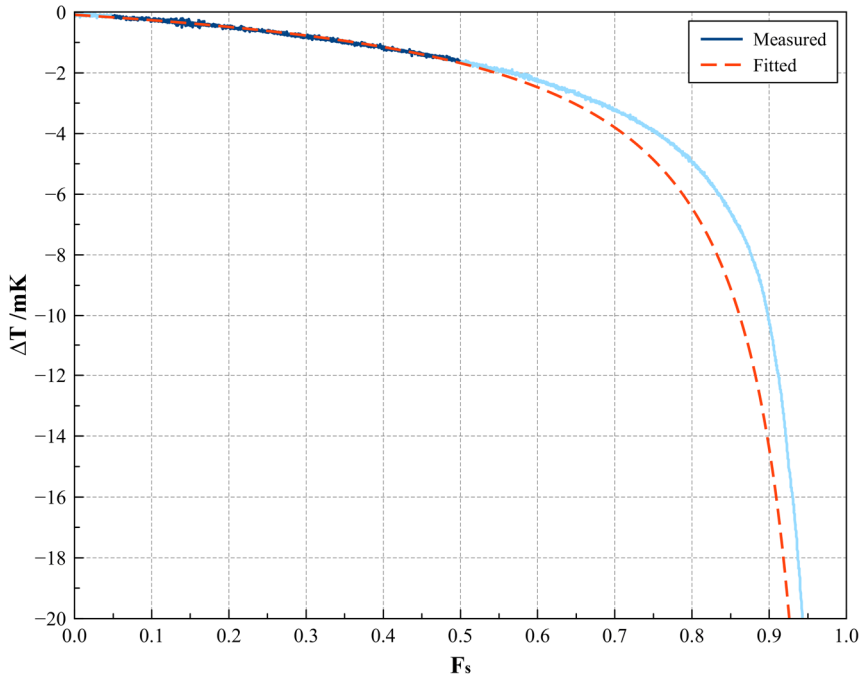

Figure 73: Scheil model applied to curve 2 measured in cell Al-S (Sumitomo). Fitting range from F_s 0.05 to F_s 0.50 (lower limit). Coefficient *k* fixed as 0.

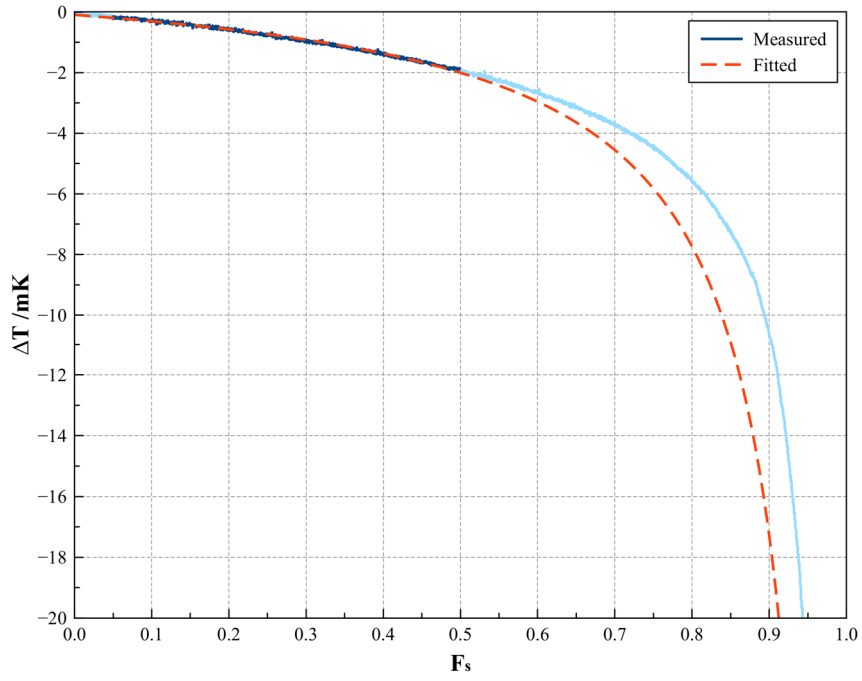

Figure 74: Scheil model applied to curve 3 measured in cell Al-S (Sumitomo). Fitting range from F_s 0.05 to F_s 0.50 (lower limit). Coefficient *k* fixed as 0.

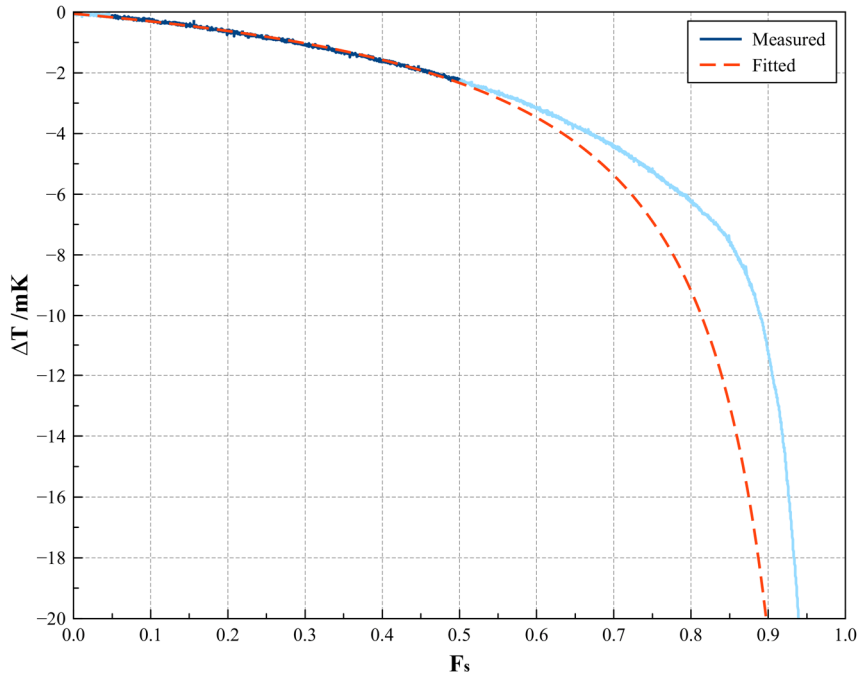

Figure 75: Scheil model applied to curve 4 measured in cell Al-S (Sumitomo). Fitting range from F_s 0.05 to F_s 0.50 (lower limit). Coefficient *k* fixed as 0.

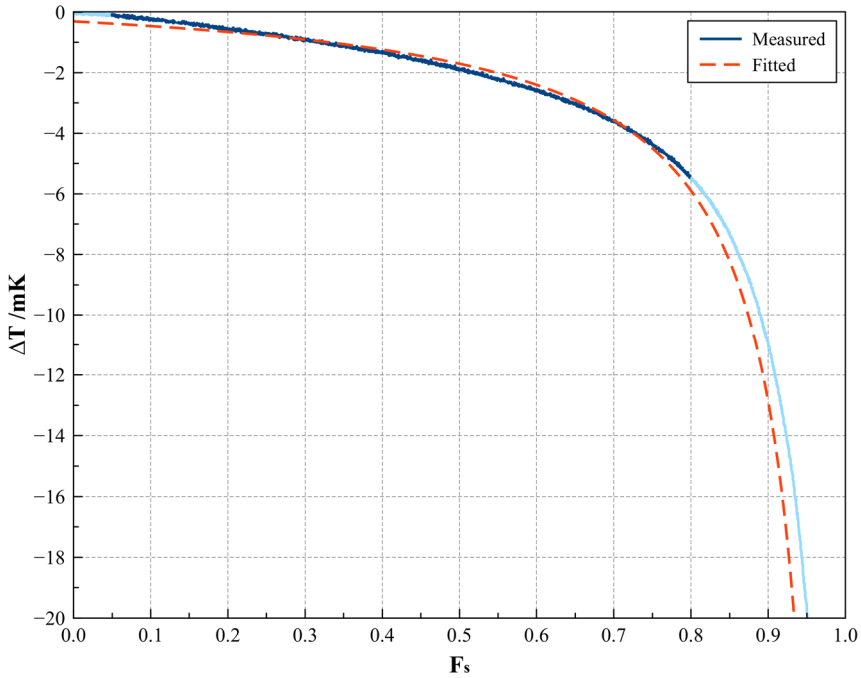

Figure 76: Scheil model applied to curve 1 measured in cell Al-S (Sumitomo). Fitting range from F_s 0.05 to F_s 0.80 (upper limit). Coefficient *k* fixed as 0.

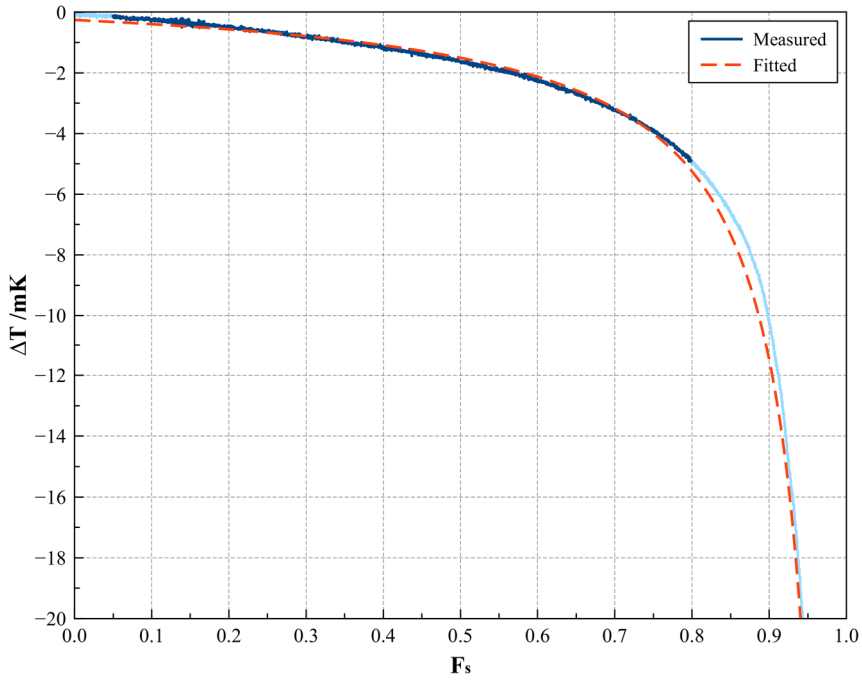

Figure 77: Scheil model applied to curve 2 measured in cell Al-S (Sumitomo). Fitting range from F_s 0.05 to F_s 0.80 (upper limit). Coefficient *k* fixed as 0.

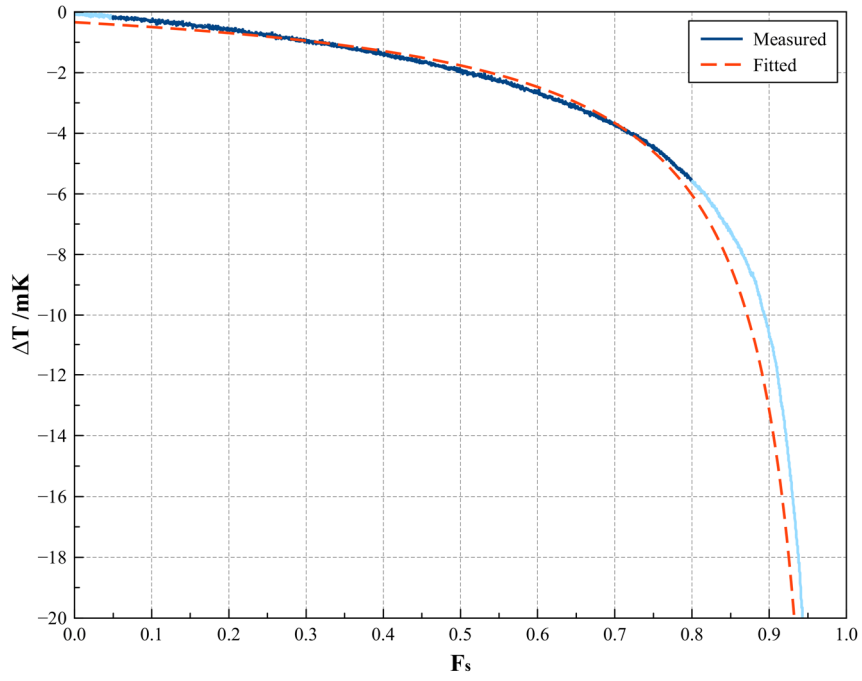

Figure 78: Scheil model applied to curve 3 measured in cell Al-S (Sumitomo). Fitting range from F_s 0.05 to F_s 0.80 (upper limit). Coefficient *k* fixed as 0.

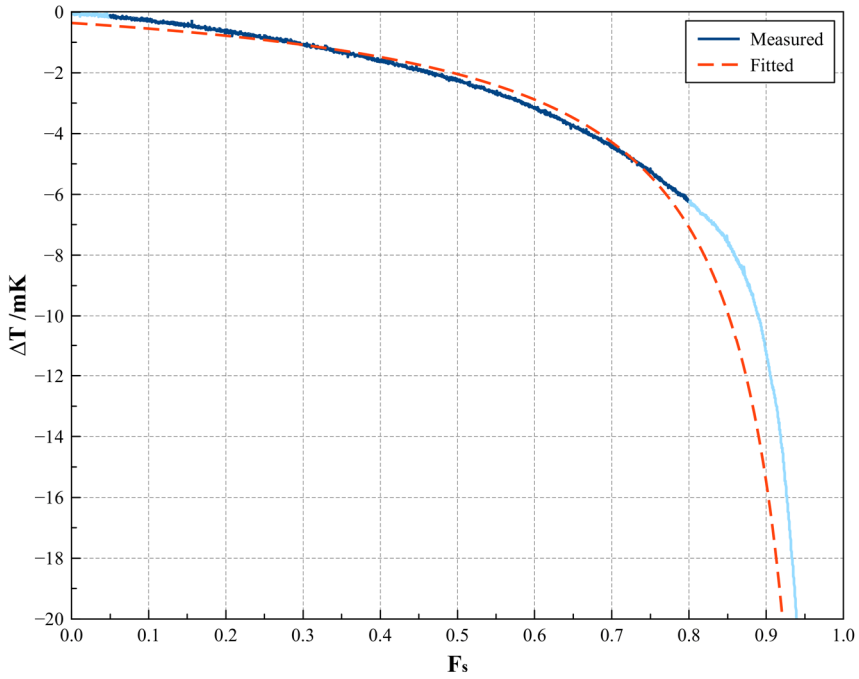

Figure 79: Scheil model applied to curve 4 measured in cell Al-S (Sumitomo). Fitting range from F_s 0.05 to F_s 0.80 (upper limit). Coefficient *k* fixed as 0.

Fitting parameters		Curve #1 mK	Curve #2 mK	Curve #3 mK	Curve #4 mK
***k* = 0**	**Range $F_{s\ 0.05-0.50}$**	– 1.90	– 1.59	– 1.91	– 2.28
	Range $F_{s\ 0.05-0.80}$	– 1.40	– 1.25	– 1.42	– 1.68

Table 47: Estimates based on least square fitting of Scheil equation to the freezing curves measured with cell Al-S (Sumitomo).

Fitting parameters		Correction mK	Uncertainty mK
***k* = 0**	**Range $F_{s\ 0.05-0.50}$**	1.92	0.28
	Range $F_{s\ 0.05-0.80}$	1.44	0.18

Table 48: Results based on least square fitting of Scheil equation to the freezing curves measured with cell Al-S (Sumitomo).

Similarly to the previous variation of the Scheil method, the corrections are given by the additive inverse of the averaged estimate for the four freezing curves, with the uncertainties being the respective standard deviations. From the results above for cell Al-S, better results were achieved with the lower range (F_s 0.05 to F_s 0.50), if the convergence of the fittings over the measured curves were taken into consideration. Despite the first freezing curve measured having a slightly flatter slope in relation to the others, as highlighted before, in this methodology the differences in the shape of the curves were smoothed out.

Because of the shape of the curves measured with cell Al-A, it would not be reasonable to fit the curves over both the steep beginning and the flatter region past F_s 0.25, since the fitted curve would not converge to the shape of the measured curve. As shown in figure 80, it was even attempted to apply the same ranges of the fittings for this cell but the convergence of the fitted curves was not appropriate for the analysis.

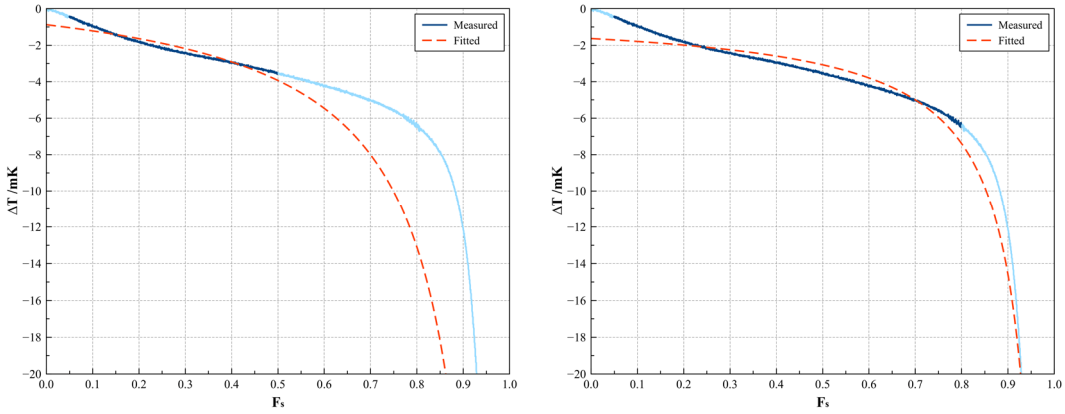

Figure 80: Scheil model (with *k* being fixed as zero) applied to curve 1 measured in cell Al-A (Alfa Aesar).

Considering that the fitting had to be performed with *k* being set as zero for this variation, it was decided to disregard the portion of the curves influenced by the high *k* impurity concentration. In order to obtain the correction values for this cell according to this variation, the temperature difference measured at F_s 0.25 was used in conjunction with the fitted value for the slope in the selected ranges. The solid fraction equivalent for the fitting range minimum was 0.2875 and the maximum values were 0.625 and 0.85 (taking into account that the curves were only 0.75x the usual duration of the curves). The fitted curves with these adjustments are given in figure 81 (upper limit at F_s 0.625) and figure 82 (upper limit at F_s 0.85). The estimates calculated based on these fittings are provided in table 49 with the results being displayed in table 50.

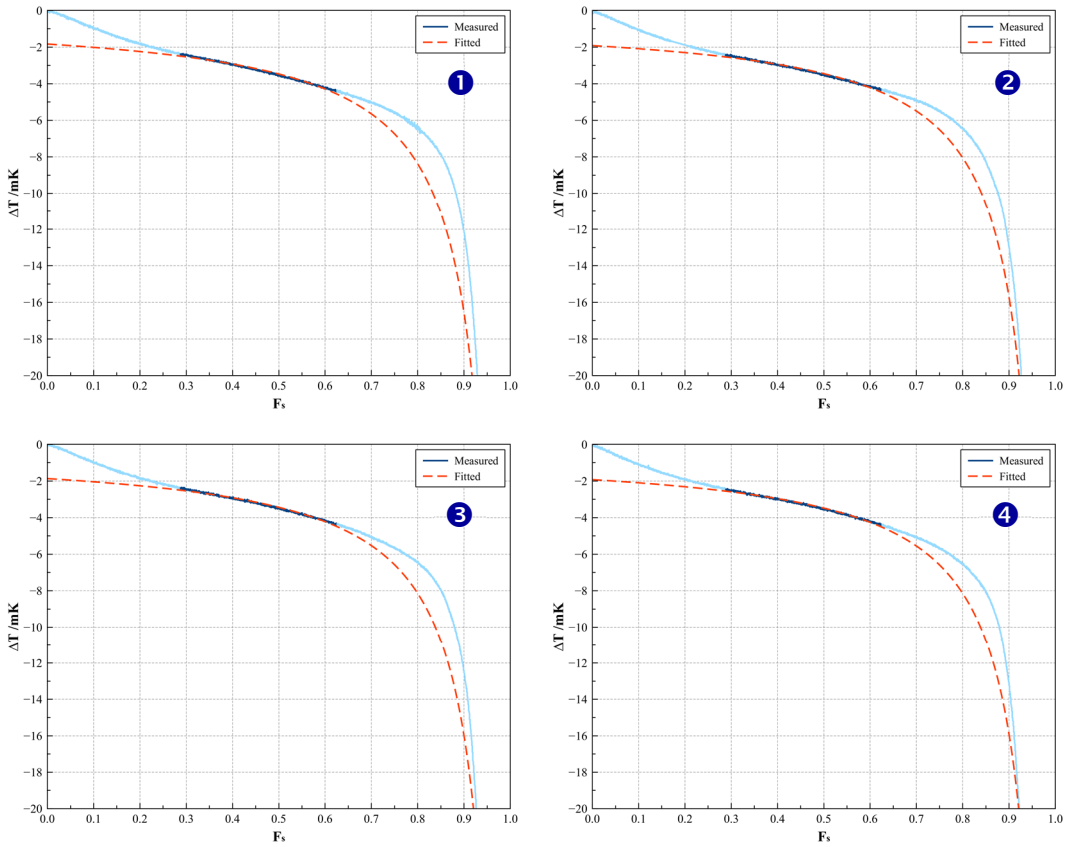

Figure 81: Curves (cell Al-A) fitted with Scheil equation after the range adjustments. Range set as F_s 0.2875 to F_s 0.625, with *k* being set as zero.

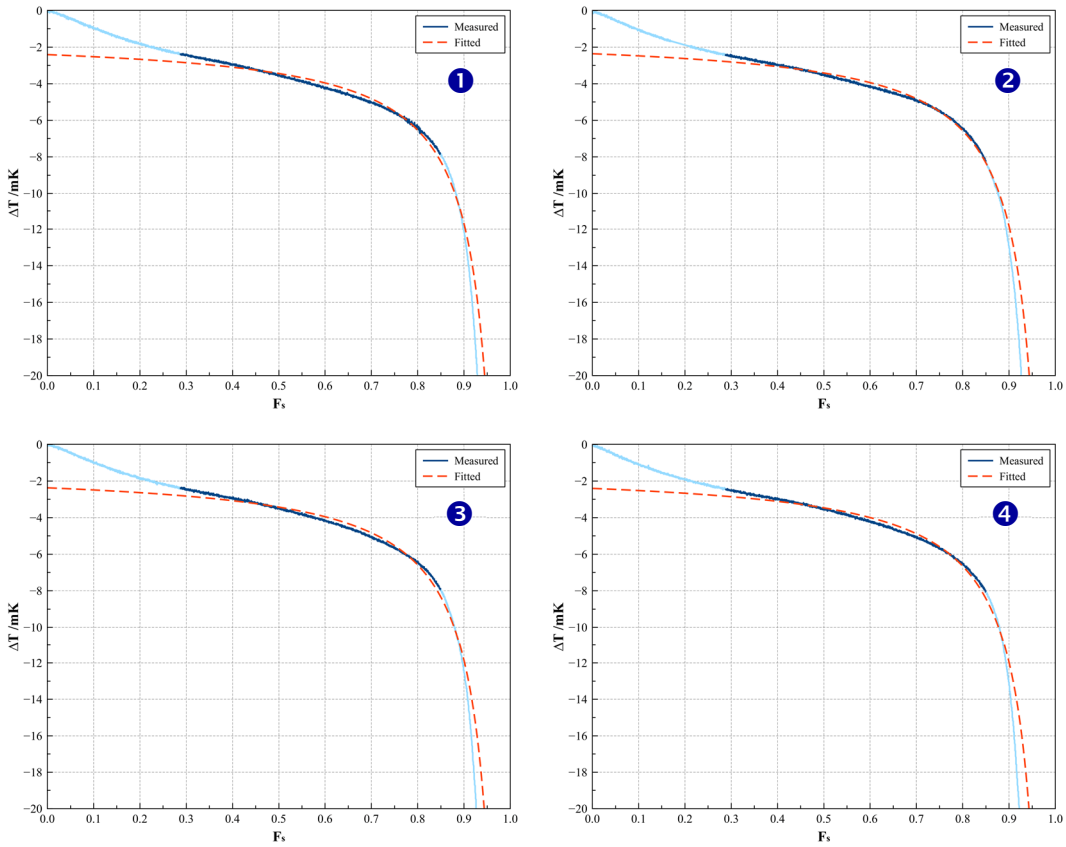

Figure 82: Curves (cell Al-A) fitted with Scheil equation after the range adjustments. Range set as F_s 0.2875 to F_s 0.85, with *k* being set as zero.

From figures 81 and 82 above, it is possible to note that the fittings performed with the range maximum set at F_s 0.625 (lower range) provided good agreement with the measured curves, whereas the fittings done based at the upper maximum (F_s 0.85) did not show much convergence to the measured curves, which indicates that the latter would not be as reliable as the former.

Fitting parameters		Curve #1 mK	Curve #2 mK	Curve #3 mK	Curve #4 mK
$k = 0$	**Correction at $T_{Fs\ 0.25}$**	+ 2.12	+ 2.17	+ 2.20	+ 2.22
	Range $F_{s\ 0.2875 - 0.625}$	– 1.64	– 1.53	– 1.57	– 1.56
	Range $F_{s\ 0.2875 - 0.85}$	– 1.03	– 1.05	– 1.05	– 1.06

Table 49: Estimates based on least square fitting of Scheil equation (with $k = 0$) to the freezing curves measured with cell Al-A (Alfa Aesar).

Fitting parameters		Correction mK	Uncertainty mK
$k = 0$	**Range $F_{s\ 0.2875 - 0.625}$**	– 0.73	0.22
	Range $F_{s\ 0.2875 - 0.85}$	– 1.13	0.03

Table 50: Results based on least square fitting of Scheil equation (with $k = 0$) to the freezing curves measured with cell Al-A (Alfa Aesar).

In order to obtain the corrections assigned for this particular cell according to the Scheil methodology ($k = 0$), the fitted values for each curve were firstly combined with the corresponding temperature value at F_s 0.25 to account for the bias at the initial portion of the curve that had prevented the application of the coefficient k fixed as zero. After this, the values were averaged and the correction taken as the additive inverse of the mean.

From the results above, it was observed that the influence of high k impurities present in this aluminium sample was greater than the estimated values of mc_0 obtained through the fittings. Again, the fittings performed in the lower range (F_s 0.2875 to F_s 0.625) provided good convergence to the measured curves. As for the fittings done in the upper range, on the other hand, the convergence was not as adequate. Given the constraints related to the peculiar shape of the freezing curves produced with cell Al-A and the fact that for this variation the coefficient k has to be

fixed as zero, these results should be regarded as illustrative only because of the limitations and adaptations that have to be done in order to achieve coherent results.

Application of the fittings for the freezing curves measured with cell Al-E (made with ESPI aluminium samples) was more straightforward than for the previous curves and showed results that were consistent with the purity of the material. The ranges applied were the same used for cel Al-S. The corresponding graphs for cell Al-E are provided in figures 83 (for the lower limit, F_s 0.50) and 84 (for the upper limit, F_s 0.80). The resulting estimates are provided in table 51, while the calculated corrections and uncertainties are shown in table 52.

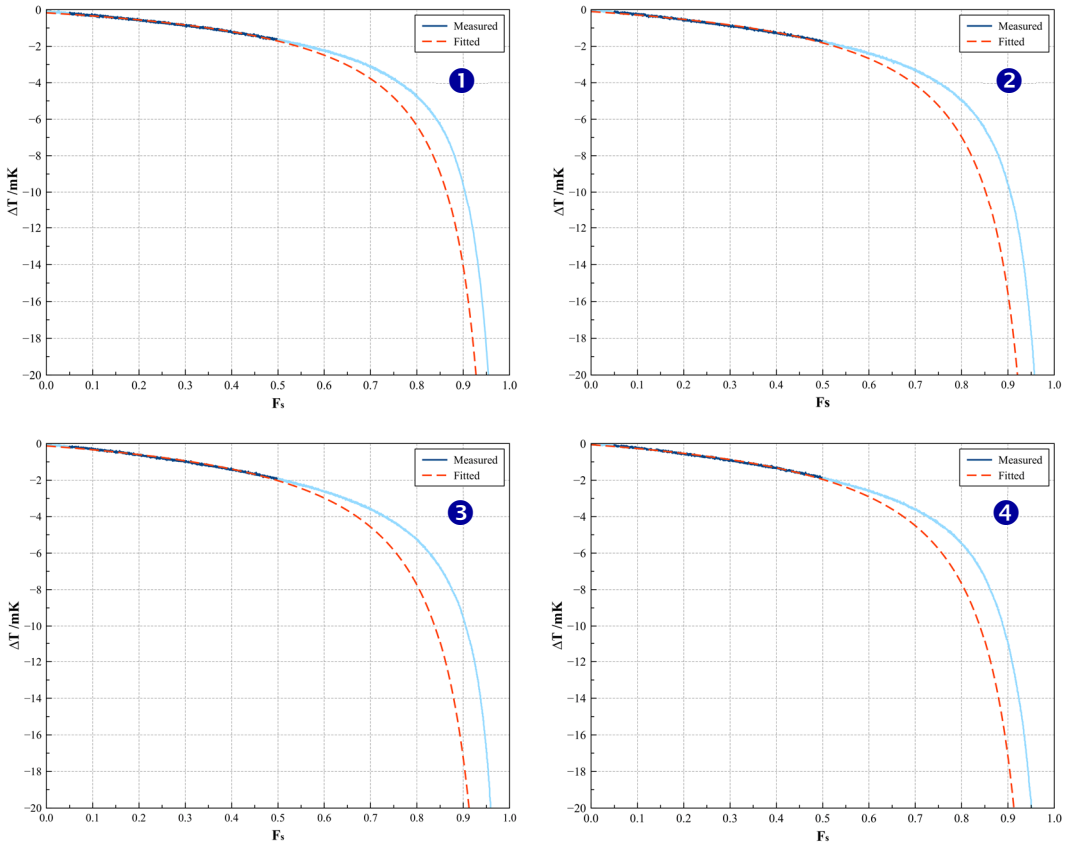

Figure 83: Scheil model applied to the freezing curves measured in cell Al-E (ESPI). Fitting range from F_s 0.05 to F_s 0.50 (lower limit). Coefficient *k* fixed as 0.

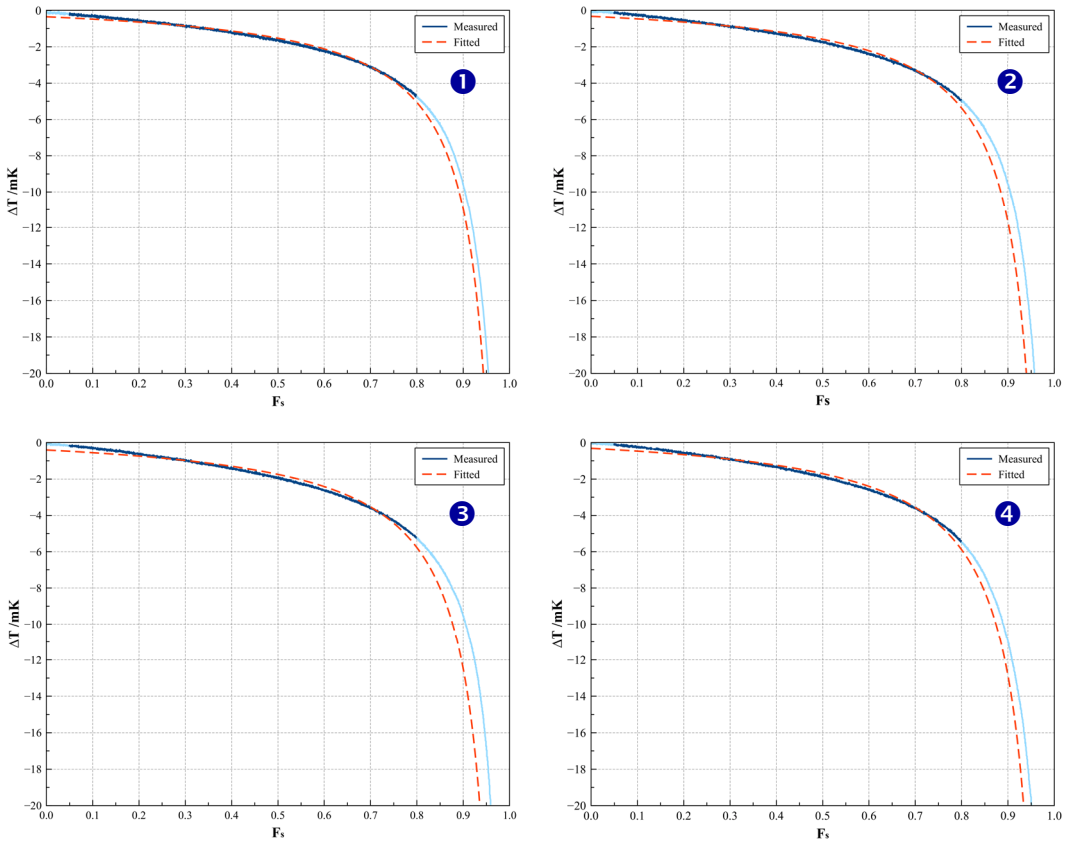

Figure 84: Scheil model applied to the freezing curves measured in cell Al-E (ESPI). Fitting range from F_s 0.05 to F_s 0.80 (upper limit). Coefficient *k* fixed as 0.

Fitting parameters		Curve #1 mK	Curve #2 mK	Curve #3 mK	Curve #4 mK
***k* = 0**	**Range $F_{s\ 0.05-0.50}$**	– 1.55	– 1.72	– 1.90	– 1.90
	Range $F_{s\ 0.05-0.80}$	– 1.18	– 1.26	– 1.34	– 1.40

Table 51: Estimates based on least square fitting of Scheil equation to the freezing curves measured with cell Al-E (ESPI).

Fitting parameters		Correction mK	Uncertainty mK
$k = 0$	**Range $F_{s\ 0.05 - 0.50}$**	1.77	0.17
	Range $F_{s\ 0.05 - 0.80}$	1.30	0.10

Table 52: Results based on least square fitting of Scheil equation to the freezing curves measured with cell Al-E (ESPI).

Based on the results for cell Al-E, it is possible to observe that the fittings in the lower range (F_s 0.05 to F_s 0.50) resulted in greater convergence with the measured curves. Again, the differences in the shape of the curves were smoothed out in this methodology.

The fittings performed with cell Al-H (made with aluminium samples supplied by Honeywell) exhibited similar characteristics to the results obtained with cells Al-E and Al-S. Figure 85 (for the lower limit) and figure 86 (for the upper limit) show the fittings on the freezing curves. The estimates obtained from the fittings are tabulated in table 53, the corrections and uncertainties are given in table 54.

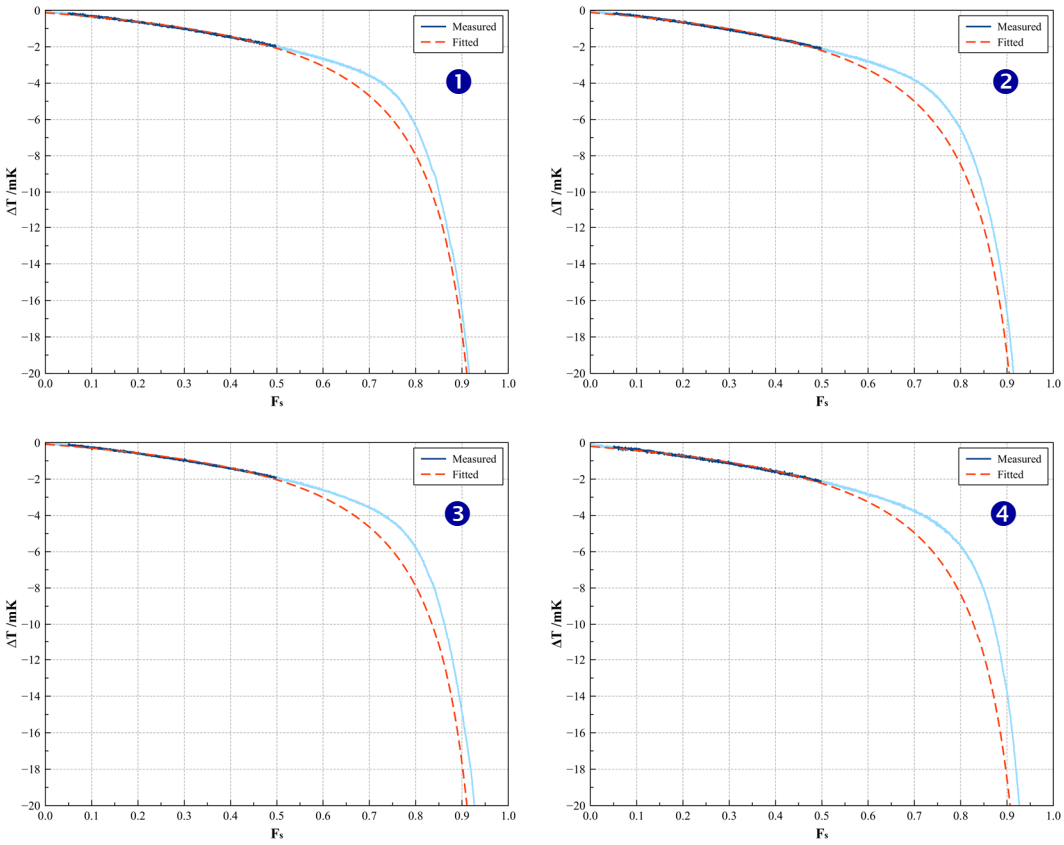

Figure 85: Scheil model applied to the freezing curves measured in cell Al-H (Honeywell). Fitting range from F_s 0.05 to F_s 0.50 (lower limit). Coefficient *k* fixed as 0.

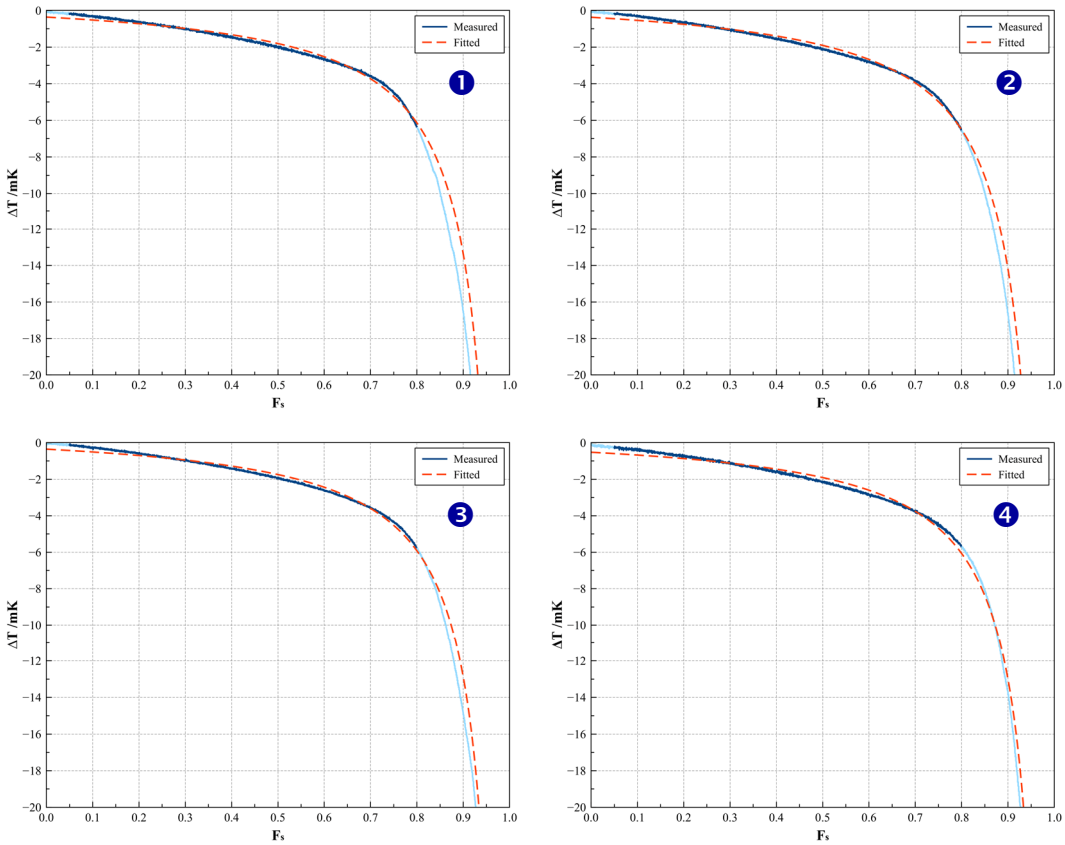

Figure 86: Scheil model applied to the freezing curves measured in cell Al-H (Honeywell). Fitting range from F_s 0.05 to F_s 0.80 (upper limit). Coefficient *k* fixed as 0.

	Fitting parameters	Curve #1 mK	Curve #2 mK	Curve #3 mK	Curve #4 mK
***k* = 0**	**Range $F_{s\ 0.05-0.50}$**	– 1.96	– 2.10	– 1.95	– 2.04
	Range $F_{s\ 0.05-0.80}$	– 1.44	– 1.54	– 1.39	– 1.39

Table 53: Estimates based on least square fitting of Scheil equation to the freezing curves measured with cell Al-H (Honeywell).

Fitting parameters		Correction mK	Uncertainty mK
$k = 0$	**Range $F_{s\ 0.05-0.50}$**	2.01	0.07
	Range $F_{s\ 0.05-0.80}$	1.44	0.07

Table 54: Results based on least square fitting of Scheil equation to the freezing curves measured with cell Al-H (Honeywell).

Despite the anomalous shape of the freezing curves measured with cell Al-N, the fittings could still be performed with the ranges used for the other cells (F_s 0.05 – 0.50 and F_s 0.05 – 0.80) not requiring a different treatment (as it happened to cell Al-A). In all freezing curves, application of the fittings in the lower range (up to F_s 0.50) was not disturbed by the discontinuity seen in the shape of the freezing plateau, towards the end of the curve. However, when it concerns the fittings done in the upper range (F_s 0.05 – 0.80), it is observed that this variation of the Scheil method was disturbed by the discontinuity. The fittings performed with cell Al-N are given in figure 87 (for the lower limit) and figure 88 (for the upper limit). The estimates obtained from the fittings are shown in table 55 and the respective corrections and uncertainties are tabulated in table 56.

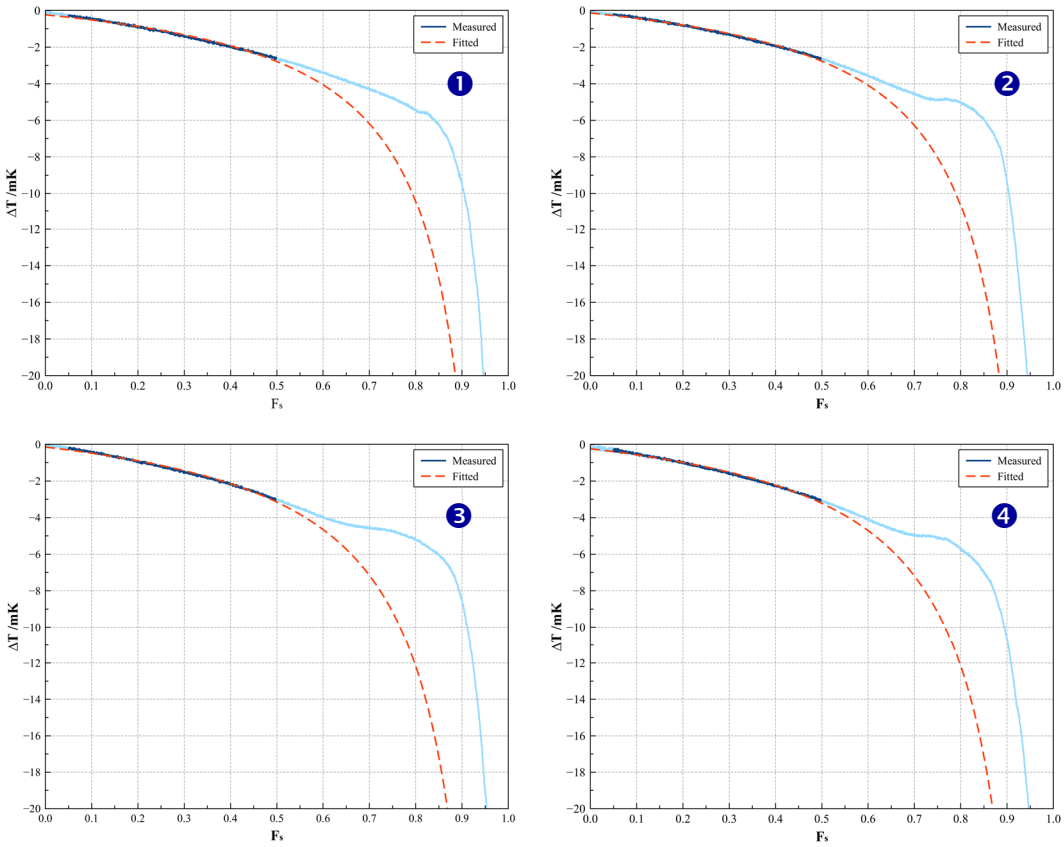

Figure 87: Scheil model applied to the freezing curves measured in cell Al-N (New Metals). Fitting range from F_s 0.05 to F_s 0.50 (lower limit). Coefficient *k* fixed as 0.

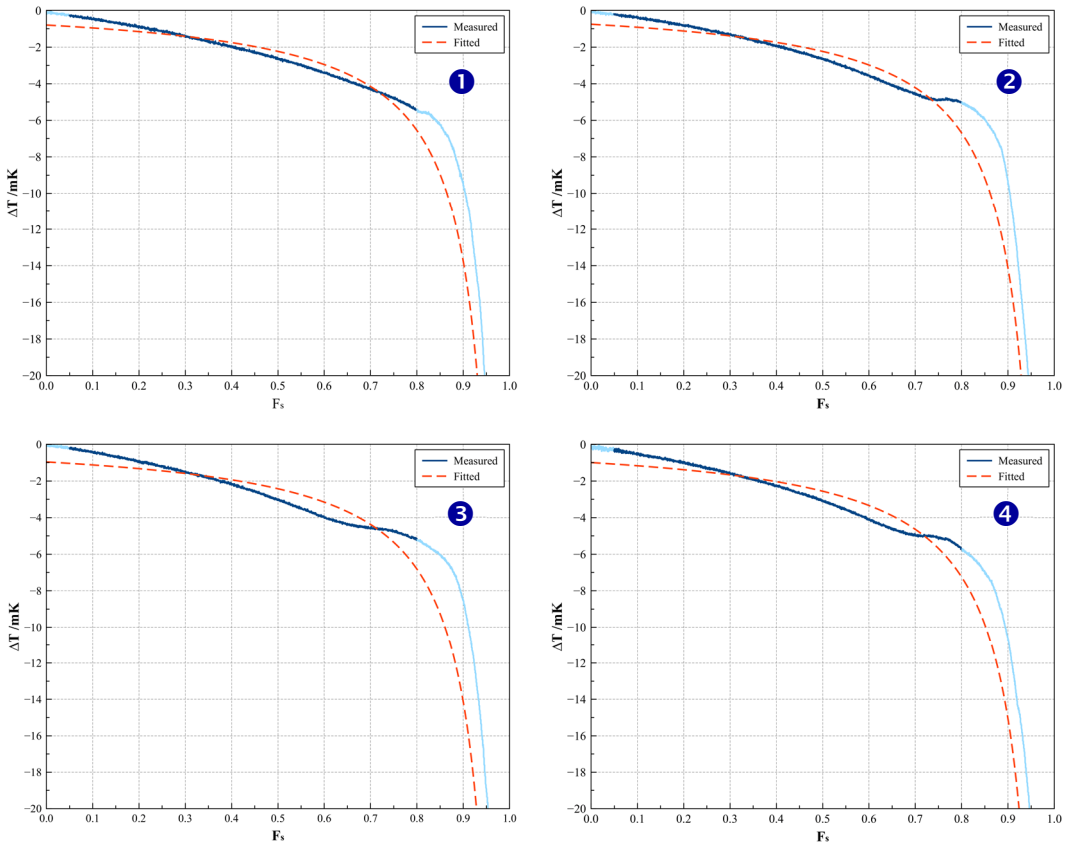

Figure 88: Scheil model applied to the freezing curves measured in cell Al-N (New Metals). Fitting range from F_s 0.05 to F_s 0.80 (upper limit). Coefficient *k* fixed as 0.

Fitting parameters		Curve #1 mK	Curve #2 mK	Curve #3 mK	Curve #4 mK
***k* = 0**	**Range $F_{s\ 0.05-0.50}$**	– 2.55	– 2.64	– 3.01	– 2.98
	Range $F_{s\ 0.05-0.80}$	– 1.44	– 1.49	– 1.46	– 1.56

Table 55: Estimates based on least square fitting of Scheil equation to the freezing curves measured with cell Al-N (New Metals).

Fitting parameters		Correction mK	Uncertainty mK
$k = 0$	**Range $F_{s\ 0.05 - 0.50}$**	2.79	0.23
	Range $F_{s\ 0.05 - 0.80}$	1.49	0.06

Table 56: Results based on least square fitting of Scheil equation to the freezing curves measured with cell Al-N (New Metals).

Differently from the performances of the cells Al-E, Al-H and Al-S in the upper range (whose fittings were comparatively not as consistent with the shape of the curves as they were in the lower range), the fittings obtained with cell Al-N in this range did not converge at all to the measured curves (figure 88). Consequently, the estimates obtained in upper range are provided for illustration only, since they lack reliability.

6.5. Gradient method correction and uncertainty calculation

After estimates were calculated according to the Scheil methodology, the gradient method was applied to the freezing curves obtained with the aluminium cells. Since this method is a shortcut to the Scheil methodology, its application was simpler, requiring a single linear fitting around the centre point of the freezing plateau, F_s 0.50. In order to achieve this with great accuracy, a linear fitting was performed over a narrow range, F_s 0.45 to F_s 0.55. Afterwards, with the resulting slope and intercept coefficients obtained, the corrections according to the gradient method were calculated through the application of equation 24.

The fittings (and schematic representation of the parameters) performed in order to obtain the corrections for cell Al-S are exemplified in figures 89 to 92, with the corresponding results tabulated in table 57. The uncertainties were given by the deviations of the coefficients and the standard deviation of the corrections all summed in quadrature.

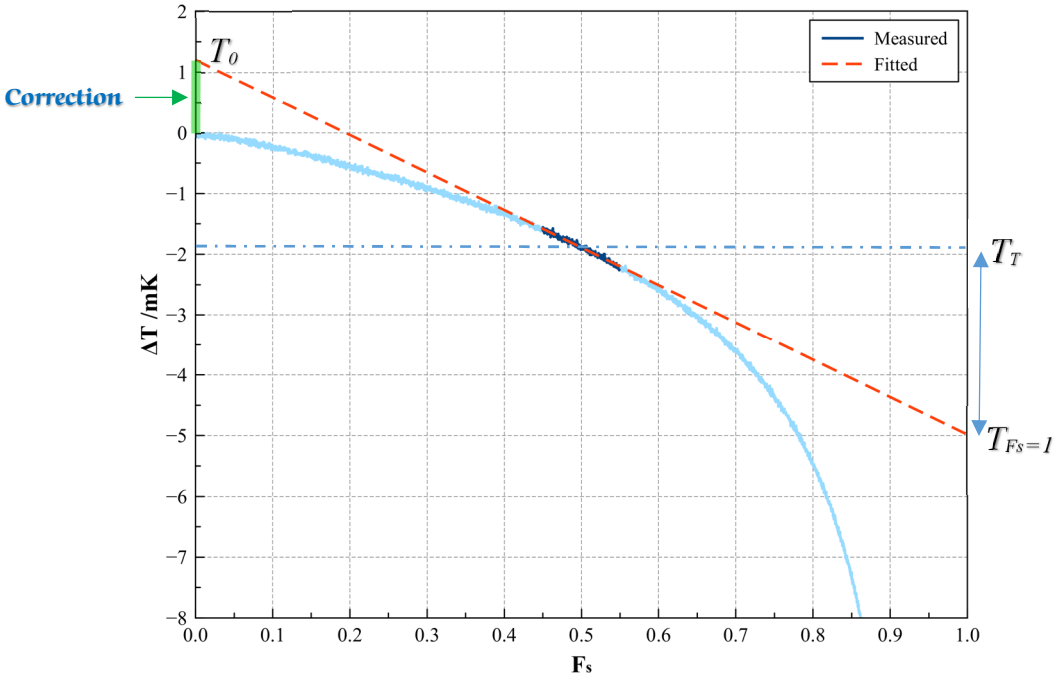

Figure 89: Gradient method applied to curve 1 measured in cell Al-S (Sumitomo). Fitting range from F_s 0.45 to F_s 0.55.

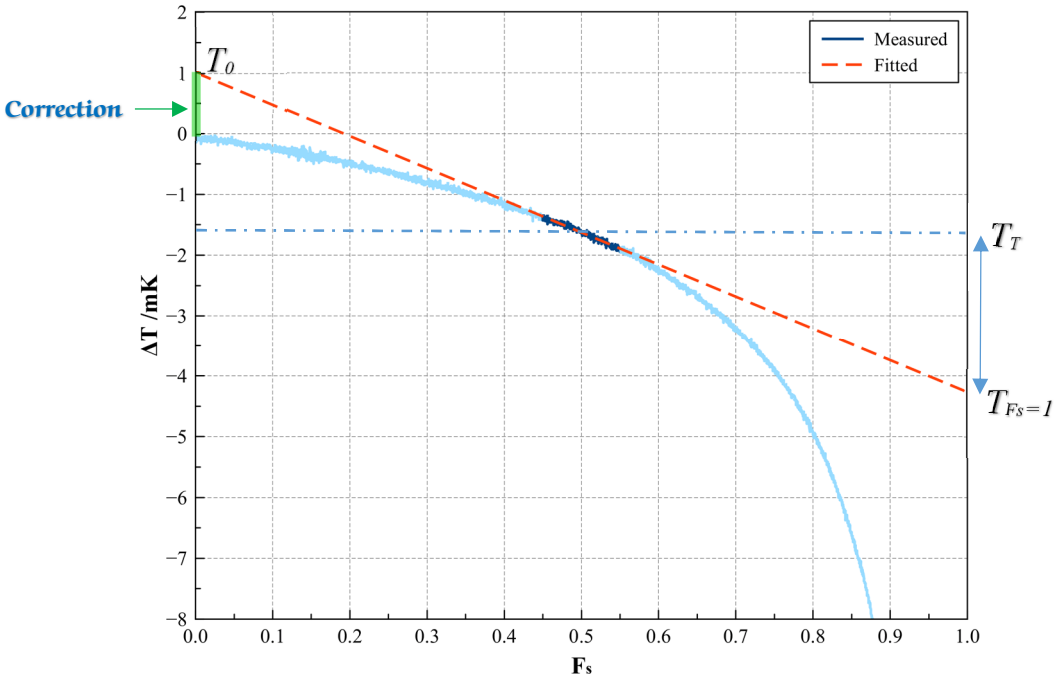

Figure 90: Gradient method applied to curve 2 measured in cell Al-S (Sumitomo). Fitting range from F_s 0.45 to F_s 0.55.

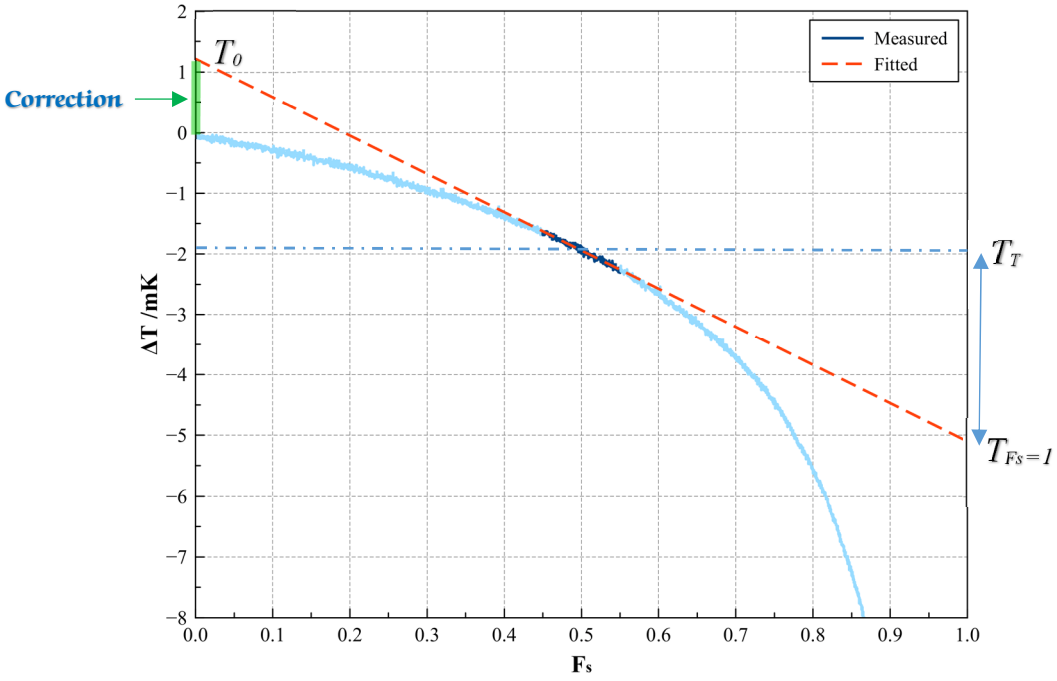

Figure 91: Gradient method applied to curve 3 measured in cell Al-S (Sumitomo). Fitting range from F_s 0.45 to F_s 0.55.

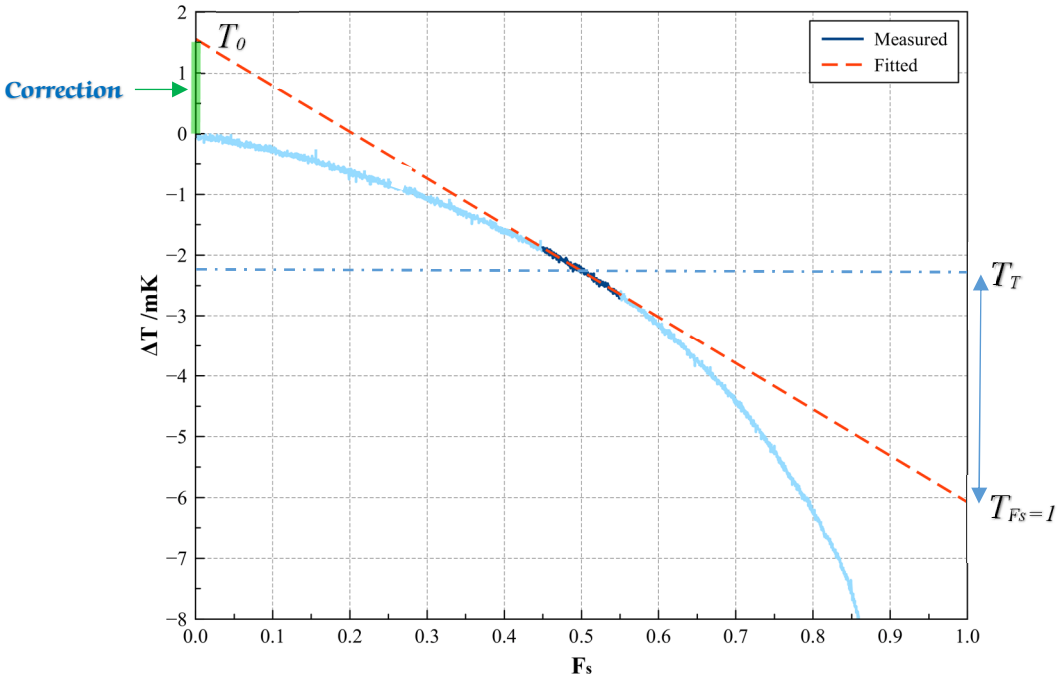

Figure 92: Gradient method applied to curve 4 measured in cell Al-S (Sumitomo). Fitting range from F_s 0.45 to F_s 0.55.

Fitting results	*a* mK	*b* mK	u_a mK	u_b mK	T_T mK	$T_{Fs=1}$ mK	ΔT mK	T_0 *(Correction)* mK
Curve #1	– 6.19	1.20	0.04	0.02	– 1.89	– 4.98	3.09	1.19
Curve #2	– 5.31	1.03	0.05	0.03	– 1.62	– 4.28	2.66	1.02
Curve #3	– 6.30	1.21	0.05	0.02	– 1.94	– 5.09	3.15	1.20
Curve #4	– 7.60	1.54	0.05	0.02	– 2.26	– 6.06	3.81	1.55

Correction	1.27 mK
Uncertainty	0.26 mK

Table 57: Results of the fittings according to the gradient method for cell Al-S.

In this methodology, the correction assigned to the cells was obtained directly by the average of the corrections calculated for each freezing curve based on equation 24. The corrections obtained are consistent with the expected corrections for the level of purity of the aluminium samples employed in the construction. Overall, the differences

observed in the freezing curves measurements did not match the gradient methodology results. The cells did present some variation in the calculated correction values but these did not match the slopes observed in the freezing curves. As an example, this can be observed for cell Al-S: the first curve presented the flattest plateau whilst the other three curves showed great reproducibility. Despite this, neither the correction calculated for the first curve was the smallest of the four nor the following curves presented very similar calculated values. The fitted curves for the other cells are presented below, together with a summary of results for each cell being given subsequently. The results are given as follows: figure 93 and table 58 show the results for cell Al-A, figure 94 and table 59 present the results for cell Al-E, figure 95 and table 60 give the results for cell Al-H while figure 96 and table 61 display the outcome obtained with cell Al-N.

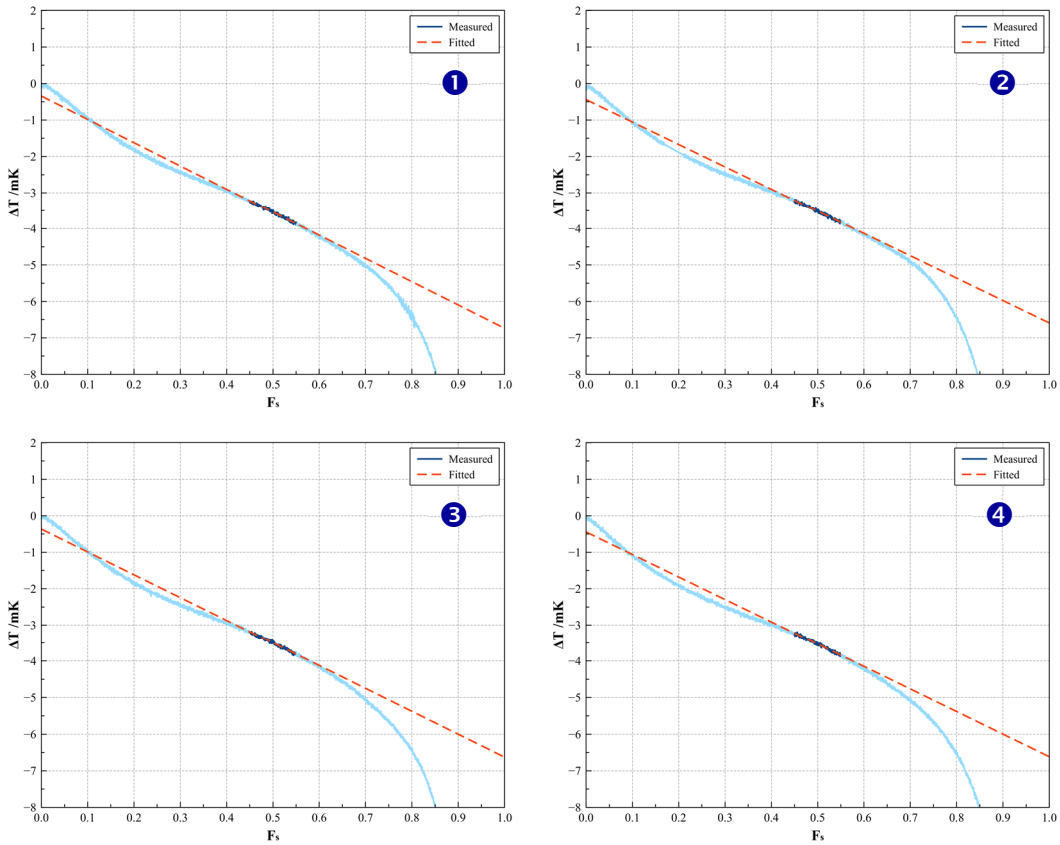

Figure 93: Gradient method applied to the freezing curves measured with cell Al-A. Fitting range from F_s 0.45 to F_s 0.55.

Fitting results	*a* mK	*b* mK	u_a mK	u_b mK	T_T mK	$T_{Fs=1}$ mK	ΔT mK	T_0 *(Correction)* mK
Curve #1	– 6.39	– 0.34	0.04	0.02	– 3.54	– 6.74	3.20	– 0.34
Curve #2	– 6.15	– 0.44	0.04	0.02	– 3.50	– 6.59	3.09	– 0.41
Curve #3	– 6.26	– 0.36	0.04	0.02	– 3.49	– 6.63	3.14	– 0.35
Curve #4	– 6.17	– 0.44	0.04	0.02	– 3.51	– 6.62	3.10	– 0.41

Correction	– 0.38 mK
Uncertainty	0.10 mK

Table 58: Results of the fittings according to the gradient method for cell Al-A (Alfa Aesar).

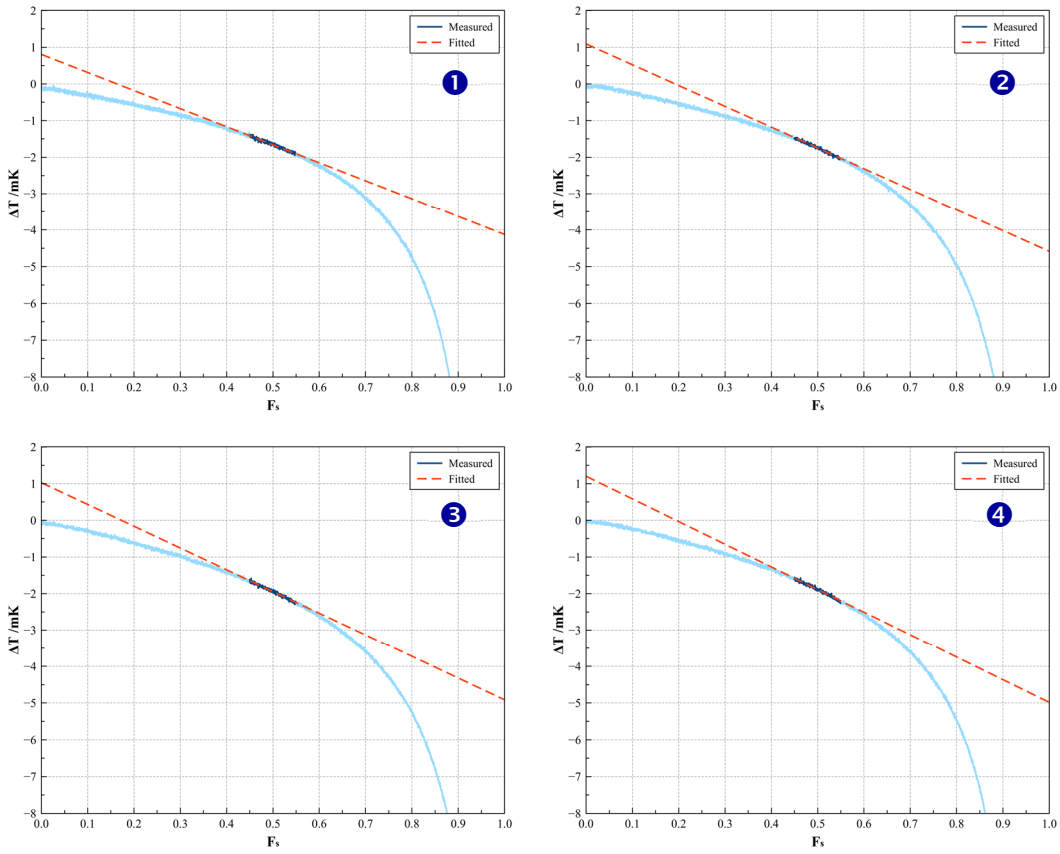

Figure 94: Gradient method applied to the freezing curves measured with cell Al-E. Fitting range from F_s 0.45 to F_s 0.55.

Fitting results	***a*** **mK**	***b*** **mK**	u_a **mK**	u_b **mK**	T_T **mK**	$T_{Fs=1}$ **mK**	**ΔT mK**	T_0 ***(Correction)*** **mK**
Curve #1	– 4.93	0.80	0.04	0.02	– 1.62	– 4.12	2.50	0.88
Curve #2	– 5.68	1.09	0.04	0.02	– 1.71	– 4.58	2.87	1.16
Curve #3	– 5.94	1.03	0.04	0.02	– 1.92	– 4.91	3.00	1.08
Curve #4	– 6.19	1.20	0.04	0.02	– 1.92	– 4.98	3.06	1.14

Correction	1.07 mK
Uncertainty	0.16 mK

Table 59: Results of the fittings according to the gradient method for cell Al-E (ESPI).

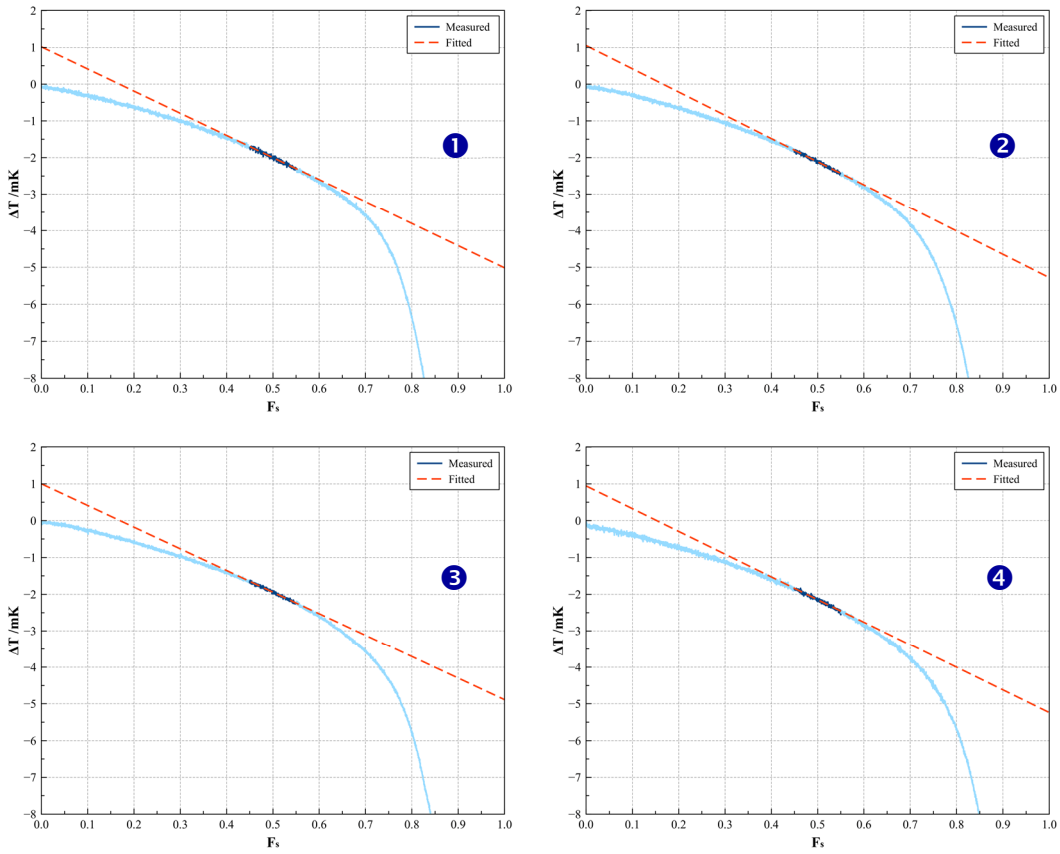

Figure 95: Gradient method applied to the freezing curves measured with cell Al-H. Fitting range from F_s 0.45 to F_s 0.55.

Fitting results	***a*** **mK**	***b*** **mK**	u_a **mK**	u_b **mK**	T_T **mK**	$T_{Fs=1}$ **mK**	**ΔT mK**	T_0 ***(Correction)*** **mK**
Curve #1	– 6.03	1.01	0.04	0.02	– 2.04	– 5.01	2.97	0.94
Curve #2	– 6.33	1.05	0.04	0.02	– 2.11	– 5.28	3.17	1.06
Curve #3	– 5.89	1.00	0.04	0.02	– 1.91	– 4.89	2.98	1.06
Curve #4	– 6.18	0.94	0.04	0.02	– 2.20	– 5.24	3.04	0.84

Correction	1.27 mK
Uncertainty	0.14 mK

Table 60: Results of the fittings according to the gradient method for cell Al-H (Honeywell).

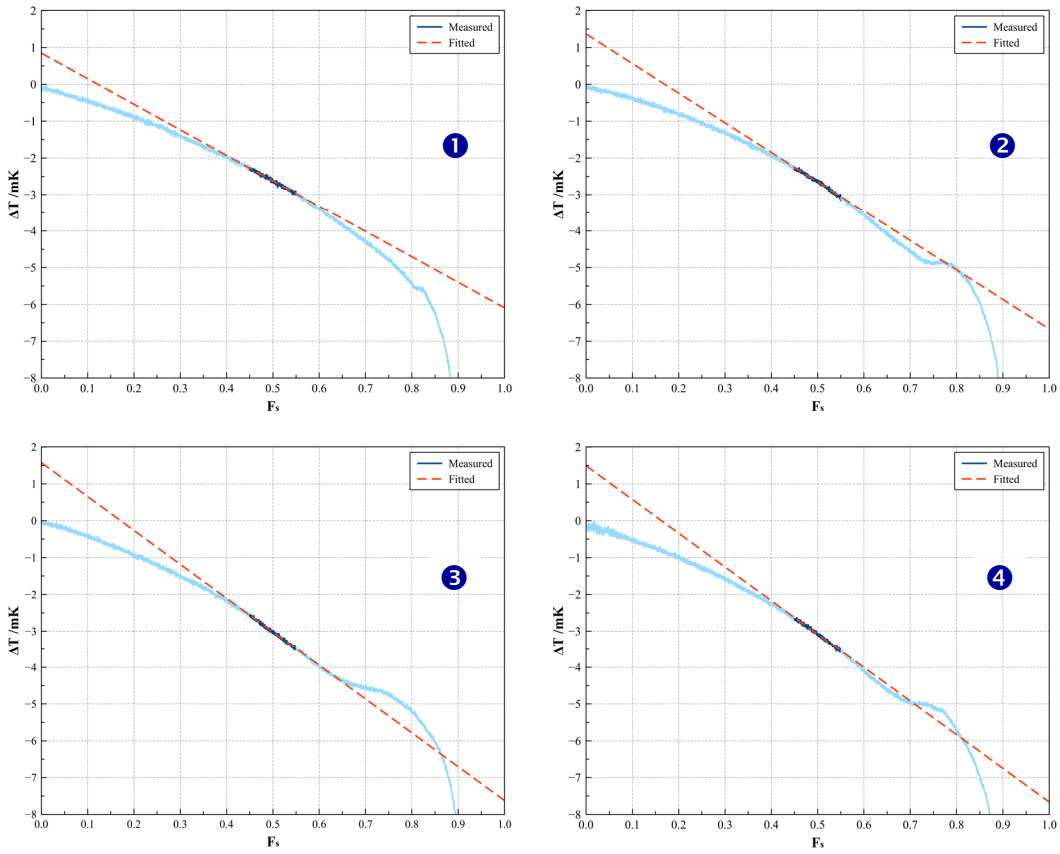

Figure 96: Gradient method applied to the freezing curves measured with cell Al-N. Fitting range from F_s 0.45 to F_s 0.55.

Fitting results	*a* mK	*b* mK	u_a mK	u_b mK	T_T mK	$T_{Fs=1}$ mK	ΔT mK	T_0 *(Correction)* mK
Curve #1	– 6.94	0.84	0.04	0.02	– 2.66	– 6.09	3.43	0.77
Curve #2	– 8.04	1.37	0.04	0.02	– 2.59	– 6.67	4.08	1.48
Curve #3	– 9.20	1.58	0.04	0.02	– 3.02	– 7.62	4.61	1.59
Curve #4	– 9.16	1.49	0.05	0.02	– 3.10	– 7.66	4.56	1.46

Correction	1.32 mK
Uncertainty	0.39 mK

Table 61: Results of the fittings according to the gradient method for cell Al-N (New Metals).

Application of this methodology was simple and all curves from the five cells were quickly fitted without the need for any adjustments. It is noticeable how the linear fits filter the differences in performance of the cells. This might be due to the nature of the methodology: as the fit takes into account the temperature where half of the metal sample is frozen (F_s 0.50), it disregards the measurement information of the beginning and end sections of the freezings. For other methodologies, however, these parts are crucial for determining the fitting slopes and the respective corrections. Since the gradient method is intended as a quick fit, the main benefit of its application, when compared to more laborious approaches, is the ease and fast response in assigning a temperature correction for the cells.

6.6. Thermal analysis correction and uncertainty calculation

The last method involving the application of least-square fitting was the thermal analysis method (also known as the 1/F method). This method was applied according to the description contained in section 2.3.2.6, which also required that the data was plotted in terms of temperature difference, ΔT, versus the inverse of liquid fraction, $1/\mathrm{F}$. The liquid fraction is given by the additive inverse of the solid fraction $\mathrm{F_s}$. The procedure is summarised as the simple transformation below (equation 31):

$$1/F = (1 - F_s)^{-1} \tag{31}$$

A linear fitting was applied for the range from 1/F=1 to 1/F=1.5. Upon the resulting slope and intercept coefficients, the curve could be extrapolated to 1/F=0, which should correspond to the hypothetical freezing temperature of the 100 % pure aluminium. Then, the correction for the cell could be obtained by subtracting the calculated value at 1/F=0 from the temperature value at 1/F=1. However, since the 1/F values involved are 0 and 1, the calculation is simplified and the temperature correction is then given directly by the fitted value for the slope *a* of the curve. Then, the value assigned as the temperature correction according to the thermal analysis methodology was given by the additive inverse of the averaged fitted values of the slopes.

The fitting performed to obtain the corrections for cell Al-S are exemplified in figures 97 to 100 below. The results are subsequently tabulated in table 62. The uncertainties were obtained by summing in quadrature the deviations of the coefficients with the standard deviation of the corrections.

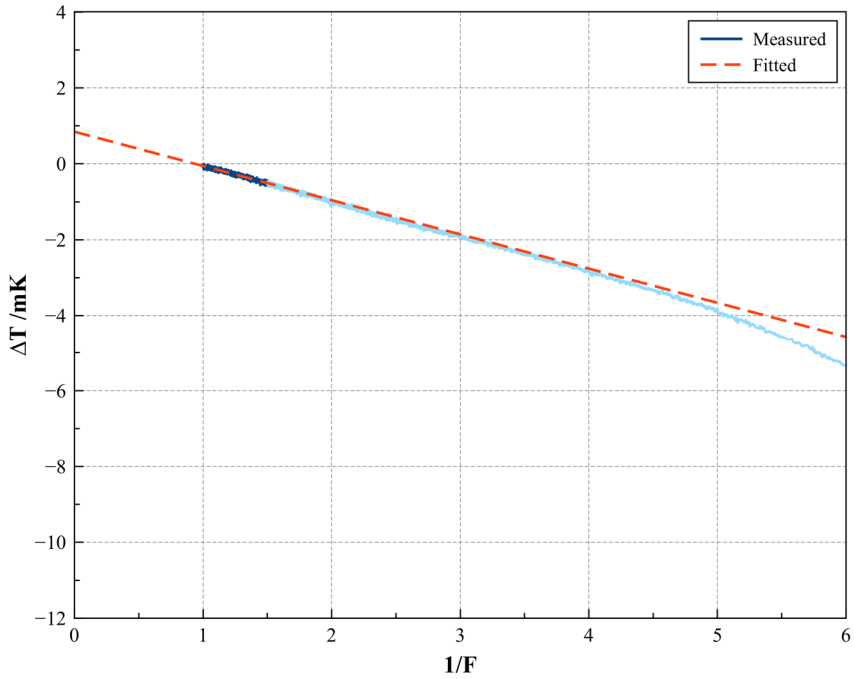

Figure 97: Thermal analysis method applied to curve 1 measured in cell Al-S (Sumitomo). Fitting range from 1/F=1 to 1/F=1.5.

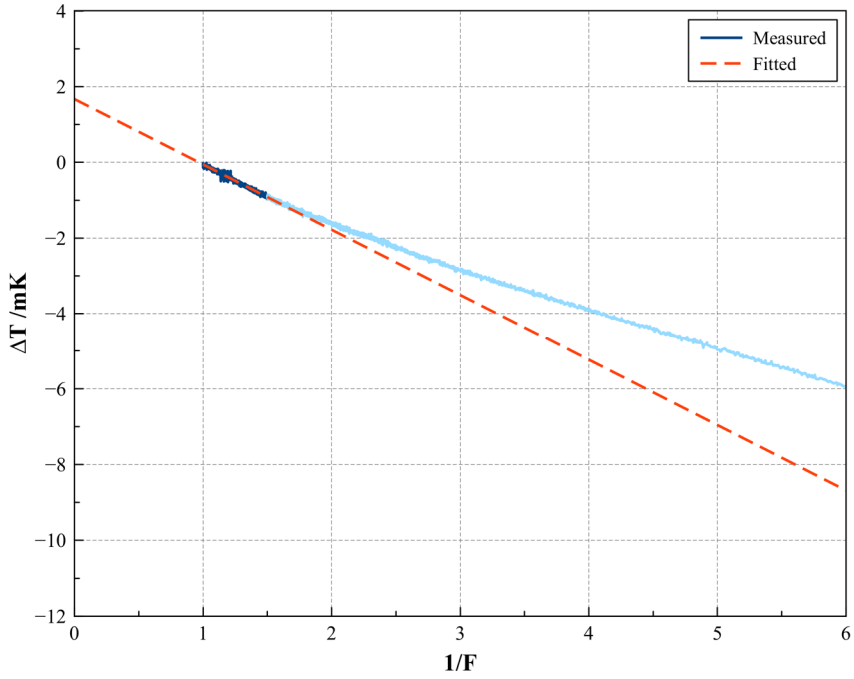

Figure 98: Thermal analysis method applied to curve 2 measured in cell Al-S (Sumitomo). Fitting range from 1/F=1 to 1/F=1.5.

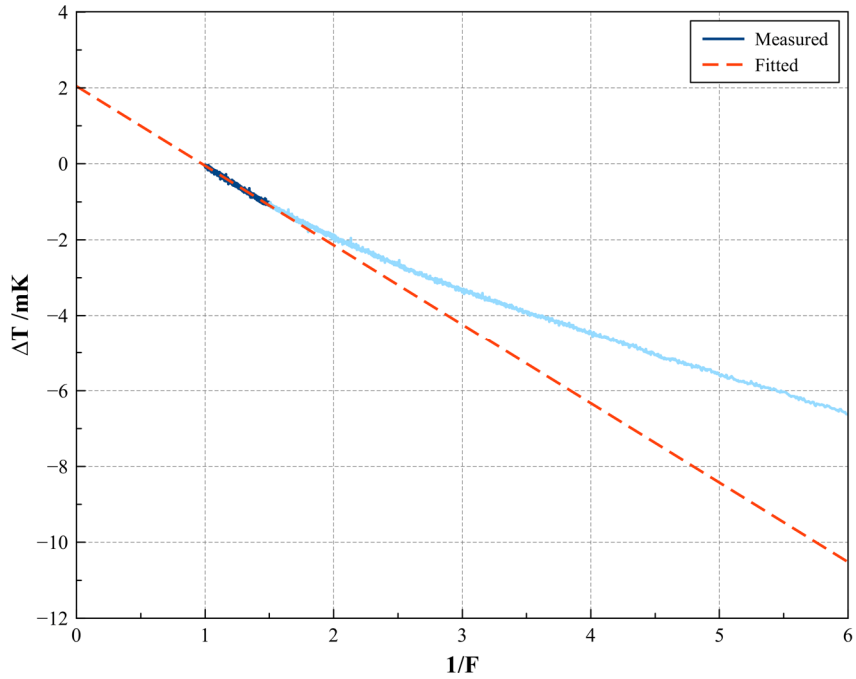

Figure 99: Thermal analysis method applied to curve 3 measured in cell Al-S (Sumitomo). Fitting range from 1/F=1 to 1/F=1.5.

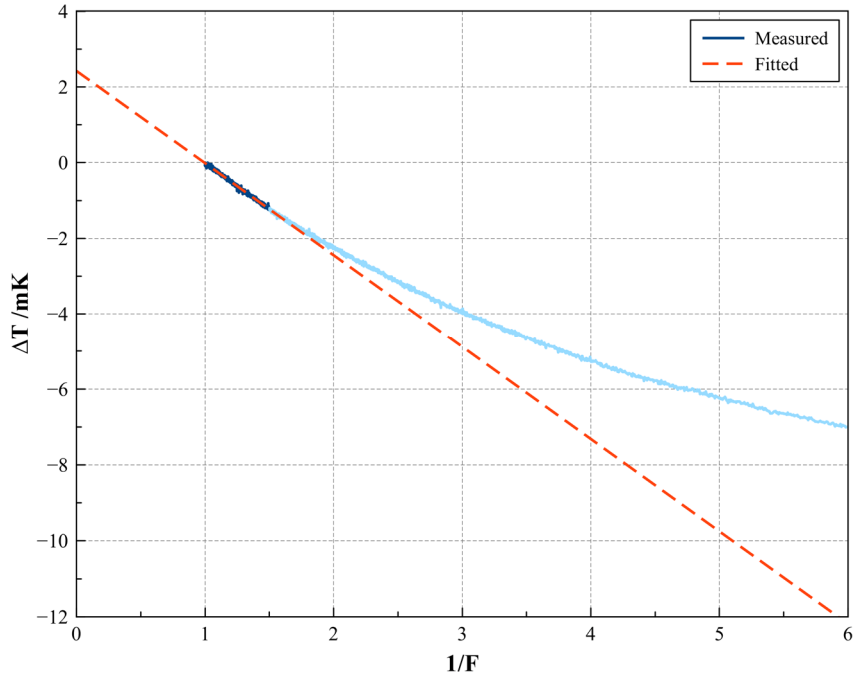

Figure 100: Thermal analysis method applied to curve 4 measured in cell Al-S (Sumitomo). Fitting range from 1/F=1 to 1/F=1.5.

Freezing curve	a mK	b mK	u_a mK	u_b mK
Curve #1	– 0.90	0.84	0.01	0.01
Curve #2	– 1.72	1.67	0.01	0.01
Curve #3	– 2.09	2.04	0.01	0.01
Curve #4	– 2.43	2.42	0.01	0.01

Correction	1.79 mK
Uncertainty	0.66 mK

Table 62: Results of the fittings according to the thermal analysis method for cell Al-S (Sumitomo).

Application of this methodology was simple and returned individual corrections that were consistent with the temperature profile of the freezing curves: the fact that the first curve measured with cell Al-S presented a less steep slope in comparison to the later three curves was also adequately translated in the results of the thermal analysis calculations. This was also observed in the other cells.

Since the fitting is performed over a portion of the data at the very beginning of the freezing, the curves measured with cell Al-A were notably affected in a manner that the fitted results would be unrealistic, not consistent with the impurity profile of the material (as shown in the GDMS assays and also observed in the shape of the freezing curves). If the fitting range 1/F=1 to 1/F=1.5 were to be maintained, the resulting correction would be approximately 5.40 mK, as if this cell presented the lowest freezing temperature from the five cells investigated, when in fact it had the highest temperature given the high *k* impurity content of the aluminium samples employed. This can be seen in figure 101.

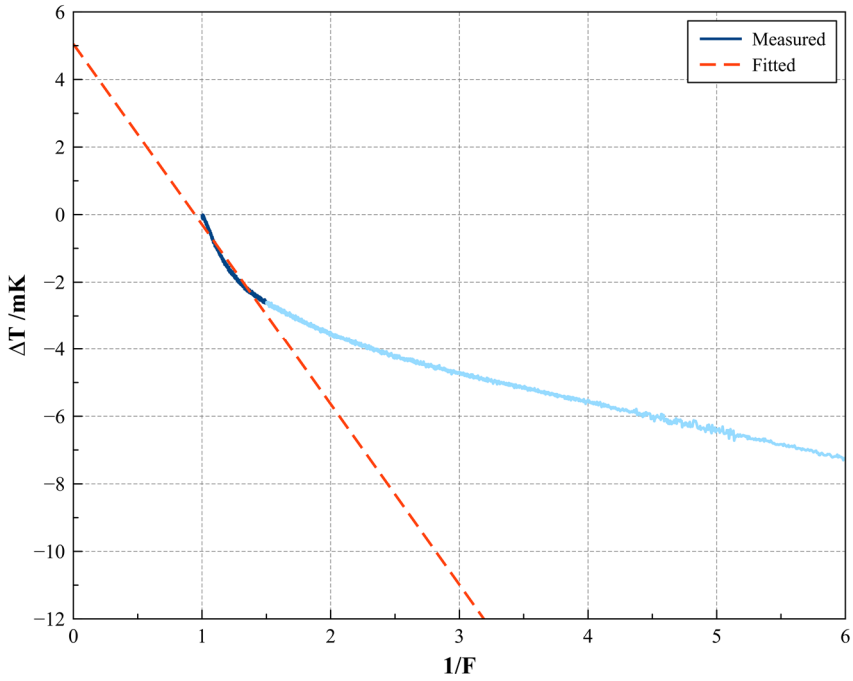

Figure 101: Thermal analysis method applied to curve 1 measured in cell Al-A (Alfa Aesar). Fitting range from 1/F=1 to 1/F=1.5.

In an attempt to apply the method to cell Al-A in a manner that would be consistent with the previously characterised impurity content of the material, the solution adopted was to shift the fitting range to a later part of the curve, immediately after the influence of the high *k* impurities was no longer observable in the graph. Then, the range chosen to perform the fitting was 1/F=1.4 to 1/F=1.9. The results for this cell would be valid after correcting the fitted values for the offsets at 1/F=1.4 (approximately 2.40 mK in average). The graphs showing the adjusted fittings for cell Al-A are given in figure 102 and the corresponding results are tabulated in table 63.

Subsequently, the fittings for the other cells are given together with a summary of results for each cell, as follows: figure 103 and table 64 display the results for cell Al-E, figure 104 and table 65 show the results for cell Al-H while figure 105 and table 66 display the outcome obtained with cell Al-N.

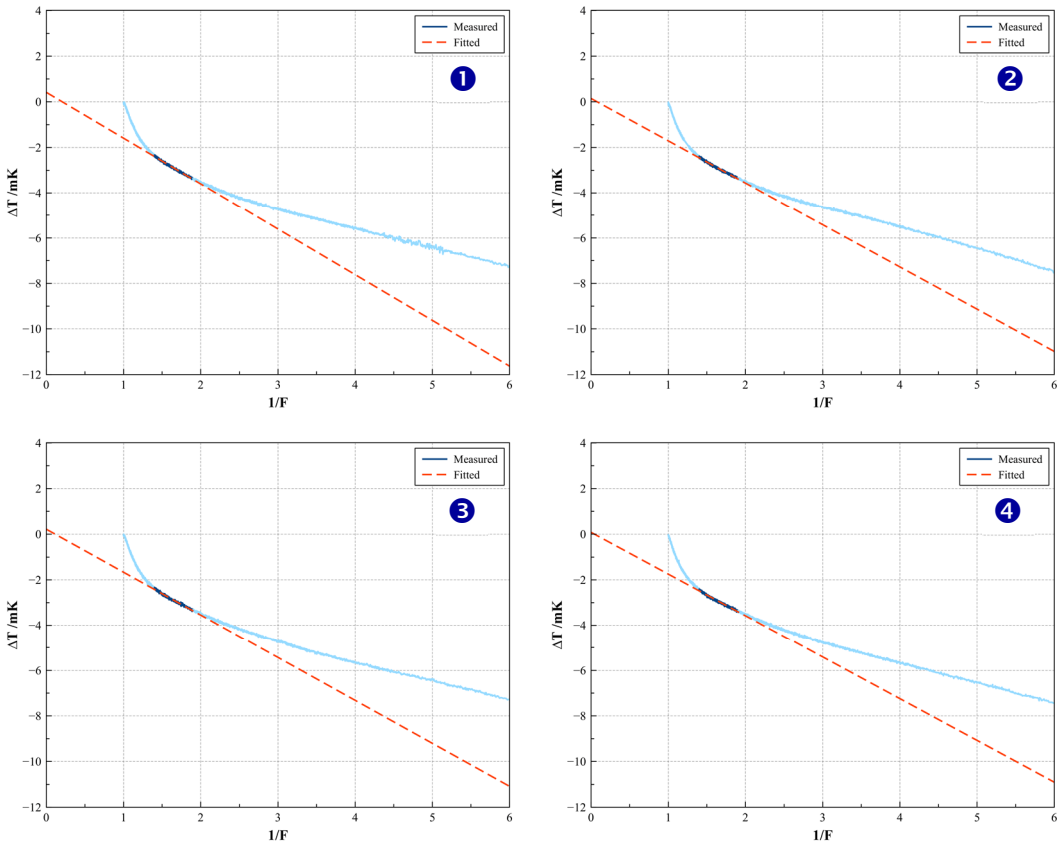

Figure 102: Thermal analysis method applied to the freezing curves measured with cell Al-A (Alfa-Aesar). Fitting range from 1/F=1.4 to 1/F=1.9.

Freezing curve	a mK	b mK	u_a mK	u_b mK	*Offset* ($T_{(1/F_{1.4})}$) mK	$a - T_{(1/F_{1.4})}$ mK
Curve #1	– 2.00	0.41	0.01	0.01	– 2.39	0.39
Curve #2	– 1.86	0.14	0.01	0.01	– 2.40	0.54
Curve #3	– 1.88	0.22	0.01	0.01	– 2.42	0.54
Curve #4	– 1.83	0.08	0.01	0.01	– 2.43	0.60

Correction	0.52 mK
Uncertainty	0.08 mK

Table 63: Results of the fittings according to the thermal analysis method for cell Al-A.

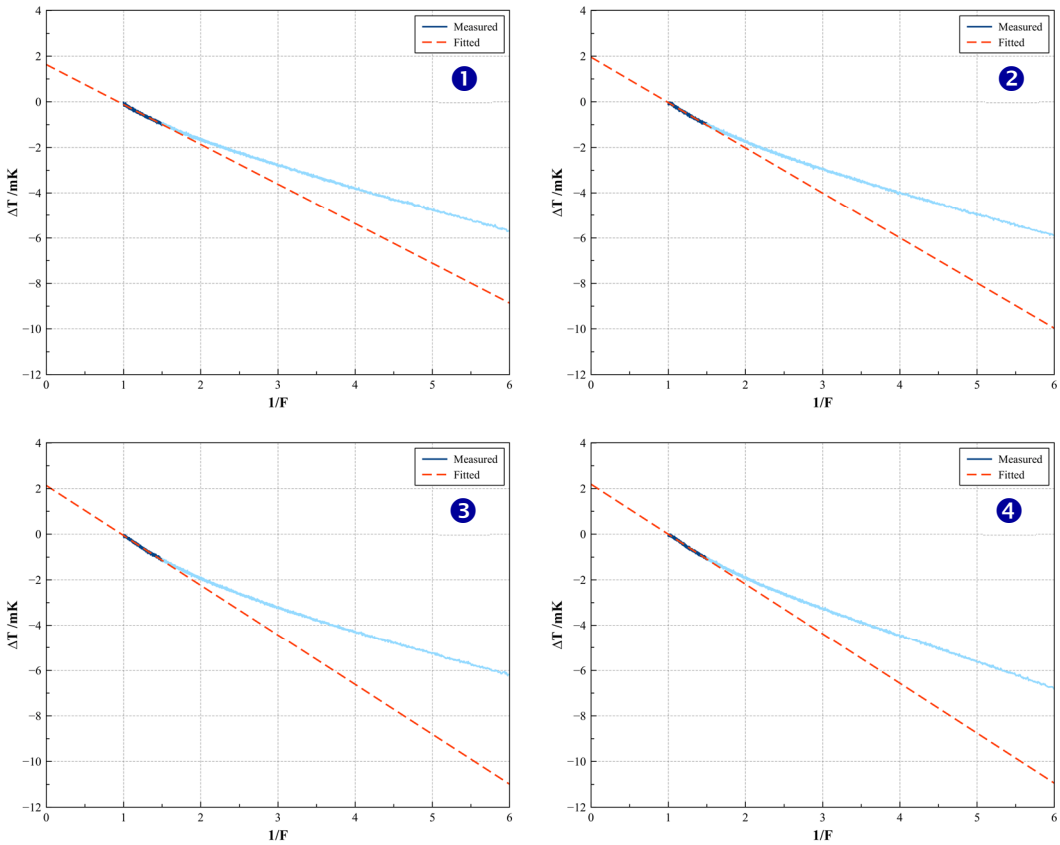

Figure 103: Thermal analysis method applied to the freezing curves measured with cell Al-E (ESPI). Fitting range from 1/F=1 to 1/F=1.5.

Freezing curve	*a* mK	*b* mK	u_a mK	u_b mK
Curve #1	– 1.75	1.63	0.00	0.01
Curve #2	– 1.99	1.95	0.01	0.01
Curve #3	– 2.19	2.13	0.00	0.01
Curve #4	– 2.19	2.19	0.01	0.01

Correction	2.03 mK
Uncertainty	0.21 mK

Table 64: Results of the fittings according to the thermal analysis method for cell Al-E (ESPI).

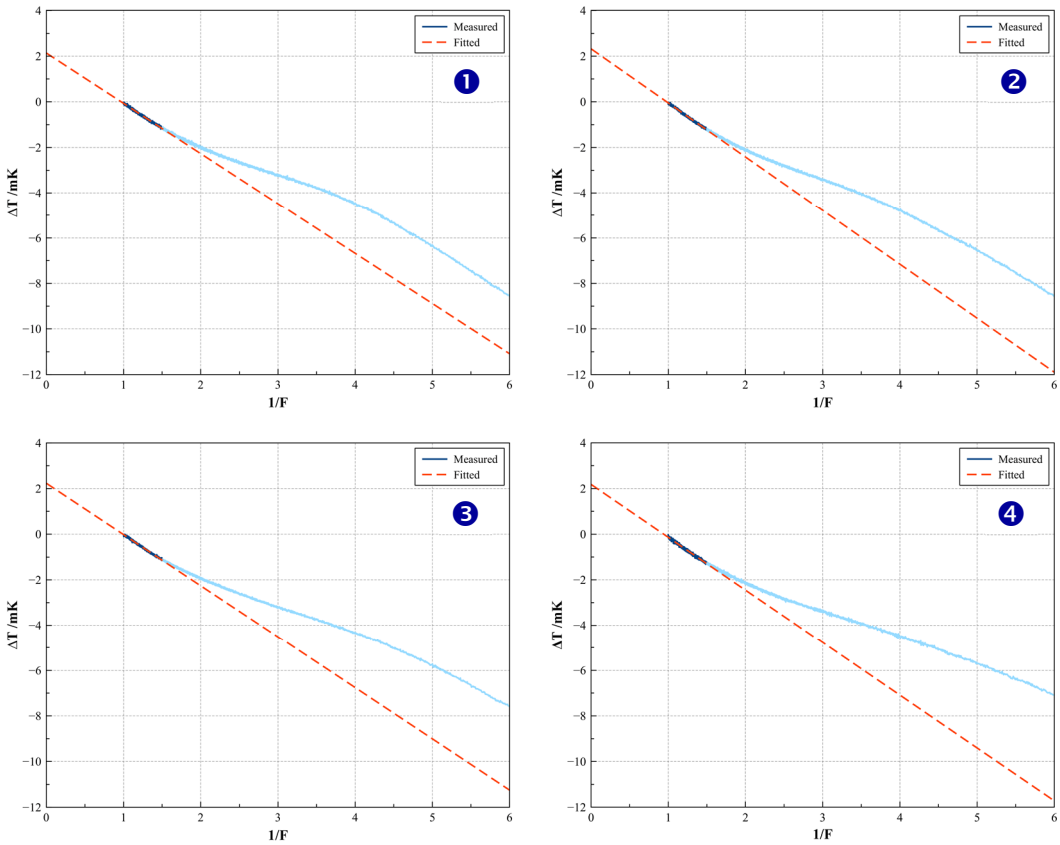

Figure 104: Thermal analysis method applied to the freezing curves measured with cell Al-H (Honeywell). Fitting range from 1/F=1 to 1/F=1.5.

Freezing curve	a mK	b mK	u_a mK	u_b mK
Curve #1	– 2.20	2.14	0.00	0.01
Curve #2	– 2.37	2.32	0.00	0.01
Curve #3	– 2.25	2.23	0.00	0.00
Curve #4	– 2.32	2.18	0.01	0.01

Correction	2.28 mK
Uncertainty	0.07 mK

Table 65: Results of the fittings according to the thermal analysis method for cell Al-H (Honeywell).

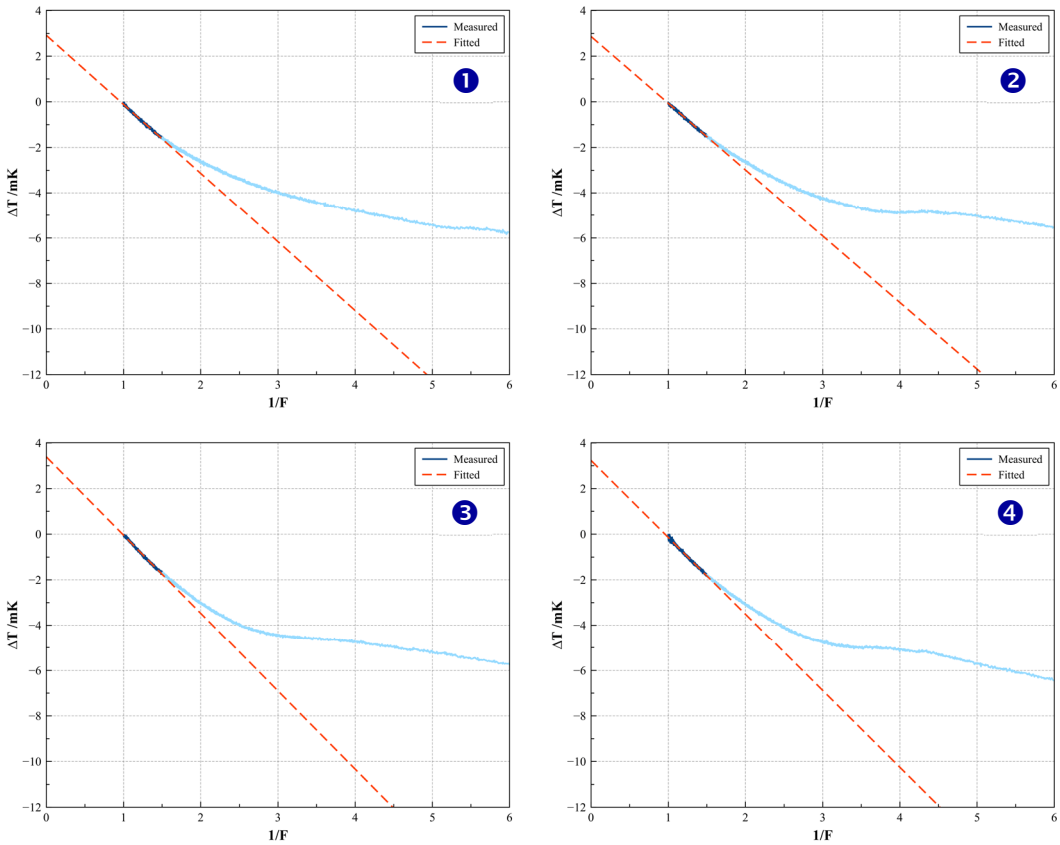

Figure 105: Thermal analysis method applied to the freezing curves measured with cell Al-N (New Metals). Fitting range from 1/F=1 to 1/F=1.5.

Freezing curve	a mK	b mK	u_a mK	u_b mK
Curve #1	– 3.03	2.91	0.01	0.01
Curve #2	– 2.92	2.86	0.01	0.01
Curve #3	– 3.43	3.39	0.01	0.01
Curve #4	– 3.37	3.23	0.01	0.01

Correction	3.19 mK
Uncertainty	0.25 mK

Table 66: Results of the fittings according to the thermal analysis method for cell Al-N.

It is important to observe that the anomalous shape of the freezing plateaus measured in cell Al-N (New Metals) did not prevent the application of the thermal analysis methodology or required any adjustments in the fitting parameters. This was due to the fact that in this methodology the fitting is done at an initial portion of the data (equivalent to 33 % of the solid fraction), which is not affected by the discontinuity observed at a later stage of the freezing curves measured with cell Al-N. Therefore, for this method, the fitting parameters only had to be adjusted for cell Al-A.

In general, this method was applied without difficulty (even though the methodology requires the abcissa to be plotted as inverse of liquid fraction, 1/F). The calculated corrections and uncertainties yielded seem to be consistent with not only the level of purity of the aluminium samples but also the variability in the performance of the cells: as observed in previous methods tested, cells Al-E, Al-H and Al-S tend to be very similar in terms of behaviour and the level of corrections assigned; cell Al-N presents a lower performance (larger corrections) while cell Al-A tend to show corrections that are close to zero or in the negative range to compensate the effect of its high *k* impurity content.

6.7. Direct cell comparison

The last method applied to the aluminium cells studied for this thesis was the direct cell comparison. Currently it is the standard method used for comparing fixed point cells even though this methodology is not intended to assign absolute corrections for impurity effects. Application of this method followed the description previously given in sections 2.3.2.7 and 4.2.2. Since the SPRT is prone to changes in its resistance after being used, especially at high temperatures, the validity of cell comparisons is only achieved by measuring the SPRT at the triple point of water and comparing the values in terms of resistance ratios, W (equation 2). All five aluminium cells were compared directly to the reference cell, which is the work standard of the NPL for the temperature 660.323 °C. This standard cell had been previously compared to the national standard for this temperature. The result of this comparison allowed the values of the five cells to be traceable to the national standard.

The measurement protocol followed the sequence: measurement at TPW as an initial check; measurement of a given aluminium cell (starting 1 h after recalescence); measurement at TPW again. For calculations, only the TPW values after the SPRT exposure to the aluminium freezing point are accounted for because of temperature drifts caused to the sensor. In each fixed point (TWP cell or Al FP cell), after becoming stable, the resistance values were measured with the thermometer being supplied with two currents (1 mA and 1.414 mA) in order to enable the measured resistance values to be extrapolated to 0 mA (excluding the influence of the Joule heating effect). Figures 106 and 107 exemplify the measurements performed at the freezing point of aluminium (cell Al-S) and subsequently at the triple point of water (cell 768).

The uncertainty of the comparison was calculated according to the protocol in use by the NPL, which accounts for the components recommended for international comparisons. Since the comparison is based upon measurements at the aluminium freezing point and TPW, components for the realisation of both fixed points are accounted. The components and their respective contribution are tabulated in the uncertainty budget given in table 67.

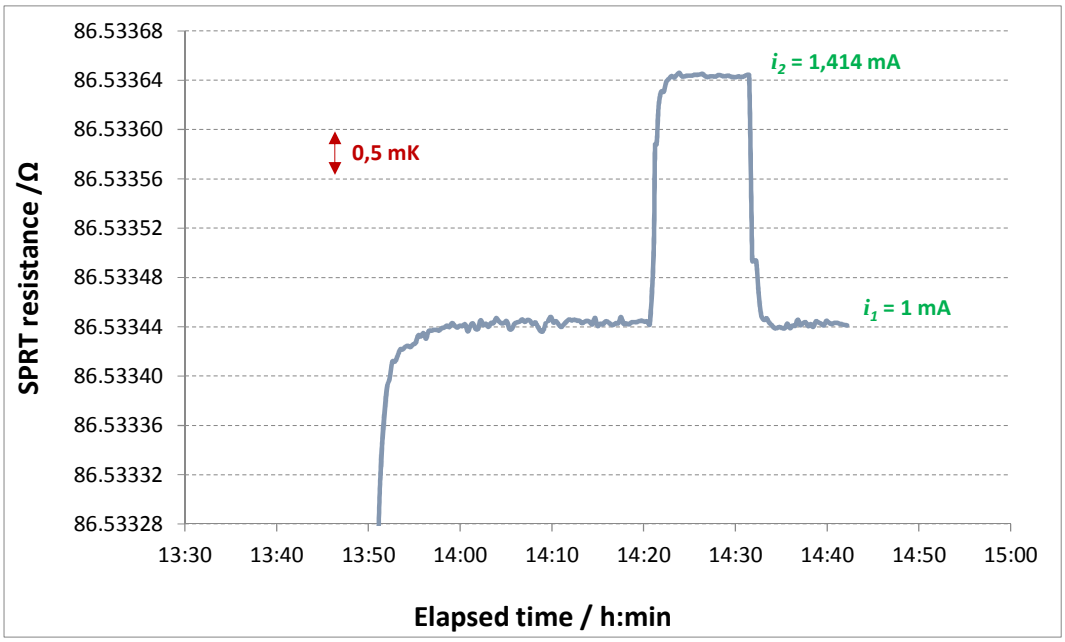

Figure 106: SPRT measurements to determine the self-heating effect of the sensor inside the aluminium cell Al-S (Sumitomo).

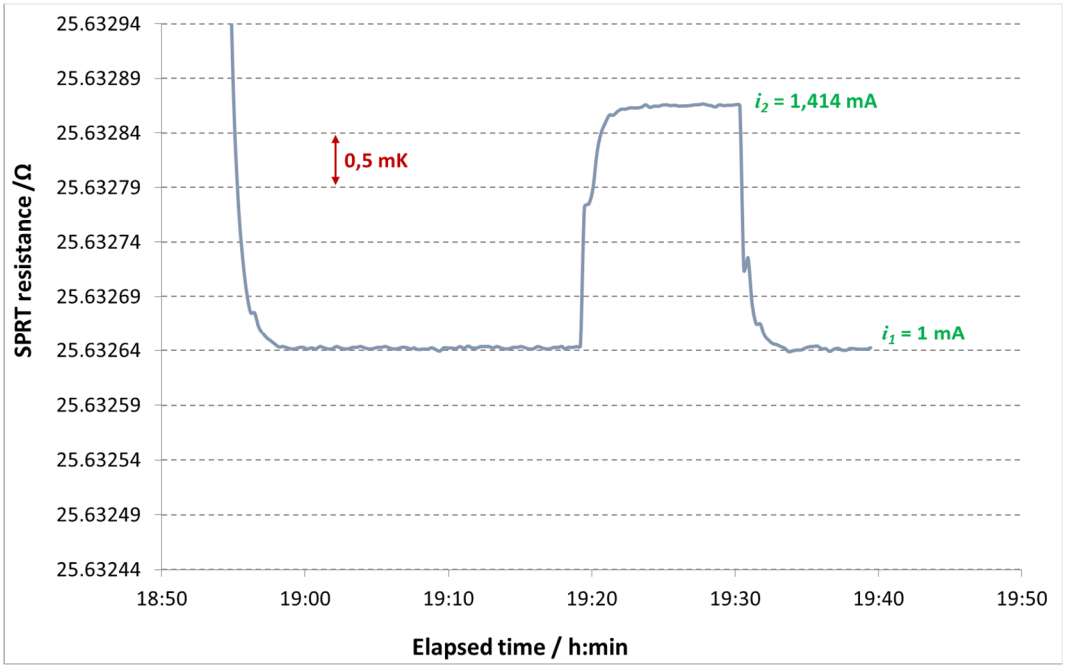

Figure 107: SPRT measurements to determine the self-heating effect of the sensor inside cell 768 (triple point of water).

Component	Description	Standard Uncertainty	Sensitivity Coefficient	Distribution	Divisor	Contribution mK
Al – A1	Repeatability of readings (0 mA)	0.4 x 10^{-7} Ω/Ω	1250 K	Normal	1	0.080
Al – B1	Uncertainty of Al reference cell	0.858 mK	1	Normal	1	0.858
Al – B2	Hydrostatic pressure correction	10 mm	1.6 mK/m	Rectangular	√3	0.009
Al – B3	Perturbing heat exchanges	0.7 mK	1	Rectangular	√3	0.214
Al – B4	Self-heating extrapolation	2% of S.H. (3 mK)	1	Rectangular	√3	0.035
Al – B5	Bridge linearity	0.5 x 10^{-7} Ω/Ω	1250 K	Rectangular	√3	0.036
Al – B6	Temperature of standard resistor	20 mK	1.05 mK/ppm	Rectangular	√3	0.022
Al – B7	AC/DC, frequency, etc	0.7 x 10^{-7} Ω/Ω	1250 K	Rectangular	√3	0.051
Al – B8	Argon pressure in cell	2.6 kPa	7.0 x 10^{-8} K/Pa	Rectangular	√3	0.106
	Sub-total at FP Al					**0.897**
TPW – A1	Repeatability of readings (0 mA)	0.05 x 10^{-7} Ω/Ω	1000 K	Normal	1	0.008
TPW – B1	Uncertainty of TPW cell	0.034 mK	1	Normal	1	0.034
TPW – B2	Hydrostatic pressure correction	5 mm	0.73 mK/m	Rectangular	√3	0.002
TPW – B3	Perturbing heat exchanges	0.01 mK	1	Rectangular	√3	0.006
TPW – B4	Self-heating extrapolation	2% of S.H. (3 mK)	1	Rectangular	√3	0.035
TPW – B5	Bridge linearity	0.5 x 10^{-7} Ω/Ω	1000 K	Rectangular	√3	0.029
TPW – B6	Temperature of standard resistor	20 mK	0.25 mK/ppm	Rectangular	√3	0.005
TPW – B7	AC/DC, frequency, etc	0.27 x 10^{-7} Ω/Ω	1000 K	Rectangular	√3	0.016
	Sub-total at TPW					**0.059**
	Equivalent at FP Al	0.059 mK	4.2			**0.250**
		Combined uncertainty (*k* = 1)				**0.931**

Table 67: Uncertainty budget for the direct comparison of cells.

The components accounted for the uncertainty are divided in two main groups, according to their source: one arising from the realization of the aluminium freezing point and the other from the water triple point. As for the type A uncertainty, only the repeatability of the readings was taken into account. As for the type B, a range of components was taken considered. Since the nominal values resulting from measurements of the SPRT at these temperatures are in different ranges, the standard uncertainties related to the measurement system (the platinum wire of the SPRT, the thermal environment, the bridge and standard resistor) will differ from one temperature to the other. The uncertainty budget was developed after thorough investigation of the measurement system to appropriately describe it, understand the factors and variables that influence it and to account each of them accordingly. The values for type B components were only assigned after extensive research and measurements to determine their magnitude, which were all performed prior to this investigation, hence the values were imported to the present budget. A more detailed description of these components is given in table 68.

Component	Description	Comments
A1	Repeatability of readings (0 mA)	Based on the standard deviation of 20 readings
B1	Uncertainty of reference cell	Imported from the reference cell budget ($k=1$)
B2	Hydrostatic pressure correction	Uncertainty in assigning the value for the hydrostatic head (the height of the fixed point material when in liquid phase)
B3	Perturbing heat exchanges	Based on immersion tests and furnace profiles
B4	Self-heating extrapolation	Uncertainty in the current ratios (difference between nominal and actual current inputs)
B5	Bridge linearity	Based on linearity checks and calibration of the bridge
B6	Temperature of standard resistor	Derived from the temperature coefficient of the standard resistor
B7	AC/DC, frequency, etc.	Accounts other sources arising from the bridge system
B8	Argon pressure in cell	Uncertainty of the measurement of pressure inside the cell (calibration of gauge)

Table 68: Detailed description of the standard uncertainties involved in the direct comparison of cells.

Taking into account that, in terms of repeatability of the measurements, the performance of the SPRT was almost constant in all cells: the standard deviations of the measurements (20 readings in each current supplied) in all tested cells were in the same magnitude. As for the other components that could be variable in the uncertainty budget, the values assigned are actually thresholds: based on a series of experiments, their values are overestimated a bit to provide a margin up to which actual measurements could vary but yet guaranteeing the same standard of performance, still under that threshold. Nevertheless, the uncertainty of the reference aluminium cell is by far the major contribution in the uncertainty calculation (approximately 90 % of the combined value), which indicates that the other components are not negligible but have a minor impact in the final result. After considering the aforementioned information (especially the fact that there were little differences in the repeatability of readings), the same uncertainty was assigned to the comparison of all five cells tested in relation to reference cell Al 10/09.

The results of the SPRT measurements and the calculation of the resistance mean values extrapolated to 0 mA are given in table 69. The detailed calculation for the cell comparison are tabulated in table 70, with the results being given in table 71. In figure 108, the results of the comparison of the cells constructed to cell Al 10/09 are shown relative to the traceability of Al 10/09 to cell ‘Al sealed’. The corrections for the cells are calculated only after the correction for the reference cell itself was considered, so that the corrections assigned are traceable to the national standard (as if they were actually compared directly to cell ‘Al sealed’).

Cell	Resistance mean (1 mA) Ω	Resistance mean (1.414 mA) Ω	Mean extrapolated to 0 mA Ω	Self heating effect mΩ
Al 10/09	86.534 785 3	86.534 989 7	86.534 580 8	0.204
TPW 1147	25.633 092 5	25.633 307 8	25.632 877 1	0.215
Al-A	86.533 263 3	86.533 463 3	86.533 063 3	0.200
TPW 767	25.632 581 4	25.632 798 2	25.632 311 3	0.217
Al-E	86.533 443 0	86.533 643 4	86.533 242 5	0.200
TPW 1148	25.632 647 4	25.632 867 4	25.632 427 3	0.220
Al-H	86.533 697 6	86.533 903 6	86.533 491 6	0.206
TPW 1148	25.632 714 0	25.632 926 5	25.632 501 4	0.212
Al-N	86.532 764 0	86.532 968 0	86.532 560 0	0.204
TPW 767	25.632 443 8	25.632 663 8	25.632 223 8	0.220
Al-S	86.532 576 2	86.532 778 1	86.532 374 2	0.202
TPW 767	25.632 367 6	25.632 585 6	25.632 149 7	0.218

Table 69: Results of the SPRT resistance measurements and the extrapolation of the means to 0 mA.

Cell	Resistance Mean (0 mA) Ω	Immersion depth mm	Hydrostatic head correction Ω	Pressure mmHg	Pressure correction Ω	*W* (corrected)
Al 10/09	86.534 580 8	174.00	– 0.000 02	760.0	0.0×10^{0}	3.375 918 350
TPW 1147	25.632 877 1	274.00	0.000 02	—	—	—
Al-A	86.533 063 3	174.21	– 0.000 02	746.6	1.0×10^{-5}	3.375 933 950
TPW 767	25.632 311 3	285.00	0.000 02	—	—	—
Al-E	86.533 242 5	173.98	– 0.000 02	760.8	-6.0×10^{-7}	3.375 925 376
TPW 1148	25.632 427 3	272.00	0.000 02	—	—	—
Al-H	86.533 491 6	174.01	– 0.000 02	760.0	0.0×10^{0}	3.375 925 358
TPW 1148	25.632 501 4	272.00	0.000 02	—	—	—
Al-N	86.532 560 0	174.15	– 0.000 02	760.5	-3.7×10^{-7}	3.375 925 435
TPW 767	25.632 223 8	285.00	0.000 02	—	—	—
Al-S	86.532 374 2	173.61	– 0.000 02	760.1	-7.5×10^{-8}	3.375 927 960
TPW 767	25.632 149 7	285.00	0.000 02	—	—	—

Table 70: Calculation of *W* values for the cells used in the comparison.

Cell	*W* (corrected)	Test cell – Al 10/09 mK	Result traceable to National standard 'Al sealed' mK	Correction (to 'Al sealed') mK
Al 10/09	3.375 918 350	—	—	3.18
Al-A	3.375 933 950	4.87	1.69	– 1.69
Al-E	3.375 925 376	2.19	– 0.99	0.99
Al-H	3.375 925 358	2.19	– 0.99	0.99
Al-N	3.375 925 435	2.21	– 0.97	0.97
Al-S	3.375 927 960	3.00	– 0.18	0.18

Table 71: Results of the corrections assigned to the five aluminium cells tested.

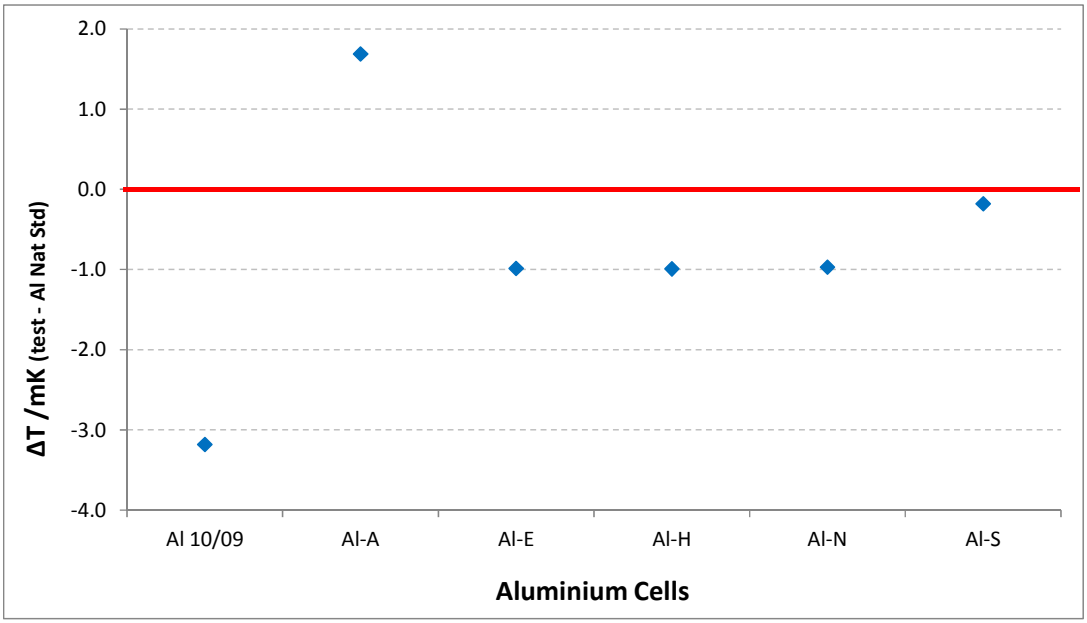

Figure 108: Results of the comparison when traced to the national standard, cell 'Al sealed'.

Based on the results of the comparison, it is possible to observe that the performance of all tested cells was consistent with the level of purity of the material employed. Besides, calculation of *W* values indicated that the values of the tested cells were greater than the reference cell Al 10/09, better approaching the reference value of the national standard. The performance of cells Al-E, Al-H and Al-N was very similar while cell Al-S resulted in the closest value to the national standard. As for cell Al-A, it is important to emphasize that the result above the reference cell is not an indicative that this cell outperformed the national standard ('Al sealed') but that this result is consistent with and confirms that the aluminium samples used in cell Al-A indeed contain a considerable amount of high *k* impurities, as it was previously observed in the other methodologies employed (considering the measurements for the comparison were taken 60 min after the onset of recalescence, when the effect of those impurities was still taking place). Given these results, it is possible to state that cells Al-E, Al-H and Al-S would make good standard cells, even being candidates to substitute the current work standard for the freezing point of aluminium of the NPL.

6.8. Summary of results

With a view to comparing more easily the results from the various methodologies investigated in this research, this section summarises all the results. Firstly, the results are given for all methodologies tested with the data organized by each cell (tables 72-76). Later, all results are tabulated in table 77 and shown as a graph in figure 109.

Assay Origin	SIE		OME		Hybrid	
	Correction mK	Uncertainty mK	Bound mK	Uncertainty mK	Correction mK	Uncertainty mK
Supplier	-0.13	0.25	0.44	0.26	1.81	0.22
AQura	-2.19	1.27	1.09	0.63	-0.65	1.27
NRC	-2.43	3.28	1.64	0.94	-1.08	3.24
NIM	33.37	35.97	32.92	19.01	0.51	2.54

Upper Limit	Scheil (free *k*)			Scheil (*k* = 0)	
	Correction mK	Uncertainty mK	*k*	Correction mK	Uncertainty mK
0.25	-3.39	0.27	4.82	-0.50	0.35
0.50	-3.85	0.32	3.72	-0.96	0.21

Gradient Method		Thermal Analysis		Cell comparison	
Correction mK	Uncertainty mK	Correction mK	Uncertainty mK	Correction mK	Uncertainty mK
-0.48	0.27	1.80	0.14	-1.69	0.93

Table 72: Corrections obtained according to the various methods tested for cell Al-A (Alfa Aesar).

Assay Origin	SIE		OME		Hybrid	
	Correction mK	Uncertainty mK	Bound mK	Uncertainty mK	Correction mK	Uncertainty mK
Supplier	0.56	0.57	0.58	0.34	2.17	0.02
AQura	0.70	0.21	1.31	0.76	2.10	0.11
NRC	0.08	0.79	1.11	0.64	1.52	0.51
NIM	3.93	4.29	4.46	2.58	1.60	0.51

Upper Limit	Scheil (free *k*)			Scheil (*k* = 0)	
	Correction mK	Uncertainty mK	*k*	Correction mK	Uncertainty mK
0.50	17.09	8.91	0.83	1.82	0.19
0.80	6.44	1.76	0.62	1.31	0.11

Gradient Method		Thermal Analysis		Cell comparison	
Correction mK	Uncertainty mK	Correction mK	Uncertainty mK	Correction mK	Uncertainty mK
1.06	0.17	2.10	0.18	0.99	0.93

Table 73: Corrections obtained according to the various methods tested for cell Al-E (ESPI).

Assay Origin	SIE		OME		Hybrid	
	Correction mK	Uncertainty mK	Bound mK	Uncertainty mK	Correction mK	Uncertainty mK
Supplier	5.62	2.63	6.54	3.78	1.27	0.53
AQura	0.20	0.15	0.72	0.42	1.93	0.13
NRC	0.08	0.50	0.88	0.51	1.79	0.38
NIM	6.08	6.13	6.82	3.94	1.72	0.56

Upper Limit	Scheil (free *k*)			Scheil (*k* = 0)	
	Correction mK	Uncertainty mK	*k*	Correction mK	Uncertainty mK
0.50	23.66	30.31	0.86	1.77	0.31
0.80	6.80	4.24	0.60	1.24	0.27

Gradient Method		Thermal Analysis		Cell comparison	
Correction mK	Uncertainty mK	Correction mK	Uncertainty mK	Correction mK	Uncertainty mK
0.90	0.18	2.01	0.36	0.99	0.93

Table 74: Corrections obtained according to the various methods tested for cell Al-H (Honeywell).

Assay Origin	SIE		OME		Hybrid	
	Correction mK	Uncertainty mK	Bound mK	Uncertainty mK	Correction mK	Uncertainty mK
Supplier	-0.23	0.45	0.32	0.18	3.15	0.31
AQura	0.13	0.10	0.47	0.27	3.35	0.08
NRC	-0.26	0.35	0.45	0.26	3.08	0.61
NIM	10.33	10.71	9.54	5.51	3.42	0.31

Upper Limit	Scheil (free *k*)			Upper Limit	Scheil (*k* = 0)	
	Correction mK	Uncertainty mK	*k*		Correction mK	Uncertainty mK
0.25	7.29	7.80	0.41	0.50	2.85	0.16
0.50	16.35	4.45	0.76	0.80	1.39	0.30

Gradient Method		Thermal Analysis		Cell comparison	
Correction mK	Uncertainty mK	Correction mK	Uncertainty mK	Correction mK	Uncertainty mK
1.50	0.20	3.32	0.28	0.97	0.93

Table 75: Corrections obtained according to the various methods tested for cell Al-N (New Metals).

Assay Origin	SIE		OME		Hybrid	
	Correction mK	Uncertainty mK	Bound mK	Uncertainty mK	Correction mK	Uncertainty mK
Supplier	-0.11	0.31	0.34	0.20	1.90	0.26
AQura	0.34	0.23	0.92	0.53	1.93	0.16
NRC	-0.04	0.34	0.49	0.28	1.92	0.27
NIM	8.13	8.00	8.42	4.86	2.10	0.36

Upper Limit	Scheil (free *k*)			Scheil (*k* = 0)	
	Correction mK	Uncertainty mK	*k*	Correction mK	Uncertainty mK
0.50	4.56	1.80	0.43	1.97	0.22
0.80	5.94	4.14	0.49	1.49	0.13

Gradient Method		Thermal Analysis		Cell comparison	
Correction mK	Uncertainty mK	Correction mK	Uncertainty mK	Correction mK	Uncertainty mK
1.41	0.33	2.12	0.23	0.18	0.93

Table 76: Corrections obtained according to the various methods tested for cell Al-S (Sumitomo).

	Methodology	Cell Al-A		Cell Al-E		Cell Al-H		Cell Al-N		Cell Al-S	
		Correction mK	U (k=1) mK	Correction mK	U (k=1) mK	Correction mK	U (k=1) mK	Correction mK	U (k=1) mK	Correction mK	U (k=1) mK
SIE	Supplier	-0.13	0.25	0.56	0.57	5.62	2.63	-0.23	0.45	-0.11	0.31
	AQura	-2.19	1.27	0.70	0.21	0.20	0.15	0.13	0.10	0.34	0.23
	NRC	-2.43	3.28	0.08	0.79	0.08	0.50	-0.26	0.35	-0.04	0.34
	NIM	33.37	35.97	3.93	4.29	6.08	6.13	10.33	10.71	8.13	8.00
OME	Supplier	0	0.44	0	0.58	0	6.54	0	0.32	0	0.34
	AQura	0	1.09	0	1.31	0	0.72	0	0.47	0	0.92
	NRC	0	1.64	0	1.11	0	0.88	0	0.45	0	0.49
	NIM	0	32.92	0	4.46	0	6.82	0	9.54	0	8.42
Hybrid	Supplier	1.81	0.22	2.17	0.00	1.27	0.53	3.15	0.30	1.90	0.26
	AQura	-0.65	1.27	2.10	0.11	1.93	0.13	3.35	0.08	1.93	0.16
	NRC	-1.08	3.24	1.52	0.51	1.79	0.38	3.08	0.60	1.92	0.27
	NIM	0.51	2.54	1.60	0.51	1.72	0.56	3.42	0.31	2.10	0.36
Scheil	Free k, lower max	-3.39	0.27	17.09	8.91	23.66	30.31	7.29	7.80	4.56	1.80
	Free k, upper max	-3.85	0.32	6.44	1.76	6.80	4.24	16.35	4.45	5.94	4.14
	k=0, lower max	-0.50	0.35	1.82	0.19	1.77	0.31	2.85	0.16	1.97	0.22
	k=0, upper max	-0.96	0.21	1.31	0.11	1.24	0.27	1.39	0.30	1.49	0.13
	Gradient	1.80	0.14	2.10	0.18	2.01	0.36	3.32	0.28	2.12	0.23
	Thermal	-0.48	0.27	1.06	0.17	0.90	0.18	1.50	0.20	1.41	0.33
	Comparison	-1.69	0.93	0.99	0.93	0.99	0.93	0.97	0.93	0.18	0.93

Table 77: Summary of the results according to the various methodologies investigated for the five aluminium cells constructed.

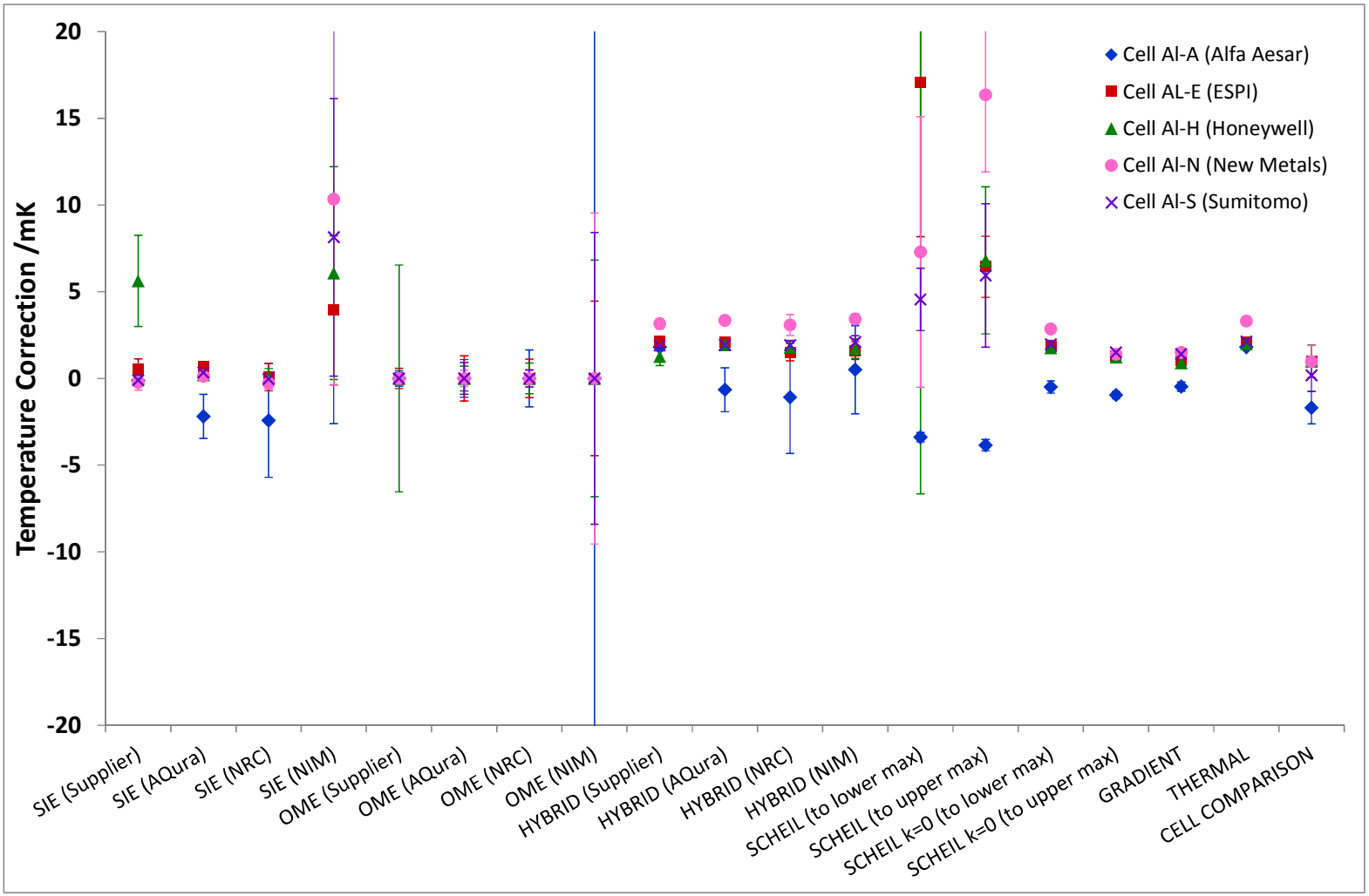

Figure 109: Comparison of the corrections yielded by the different methods investigated, for the five cells.

Considerable variation in the quality of the chemical analyses was observed. Very little information was provided regarding the uncertainty of the measurements. Unless otherwise stated, the uncertainty was assumed to be equal in magnitude to the stated amount of impurity.

An ICP-AES (inductively coupled plasma atomic emission spectroscopy) analysis was performed for the aluminium supplied by Honeywell (supplier's assay). Since this technique does not have sufficient sensitivity to detect impurities at the level of parts per billion, it was detrimental to the reliability of the estimates that depended on this result. The analyses using the suppliers' own assays are therefore included for illustration only. A similar issue occurred to the ESPI sample (when the supplier's assay was considered) but in this case it was due to the fact that only one major impurity was detected which, in comparison to the GDMS from the independent laboratories, does not seem to be true. Consequently, it is paramount that metals at this level of purity are supplied with GDMS analysis in order to enable the users to apply correction methodologies that requires knowledge of the impurity content or to guide the application of other correction methods.

Despite showing poor agreement with each other in general, the GDMS results from labs AQura, NRC and NIM for the metal from Supplier A were very consistent with respect to the titanium (Ti) content of the material. Ti is a significant impurity in Al because it is commonly observed in relatively large concentrations, and because it has a high value of k (approximately 6.4). However, for Ti the uncertainty declared by NRC is a factor of 10 larger than that of AQura. This explains why the SIE and hybrid SIE/modified OME corrections for AQura and NRC are similar but the uncertainties are quite different. The metal supplied by Alfa Aesar was remarkable because the consistently high levels of titanium indicated by the various GDMS analyses coincided with the observed shape of the freezing curve, which exhibited a large downward slope at the beginning of the freeze, consistent with the shape that would be expected from a high k impurity [22]. This is evident in Figure 41 and 46 (section 5.3).

The GDMS analysis from NIM presented some uncommon peaks of selenium (varying from 13 ppm to 113 ppm) in the metal from all suppliers, which does not correspond to the nominal purity of the samples, whose maximum nominal impurity content should be less than 1 ppm. Since this was unique to the results from this laboratory, it is suspected that

some contamination could have occurred during the execution of the GDMS analysis procedure.

The results from AQura for the ESPI metal showed an unusually high peak of Bi (1.7 ppm). This laboratory reported that the sample had been checked with a second GDMS apparatus and the Bi peak proved to be reproducible, even though it just appeared in the results from this lab. Nevertheless, the liquidus slope of bismuth in aluminium is very small (– 0.039 mK/ppm), so the overall contribution from this high peak corresponds to only 66 μK, therefore not producing a major observable effect on the freezing curve.

The OME results based on the analysis performed by NRC on the metal supplied by Alfa Aesar yielded a large estimate due to unusually high levels of Co, Fe, Ni, Si, and Ti (amounting to about 60 % of the total impurity concentration). It does not affect the SIE because the influence of Co, Fe, Ni and Si oppose and lower the correction coming from the titanium peak. As for the hybrid method, only Fe, Ni and Ti are accounted in the hybrid SIE component (in which Fe and Ni lower the Ti influence).

The supplier's chemical analysis results for ESPI metal showed only 0.9 ppm of silicon as a detected impurity. No further information was available concerning either which elements were analysed, or the detection limits and uncertainties. Since the hybrid SIE/OME method uses GDMS data only for impurity with $k < 0.1$, the hybrid SIE component was zero.

Fitting of the Scheil model was performed over selected ranges using a lower limit of F_s 0.05 and upper limits of both F_s 0.50 and F_s 0.80, to give an indication of the sensitivity of the method to the range of the freezing curve over which fitting was performed. However, these limits were not possible for the metals A and N. For these two metals, upper limits of F_s 0.25 and F_s 0.50 were employed (except for the $k = 0$ variation of the Scheil method for the cell Al-N, which did not require adjustments of the ranges applied). Metal A consistently presented a high peak (about 2 mK above the mean temperature of the plateau) at the beginning of the freeze, indicating the presence of a high k impurity, almost certainly Ti, as a high Ti concentration was indicated by all the GDMS analyses. For the fitting of the Scheil model with k fixed at zero, this peak at the beginning had to be excluded from the fit.

A key result which is evident in figure 109 is the relatively large variation in the corrections which depend on the GDMS analysis. This is attributable to the very large

inconsistencies in the GDMS results from different providers, for the same metal samples. The methods which exhibited the best consistency (i.e. quantitative agreement) were the Hybrid SIE/Modified-OME method, and the Scheil method (provided k was fixed at zero in the fit). Both these methods are insensitive to errors in the GDMS analysis. This is because the SIE component of the hybrid SIE/Modified-OME method only takes into account impurities with $k > 0.1$, so that relatively large amounts of impurity are needed to effect a given temperature depression compared with impurities having $k < 0.1$, while the Scheil method does not rely on the GDMS analysis at all.

All methodologies investigated in this thesis are advocated by one or more National Metrology Institutes. As this thesis has shown, each of these methods yield a different estimate, which makes it difficult to establish a comparability pattern among them. This subject still demands further studies in order to substantiate the adoption of a method that can appropriately encompass all the aspects inherent to the influence caused by impurities in high purity fixed-point materials. Despite all methodologies proposed, the methods hitherto endorsed by the BIPM/CCT are still the SIE (and OME if the SIE is not feasible) and the direct comparison of cells, which is the method currently used to account for the impurity effects (which actually supersedes this and any other effects) in international comparisons at the level of NMIs. The comparison of cells keeps the traceability and comparability of the fixed-point temperature realisations performed by the various NMIs and metrology laboratories across the world, notwithstanding particular effects caused by impurities in the cells involved since these effects would be accounted for by the temperature differences found in between the cells.

Chapter 7

Conclusions and suggestions for further research

ITS-90 temperature fixed points have to be constructed using materials of very high purity since the scale is based upon phase transformations of ideally pure substances. Currently, improvements in measurement capabilities at the level of National Metrology Institutes are impeded mostly by impurities in fixed point cells, either present in the raw material or arising from contamination during construction. Residual impurities below ppm levels can cause a temperature difference of the order of a few millikelvins, the most substantial contribution to the uncertainty of primary SPRT calibrations. In order to tackle this issue, in 2005 two methods were recommended by the CCT but it was only recently that some advances and publications allowed their implementation in full. Since then, a number of complementary methods have been proposed, which are based on the shape of the freezing curve itself. These complementary methods would present as their main advantage the lack of dependence on chemical assays; however, the disadvantage is that they rely heavily on various assumptions about the relationship between the shape of the freezing curve and the impurities.

This thesis was based on measurements made at the freezing point of aluminium, 660.323 °C as defined by the ITS-90. The main reason for this ITS-90 fixed point being chosen for this study is that it is the highest temperature fixed point accessible to SPRTs and a key fixed point for the calibration of high temperature SPRTs. The purpose of the present thesis was to construct a suite of five aluminium fixed point cells, each using metal from a different source (hence exhibiting a wide range of impurity effects) and systematically apply the available impurity correction methods to all cells to identify the consistency of the methods and any difficulties in implementing them.

The fixed point cells were constructed using batches of nominally 99.9999 % (6N) pure aluminium obtained from five different suppliers: Alfa Aesar (USA), ESPI Metals (USA), Honeywell (USA), New Metals and Chemicals (UK) and Sumitomo Corporation (Japan). The aluminium was supplied in the form of shots/slugs, the only exception being a monolithic block supplied by Sumitomo. The purity of the graphite parts was declared to be 99.9995 % by the supplier (SGL Carbon). The argon used within the cell was contained in a dedicated cylinder and its purity was declared to be 6N grade.

The design of the cell was basically one which has been in use by the thermometry team at NPL for a long time. This could be advantageous as the equipment and procedures used in various world leading NMIs are similar so that the results of this thesis could be directly applied to other standards. In essence, the cell consists of an aluminium ingot contained within a graphite crucible (with graphite felt disks interspersed with graphite heat shunts on top), all enclosed in a quartz tube. The cell, which also has a quartz re-entrant well for the insertion of the SPRTs, is sealed with a (water cooled) metal cap that is connected to an external gas handling system for pumping and backfilling with pure argon.

The construction of all cells meticulously followed the same procedure to ensure the investigation could be performed as systematically as possible. Great care was taken to avoid the contamination of the materials. Prior to use, the graphite pieces were baked in vacuum at 1100 °C for a period of 48 hours, while the graphite felt discs were cut and baked at around 1000 °C for 40 hours. Each set of components was baked separately in the same dedicated clean quartz tube. The casting of the aluminium fixed point ingot could be completed in two stages: the first containing a 200 g load and the second stage containing the remainder mass (approximately 32 g) and the insertion of the graphite re-entrant well. This was performed at a temperature of about 670 °C in argon atmosphere (pressure around 103 kPa). In average, a total of 231.9 g was employed in each cell, which is equivalent to an immersion depth of 172 mm for SPRTs inside the thermometric well (column of liquid aluminium).

In order to perform the measurements with the cells, equipment of the best kind currently available were used: a Fluke 9114 three-zone furnace coupled with water cooling circulation; two brand new 25.5 ohm SPRTs; an ASL F900 thermometry bridge (previously calibrated and adjusted to provide optimal performance) connected to a calibrated 25 ohm standard

resistor maintained at 20 °C in an oil bath (long term stability of 0.004 °C). Before use, the furnace had been optimised for use with these aluminium cells through a series of tests to identify the best controller parameters to guarantee optimal thermal stability and uniformity during the freezing realisations. These tests were performed at a temperature around 658 °C. The long term stability of the furnace was 32 mK (peak to peak, over a period of 50 hours) and the uniformity was equivalent to 13.3 mK, in an ascending gradient as measured up to 14 cm from the bottom of the re-entrant well. As for the SPRTs, before being used for the measurements they were properly annealed and selected as the most stable sensors from a suite of six thermometers extensively tested. After reaching stability, their resistance drift at the triple point of water (in consecutive measurements after being soaked at 670 °C during the annealing) did not exceed 0.1 mK, showing an outstanding performance. The measurements considered in this thesis were made with the SPRT manufactured by Chino Corporation, model R800-2, serial number RS129-03.

Apart from the equipment described above, the investigation also employed one reference aluminium cell Al 10/09 (setup in a dedicated furnace) and four triple point of water cells from the NPL batch of standard cells. The correction for the aluminium cell was 3.18 mK ± 1.72 mK (k = 2). As for the TPW cells, they were used only when their ice mantles were adequately annealed and had no corrections assigned for them but the uncertainty for their calibration was ± 70 µK (k = 2).

The measurements were recorded via bespoke software that communicated with the thermometry bridge via IEEE-488 interface, controlling it and acquiring the data. The measurements used for this thesis were based, for each cell, on an initial measurement of the SPRT Chino at the TPW, followed by four sets of melting/freezing point realisations in the aluminium cell (plus a further freeze specific for the comparison) and the final measurement at the TPW. For the melting curves, the furnace temperature was adjusted to 5 °C above the melting point and the fixed point material left molten for 20 hours to allow the diffusion of impurities in the metal. As for the freezing curves, after the inner solid/liquid interface was induced, the furnace temperature was set to 0.4 °C below the freezing point. Both melting and freezing realisations were made with the cell filled with pure argon to a pressure of 1 atm (101 325 Pa). The freezing curves used for the calculations of the cell comparison included a procedure to evaluate the self-heating effect of the SPRT in the cells. The cells

were compared in terms of $W(T_{90})$, after corrections for the self-heating effect and differences in hydrostatic head were appropriately applied.

In order to better characterise the impurity profile of the metal samples and to implement some of the correction methodologies investigated, samples were prepared and sent to three third party laboratories (AQura, NRC and NIM) to be chemically analysed by the technique known as glow discharge mass spectrometry (GDMS). This technique is capable of detecting impurities at sub-ppb levels. Since the samples had to be cast and prepared according to the GDMS suppliers' requirements, further analyses were performed (X-ray photoelectron spectroscopy, XFR, and scanning electron microscopy, SEM) and they confirmed the samples were not contaminated during the process of sample preparation.

In total, seven methodologies were investigated. They were: the sum of individual estimates (SIE), the overall maximum estimate (OME), the hybrid SIE/modified OME method (the hybrid method), the Scheil method, the gradient method, the thermal analysis method (1/F method) and the direct comparison of cells. For the hybrid method, only the impurities with $k \geq 0.1$ were calculated via SIE, while the modified OME component was estimated via least-squares fitting applied to the measured freezing curves over the F_s range from 0.05 to 0.20. The Scheil method was applied to two ranges of F_s from 0.05 to 0.50 and 0.05 to 0.80 in two configurations (firstly with the Scheil equation variables T_0, mc and k set as free parameters, and secondly with T_0, mc set as free parameters but k fixed as zero). As for the gradient method, it was calculated through a linear fitting to the freezing curve in the F_s range from 0.45 to 0.55, while the thermal analysis was calculated via a linear regression applied to the range 1/F=1 to 1/F=1.5.

Large discrepancies were exhibited by the various GDMS assay results from the three laboratories. The impurity profile of the new results are very different from the impurity distribution indicated by the original assays supplied with the aluminium samples, notably the overall impurity content. Much more impurities were detected (in both quantity and type) by the third party labs than the suppliers' own assays, which implies that the latter may be incomplete. Furthermore, this characterises the material only before it is cast into an ingot and used in the fixed point cell, as further reactions take place which potentially degrades the material purity.

The vast majority of laboratories that construct fixed point cells make use of only the information given in the assays supplied with the samples, not ordering a further independent chemical analysis. This means that evaluations based solely on this information would yield incomplete accounts/assumptions about the impurities and corrections that are due. Still, measurement uncertainties are rarely declared in the assays. Such issues call for an urgent need for the traceability of GDMS instruments (calibration and comparison methods). These facts hinder considerably the application and reliability of the correction methodologies that solely depend on the chemical analysis, namely the SIE and the OME methods (the ones recommended by the CCT) at present.

From the five cells which were constructed and measured for this study, two of them (cells Al-A and Al-N) presented an abnormal, i.e. non-monotonic, shape of the freezing curves despite all the care taken to avoid contamination of the materials. The steep beginning of the freezing curve in cell Al-A (equivalent to about 2.2 mK) was possibly caused by the expressive concentration of titanium (479 ppb, 600 ppb and 640 ppb) detected by the GDMS providers. This assumption was guided and reinforced by the chemical analysis. It is important to highlight here that, as mentioned in the previous paragraph, were it not for these extra analyses, this connection would not be verified since according to the assay provided by Alfa Aesar the titanium content was only 37 ppb. As for the discontinuity towards the end of the freezing slope measured in cell Al-N, it was speculated that somehow the impurities that caused this behaviour were predominantly effective in a later stage of the freezing curve due to inhomogeneous distribution of the impurities.

Given the results obtained from the calculations according to the various methodologies investigated, it was shown that indeed the methods recommended by the CCT were the most inconsistent results, along with the Scheil method (the '*free k*' variant). The most consistent methods, on the other hand, were the hybrid SIE/modified OME and the Scheil method with the distribution coefficient fixed at zero (Scheil method, $k = 0$). Since the hybrid method is partly based on the chemical analysis and partly derived from the actual freezing curve measurements, any differences in the GDMS assay will tend to have a smaller impact on the overall result.

To conclude, this is the first time that a suite of five aluminium fixed point cells, each constructed following the same rigorous procedure using aluminium from a different source,

has been subjected to a systematic analysis of impurity correction methodologies by obtaining a series of freezing curves measured under identical conditions for all five cells. Also for the first time, GDMS samples were meticulously prepared and analyses were obtained from three different providers for each of the five metals used.

7.1. Suggestions for further research

As future investigations and suggestions for improvements, much still has to be done with regards to the GDMS analysis. To date it is the most appropriate technique to analyse high purity metals (overall impurity concentration equivalent to 1 ppm or better), performing multi-element analysis with direct solid sampling capabilities. However, the main drawback of the technique (maybe for all chemical analysis types) is the lack of agreement in the results from different suppliers, and the absence of any declaration of uncertainty. There are few laboratories that commercially provide this type of analysis but their results must agree within a reasonable level. This issue calls for the intervention of an international organisation (most probably the Consultative Committee for Amount of Substance, CCQM) to enforce guidelines, standards, calibration regimes and procedures (using certified reference materials to calibrate the analysers), inter-comparisons, etc.

One issue to be investigated would consist of repeating the GDMS analyses but swapping the samples that were returned among the laboratories. Essentially, that would mean that the same sample would be measured by the three laboratories used: the samples originally measured by AQura would be also sent to NRC and later to NIM, and so on. This would be another proof of the inconsistencies in the analysis and ultimately it would be a blind inter-comparison. Furthermore, it could also be extended to chemical analysis of samples extracted from the aluminium ingots, right after the construction of the cell was completed and also after a given number of hours in use. This would provide evidence of the changes/evolution in the impurity profile from the initial raw material, to the material after an initial reaction with the other materials during casting, and after some aging of the cell.

Given the current limitations related to the reliability of the GDMS analysis, the application of the SIE correction methodology lacks credibility. Therefore, the CCT endorsement of this methodology ought to be reviewed in the near future, leading to further

investigations and the continuation of the discussion on how the effect of impurities in fixed point cells should be dealt with: apply the estimate as corrections, use the estimate as an uncertainty component (while the correction assigned should be relative to comparisons with reference cells), which method(s) should be endorsed (if so, in which circumstances) and so on. Hopefully the present investigation described in this thesis will help substantiate these changes. No matter what the outcome of this will be, surely the scientific community, especially the thermometry laboratories in NMIs, will benefit from an up-to-date, unified approach that is in line with the available technologies, measurement capabilities and theoretical/experimental data.

References

[1] Childs P R N Practical Temperature Measurement. Oxford: Butterworth Heinemann; 2001.

[2] A story of temperature measurement. London: Negretti & Zambra; 1850.

[3] Quinn T J Temperature. 2nd ed. London: Academic Press Limited; 1990.

[4] Mc Gee T D Principles and methods of temperature measurement. New York: John Wiley & sons; 1988.

[5] Göpel W *et al* Sensors: a comprehensive survey. Volume 4 - Thermal sensors. Weinheim: VCH Publishers; 1990.

[6] Bentley R E Handbook of temperature measurement. Volume 1: temperature and humidity measurement. Singapore: Springer-Verlag; 1998.

[7] Thermodynamic and practical temperature scales. Available from: http://www.bipm.org/en/measurement-units/history-si/temperature-scales/ [Accessed: 10th Feb 2015].

[8] Preston-Thomas H 1990 The International Temperature Scale of 1990 (ITS-90) *Metrologia* 27 3-10 and 107

[9] Guide to the realization of ITS-90: Introduction. Available from http://www.bipm.org/en/committees/cc/cct/guide-its90.html [Accessed: 21st March 2015].

[10] Mangum B W *et al* 1999 On the influence of impurities on fixed-point temperatures *Working Document* CCT-WG1 CCT/99-11

[11] Fellmuth B *et al* 2005 Methodologies for the estimation of uncertainties and the correction of fixed-point temperature attributable to the influence of chemical impurities *Working Document* CCT-WG1 CCT/05-08

[12] Pearce J 2014 Distribution coefficients of impurities in metals *Int. J. Thermophys.* 35 628

[13] Pearce J V, Gisby J A and Steur P P M 2016 Liquidus slopes of impurities in ITS-90 fixed points from the mercury point to the copper point in the low concentration limit *Metrologia* 53 1101

[14] Hill K D and Rudtsch S 2005 Thermometry's dependence on chemical metrology: a needs-based assessment *Metrologia* 42 L1

[15] Ripple D *et al* 2003 Report presented to the CCT by Working Group 1 *Working Document* CCT-WG1 CCT/03-23

[16] Moiseeva N P 2003 The role of the impurity component in the budgets of uncertainties, *Working Document* CCT-WG1 CCT/03-24

[17] Yamazawa K *et al* 2008 Limits of the SIE and the thermal analysis on impurity effect evaluation *Working Document* CCT-WG1 CCT/08-03

[18] Widiatmo J V 2004 A survey on the uncertainty in the realization of ITS-90 metal fixed points due to impurities *AIST Bulletin of Metrology* vol. 3 2 318

[19] Widiatmo J V, Harada K and Arai M 2004 Analyzing metal fixed-point cells from their plateaus *Proc. SICE Annual Conf.* 1936

[20] Widiatmo J V *et al* 2006 Estimation of impurity effect in aluminium fixed-point cells based on thermal analysis *Metrologia* 43 561

[21] Head D I *et al* 2008 The comparison of MTDATA with the melting/freezing point curves of ITS-90 metal fixed points *Int. J. Thermophys.* 29 1796

[22] Pearce J V, Veltcheva R I and Large M J 2013 Impurity and thermal modelling of SPRT fixed-points *Temperature: Its Measurement and Control in Science and Industry* vol. 8, Proc. AIP Conf., 1552 283

[23] Malik Z *et al* 2011 A solidification approach to correcting for the effect of impurities in fixed points *Int. J. Thermophys.* 32 1589

[24] Pearce J V *et al* 2012 Optimization of SPRT measurements of freezing in a zinc fixed-point cell *Metrologia* 49 359

[25] Renaot E, Valin M H and Elgourdou M 2008 Influence of impurities and filling protocol on the aluminium fixed point *Int. J. Thermophys.* 29 852

[26] Ancsin J 2003 Impurity dependence of the aluminium point *Metrologia* 40 36

[27] Ancsin J 2003 ITS-90: the instability of the Al point *Metrologia* 40 232

[28] Renaot E 2008 Evidence of furnace-related aluminium cell contamination *Acta Metrologica Sinica* 29

[29] Renaot E and Martin C 2011 Aluminium fixed point: impact of the time spent in the liquid phase on the liquid-solid transition and obviousness of the pollution of the ingot *Int. J. Thermophys.* 32 1496

[30] Head D I, Petchpong P and Au J Y H 2008 Effects of impurities on the melting curve of the aluminium fixed point *Acta Metrologica Sinica* 29

[31] Petchpong P and Head D I 2011 The influence of titanium on the aluminium fixed-point temperature *Int. J. Thermophys.* 32 1507

[32] BIPM. Supplementary information for the International Temperature Scale of 1990. Sèvres: BIPM; 1997.

[33] BIPM. Techniques for approximating the International Temperature Scale of 1990. Sèvres: BIPM; 1997.

[34] Mise en pratique for the definition of the kelvin. Available from http://www.bipm.org/utils/ en/pdf/MeP_K.pdf. [Accessed 25th May 2016].

[35] Standard guide for use of freezing-point cells for reference temperatures (2003) *ASTM Standards* document E 1502-98

[36] Fellmuth B and Hill K D 2006 Estimating the influence of impurities on the freezing point of tin *Metrologia* 43 71

[37] Rudtsch S 2005 Cryoscopic constant, heat and enthalpy of fusion of metals and water *Working Document* CCT/05-04/rev

[38] White D R *et al* 2009 Uncertainties in the Realisation of the SPRT Subranges of the ITS-90 *Working Document* CCT/08-19/rev (http://www.bipm.org/cc/CCT/ Allowed/24/D19_rev_WG3_Doc_rev_10July2009.pdf)

[39] Rudtsch S *et al* 2008 High-purity fixed points of the ITS-90 with traceable analysis of impurity contents *Int. J. Thermophys.* 29 139

[40] Ripple D *et al* 2008 Recommended list of common impurities for metallic fixed-point materials of the ITS-90 *Working Document* CCT/08-16

[41] Fahr M and Rudstch S 2008 A new method for the quantification and correction of thermal effects on the realization of fixed points *Int. J. Thermophys.* 29 126

[42] Fahr M, Rudtsch S and Aulich A 2011 Further findings of impurity precipitation in metal fixed points *Int. J. Thermophys.* 32 2239

[43] Fahr M and Rudtsch S 2009 Oxides in metal fixed points of the ITS-90 *Metrologia* 46 423

[44] Rudtsch S *et al* 2011 Procedure for the impurity-related correction at the indium fixed-point *Int. J. Thermophys.* 32 126

[45] Strouse G F NIST methods of estimating the impurity uncertainty component for ITS-90 fixed-point cells from the Ar TP to the Ag FP (Document CCT/03-19). Sèvres: BIPM, 2003.

[46] Hashimoto E *et al* 1995 Purification of ultra-high purity aluminium. *Journal de Physique IV*. Available from https://hal.archives-ouvertes.fr/jpa-00254008/document [Accessed 7th April 2014].

[47] Mangum B W *et al* 2002 Summary of comparison of realizations of the ITS-90 over the range 83.8058 K to 933.473 K: CCT Key Comparison CCT-K3 *Metrologia* 39 179

[48] Heyer D *et al* 2008 Final report on EUROMET T-K4 (EUROMET Project 820): Comparison of the realizations of the ITS-90 at the freezing points of Al (660.323 °C) and Ag (961.78 °C) *Metrologia* 45 Tech. Suppl. 03003

[49] The BIPM key comparison database. Available from http://kcdb.bipm.org/ [Accessed 12th June 2016].

[50] Wieser M E *et al* Atomic weights of the elements 2011 (IUPAC technical report). Pure Appl. Chem., Vol. 85, No. 5, pp. 1047, 2013.

[51] CIAAW Commission on Isotopic Abundances and Atomic Weights. Table of Standard Atomic Weights 2013. Available from http://www.ciaaw.org/pubs/ TSAW2013_xls.xls [Accessed 9th Jan 2015].

[52] 9114 freeze point furnace user's guide. Fluke corporation. American Fork: 2006.

[53] Guide to the realization of ITS-90: triple point of water. Available from http://www.bipm.org/en/committees/cc/cct/guide-its90.html [Accessed: 21st March 2015].

[54] Da Silva R *et al* Investigation of gallium melting point as a crosscheck for water triple point measurements. Proceedings of TEMPMEKO & ISHM 2010.

[55] Mangum, B W *et al* On the International Temperature Scale of 1990 (ITS-90). *Metrologia*, 36, 79-88. 1999.

[56] Guide to the Realization of the ITS-90: Metal Fixed Points for Contact Thermometry Available from http://www.bipm.org/en/committees/cc/cct/guide-its90.html. [Accessed: 21st March 2015].

[57] Guide to the Realization of the ITS-90: Platinum Resistance Thermometry Available from http://www.bipm.org/en/committees/cc/cct/guide-its90.html. [Accessed: 21st March 2015].

[58] Da Silva R, Pearce J V and Machin G 2017 A systematic evaluation of contemporary impurity correction methods in ITS-90 aluminium fixed point cells. *Metrologia*, 54, 365-380 (https://doi.org/10.1088/1681-7575/aa6ab3)

Appendix A